Modelling Colliding-Pulse Mode-Locked Semiconductor Lasers

Svend Bischoff

LYNGBY 1997
Ph.D-Thesis

IMM

Printed by IMM, DTU

Preface

The present Thesis is written in partial fulfilment of the requirements for the Ph.D. degree from the Technical University of Denmark. The work was supported by a scholarship from the Technical University of Denmark and carried out at the Department of Mathematical Modelling (IMM) under the supervision of Associate Professor, lic. techn. Mads Peter Sørensen (main supervisor, IMM), Associate Professor, dr. techn. Peter L. Christiansen (IMM) and Associate Professor, lic. techn. Jesper Mørk (Mikroelectronic Centeret, MIC).

The experimental measurements presented in chapter 2 have been made by S. D. Brorson, T. Franck, M. Hofmann and L. Prip at Tele Danmark R & D.

Abstract

A discussion of three topics in the field of non-linear optics is presented.

We begin with the Colliding-Pulse Mode-locked (CPM) Quantum Well (QW) laser. A large signal model consisting of a wave-propagation equation for the electrical field and a rate equation model for the material response is derived. The wave-propagation equation of the electrical field is derived from Maxwell's equations in the slowly varying amplitude approximation. The material dynamics are derived from semiclassical density matrix equations. The model for the saturable absorber (a reverse biased semiconductor waveguide) is improved by fitting critical parameter values in such a way that the model response corresponds to many-body gain calculations.
The large signal model is used to explain femtosecond pump-probe measurements on semiconductor waveguide structures, which are identical to those employed in the CPM lasers fabricated at Tele Danmark R & D. The femtosecond pump-probe measurements show that the semiconductor waveguide response is made up of fast and slow dynamics. The fast dynamics are attributed to spectral hole burning and carrier heating, while the slow dynamics are attributed to carrier transport mechanisms in the semiconductor waveguide.
The incorporation of these fast and slow material dynamics in the large signal model are found to be important for understanding the operation principles of the CPM QW laser. Thus, our large signal model is used to explain the operation principles of the CPM QW laser. The pulse-width is found to be determined by a balance between pulse broadening in the

gain sections (forward bias) and pulse shortening in the saturable absorber (reverse bias). Also, the instantaneous wavelength chirp of the CPM pulses is found to be determined by a complicated interplay between the gain and saturable absorber dynamics.
The effect of pulse-broadening upon an increased injection current is attributed to the fast gain dynamics in the gain sections. Furthermore, the optical power spectrum is seen to broaden with increasing injection current, which can be attributed to the effect of an enhanced self-phase modulation in the gain section. The variation of the DC component of the reverse bias on the saturable absorber results in minor changes in the optical power spectrum and pulse width.
Hybrid mode-locking of the CPM lasers is achieved by modulating the reverse bias on the saturable absorber. The synchronization of the CPM pulse train with the external modulation frequency is the result of the Quantum Confined Stark Effect (QCSE). The instantaneous wavelength chirp is in agreement with our large signal model found to critically depend on the modulation frequency of the AC component of the reverse bias.

The CPM laser is an edge emitting laser, where the light propagation is within the plane of the active layer. In Vertical Cavity Surface Emitting Lasers (VCSEL) the light propagation is perpendicular to the active layer. The operation principles of VCSEL differ from the edge emitting laser due to the different device design. However, we have not investigated the operation principles of VCSEL in this thesis.
The second topic of this thesis is the theoretical study of the excitonic semiconductor response for varying material thickness in the case of linear optics. The presented model can be viewed as the initial stage of developing a model for VCSEL with active layers, which material response cannot be approximated to yield the ideal 2-D (two-dimensional) or 3-D (three-dimensional) case.
The light propagation perpendicular to the semiconductor slab is determined by analytically solving Maxwells equations. The material response is described by the semiconductor Bloch equations which are derived from the system Hamiltonian. The material thickness is varied between 1 - 80 nm. The theoretical study shows that we, for a material thickness of less than 8 nm to a good approximation can assume the material response to be close to the ideal 2-D case. The ideal 3-D case is almost reached at a thickness

of 80 nm.
In addition to studying the stationary material response like linear "transmission" (absorption) spectra, we have also studied the non-stationary effects. Here we see the development of an exciton free layer (the so called "dead layer") which is an important factor in the theories applied for solving the half-space problem.

Modulational Instability (MI) in optical fibers with periodic or random variations in the fiber core is the third and final topic in the field of non-linear optics discussed in this thesis. The wave propagation in optical fibers with a fluctuating fiber core is described by the non-linear Schrödinger equation, where the coefficient in front of the non-linearity is periodically or randomly varied corresponding to periodic or random changes in the fiber core. We show analytically and numerically the existence of modulational instability in the case of normal and anomalous dispersion. Furthermore, the influence of the self-steepening effect on the process of modulational instability is investigated. Parametric resonance (MI) is shown to exist for any perturbation of the steady state solution in the case of random fluctuations of the non-linearity.

Resumé

En diskussion af tre emner inden for området af ikke-lineær optik præsenteres.

Vi diskuterer først den "kolliderende" puls fase-låste laser. Der udledes en stor-signal model, der består af en ligning, der beskriver det elektriske felts bølge-udbredelse, og et sæt af rate-ligninger, der beskriver materiale egenskaberne. Bølgeligningen, der beskriver det elektriske felts udbredelse, er udledt fra Maxwells ligninger, hvor vi har lavet den langsomt-varierende-amplitude-approksimation. Materiale egenskaberne er udledt fra semi-klassiske tætheds matrix ligninger. Modellen for den mætbare absorber (en negativ forspændt halvleder) er blevet forbedret ved at fitte kritiske parametre, således at materiale egenskaberne er i god overensstemmelse med mange-legems beregninger af absorptionen. Stor-signal modellen er brugt til at forklare femtosekund pumpe-probe målinger lavet på halvleder bølgeledere, som er identiske med dem brugt i fremstillingen af den "kolliderende" puls fase-låste laser hos Tele Danmark R & D. Femtosekund pumpe-probe målingerne viser, at materialeresponset består af både hurtige og langsomme effekter. De hurtige effekter skyldes spektral hulbrænding og ændringer i ladningsbærer-temperaturen, medens de langsomme effekter er resultatet af ladningbærertransport i halvlederstrukturen.
Det vises at inkluderingen af de hurtige og langsomme materialeprocesser af halvlederen i vores stor-signal model er vigtig, for at forstå den "kolliderende" puls fase-låste kvantebrøndslasers virkemåde. Puls bredden af laseren er bestemt ved en balance mellem puls-forbredning og komprimer-

ing i henholdsvis forstærknings- og absorbersektionerne. Den instantane bølgelængde (”chirpet”) bestemmes ligeledes til at være betemt ved en kompliceret balance mellem effekterne af forstærker- og absorbersektionerne.
Pulsforbredningen for øget strøm til forstærkersektionerne vises at være resultatet af de hurtige effekter relateret til spektral hulbrænding og ladningsbærertemperatur ændringer. Derudover vises det, at forbredningen af det optiske effektspektrum for øget strøm skyldes en øget selv-fase modulation i forstærker sektionerne. Derimod resulterer ændringer i DC værdien af den negative spænding påtrykt den mætbare absorber ikke i de store ændringer af hverken pulsbredde eller det optiske effektspektrum.
Hybrid fase-låsning af den ”kolliderende” puls fase-låste kvantebrønds laser opnås ved, at modulere spændingen på den negativt forspændte absorbersektion. Synkroniseringen af det fase-låste pulstog med den eksterne modulationsfrekvens er her bestemt til at være resultatet af, at båndgabet varierer med den eksterne påtrykte spænding (”Quantum Confined Stark Effect”). I overensstemmelse med eksperimenter finder vi at chirpet af pulserne i tilfældet af hybrid fase-låsning afhænger af den påtrykte modulationsfrekvens.

Den ”kolliderende” puls fase-låste laser er en laser, hvor lysudbredelsen foregår i selve planen af det aktive lag. I ”vertikale-overflade-emitterende-lasere” (VCSEL) er lysudbredelsen vinkelret på det aktive (forstærkende) lag. Operationsprincipperne af de to lasere er således forskellige på grund af deres forskellige design. Vi undersøger ikke en ”vertikale-overflade-emitterende-laser” i denne afhandling, men ser kun på lysudbredelsen igennem en halvleder for varierende materialetykkelse i tilfældet af lineær optik. Den udledte model kan betragtes som en begyndende udvikling af en model til beskrivelse af VCSELs, som har et aktivt lag, hvis materiale egenskaber ikke kan approksimeres til at være beskrevet ved det ideelle to- eller tre-dimensionale tilfælde.
Lysudbredelsen vinkelret på det aktive lag er bestemt ved Maxwells ligninger, som er løst analytisk. Materialeegenskaberne af det aktive lag er beskrevet ved halvleder-Bloch-ligningerne, som er udledt fra systemets Hamliton. Det aktive lags materialetykkelse er varieret mellem 1 og 80 nm. Den teoretikse undersøgelse viser, at vi for en lagtykkelse på mindre end 8 nm kan approksimere materiale-egenskaberne til stort set, at svare til tilfældet af en ideel to-dimensional struktur; medens materiale-egenskaberne for et aktivt lag på 80 nm næsten svarer til det ideelle tre-dimensionale tilfælde.

Vi har ikke kun undersøgt det stationære materialerespons, men også undersøgt de ikke-stationære egenskaber. Vi observerer således udviklingen af et exciton-frit område (det såkaldte "dead layer") i grænselaget af det aktive lag. Dette exciton-frie område er en vigtig komponent i teorierne anvendt for løsningen af halvrums problemet.

Modulations instabilitet (MI) i optiske fibre med periodisk og tilfældig variation af fiberdiameteren er det tredie og sidste emne inden for ikke-lineær optik, som behandles i denne afhandling. Lysudbredelsen i en optisk fiber med varierende diameter kan teoretisk beskrives ved den ikke-lineære Schrödingerligning, hvor det ikke-lineære led varieres, svarende til variationen af fiberdiameteren. Vi viser analytisk og numerisk eksistensen af MI for både normal og anormal dispersion. Herudover, undersøges det, hvilken indflydelse "self-steepening" effekten har på MI områderne. Desuden vises det at MI eksisterer for en hvilken som helst perturbation af "steady state" løsningen i tilfældet af en tilfældig modulation af ikke-lineariteten i den ikke-lineære Schrödingerligning.

Acknowledgements

I would like to express my sincere gratitude to my supervisors, Mads P. Sørensen, Peter L. Christiansen and Jesper Mørk for their guidance throughout the project.

Special thanks go to Jesper Mørk for his great dedication and patience in our many scientific discussions and when writing publications. He is also thanked for making it possible for me to be at Tele Danmark R & D for one year of my studies.

Special thanks also to Stuart D. Brorson, Thorkild Franck and Martin Hofmann for the good team work and stimulating discussions on the colliding-pulse mode-locked quantum well laser. Krister Fröjdh is thanked for providing the many-body theory gain calculations for the case of a reverse biased semiconductor waveguide.

I wish to thank Stephan W. Koch for inviting me to visit the Department of Physics and Material Sciences center at the Philipps-University in Marburg, Germany, and for introducing me to the field of many-body theory. Special thanks also to Andreas Knorr for his great dedication and patience in our many scientific discussions. I also wish to thank all group members at the Department of Physics and Material Sciences center for the pleasant stay.

Fakthulla Kh. Abdullaev is thanked for introducing me to the field of modulational instability.

Carl B. Clausen and Nerys E. John are thanked for proof reading parts of this thesis.

Finally I wish to thank my colleagues at the mathematical physics group at IMM for good collaboration, and especially our secretaries Lise Gudmandsen and Dorthe Thøgersen, for always being kind and helpful.

List of publications

* "Modulational Instability in Optical Fibers Near the Zero Dispersion Point". F.Kh. Abdullaev, S. Bischoff, P.L. Christiansen, S. Darmanyan, and M.P. Sørensen. Optics Communications, **108**, pp. 60-64, 1994.
* "Physics of Colliding-Pulse Mode-Locked Quantum-Well Lasers", S. Bischoff, M. P. Sørensen, J. Mørk, S. D. Brorson, J. M. Nielsen, A. Møller-Larsen and L. Olofsson. Proc. CLEO/USA, (Baltimore), 1995, Paper CThI43.
* "Physics of Modelocking in Monolithic CPM Lasers", S. D. Brorson, T. Franck, S. Bischoff, Z. Wang, A. Møller-Larsen, J. M. Nielsen, M. P. Sørensen and J. Mørk. Proc. CLEO/Pacific Rim, Chiba, Japan, 1995, Paper FV4.
* "Characterization of Wavelength Chirping in Modelocked Semiconductor Lasers", S. D. Brorson, Z. Wang, T. Franck, S. Bischoff, A. Møller-Larsen, J. M. Nielsen, J. Mørk and M. P. Sørensen. Proc. ECOC'95 (Belgium), 1995, Paper We.P.38.
* "Characterization of Wavelength Chirping in Modelocked Monolithic CPM Lasers", S. D. Brorson, Z. Wang, T. Franck, S. Bischoff, A. Møller-Larsen, J. M. Nielsen, J. Mørk and M. P. Sørensen. IEEE Photonics Technology Letters, **7** no. 10, (1148-1150) 1995.
* "Pulse-Shaping Mechanism in Colliding-Pulse Mode-Locked Laser Diodes", S. Bischoff, M. P. Sørensen, J. Mørk, S. D. Brorson, T. Franck, J. M. Nielsen and A. Møller-Larsen. Applied Physics Letters, **67** no. 26, (3877-3879) 1995.

* "Modelling and Characterization of Colliding Pulse Mode-Locked (CPM) Quantum Well Lasers", S. Bischoff, S. D. Brorson, T. Franck, M. Hofmann, L. Prip, M. P. Sørensen and J. Mørk, SPIE Conference "Physics and Simulation of Optoelectronic devices IV", San Jose, California, USA, SPIE, **2693**, pp. 477-488, 1996.
* "Pulse Shape Characterisation of Colliding Pulse Modelocked Laser Diodes", T. Franck, M. Hofmann, L. Prip, S. Bischoff, S. D. Brorson and J. Mørk, CLEO'96, Anaheim, California USA, 1996, Paper CTuL10.
* "Femtosecond Carrier Dynamics and Modelocking in Monolithic CPM Lasers", S. D. Brorson, S. Bischoff, J. Mørk, A. Møller-Larsen and J. M. Nielsen. IEEE Photonics Technology Letters, **8** (10), p. 1308-1310, 1996.
* "Modulational Instability of Electromagnetic Waves in Media with Varying Nonlinearity", F. Kh. Abdullaev, S. A. Darmanyan, S. Bischoff and M. P. Sørensen. Jour. Opt. Soc. Am. B, **14** (1), pp. 27-33, 1997.
* "Theoretical Investigation of the Excitonic Semiconductor Response for Varying Material Thickness: Transition from Quantum-Well to Bulk", S. Bischoff, A. Knorr and S. W. Koch. Physical Review B, **55** (12), pp. 7715-7725, 1997.
* "Chirp of Hybridly Modelocked Monolithic CPM Diode Lasers", M. Hofmann, S. Bischoff, T. Franck, L. Prip, K. Föjdh, S. D. Brorson and J. Mørk. Applied Physical Letters, **70** (19), may 1997.
* "Monolithic Colliding Pulse Mode-Locked Semiconductor Lasers", S. Bischoff, J. Mørk, T. Franck, S. D. Brorson, M. Hofmann, K. Fröjdh, L. Prip and M. P. Sørensen. Accepted (invited paper) for publication in Quantum Semiclass. Opt.
* "Pulsewidth Dependence upon Gain Current and Absorber Voltage in Monolithic CPM Lasers", S. D. Brorson, T. Franck, S. Bischoff, L. Prip, M. Hofmann, J. M. Nielsen, and J. Mørk. Submitted for publication in IEEE Photonics Technology Letters.
* "Propagation of Optical Solitons in Random Media", F. Kh. Abdullaev, J. H. Hensen, S. Bischoff and M. P. Sørensen. In preparation.

Contents

Chapter 1

General Introduction

It is the goal of applied mathematics to study mathematical models of physical systems to elucidate their operation principles. The development of simple theoretical models requires a strong interaction between experimentalists and theoreticians. In general many parameter values entering a derived or proposed model are determined by experiments while the theoretical models are typically used to improve the device design or to determine the optimum operation conditions.

The purpose of this thesis is to elucidate some of the physics of interest in the field of semiconductor laser modelling, semiconductor optics and fiber optics. To be more specific we will investigate: The Colliding-Pulse Mode-Locked (CPM) Quantum Well (QW) laser diode; the excitonic semiconductor response for varying material thickness in the case of linear optics; and modulational instability of electromagnetic waves in media with spatially varying non-linearity.

1.1 The CPM laser diode

Edge emitting semiconductor lasers are extensively used in today's optical communication networks due to their compactness, reliability and high speed modulation properties [1, 2, 3]. Furthermore, semiconductor lasers can be designed to operate at a wavelength where the fiber loss is minimal [4]. The direct modulation speed of semiconductor lasers can be improved by using an active layer made up of quantum wells (two-dimensional structure) instead of a bulk layer (three-dimensional structure). The improvement in modulation speed is attributed to the difference in the density of states function for two-dimensional (2-D) and three-dimensional (3-D) structures which results in a higher differential gain for the two-dimensional structures [1, 2, 3].

Semiconductors can, by simply modulating the gain current, be modulated at frequencies of up-to 10-30 GHz [1, 2]. Another promising device is the electro-absorption modulator [5, 6] where a multiple QW semiconductor waveguide is reverse biased. The intensity modulation of the electro-absorption modulators is based on the Quantum Confined Stark Effect (QCSE) [7, 8, 9]. QW electro-absorption modulators have been monolithically integrated with Distributed Feed Back (DFB) lasers. These devices have been used in multi-gigabit transmission systems (10 GHz) [10, 11]. Furthermore, one has good control of the lasing wavelength of DFB lasers through the device design which makes the monolithic integrated DFB QW electro-absorption modulator laser a suitable device for Wavelength Division Multiplexed (WDM) optical networks [12].
The generation of optical pulses in excess of 50 GHz is presently not possible with electrically modulated semiconductor lasers. However, pulse repetition rates beyond 50 GHz can be generated by monolithical Colliding-Pulse Mode-Locked (CPM) QW laser diodes [13, 14, 15]. The CPM laser diodes have been demonstrated to produce pico- to sub-picosecond pulses at repetition frequencies from 16 to 350 GHz [13, 16, 17, 18], and have been proposed as a promising pulse source for Time Division Multiplexed (TDM) optical networks [19].

The monolithic CPM semiconductor waveguide is a three contact laser diode, where the two outer sections are forward biased and provide gain, while a short center section acts as a saturable absorber (reverse bias) [13]. A schematic plot of a CPM laser is shown in fig. 2.1. Passive mode-locking occurs by applying an appropriate DC-current value to the gain sections and an appropriate DC-reverse bias to the saturable absorber section. Steady state mode-locked operation is characterized by two counter propagating pulses which collide in the absorber and thus help each other to bleach the saturable absorber. The pulse repetition frequency of the CPM laser is determined by the cavity length.

In chapter 2 we have derived a large signal model for the CPM QW laser. The derived large signal model is quite general and may also be used to simulate electro-absorption modulators or other multi-contact lasers as proposed in Refs. [17, 20, 21]. However, in chapter 2 the large signal model has been used to elucidate the operating principles of the "standard" (three contact) CPM laser diode. The pulse-shaping mechanisms are attributed to an interplay of the material dynamics in the gain and absorber regions. Furthermore, the temporal and spectral properties of the CPM pulses are investigated for varying current and bias conditions, which show a good agreement between theory and measurements. We also study hybridly mode-locked CPM lasers where the reverse bias to the absorber section is modulated.
In App. A the derivation of the rate equation model describing the material dynamics is shown in detail. Furthermore, we discuss the CPM pulse width for different cavity and saturable absorber length in App. B.

1.2 Excitonic semiconductor response for varying material thickness

Vertical Cavity Surface Emitting Laser (VCSEL) diodes [1, 2] have in recent years attracted a lot of attention. The modelling of VCSELs is normally performed under the assumptions of an ideal two-dimensional [22, 23] or three-dimensional active layer. However, it has been shown that propagation effects through the active layer result in significant changes in the transmission spectrum [24]. (Here, the transmission spectrum denotes the in experimental measurements so called absorption spectrum, since propagation effects through the sample are also taken into account [24].)

In chapter 3 we present calculated transmission spectra for the case of linear optics showing that the approximation of only one quantized state in a QW only holds for QW widths of less than 8 nm. For a material thickness of 80 nm we are close to the three dimensional limit.

1.3 Modulational instability of electromagnetic waves in media with periodic or random perturbations

The growth of an initially small perturbation of the steady state solution resulting from the joint action of nonlinear and dispersive effects is often referred to as Modulational Instability (MI) [4, 25]. MI is a phenomena, which exists for a wide class of nonlinear systems such as in the field of plasma physics, deep water waves, optical waveguides etc. [4, 25].
In this thesis the process of MI is investigated for an optical fiber, where the fiber core is periodically or randomly varied. The propagation of electromagnetic waves in optical fibers is theoretically described by the Non-Linear Schrödinger Equation (NLSE) [4, 25, 26], where perturbation terms for the processes of loss, gain, self-steepening etc. can be added [4, 27]. The process of MI is investigated and shown to exist for both normal and anomalous dispersion. Furthermore, the influence of the self-steepening effect on MI is discussed. It is shown that the steady state solution of the NLSE is unstable for any perturbation in the case of random fluctuations of the nonlinearity in the NLSE.

Bibliography

[1] G. P. Agrawal, N. K. Dutta, "Semiconductor Lasers", Van Nostrand Reinhold, New York, 1993.

[2] P. S. Zory, Jr., "Quantum Well Lasers", Academic Press, INC., New York, 1993.

[3] N. Peyghambarian, S. W. Koch, A. Mysyrowicz, "Introduction to Semiconductor Optics", Prentic Hall, New Jersey, 1993.

[4] G. P. Agrawal, "Nonlinear Fiber Optics", Academic Press, San Diego, 1989.

[5] J. Langanay, C. Starck, M. Boulou, M. Nicolardot, J. C. Emerry, C. Fortin, P. Aubert, D. Lesterlin, "Low Spectral Chirp and Large Electroabsorption in a Strained InGaAsP/InGaAsP multiple Quantum Well Modulator", Appl. Phys. Lett., **62** (17), pp. 2066-2068, 1993.

[6] J. A. J. Fells, I. H. White, M. A. Gibbon, R. V. Penty, G. H. B. Thompson, A. P. Wright, R. A. Saunders, C. J. Armistead, "Controlling the Chirp in Electroabsorption Modulators under Digital Modulation", IEEE Electronics Lett., **30** (24), pp. 2066-2067, 1994.

[7] C. Weisbuch, B. Vinter, "Quantum Semiconductor Structures", Academic Press, Inc., San Diego, 1991.

[8] H. Haug, "Optical Nonlinearities and Instabilities in Semiconductors", Academic Press, San Diego, 1988.

[9] K. Fröjdh, "Carrier Transport Effects in Semiconductor Heterostructures for Optical Applications", Doctoral Thesis, Royal Inst. of Technol., Stockholm, Sweden, 1996.

[10] K. Morito, R. Sahara, K. Sato, Y. Kotaki, H. Soda, "MQW Modulator Integrated DFB Lasers for Multigigabit Transmission Systems", Proc.

21st Eur. Conf. on Opt. Comm. (ECOC'95-Brussels), paper Th.B.2.1, pp. 887-891, 1995.

[11] K. Wakita, K. Sato, I. Kotaka, Y. Kondo, M. Yamamoto, "Short Optical Pulse Generation and Modulation by a Multi-Section MQW Modulator/DFB Laser integrated Light Source", IEICE Trans. Electron. **E78-C** (1), pp. 50-54, 1995.

[12] G. Raybon, M. G. Young, U. Koren, T. L. Koch, "Integrated Laser/Modulator Arrays for High Speed Optical Transmission Systems", SPIE'96, High-Speed Semiconductor Laser Sources, **2684**, pp. 102-107, San Jose, January 1996.

[13] Y. K. Chen, M. C. Wu, T. Tanbbun-Ek, R. A. Logan, M. A. Chin, "Subpicosecond Monolithic Colliding-Pulse Mode-Locked Multiple Quantum Well Lasers", Appl. Phys. Lett. **58** (12) pp. 1253, 1991.

[14] M. C. Wu, Y. K. Chen, T. Tanbun-Ek, R. A. Logan, M. A. Chin, and G. Raybon, "Transform-limited 1.4 ps optical pulses from a monolithic colliding-pulse mode-locked quantum well laser", Appl. Phys. Lett., **57**, pp. 759-761, 1990.

[15] Y.-K. Chen, M. C. Wu, "Monolithic Colliding-Pulse Mode-Locked Quantum Well Lasers", IEEE Jour. Quantum Electron., **28** (10), pp. 2176-2185, 1992

[16] D. J. Derickson, R. J. Helkey, A. Mar, J. R. Karin, J. G. Wasserbauer, J. E. Bowers, "Short Pulse Generation Using Multisegment Mode-Locked Semiconductor Lasers", IEEE Jour. Quantum Elec. **28** (10) pp. 2186, 1992.

[17] J. F. Martins-Filho, E. A. Avrutin, C. N. Ironside, J. S. Roberts, "Monolithic Multiple Colliding Pulse Mode-Locked Quantum-Well Lasers: Experiment and Theory", IEEE Journal of Selected Topics in Quantum Electronics, **1**, (2), pp. 539, 1995.

[18] S. D. Brorson, T. Franck, S. Bischoff, L. Prip, M. Hofmann, J. M. Nielsen, J. Mørk, "Pulsewidth Dependence upon Gain Current and Absorber Voltage in Monolithic CPM Lasers", Submitted to IEEE Photon. Technol. Lett.

[19] Z. Wang, J. M. Nielsen, S. D. Brorson, B. Christensen, T. Franck, N. G. Jensen, A. M. Larsen, J. Nørregaard, E. Bødtker, "15.8 Gbit/s System Transmission Experiment using a 5.2 mm Long Monolithic Colliding-Pulse Modelocked Quantum Well Laser Diode", Electron. Lett. **31** pp.272, 1995.

[20] R. J. Helkey, "Subpicosecond Pulse Generation Using Modelocked

Semiconductor Laser Diodes", Department of Electrical and Computing Engineering, University of California at Santa Barbara, 1993.

[21] R. G. M. P. Koumans, R. van Roijen, "Theory for Passive Mode-Locking in Semiconductor Laser Structures Including the Effects of Self-Phase Modulation, Dispersion and Pulse Collisions", IEEE Journal of Quantum Electronics, **32** (3), pp. 478, 1996.

[22] F. Jahnke, H. C. Schneider, S. W. Koch, "Ultrashort Dynamic Response of Vertical-Cavity Surface-Emitting Quantum Well Lasers", SPIE'96, Physics and Simulation of Optoelectronics Devices IV, **2693**, pp. 322-328, San Jose, January 1996.

[23] M. Kira, F. Jahnke, S. W. Koch, "Ultrashort Pulse Propagation Effects in Semiconductor Microcavities", to appear in Solid State Communications.

[24] T. Strouken, A. Knorr, S. W. Koch, M. Hübner, J. Kuhl, "Propagation Effects in Semiconductor Multiple Quantum Well Structures", SPIE'96, Physics and Simulation of Optoelectronics Devices IV, **2693**, pp. 238-249, San Jose, January 1996.

[25] F. Abdullaev, S. Darmanyan, P. Khabibullaev, "Optical Solitons", Springer series in Nonlinear Dynamics, Springer-Verlag, Berlin Heidelberg, 1993.

[26] R. K. Dodd, J. C. Eilbeck, J. D. Gibbon, H. C. Morris, "Solitons and Nonlinear Wave Equations", Academic Press, San Diego, 1988.

[27] J. G. Caputo, M. P. Sørensen, N. Lazaridis, "The Fiber Ring Laser Studied by Collective Coordinates", Jour. Optic. Soc. America B, **12** (1), 1995.

Chapter 2

Monolithic Colliding-Pulse Mode-Locked Lasers

In this chapter we present our large signal model for the CPM laser and illustrate its applications to the case of passively and hybridly mode-locked CPM lasers. Comparison with experimental results are made that elucidate the importance of incorporating details of the ultrafast gain and index dynamics. The ultrafast gain and loss dynamics of the CPM waveguide structure are observed by femtosecond pump-probe measurements on waveguides identical to those employed in the CPM laser fabricated at Tele Danmark R & D. These measurements are in good agreement with theoretical results, where the CPM laser model has been used to simulate the pump-probe experiment.

Thereafter, the model is used to characterize the operational principles of the CPM laser diode. The pulse-shaping and wavelength chirp of the CPM pulses is found to be the result of a complicated interplay between the gain and saturable absorber dynamics. The experimentally measured pulse-width dependence upon variation of gain current and applied reverse bias on the saturable absorber is explained by fast gain dynamics. The experimentally observed broadening of the optical power spectrum with gain current is found to be mainly due to self-phase modulation in the gain sections.

The large signal model is presented in section 2.2. The important material dynamics in the CPM semiconductor waveguide are elucidated by the pump-probe data which are presented in section 2.3. This section gives a basic understanding of the material dynamics which have been incorporated in the derived rate equation model. In section 2.4 we discuss the results obtained by the model in the passive mode-locking case, where we focus on the temporal and spectral pulse-shaping mechanisms. In section 2.5 hybrid mode-locking of the CPM laser is discussed for the case of variation of the DC values of the current to the gain sections and the externally applied reverse bias to the saturable absorber. We also discuss the effect of detuning the external modulation frequency from the passive repetition frequency. Finally, we give a short summary of our main results in section 2.6.

2.1 Introduction

Cheap, compact and reliable sources of short optical pulses are needed for high bit-rate time division multiplexed (TDM) optical networks. One of the proposed light sources is the monolithic colliding-pulse mode-locked (CPM) quantum-well (QW) laser [1, 2]. The monolithic CPM laser is a compact light source which is thermally and mechanically very stable since there are no moving parts. Furthermore, the undesirable intracavity reflections, which produce multiple pulses per round-trip in the case of external cavity mode-locked lasers, are minimized. The monolithic CPM laser has been experimentally demonstrated to produce pico- to sub-picosecond pulses at repetition frequencies from 16 to 350 GHz [2, 3, 4, 5, 6]. Furthermore, system experiments have shown the potential of the CPM laser as a pulse source for high-speed TDM transmission systems [5]. A schematic plot of a monolithic CPM laser is shown in Fig. 2.1. To illustrate the CPM mode of operation, Fig. 2.1 also shows the computed pulse propagation in a 5 mm CPM laser cavity for a single round-trip at steady state. The initial left-hand pulse travels towards the absorber, collides with the left propagating pulse in the saturable absorber and continues towards the right-hand laser facet where it is reflected back into the laser.

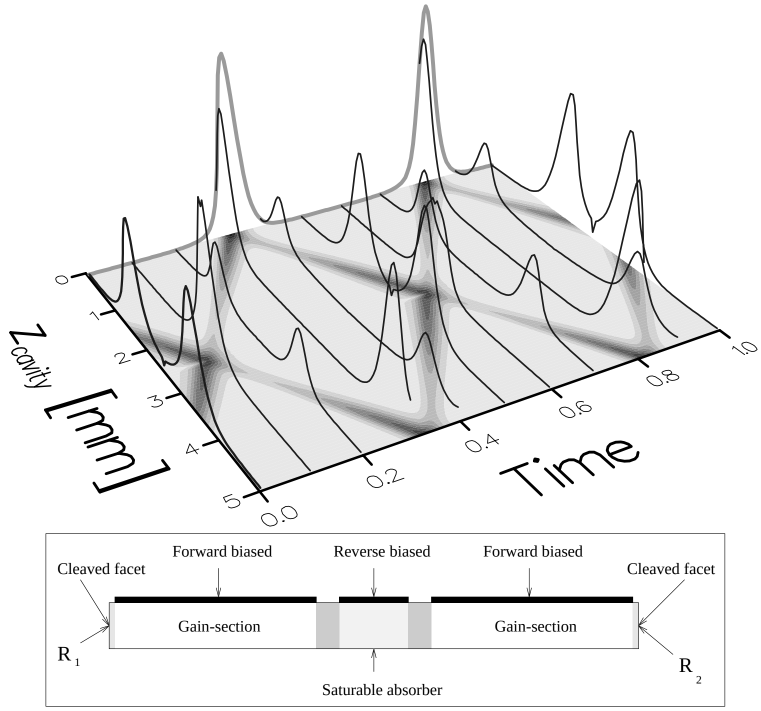

Figure 2.1: Schematic plot of a monolithic CPM laser (lower figure). The top figure shows the pulse propagation in the laser cavity for a single round-trip, when steady state is reached.

The demonstration and experimental characterization of the monolithic semiconductor CPM laser has been followed up by theoretical models which elucidate the operation principles of the CPM laser [4, 7, 8, 9, 10]. The widely accepted slow saturable absorber mode-locking theory developed by Haus [11, 12] has been used to determine the stable operation regime of the CPM laser [10, 13]. The pulse-width is, in this approach, found to be determined by the bandwidth limiting elements due to gain and index dispersion. However, based on a detailed large signal model of the CPM laser, we found that the pulse-width of the CPM laser is rather determined by the interplay of pulse broadening in the gain sections and pulse compression in the saturable absorber due to saturation effects [9]. The effect of index and gain dispersion was found to result in only minor changes of the pulse-width [14]. The pulse-width dependence upon saturable absorber length and the recovery time of the saturable absorber has been investigated in Refs. [7, 8]. The pulse-width is found to decrease with decreasing saturable absorber recovery time. This is in good agreement with the experimental observations [15, 16], where it is found that the pulse-width decreases with increasing reverse bias. However, an increased reverse bias results not only in a faster recovery time [17, 18] of the saturable absorber, but also shifts the gain spectra to lower energies [19, 20, 21], which, we will show, is an equally important effect.

2.2 CPM laser model

Optical network specifications normally require optical pulses with low chirp and a predefined pulse width. The optimization of a possible pulse source to fulfill these requirements could be done experimentally, but this can be a cumbersome job due to the many - and often not independent - parameters that make up a laser design. Often, it is therefore more convenient to develop a model for the pulse source from which the physical understanding of the device can be improved and which can be used as the basis for device optimization. Furthermore, the model can be used to predict the parameter range, where the pulse-source fulfills the optical network specifications.

2.2.1 Basic equations of the CPM laser model

Our large signal model for the CPM laser consists of a wave-propagation equation for the slowly varying electrical field amplitude and a rate equation model describing the material dynamics of the semiconductor waveguide. The wave-propagation equation [22, 23] is derived from Maxwell's equations, where we have made the slowly varying envelope approximation. The rate equation model describing the material dynamics has been derived from semi-classical density matrix equations [24, 25, 26, 27], where we phenomenologically have added a rate equation describing the carrier transport through the separate confinement region [28, 29]. The derivation of the rate equation model is presented in appendix A.1. Many-body theory calculations of the absorption in the case of a reverse bias [21] show that the derived saturable absorber model can be improved by introducing a reverse bias and carrier density dependent bandgap shrinkage parameter. The changes in the model parameter values upon varying bias are described in appendix A.3. In this section we will only present the final rate equation model derived in appendix A.

The wave propagation equation for the right (A^+, Φ^+) and left (A^-, Φ^-) travelling electrical field envelope function is [22, 23]

$$
\begin{aligned}
+\frac{1}{v_g}\frac{dA^\pm}{dt} &= \mp\frac{dA^\pm}{dz} + \frac{1}{2}(\Gamma g - \alpha_{int})A^\pm + \frac{\beta_{sp} B N_{qw}^2}{2A^\pm} \\
&\quad + \frac{\Gamma}{2}\frac{dg}{d\omega}A^\pm\frac{d\Phi^\pm}{dt} + \frac{\Gamma}{4}\frac{d^2 g}{d\omega^2}\left(\left(\frac{d\phi^\pm}{dt}\right)^2 A^\pm - \frac{d^2A^\pm}{dt^2}\right) \\
&\quad - \frac{\beta_2}{2}\left(\frac{d^2\phi^\pm}{dt^2}A^\pm + 2\frac{d\phi^\pm}{dt}\frac{dA^\pm}{dt}\right) \quad , \qquad (2.1a)\\
+\frac{1}{v_g}\frac{d\Phi^\pm}{dt} &= \mp\frac{d\Phi^\pm}{dz} - \Gamma\Delta k - \frac{\Gamma}{2}\frac{dg}{d\omega}\frac{1}{A^\pm}\frac{dA^\pm}{dt} \qquad (2.1b)\\
&\quad - \frac{\Gamma}{4}\frac{d^2g}{d\omega^2}\left(\frac{d^2\Phi}{dt^2} + \frac{2}{A^\pm}\frac{d\Phi^\pm}{dt}\frac{dA^\pm}{dt}\right) \\
&\quad - \frac{\beta_2}{2}\left(\left(\frac{d\Phi}{dt}\right)^2 - \frac{1}{A^\pm}\frac{d^2A^\pm}{dt^2}\right) \quad .
\end{aligned}
$$

Here, $A^\pm$ is the slowly varying amplitude and $\Phi^\pm$ is the phase of the electrical field envelope function. The field is normalized so that the photon density is $S = |A^+|^2 + |A^-|^2$. The constant v_g is the group velocity, Γ is the confinement factor, α_{int} is the internal loss and $\beta_{sp} B N_{qw}^2(z,t)$ accounts for spontaneous emission. β_2 derives from the index dispersion and $\frac{dg}{d\omega}$ and $\frac{d^2g}{d\omega^2}$ describes gain dispersion. The second derivatives of the electrical field (both $A^{\pm}$ and $\Phi^{\pm}$) with respect to time are estimated by the previous time step in our numerical scheme, (see App. A.4). The error introduced by this approximation is within the range of a few percent.

The gain g and wavenumber change Δk (refractive index change Δn) depend on the carrier distribution,

$$
\begin{aligned}
g &= \frac{a_N(n_c + \overline{n}_v - N_0)}{1 + v_g a_N \tau_{1,v} S} \quad , &(2.2a)\\
\Delta k &= \frac{\omega_0}{c}\Delta n \quad , &(2.2b)\\
&\approx \frac{\omega_0}{c}\left(\frac{dn}{dN_{qw}}\Delta N_{qw} + \frac{dn}{dT_c}\Delta T_c\right) \quad , &(2.2c)\\
&\approx -\alpha_{N_{qw}}\frac{\Delta g_{N_{qw}}}{2} - \alpha_{T_c}\frac{\Delta g_{T_c}}{2} \quad . &(2.2d)
\end{aligned}
$$

Here, n_c is the "local" (gain determining) carrier density in the conduction band at the optical transition energy [24, 30], (see also App. A). The term $v_g a_N \tau_{1,v} S$ accounts for gain suppression resulting from the "local" gain determining carrier density in the valence band, which has been adiabatically eliminated. $\tau_{1,v}$ is the relaxation time of the local carrier density in the valence band towards its quasi-Fermi-equilibrium. a_N is the maximum obtainable differential gain, see Eq. (2.6), and N_0 is related to the density of states [24, 30], (see App. A.1). Index c and v stands for conduction and valence band, respectively. $\alpha_{N_{qw}}$ and α_{T_c} are the line-width enhancement factors related to the carrier density and temperature, respectively. The carrier density induced refractive index changes in the saturable absorber section are not approximated by an $\alpha_{N_{qw}}$, since many-body theory calculations [21] showed that the change in refractive index could not be captured by an $\alpha_{N_{qw}}$-parameter. Instead a non-linear function has been found, which fits the carrier induced refractive index changes (Δn), (see App. A.3).

The dynamics of the material gain is influenced by a number of processes, which are shown schematically in Fig. 2.2. The carriers are injected into a carrier reservoir N_d, from which the carriers drift and diffuse towards the quantum well with the typical time constant τ_d. The "local" (gain determining) carrier density is related to the total carrier density N_{qw} in the quantum wells, see App. A.1, but is also affected by the effects of spectral hole burning (SHB) and carrier heating, see Fig. 2.2.a and 2.2.b. The material dynamics illustrated in Fig. 2.2 can be described by a rate equation model. The rate equations describing the material dynamics in

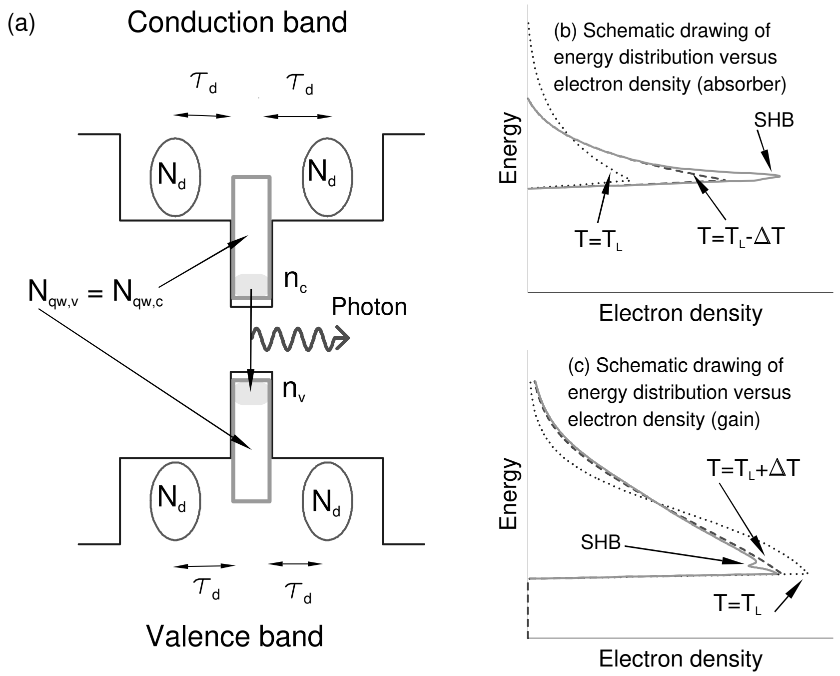

Figure 2.2: (a) Schematic drawing of the carrier injection model. In figure (b) and (c) a schematic is shown of the typical effects of spectral hole burning (SHB) and carrier temperature changes in the absorber and in the gain section, respectively.

the gain sections are

$$\frac{dN_d}{dt} = \frac{I}{eAL_d} - \frac{M_{qw} L_{qw}}{L_d} \frac{\eta_d N_d - N_{qw}}{\tau_d} - \frac{N_d}{\tau_{s_d}} \quad , \tag{2.3a}$$

$$\frac{dN_{qw}}{dt} = \frac{\eta_d N_d - N_{qw}}{\tau_d} - v_g g S(z,t) - \frac{N_{qw}}{\tau_{s_{qw}}} \quad , \tag{2.3b}$$

$$\frac{dT_c}{dt} = -\frac{T_c - T_L}{\tau_{h,c}} + \left(\frac{dU_c}{dT_c}\right)^{-1} \Bigg[\sigma_x N_{qw} \hbar\omega_0 \tag{2.3c}$$

$$+ \left(\frac{dU_c}{dN_{qw}} - E_{c,0}\right) g(n_c, \overline{n}_v) \Bigg] v_g S(z,t) \quad ,$$

$$\frac{dn_c}{dt} = -\frac{n_c - \overline{n}_c}{\tau_{1c}} - v_g g(z,t) S(z,t) \quad . \tag{2.3d}$$

Apart from the introduction of a carrier reservoir N_d in the barrier to account for the finite transport time across the separate confinement region [28, 29], these equations correspond to those given in Refs. [24, 30, 31] and were found to give a good explanation of ultrafast gain dynamics in laser amplifiers [32, 33], see also section 2.3. Other parameter values are: M_{qw}, number of quantum wells; L_{qw} and L_d, width of the quantum wells and the carrier reservoir, respectively; η_d, ratio between the carrier density in the reservoir (N_d) and in the quantum wells (N_{qw}) at thermal equilibrium; T_L, lattice temperature; τ_{s_d} and $\tau_{s_{qw}}$, carrier lifetimes for N_d and N_{qw}; σ_c, free carrier absorption (FCA) cross section; k_B and $\hbar$, Boltzmann and Planck constant; $E_{c,0}$, electron energy measured from the conduction band edge into the band; $\tau_{h,c}$, relaxation time of the carrier temperature towards the lattice temperature in the conduction band. The temperature effects in the valence band are not taken into account. The "local" carrier density relaxes towards its quasi-equilibrium value with a time constant $\tau_{1,c}$ determined by carrier-carrier scattering.

The rate equation model for the saturable absorber is similar to the rate equations in the gain sections. However, the rate equation for the carrier temperature is derived for the case of a Maxwell-Boltzmann distribution, since we can assume the carrier density to be low in the saturable absorber:

$$\frac{dN_d}{dt} = -\frac{N_d}{\tau_{sw}} - \frac{M_{qw} L_{qw}}{L_D} \frac{\eta_d N_d - N_{qw}}{\tau_d} - \frac{N_d}{\tau_{s_d}} \quad , \tag{2.4a}$$

$$\frac{dN_{qw}}{dt} = \frac{\eta_d N_d - N_{qw}}{\tau_d} - v_g g(z,t) S(z,t) - \frac{N_{qw}}{\tau_{s_{qw}}} \quad , \tag{2.4b}$$

$$\frac{dT_c}{dt} = -\frac{T_c - T_L}{\tau_{h,c}} + \frac{\sigma_c}{k_B}\hbar\omega_0 v_g S(z,t) + \left(\left(T_c - \frac{E_{c,0}}{k_B}\right)\frac{g(z,t)}{N_{qw}}\right) v_g S(z,t) \quad , \tag{2.4c}$$

$$\frac{dn_c}{dt} = -\frac{n_c - \overline{n}_c}{\tau_{1c}} - v_g g(z,t) S(z,t) \quad . \tag{2.4d}$$

Here, τ_{sw} is the time constant describing the removal of carriers from the carrier reservoir. The density dependent dephasing time of the polarisation, τ_2, may be obtained by many-body calculations [34]. However, here τ_2 is chosen such that the agreement between the gain spectra calculated by the method in [21] are in good agreement with the gain spectra in Figs. 2.5 and 2.6. The relaxation time for $\tau_{1,c}$ is actually calculated by many-body theory. $\tau_{1,c}$ is calculated by the famous Boltzmann equation [34, p.144], where we have assumed the carrier distribution to be described by the Fermi-Dirac distribution function. The relation between the different relaxation times is [34]

$$\frac{1}{\tau_2} = \frac{1}{2}\left(\frac{1}{\tau_{1,c}} + \frac{1}{\tau_{1,v}}\right) \tag{2.5}$$

Figure 2.3 shows the carrier density dependence of the different relaxation times $\tau_{1,c}$, $\tau_{1,v}$ and τ_2. The effect of gain suppression due to spectral hole burning and carrier temperature effects is proportional to the relaxation time τ_2, since the maximum differential gain is

$$a_N = \frac{|d_k|^2 \tau_2 \omega_0}{\hbar \epsilon_0 n c} \quad , \tag{2.6}$$

where d_k is the dipole moment, ω_0 is the optical carrier frequency, n is the refractive index, c is the speed of light in vacuum and ϵ_0 is the electric permitivity. The "local" carrier density at thermal equilibrium is determined by the Fermi-Dirac distribution,

$$\overline{n}_c = \frac{N_0}{1 + e^{\frac{E - E_f}{k_B T_c}}} \quad , \tag{2.7}$$

where E is the photon energy and E_f is the Fermi energy. The Fermi energy E_f can in the case of a quantum well be expressed by the total carrier density N_{qw} (App. A.1.1),

$$E_{f,c} = k_B T_c \ln\left(e^{\frac{N_{qw}\pi L_{qw}\hbar^2}{m_c k_B T_c}} - 1\right) \quad . \tag{2.8}$$

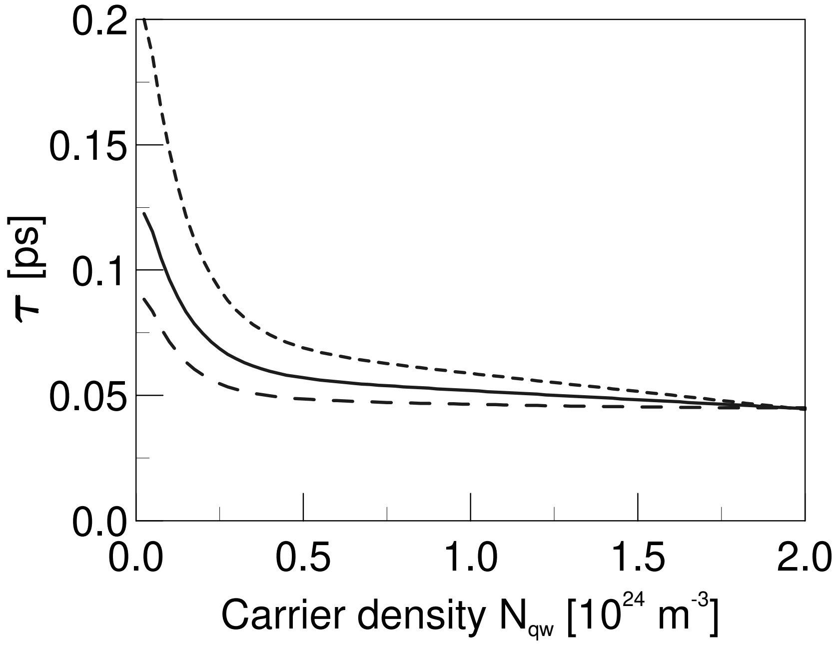

Figure 2.3: The dephasing time of carriers in the conduction band $\tau_{1,c}$ (- - -) and the valence band $\tau_{1,v}$ (– –). τ_2 (—) is the dephasing of the polarisation.

Here, the energy is measured from the band edge into the band. From the model, both the gain and - by Kramers-Kronig transformation - the refractive index can be calculated. However, the model as presented does not include the effect of an applied reverse bias. In [21] calculations are presented for the case of a saturable absorber with reverse bias and a variable (low) carrier density. The calculations incorporate the different layers of the semiconductor structure i.e. quantum wells, barriers etc. In order to treat the case of a reverse bias within our model, we allow the bandgap energy and the differential gain to depend on the reverse bias, and fit these variations to get a good agreement with [21]. Figs. 2.4-2.6 show the resulting index and gain spectra that are subsequently used in the CPM laser modelling. The nonlinear function describing the refractive index is given in App. A.3.

The refractive index spectra at quasi-equilibrium ($T = T_L$) are shown in figure 2.4 for the case of an externally applied reverse bias of 0.0 V.

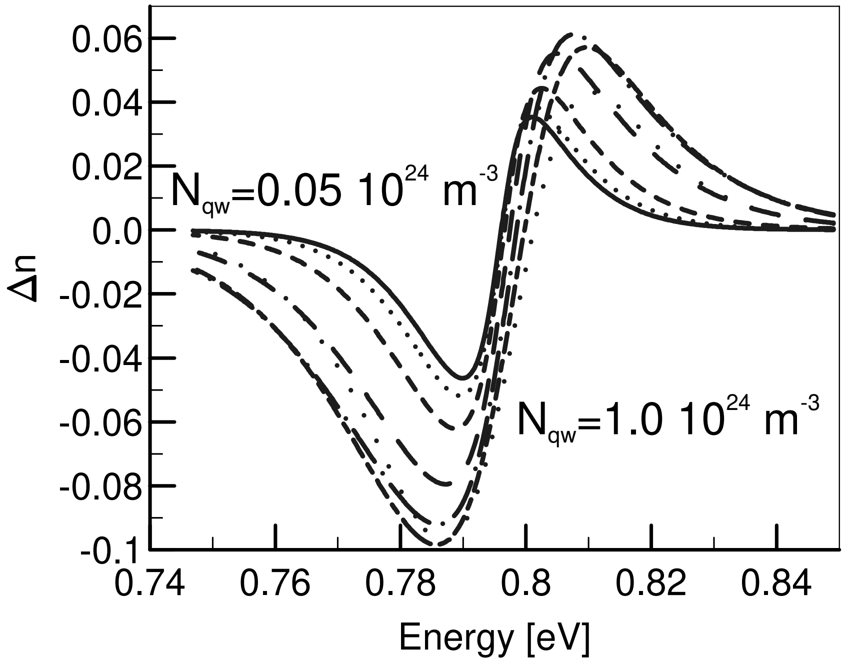

Figure 2.4: The change in refractive index for different carrier densities as function of energy. $N_{qw} = 0.05 \cdot 10^{24} m^{-3}$ (—), $N_{qw} = 0.1 \cdot 10^{24} m^{-3}$ ($\cdot\cdot\cdot$) $N_{qw} = 0.2 \cdot 10^{24} m^{-3}$ (- - -) $N_{qw} = 0.4 \cdot 10^{24} m^{-3}$ (– – –), ..., $N_{qw} = 1.0 \cdot 10^{24} m^{-3}$ ($\cdot \quad \cdot \quad \cdot$). The reverse bias is 0.0 V.

The gain spectra corresponding to Fig. 2.4 are shown in Fig. 2.5. The differential gain a_N is for low carrier densities a function of both the carrier density and the reverse bias. Thus, the differential gain decreases with increasing carrier density and with increasing reverse bias. The Quantum Confined Stark Effect (QCSE) is taken into account by defining a reverse bias dependent bandgap shrinkage parameter. The gain spectra for carrier densities higher than $1.0 \cdot 10^{24} m^{-3}$ are not influenced by a reverse bias and here the differential gain a_N is given by Eq. (2.6). Furthermore, the

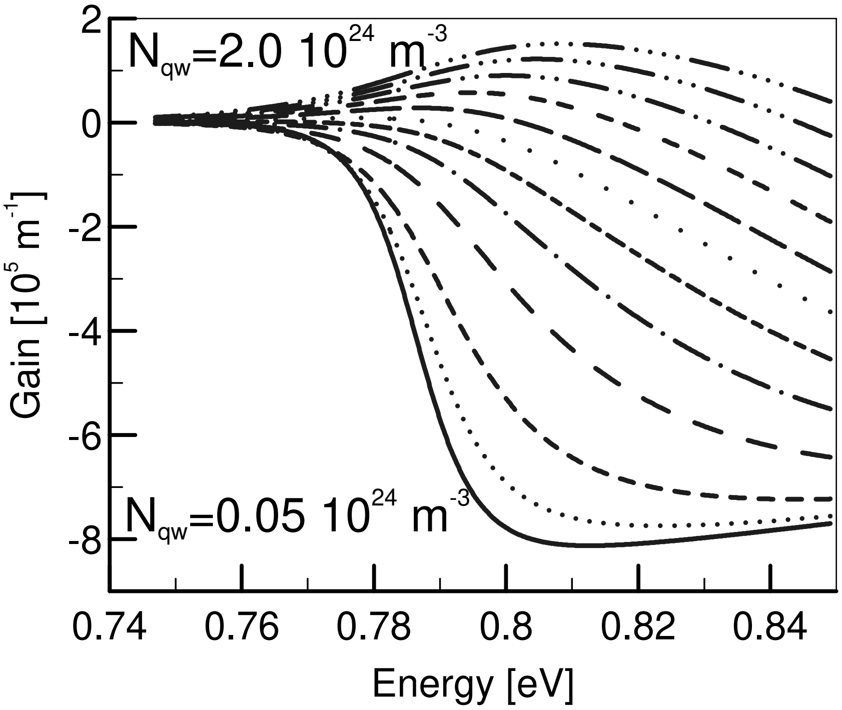

Figure 2.5: Gain spectra for different carrier densities as function of energy. $N_{qw} = 0.05 \cdot 10^{24} m^{-3}$ (—), $N_{qw} = 0.1 \cdot 10^{24} m^{-3}$ ($\cdots$), $N_{qw} = 0.2 \cdot 10^{24} m^{-3}$ (- - -), $N_{qw} = 0.4 \cdot 10^{24} m^{-3}$ (– – –), ..., $N_{qw} = 2.0 \cdot 10^{24} m^{-3}$ (– $\cdot\cdot\cdot\cdot$ –). The gain spectra for $N_{qw} \leq 0.8 \cdot 10^{24} m^{-3}$ are calculated for a reverse bias of 0.0 V.

refractive index changes are in the gain sections included by α-parameters found in the literature [22]. We have not included the effect of carrier density dependent bandgap shrinkage in the gain sections ($N_{qw} \geq 1.0 \cdot 10^{24} m^{-3}$). The spectra of the gain sections have thus to be shifted by a few meV [22]. The effect of the variable maximum differential gain and QCSE for low carrier densities can be seen by comparing the gain spectra in Fig. 2.5 (0.0 V) with the gain spectra in Fig. 2.6 (-2.0 V). The two figures show that the QCSE results in a strong shift of the absorption spectra to the lower energy

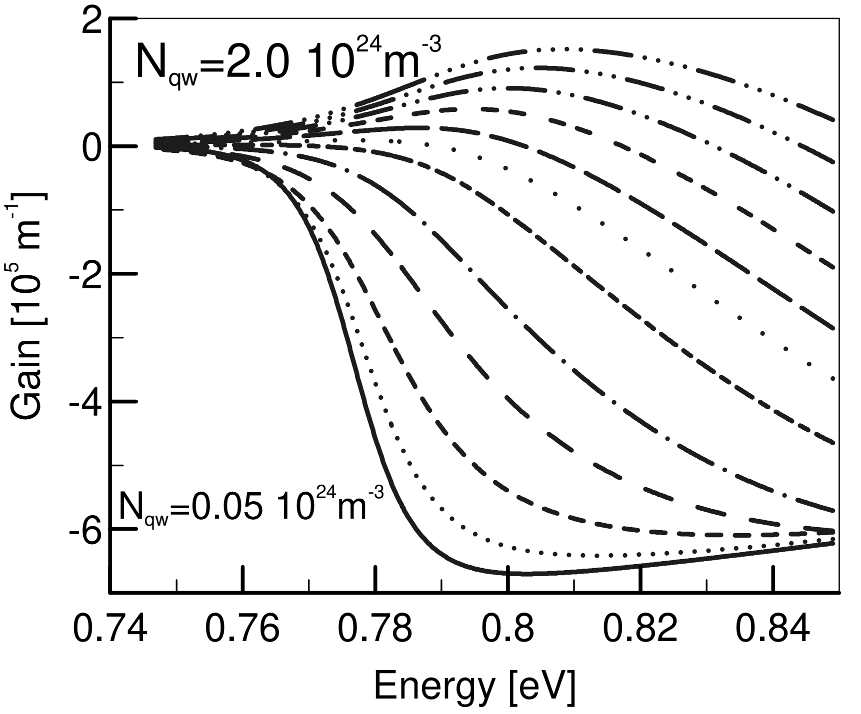

Figure 2.6: Gain spectra for different carrier densities as function of energy. $N_{qw} = 0.05 \cdot 10^{24} m^{-3}$ (—), $N_{qw} = 0.1 \cdot 10^{24} m^{-3}$ ($\cdots$), $N_{qw} = 0.2 \cdot 10^{24} m^{-3}$ (- - -), $N_{qw} = 0.4 \cdot 10^{24} m^{-3}$ (– – –), ..., $N_{qw} = 2.0 \cdot 10^{24} m^{-3}$ (– $\cdots\cdot$ –). The gain spectra for $N_{qw} \leq 0.8 \cdot 10^{24} m^{-3}$ are calculated for a reverse bias of -2.0 V.

side (longer wavelength) with increasing reverse bias. Furthermore, the peak value of the absorption decreases with increased reverse bias, corresponding to a change in a_N.

Typical parameter values used in our large signal model are given in table 2.1. Here, in particular the drift/diffusion time (recovery time) of the saturable absorber is a critical value, which decreases with increasing reverse bias on the saturable absorber [17, 18].

Other parameter values in table 2.1 are mainly found in the literature or have been calculated. The material dispersion was measured for InGaAs in [35] and found to be smaller by a factor of 5-10 compared to the values used in [10, 36, 37]. The value of dU_c/dT_c has been calculated and found to be almost constant over a broad carrier density region, when the carrier density is higher than $1.2 \cdot 10^{24} m^{-3}$. The α-parameters have been chosen in agreement with parameter values typically used in the literature [22, 31, 34, 38]. The effective electron and hole masses for InGaAs, where taken from Ref. [39]. Furthermore, the carrier life-times are determined by

$$\tau_{s_{qw}} = \left(BN_{qw} + CN_{qw}^2\right)^{-1} \quad , \tag{2.9}$$

where $B = 1.3 \cdot 10^{-16} m^3 s^{-1}$ [40] accounts for the radiative recombination rate and $C = 1.0 \cdot 10^{-40} m^6 s^{-1}$ [40] accounts for non-radiative Auger recombinations. The carrier lifetime in the carrier reservoir is also determined by the use of Eq. (2.9) by replacing N_{qw} by N_d. The typically used relaxation times of the carrier temperature ($\tau_{h,c}$ and $\tau_{h,v}$) and the FCA cross section were found in the literature [24, 27, 31, 41].

2.2.2 CPM laser model: Discussion

The model presented here is derived by starting from a quite general set of equations such as Maxwell's equations describing the electrical field and the semi-classical density matrix equations describing the material properties. These equations are then simplified by making certain approximations such as the slowly varying envelope approximation etc. Furthermore, during the derivation of the basic equations, describing the CPM laser model, we have neglected some physical processes which should be included in future CPM laser models to elucidate their influence on the mode-locking properties of the CPM laser.

The neglection of the carrier temperature effects in the valence band will only result in minor changes in the predicted CPM laser operation, since $\tau_{h,v}$ is $\approx 200fs$ which is much faster than the temperature relaxation constant

Symbol	Name	Value
M_{qw}	Number of QW	3
L_{qw}	QW thickness	8 nm
Γ	Confinement factor	0.03
n_g	Group refractive index	3.56
σ_c	Free carrier absorption coefficient	$3.5 \cdot 10^{-22}$ m^2
L_d	Length of diffusion region	0.2 μm
$\eta_{d,gain}$	-	20
$\eta_{d,abs}$	-	48
$\tau_{d,gain}$	Diffusion time (gain)	100 ps
$\tau_{d,abs}$	Diffusion time (absorber)	4-16 ps
$\tau_{h,c}$	Temperature relaxation time (conduction band)	0.65 ps
T_L	Lattice temperature	300 K
$\frac{dU_c}{dT_c}$	-	24 J/K
m_0	Electron mass	$9.1095 \cdot 10^{-31}$ kg
m_c	Effective electron mass	0.041 m_0
m_v	Effective hole mass	0.460 m_0
α_{int}	Internal loss	1000-2000 m^{-1}
β_2	Material dispersion	$2.0 \cdot 10^{-24}$ $s^2 m^{-1}$
τ_{sw}	-	0.1 ps
R	Facet reflectivities	0.3
$\alpha_{N_{qw}}$	α-parameter in gain section	2-4
α_{T_c}	α-parameter for carrier temperature	0-1.5

Table 2.1: Typical parameter values used in the CPM laser simulations.

$\tau_{h,c}$ in the conduction band [30, 31]. Thus, the carrier temperature effects in the valence band may, to a good approximation, be included in the gain compression factor in Eq. (2.2a).

The semiconductor waveguide structure investigated throughout this chapter is a QW well laser. The carrier transport in QW structures has been investigated in great detail in many works, where the effect of carrier capture (escape) of carriers by the quantum wells is found to be one of the limiting processes in obtaining high modulation speeds [42]. The CPM laser model presented does not take into account the effects of carrier capture (escape). However, the CPM laser model has been continuously improved during the duration of this project. Thus, we initially had a rate equation which included the effects of carrier capture processes of the quantum wells, but since the introduction of the carrier temperature resulted in an effect with approximately the same time constant as the carrier capture process we simplified our rate equation model by neglecting the carrier capture processes. This approximation is justified by the results in section 2.3 which show that our model captures both qualitatively and quantitatively the measured material dynamics of QW semiconductor waveguides [33] quite accurately. However, the saturable absorber model may be considerably improved by using a more detailed model for the carrier transport as shown in Ref. [21].

The CPM laser diode is based on the principle that the two colliding pulses help each other to bleach the saturable absorber. This technique was first used in CPM dye lasers [43]. The two pulses will, due to their mode-locked phases, form a standing wave when they collide [44, 45], which will result in the generation of a carrier grating [10, 45]. So far these carrier gratings have only been considered present in the saturable absorber section [7, 8, 10]. However, the formation of carrier gratings should also be taken into account in the gain sections since the spatial width of the pulses are typically broader than the saturable absorber section, and because the counter propagating pulses will collide with themselves at the cleaved facets.
However, it has been shown in Ref. [45] that the resulting change in absorption due to the formation of a carrier grating in the saturable absorber is very small. Accordingly, the influence of these carrier gratings is found to be negligible, when one studies the mode-locking properties of CPM semi-

conductor waveguides [45], which justifies that we do not take into account the effects of these carrier gratings in our large signal model.

Future improvements of the large signal model should address the inclusion of noise such that the effects of amplitude noise and timing jitter of the mode-locked pulses can be studied. Some work has already been performed in this area in Refs. [4, 7, 8]. However, so far, the effect of noise on the mode-locking properties of semiconductor lasers has only received modest attention.

Our large signal model can, as discussed, be improved with respect to many aspects. But as the theoretical results and their comparison with measurements show, our model reproduces the observed CPM laser characteristics very well and is as such expected to be a useful model.

The results presented in this chapter have mainly been obtained with the large signal model presented. However, the saturable absorber model has been continuously improved during this project. Some theoretical results are thus obtained with a simpler model (Sec. 2.3 and App. B).

Finally, we want to emphasise that the model has been derived with the goal of investigating the CPM laser diode. However, the model is quite general and may be used to investigate other QW semiconductor devices such as amplifiers, electro-absorption modulators etc.

2.3 Carrier dynamics in CPM semiconductor waveguides

In this section we discuss the gain and loss dynamics of semiconductor waveguide structures identical to those employed in the CPM lasers fabricated at Tele Danmark R & D. The gain and loss dynamics are characterized by femtosecond pump-probe measurements on forward and reverse biased semiconductor waveguides, respectively. These measurements are reproduced by the large signal model developed for the CPM laser in section 2.2.

The experimental pump-probe data are presented in section 2.3.1, where we also discuss the CPM semiconductor waveguide structure fabricated at Tele Danmark R & D. In section 2.3.2 we attribute the femtosecond pump-probe response to the effects of spectral hole burning, carrier heating and carrier density changes. Furthermore, this section shows qualitatively the effects of the different terms in the rate equation model. Finally, a summary of our results is given in section 2.3.3.

2.3.1 Femtosecond pump-probe measurements

The CPM lasers fabricated at Tele Danmark R & D consists of three InGaAs quantum wells separated by Q(1.3) barriers incorporated in a graded-index separate confinement heterostructure (GRIN-SCH). Lateral confinement is provided by an ≈ 2 μm ridge waveguide [5, 46]. The CPM laser itself is typically ≈ 5000 μm long [9, 16, 46] and is divided into three sections: two outer ≈ 2460 μm gain sections and an 80 μm saturable absorber section in the center.

For the pump-probe experiments we utilized a section of the CPM waveguide cleaved to a length of 250 μm. This waveguide section is anti-reflection coated on both ends to suppress lasing. The waveguide was mounted on a standard mounting block, and is held at a temperature of 20 °C during the experiment. To emulate the behavior of the gain and absorber in our waveguide sections, we forward bias the device in order to study the dynamics of the gain, and we reverse bias it in order to study the loss dynamics.

To measure femtosecond gain and loss dynamics, the device was inserted into a standard pump-probe set-up [17, 18, 47, 48]. The source of femtosecond pulses was an additively-mode-locked color center laser (APM) [50] producing pulses with a center wavelength λ_0 of approximately 1530 nm. The APM's pulse duration was typically 150 fs. The pump pulse had a TM (transverse magnetic) polarization with respect to the waveguide, whereas the probe polarization was TE (transverse electric). The CPMs themselves lase with TE polarization. After the waveguide section, a polarizer was used to reject the TM light from the pump, and the TE probe was detected with a cooled Ge (Germanium) photo-diode.

It is important to note that both the pump and probe energies used here were kept extremely low in order to reproduce the conditions identical to those when a pulse is propagating through a mode-locked CPM laser. Since the pulse energy inside an operating CPM laser is on the order of ≈ 0.1 pJ – 0.2 pJ, we used an APM pulse energy of ≈ 0.65 pJ, corresponding to an average power of ≈ 0.05 mW at the input to the device. (Lower powers gave degraded signal-to-noise performance in the reverse-biased experiments.) The power in both pump and probe beams was equal. Another investigation of femtosecond dynamics in a saturable absorber [17, 18] (i.e. reverse biased active waveguide) used pump and probe pulses 20 times larger than those reported here. Discrepancies between the results reported here and those in Refs. [17, 18] are likely due to the excessively high power used in that experiment. In order to reach the necessary level of sensitivity to measure at this low power, we used a double-chop and lock-in detection scheme. In this scheme, the pump was mechanically chopped at 2 kHz, whereas the probe was chopped with an acousto-optic modulator at 3 kHz. The reference outputs of these two choppers were used to synthesize a sum signal at 5 kHz which was used as the reference signal at the lock-in detector.

Pump-probe results are shown in Fig. 2.7 for both forward bias (Fig. 2.7.a) as well as reverse bias (Fig. 2.7.b) conditions. Fig. 2.7 shows the change in probe transmission ΔT as a function of the delay time between pump and probe pulse. Here, $\Delta T = T - T_0$ is the change in energy of the transmitted probe pulse, where T is the transmitted probe pulse energy, while T_0 is the energy of the transmitted probe pulse in the absence of a pump pulse. Negative delay times imply that the probe pulse passes through the semiconductor waveguide ahead of the pump pulse, while positive delay times correspond to the case, where the pump pulse passes through the device ahead of the probe pulse. Accordingly, Fig. 2.7 displays the changes in gain (absorption) induced by the pump pulse. A reduced probe transmission signal corresponds to a pump induced reduction in the gain, while an increased probe transmission signal corresponds to a pump induced reduction in the

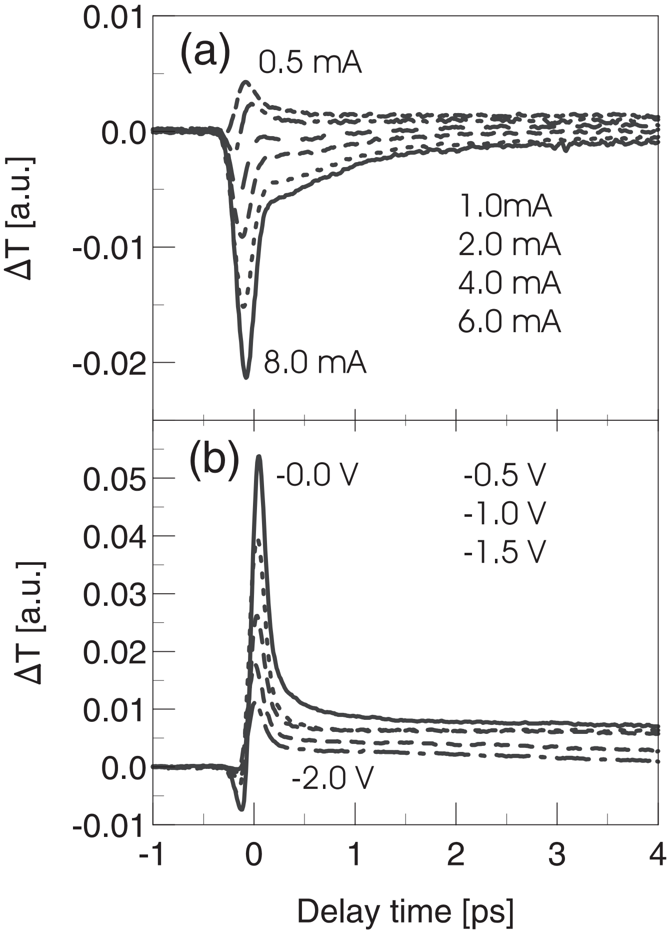

Figure 2.7: (a) Measured pump-probe transmission data on forward biased structures, corresponding to the gain sections of the CPM lasers. Ultrafast gain saturation and recovery after femtosecond pumping is evident. (b) Measured pump-probe transmission data on reverse biased structures. The occurrence of ultrafast absorption saturation (bleaching) is evinced by the fast initial transient coincident with the pump pulse.

absorption of the semiconductor waveguide.

As is evident from Fig. 2.7, fast and slow dynamics are present for both forward and reverse bias on the semiconductor waveguide. The dynamic processes operant in the gain sections (forward biased waveguides) have been discussed in great detail in Refs. [24, 30, 32], and it is well known that the signal observed in the gain section may be attributed to the processes of spectral hole burning, carrier heating and carrier density changes.
Shown in Fig. 2.7.b are pump-probe traces recorded in a reverse biased waveguide for voltages V = 0.0, -0.5, -1.0, -1.5, and -2.0 V. In each case, significant absorption saturation occurs during the pump pulse itself, as is evinced by the ultrafast initial peak. Following this femtosecond absorption bleaching, the sample transmission recovers to nearly its initial value; however, a residual saturation persists over a longer time scale, which can most likely be attributed to the presence of carriers in the saturable absorber. This hypothesis is supported by the fact that the residual saturation signal's decay time manifestly decreases with increasing reverse bias voltage, consistent with speedier carrier sweep out under the influence of the increasing field [17, 18].
The size of the long-time (ns) residual signal is strongly dependent on the pump and probe center wavelength λ_0 and applied voltage. Other measurements (not shown here) indicate that at shorter wavelengths the long-time signal ΔT is negative for larger reverse biases, implying that the absorber's absorption increases upon pumping [21]. At the longer wavelengths corresponding to the CPM lasing wavelength the signal is positive, but still depends on the voltage.
Another effect upon varying the applied voltage is the decrease of the fast peak height with increasing reverse bias. The experimental measurements reveal an increase in the material absorption with increasing reverse bias. A higher value of the material absorption results in more photo-generated carriers by the pump pulse, which should result in a larger change in absorption. These arguments imply, that the peak height should increase with increasing bias. However, our argument is in disagreement with the observed decrease of the fast peak height, since we do not take into account the effect of the carrier dependent dephasing time of the polarization, τ_2. The value of τ_2, decreases with increasing carrier density, such that the gain does not change linearly with the carrier density. The importance and in-

fluence of the dephasing time of the polarization will be further elucidated in the discussion on the calculated pump-probe responses in the following section.

2.3.2 Pump-probe response: Theory

Our large signal model developed for the CPM laser model is in this section used to simulate the pump-probe experiment. A femtosecond pulse with a FWHM of 150 fs and an energy of 0.65 pJ is injected at the left-hand side facet and detected at the right-hand side facet. The facet reflectivities are assumed to be zero corresponding to perfect anti-reflection coatings such that we can neglect the effect of a counter propagating pulse with respect to the pump and probe pulse. The pump and probe pulses are described by separate wave-propagation equations, where we have neglected the effects of index (β_2) and gain dispersion ($d^2g/d\omega^2$). The probe energy is as in the experimental measurements equal to the energy of the pump pulse.

Our rate equation model for the material dynamics has during the duration of this project been continuously improved. The presented data in this section are thus obtained by a large signal model, which differs slightly from the model presented in section 2.2. Here, we have not taken into account the bias and carrier density dependent bandgap shrinkage in the case of a reverse biased device. Instead, the effect of the reverse bias is phenomenologically taken into account by an appropriate shrinkage of the bandgap energy for changing bias conditions. Using the model presented in section 2.2 to calculate the pump-probe response is only expected to result in minor and insignificant changes of the pump-probe responses shown in Fig. 2.8.b.

Shown in Fig. 2 are theoretical calculations of the change in probe transmission as function of the delay time between the pump and probe pulse for both forward and reverse biased devices. The bandgap energy values in Fig. 2.8.b correspond to different applied reverse bias values. A bandgap energy of E_g = 0.744 eV corresponds to 0.0 V, and E_g = 0.715 eV corresponds to -2.0 V. The assumed bandgap shrinkage due to the QCSE is in good agreement with the gain spectra for 0.0 V and -2.0 V shown in Fig. 2.5 and Fig. 2.6, respectively.

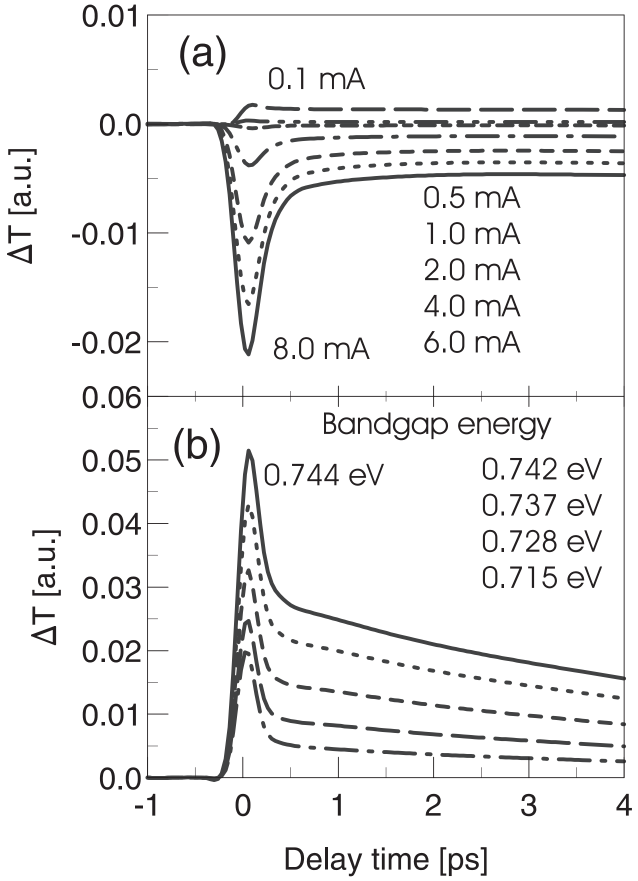

Figure 2.8: (a) Theoretical pump-probe trace in a forward biased waveguide. The agreement between this trace and that shown in Fig. 2.7.a is quite good. (b) Theoretical pump-probe trace calculated for a reverse biased waveguide. Again, the model captures the essential features observed in the experimental curve shown in Fig. 2.7.b, including both the initial ultrafast transient as well as the subsequent long-time relaxation.

The model captures the observed gain dynamics (forward bias) quite accurately (Fig.2.8.a). Indeed, the rate equation description used here was originally developed to describe the propagation of femtosecond laser pulses through forward biased semiconductor laser amplifiers [24, 30, 32]. The pump-probe response may as stated previously be attributed to the three processes of spectral hole burning, carrier heating and carrier density changes. In Fig. 2.9 we have shown the measured change in probe transmission in the case of a forward bias of 8 mA, where we have split the response into three parts. The long dashed curve shows basically the effect of SHB, the solid curve shows the effect of carrier heating and the dotted curve shows the effect of carrier density changes in the quantum wells. The different processes are of course simultaneously present, but their effects are dominant in certain time intervals due to their governing time constants.

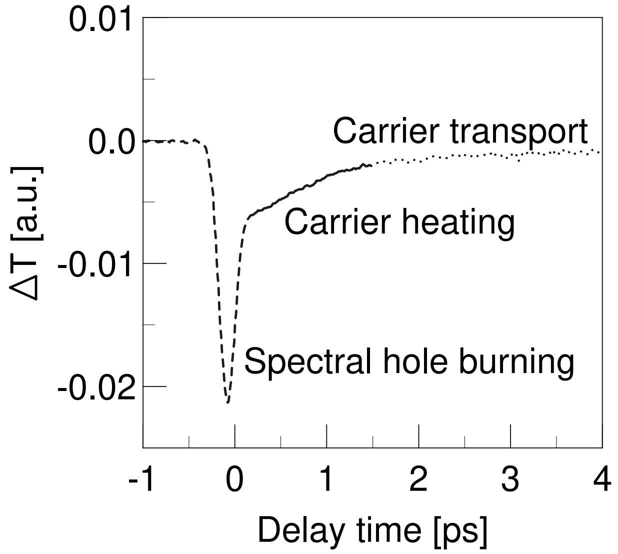

Figure 2.9: Measured pump-probe trace for the case of a forward bias of 8 mA. Dashed curve shows the effect of spectral hole burning, solid curve shows the effect of carrier heating, dotted curve shows the change in gain due to carrier density changes.

The initial ultrafast saturation transient observed is thus the result of SHB.

In the case of gain the pump pulse burns a "hole" in the carrier distribution. Thus, electrons (holes) in the conduction (valence) band are "removed", see Fig. 2.2.c. Carrier-carrier scattering "fills in" the "hole" within a characteristic time of less than 100 fs, $\tau_{1,c}$. Thus, the carrier distribution relaxes towards its quasi Fermi-Dirac distribution described by a carrier temperature T_c (conduction band).
The carrier temperature differs from the lattice temperature, since carriers at a particular energy have been "removed". The carrier temperature will be higher than the lattice temperature, if we assume that carriers close to the band edge have been "removed" by the pump pulse, see Fig. 2.2.c. The carrier temperature relaxes towards the lattice temperature on a time scale of one picosecond determined by the process of carrier-phonon scattering. The change in probe transmission resulting from changes in the total carrier density N_{qw} are relatively small, see Fig. 2.9. The total carrier density relaxes towards an equilibrium carrier density determined by the injection current and the carrier life times in the quantum wells and separate confinement region.

So far we have only discussed the semiconductor waveguide response in the case of forward bias. However, the reverse biased semiconductor waveguide is especially interesting, since the saturable absorber is a key component for passive mode-locking of the monolithic colliding-pulse mode-locked laser.

Fig. 2.8.b shows calculated femtosecond pump-probe responses in the case of a reverse biased device. The agreement between experiment and theory is not as good as in the case of a forward biased device, but the rate equation model qualitatively captures both the ultrafast transient (SHB) as well as the subsequent long-time tail. The recovery time (long-time tail) of the saturable absorber is in our model described by the time constant τ_d determined by the process of drift and diffusion in the separate confinement region. The drift/diffusion time depends on the applied reverse bias and varies between 16 ps and 4 ps [17, 18] for an external reverse biases of 0.0 V (E_g=0.744 eV) and -2.0 V (E_g=0.715 eV), respectively.
The significant absorption saturation occuring during the pulse itself can again be attributed to SHB. Here, photo-generated carriers are generated at a particular energy, see Fig. 2.2.b. The photo-generated carrier distribution relaxes on a femtosecond time scale towards its quasi Fermi-Dirac distribu-

tion described by a characteristic carrier temperature due to carrier-carrier scattering. The carrier temperature relaxes towards the lattice temperature on a picosecond time scale determined by carrier-phonon scattering. Finally, the carriers are swept out of the quantum wells due to the reverse bias on the device.
The material absorption increases with reverse bias in the calculated pump-probe responses shown here. The decrease of the ultrafast saturation response is in this case only observed when the values of the dephasing times of the "local" carrier densities and the polarization depend on the total carrier density N_{qw}. The value of τ_2 decreases, when the material absorption increases, since the amount of photo-generated carriers is proportional to the material absorption. Hence, the ultrafast saturation peak is expected to decrease with increasing reverse bias, because the strength of SHB is proportional to the value of the dephasing time τ_2.

The moderate agreement between the measured and calculated pump-probe response of the reverse biased devices can be attributed to the neglection of the carrier induced screening of the external applied field. Other measurements (not shown here) indicate that at shorter wavelengths the long-time tail is negative for larger reverse biases, implying that the absorber's saturation increases upon pumping [21]. At longer wavelengths corresponding to the CPM lasing wavelength the long-time signal is found to be positive, but still depends on the reverse bias as displayed in Fig. 2.7. These long-time pump-probe responses have been modelled by a carrier injection model, which includes a detailed description of the carrier injection (sweep out) processes in quantum well semiconductor devices [21]. Here, the increase in absorption upon optical pumping is attributed to the process of dynamical screening of the external applied field. However, we see that our large signal model already gives a moderately good description of the material dynamics in the reverse biased device. Therefore, we have chosen not to use the more detailed model for the carrier injection (sweep out) presented in Ref. [21], since the use of this detailed model would have increased the complexity and computing times of our large signal model considerably.

2.3.3 Summary

Femtosecond pump-probe measurements have, in this section, been shown to be in good agreement with the calculated pump-probe response of our CPM laser model in the case of a forward bias while the agreement in the case of a reverse bias was moderate. The pump-probe response is attributed to the three processes of spectral hole burning, carrier heating and carrier density changes. A detailed modelling of carrier transport through the semiconductor waveguide and the inclusion of carrier induced screening of the external applied field has in Ref. [21] been shown to improve the agreement between the calculated and the measured "long-time tail" of the pump-probe data.

2.4 Passive mode-locking

Passive mode-locking of the CPM laser is accomplished by applying a DC current to the gain sections and a DC reverse bias to the saturable absorber section. Under proper operation conditions the CPM laser will produce narrow optical pulses at a repetition-rate corresponding to half the round-trip time of the laser cavity, see Fig. 2.1. In this section we will discuss the temporal and spectral properties of passive mode-locked monolithic CPM pulses.

2.4.1 Temporal CPM laser characteristics

The CPM laser model is self-starting and describes successfully the formation of CPM pulses for appropriate current and reverse bias values. To illustrate the stability of the CPM operation regime further, the CPM pulses may initially be spatially displaced such that they do not collide in the saturable absorber. The CPM pulses will then adjust their spatial displacement such that they collide in the saturable absorber.
At steady state the cavity losses due to the saturable absorber, internal

losses and the final cleaved facet reflectivities have to be balanced by the amplification in the gain sections during a single pass through the cavity. Fig. 2.10 shows the change in pulse amplitude and pulse width for a pulse travelling from the left-hand facet towards the right-hand facet at steady state for a 5 mm and a 1 mm cavity. The saturable absorber length for the 5 mm and 1 mm cavity is 80 μm and 30 μm, respectively. As expected the pulse amplitude increases in the gain sections, while the pulse is attenuated in the saturable absorber section. The pulse-width exhibits the same behavior, meaning that the pulse broadens in the gain section and is compressed in the absorber. The steady state pulse is characterized by a balance between these opposite effects. This implies that the CPM diode laser is not an example of "pure slow saturable absorber" mode-locking [11], since in that case, pulses are shortened by both the gain and absorber section. In particular, one expects in the case of "pure slow saturable absorber" mode-locking that the saturable absorber shaves off the front of the pulse, while the pulse tail should be more or less unaffected. In Fig. 2.11 a pulse is shown in front of (dashed line) and after passage of (solid line) the saturable absorber at steady state. The absorber recovery time in the 5 mm cavity and 1 mm cavity were 16 ps and 4 ps, respectively. This range of time constants is in good agreement with the saturable absorber recovery times measured in Refs. [17, 18]. The saturable absorber recovery time is thus comparable with the final pulse-width. However, the fast gain dynamics attributed to SHB and carrier temperature dynamics still have a significant influence on the final pulse-width, which will be further elucidated in section 2.5.

In contrast to the results previously published in Ref. [9] the fast gain dynamics of the saturable absorber are not a necessity to obtain mode-locking for the 1 mm laser cavity. The pulse-compression effect of the saturable absorber due to SHB and carrier temperature effects is reduced here in comparison to [9], since the maximum differential gain a_N is a function of $\tau_2(N_{qw})$. In [9] τ_2 had a fixed value of $\approx$ 100 - 150 fs in the saturable absorber. This fixed τ_2 time allowed us to use recovery times of 8 - 16 ps for the saturable absorber, while still obtaining 1 ps pulses in the 1 mm cavity case. Here, the dephasing time τ_2 depends on the total carrier density in the saturable absorber, and hence a faster recovery time of the saturable absorber is needed to ensure the presence of a fast component in the absorber response.

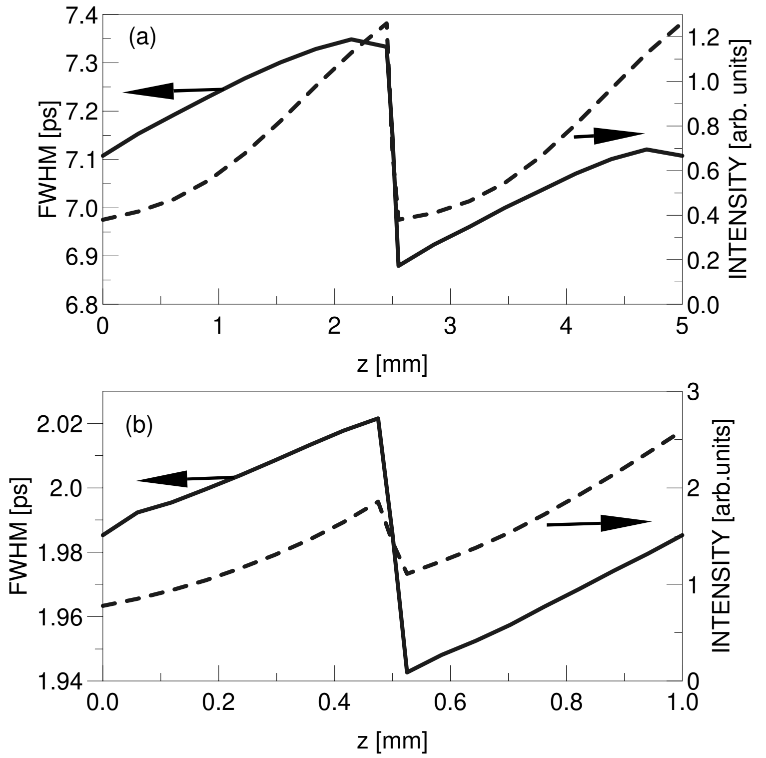

Figure 2.10: Pulse width and amplitude displayed for the pulse travelling to the right for one pass through a 5 mm (a) and a 1 mm (b) laser diode.

Another parameter, which has a significant influence on the mode-locking behavior, is the optical field confinement factor Γ. The pulse shaping of both the absorber and gain sections is stronger for high values of the confinement factor Γ. In this section we have used a field confinement factor Γ of 0.03, corresponding to three quantum wells with a width of 8 nm each [49]. By increasing the quantum well thickness or the number of quantum wells the value of the confinement factor will be increased. However, changing the quantum well thickness will alter the lasing wavelength [22, 48], and the number of quantum wells should be below on the order of 10 to have an

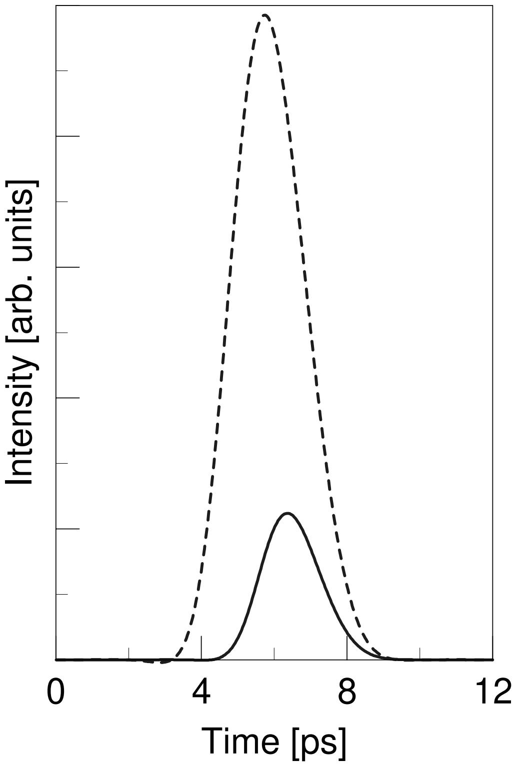

Figure 2.11: Steady state pulse inside the cavity in front of the saturable absorber (dashed line) and after the saturable absorber section (solid line) for a 5 mm cavity with a 80 μm saturable absorber. Here, the confinement factor is Γ=0.12 (M_{qw}=5, L_{qw}=10nm) to enhance the pulse-shaping of the saturable absorber.

efficient carrier injection. Additional quantum wells will mainly be raised to their transparency point by photon assisted carrier transport [28, 29], which is not included in our model.

Increasing the quantum wells to a thickness of 10 nm and considering the case of 5 quantum wells, the confinement factor is in the range of 0.1-0.2. Under these conditions the CPM pulses experience an enhanced pulse broadening/compression in the gain/absorber section during a single round-trip. The steady state CPM pulses are then found to be narrower than in the case of a low confinement factor, $\Gamma = 0.03$. In Fig. 2.11 we have used a confinement factor of 0.12 corresponding to the case of 5 quantum wells with a width of 10 nm. The steady state output pulse has a Full Width at Half Maximum (FWHM) of approximately 2 ps. The figure shows the pulse in front of the saturable absorber (dashed line) and after passage of the saturable absorber (solid line). The reduction in peak height is approximately a factor 5, which should be compared to a factor 3 in the case of Γ=0.03. Furthermore, the pulse compression upon a single pass is much more significant for Γ=0.12. The two pulses in Fig. 2.11 are shown in a coordinate system moving with the group velocity v_g. The pulse front is effectively cut-off by the saturable absorber, while the pulse tail experiences a much smaller attenuation. Accordingly the pulse is shifted backwards in time after passage through the saturable absorber.

It should be mentioned that the fast gain dynamics in the saturable absorber have a stronger effect in the case of a high confinement factor. The amplitude changes within a single round-trip increase with an enhancement of the confinement factor. Thus, the maximum amplitude when entering the absorber will be higher in the case of a high Γ value. This results in a stronger gain (absorption) suppression due to SHB and carrier temperature effects resulting in an enhanced pulse compression in the case of the saturable absorber. This is confirmed by simulations, where we do not take into account the fast gain dynamics. Starting from the steady state pulses in figure 2.11 the laser starts to self-pulsate, which confirms that the fast gain dynamics in the saturable absorber compared to the gain sections dominate for Γ=0.12. Thus, no stable CPM mode-locking can be obtained for the chosen parameter values without the inclusion of the fast gain dynamics.

However, a high confinement factor does not only result in a narrower pulsewidth, but causes also the spectrum to broaden due to the enhanced carrier induced refractive index changes. So, a high confinement factor does not necessarily improve the pulse quality.

2.4.2 Spectral CPM laser characteristics

So far we have discussed the pulse-shaping mechanisms in the case of a passive mode-locked CPM laser without discussing the spectral properties of the CPM pulses. However, the instantaneous wavelength can be obtained by the equation for the phase, Eq. (2.1b). The steady state CPM pulse and instantaneous wavelength is shown in Fig. 2.12.a and 2.13.a for a 5 mm and 1 mm cavity, respectively. Here, the confinement factor has a value of 0.03. The time-band-width product of the 1 mm cavity is close to the transform limit, while the time-bandwidth product for the 5 mm cavity is several times larger than the transform limited value. The pulse-width and instantaneous wavelength will change for different parameter values. Typically, the pulse-width decreases with a decreasing drift/diffusion time τ_d [7, 8], while the wavelength chirp is proportional to the value of the line-width enhancement factor $\alpha_{N_{qw}}$ in the gain sections.

The steady state pulse-width is as stated previously determined by the interplay between pulse broadening in the gain sections and pulse compression in the saturable absorber. The pulse-width is found to be proportional with the cavity length, which is in fairly good agreement with experimental results, where the shortest CPM pulses were obtained by a short CPM laser diode [2]. The wavelength chirp of the pulses seems also to be proportional to the cavity length, which implies large time-bandwidth products for long laser diodes, while short cavities should lead to pulses closer to being transform-limited. The theoretical results are in good agreement with experimental results in Refs. [16, 15, 51], where cavities with a length of less than 2 mm were found to produce almost transform limited pulses, while a 5 mm cavity [16] is found to have a time-bandwidth product of 1-2.

Passively mode-locked lasers typically generate pulses, which are blue-chirped [36, 37] i.e., the instantaneous frequency increases from the front to the tail of the pulse. This is in good agreement with the frequency chirp of the CPM pulses in Fig. 2.12 and 2.13, which are strongly blue-chirped. The wavelength-chirp of the CPM pulses is determined by a complicated interplay between the dynamics of the gain and saturable absorber section, which we try to elucidate below.

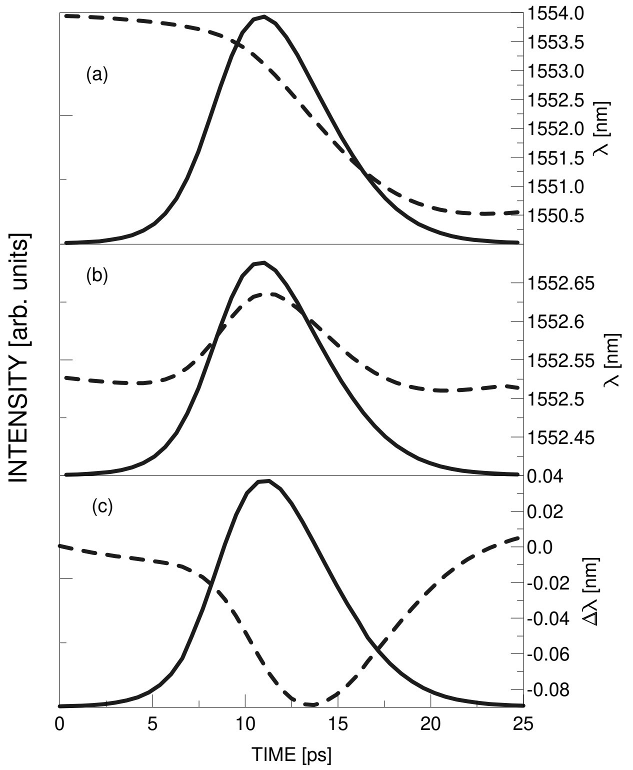

Figure 2.12: (a) Steady state output pulse (—) and instantaneous wavelength (- - -). (b) Pulse intensity (—) and self phase modulation from a single pass through the cavity. The initial chirp of the steady state pulse was reset to zero. (c) The change in wavelength (- - -) resulting from the time-shift of the pulse during a single pass through the cavity. The cavity length is $L = 5.0$ mm and the absorber length $L_{abs} = 80$ μm.

The steady state conditions for the CPM laser are that the pulse shape and wavelength chirp do not change on successive round-trips. Previously we showed how the pulse-width and amplitude changed during propagation from the left-hand facet to the right-hand facet. In Figs. 2.12.b and 2.13.b we have plotted the induced wavelength chirp for a single pass through the

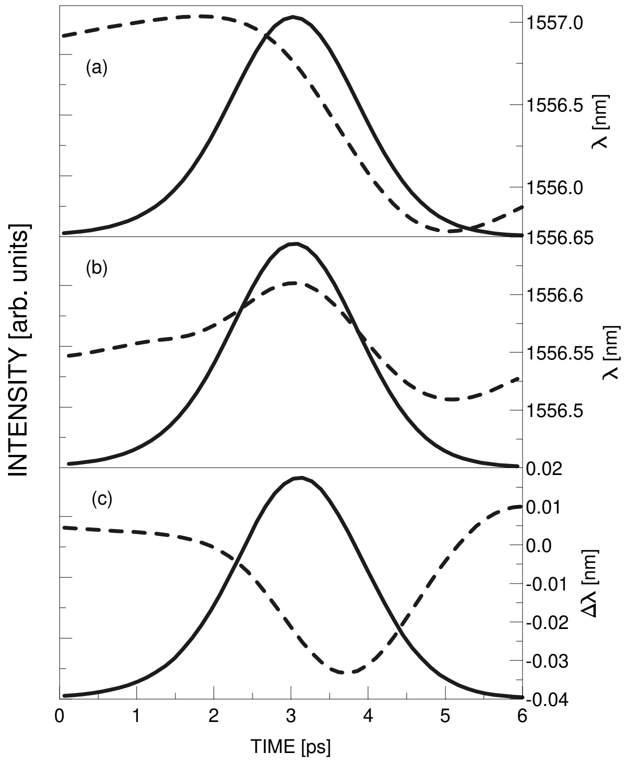

Figure 2.13: (a) Steady state output pulse (—) and instantaneous wavelength (- - -). (b) Pulse intensity (—) and self phase modulation from a single pass through the cavity. The initial chirp of the steady state pulse was reset to zero. (c) The change in wavelength (- - -) resulting from the time-shift of the pulse during a single pass through the cavity. The cavity length is $L = 1.0$ mm and the absorber length $L_{abs} = 30$ μm.

5 mm and 1mm cavity, respectively. The induced single pass wavelength chirp is obtained by resetting the steady state instantaneous wavelength to the average value of the instantaneous wavelength just before the pulse is reflected by the left-hand facet. The induced wavelength chirp close to steady state conditions is then obtained by detecting the output pulse at

the right-hand facet. The induced wavelength chirp during a single pass at steady state conditions for the 5 mm cavity in Fig. 2.12.b shows that the pulse experiences a red-chirp on the pulse front and a blue-shift on the pulse tail. The origin of this induced wavelength chirp during a single pass is the carrier density induced refractive index change [36, 37]. This is in agreement with the result for the 1 mm cavity, Fig. 2.13.b. Here, the wavelength chirp induced during a single pass through the cavity again follows the pulse shape. However, the induced wavelength chirp is smaller due to the shorter gain sections. Furthermore, due to the faster absorber recovery and shorter gain-sections the saturable absorber also induces a significant wavelength chirp in the tails of the pulse. The induced wavelength chirp upon a single pass at steady state was expected to be zero, since the output pulse is stable. So, there must be an additional effect, which has to be taken into account to explain the steady state behavior of the CPM pulses.

It is well known that under the action of a slow saturable gain, the pulse will propagate at a slightly higher "speed" [52] than the group velocity, since the pulse front experiences a higher amplification than the pulse peak and tail. The opposite effect happens in an slow saturable absorber, where the pulse amplitude will propagate with a "speed" slightly below the group velocity, see Fig. 2.11. This "speed up" (gain) or "slowing down" (absorber) is a result of the saturable amplification or attenuation of the pulse. The phase and thus the instantaneous frequency (wavelength) of the pulse will not be affected by this effect. The pulse amplitude expirences thus a time-shift with respect to the steady-state wavelength chirp, if the time-shift of the pulse-amplitude is dominated by either the gain or saturable absorber section.

Our large signal model shows that it is actually the saturable absorber, which gives the dominant time-shift. The pulse amplitude is thus shifted backwards in time with respect to the initial wavelength chirp upon a single pass through the cavity. The change in wavelength chirp due to this time shift is shown in Fig. 2.12.c and 2.13.c for a 5 mm and 1 mm cavity, respectively. The chirp resulting from this time shift at steady state is seen to approximately compensate for the frequency chirp resulting from the material response during a single pass through the cavity. The compensation is not complete, because the coupling between the amplitude and phase equations due to dispersion also contributes.

The wavelength chirp of the steady state pulse thus depends strongly on the time-shift the pulse experiences during a single pass through the cavity. A time-shift backwards in time gives blue-chirped pulses, when the self phase modulation due to depletion of the carrier density in the gain sections is dominant. In the case of a forward time shift we would expect to see red-chirped pulses. Red-chirped pulses are typically observed for actively mode-locked laser diodes. However, to investigate this one has to control the repetition frequency of the CPM laser. This is done in section 2.5, where the case of hybrid mode-locking is investigated.

2.4.3 Summary

In this section we have discussed the pulse-shaping mechanisms of monolithic CPM laser diodes. We find that the steady state pulse width is characterized by a balance between pulse broadening in the gain sections and pulse compression in the saturable absorber section.
The wavelength chirp of the CPM pulses is explained by the interplay of an effective "time-shift" backwards in time of the CPM pulses and self-phase modulation in the gain sections. The saturable absorber results in a "time-shift" of the CPM pulse amplitude backwards in time compared to the pulse phase (instantaneous wavelength), since the saturable absorber shaves off the pulse front. However, the phase of the pulse is not affected by the attenuation, but changes only due to the carrier induced refractive index changes. The wavelength chirp induced on a single pass due to self-phase modulation has thus to balance the wavelength chirp induced by the "time-shift" of the pulse.

2.5 Hybrid mode-locking

CPM-lasers can be hybridly mode-locked by modulating the reverse bias on the saturable absorber [16, 46, 51], or by modulating the gain current to a small fraction of the gain sections [6, 15]. The synchronization of the pulse train to the external modulation frequency is obtained for a narrow frequency band close to the repetition frequency of passive mode-locking.

In this section we will present theoretical and experimental results for a hybridly mode-locked CPM laser fabricated at Tele Danmark R & D, see section 2.3. The CPM laser is 5 mm long and divided into three sections, two outer gain sections with a length of 2460 μm and a 80 μm saturable absorber section at the center of the cavity. Hybrid mode-locking is in this case obtained by forward biasing the gain sections and applying a microwave sinusoid to the reverse biased absorber section through a microwave bias T. The hybrid mode-locking scheme is investigated for the case of varying the DC-current to the gain sections for a fixed reverse bias as well as for varying DC-reverse biases on the saturable absorber for fixed gain current. The pulse broadening obtained upon increasing the DC-current and pulse compression upon increasing the DC-bias values are also observed in the case of passive mode-locking. However, the experimental measurements at Tele Danmark R & D were made for the case of hybrid mode-locking.
Furthermore, we investigate the hybrid mode-locked CPM laser characteristics, when the external modulation frequency is varied.

2.5.1 Variation of the external modulation frequency

In this section the CPM pulse characteristics are discussed for the case, where the external modulation frequency applied to the saturable absorber is varied within a narrow frequency band close to the repetition frequency of passive mode-locking. In Fig. 2.14 the theoretical steady state CPM-pulses are shown for three different modulation frequencies. The repetition frequency of 16.820 GHz is very close to the passive mode-locked repetition frequency. The synchronization of the pulse repetition frequency with the external modulation is found to be due to the Quantum Confined Stark Effect (QCSE), (bandgap shrinkage resulting from the external modulation of the voltage on the saturable absorber). The modulation of the saturable absorber recovery time, without inclusion of the QCSE did not result in an effective synchronization. The frequency band, which results in synchronization, has a width of approximately 80 MHz. This is in good agreement with experimental results, where the modulation frequency could be tuned by approximately 100 MHz [46, 51].

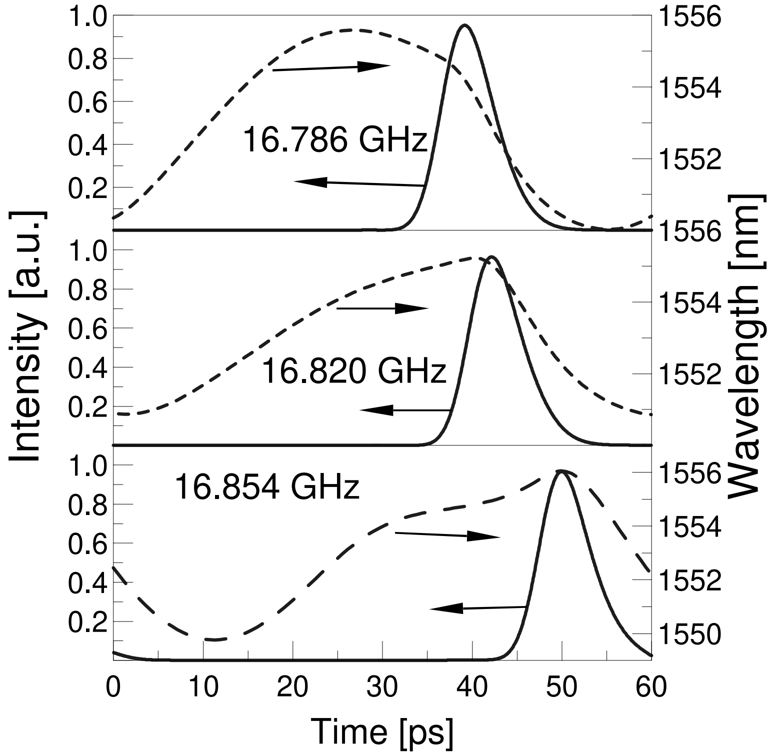

Figure 2.14: Calculated hybrid mode-locked output pulse and pulse chirp for different modulation frequencies ($\alpha_{N_{qw}} = 2.0$).

The instantaneous wavelength chirp obtained for different modulation frequencies agrees very well with our qualitative description given in section 2.4. The pulse is strongly blue-chirped in the case where the modulation frequency is close to the passive pulse repetition frequency (16.820 GHz). However, when the modulation frequency is increased to 16.854 GHz the time-shift backwards in time is actually very small and the wavelength chirp is accordingly small across the pulse. Actually the pulse starts to develop red-chirp on the pulse front and is still blue-chirped on the pulse tail. Increasing the modulation frequency further is expected to result in a pulse, which becomes more red-chirped. Unfortunately, the CPM-laser does not mode-lock at higher modulation frequencies, so we do not see the transition to entirely red-chirped pulses. In the case of modulating the laser at low modulation frequencies (16.786) the pulse exhibits an even stronger blue-chirp. These theoretical observations are in very good agreement with experimental results.

In Fig. 2.15 the experimental streak-camera measurements of a hybrid mode-locked CPM laser diode are shown. The pulse chirp shifts from being weakly red-chirped at 16.740 GHz to being strongly blue-chirped at a low modulation frequency of 16.652 GHz. The red-chirp is only obtained at the highest modulation frequencies, while the blue-chirped pulses are dominant in most of the locking band.

Previously we stated that the chirp is closely related to the line-width enhancement factor $\alpha_{N_{qw}}$ in the gain sections. This is confirmed by increasing $\alpha_{N_{qw}}$ in the gain sections by a factor of two (Fig. 2.16), other parameter values being equal to the parameter values used in Fig. 2.14. The instantaneous wavelength chirp shows the same behavior as previously. It shifts from strongly blue-chirped (16.786 GHz) to red-chirp in the pulse front and blue-chirp in the pulse tail (16.854 GHz). However, due to the enhanced $\alpha_{N_{qw}}$ in the gain sections the instantaneous wavelength chirp of the CPM pulses increases as expected.

As is evident from Figs. 2.14-2.16 the wavelength chirp of the hybridly mode-locked CPM laser can be controlled to some degree by the external synchronization frequency. However, since the chirp is related to the carrier density induced refractive index change, the value of the α-parameters has to be minimized to obtain pulses with small wavelength chirp. The α-parameters can be minimized by growing strained quantum wells [42]. These structures are thus expected to generate pulses, which are closer to their transform-limited value.

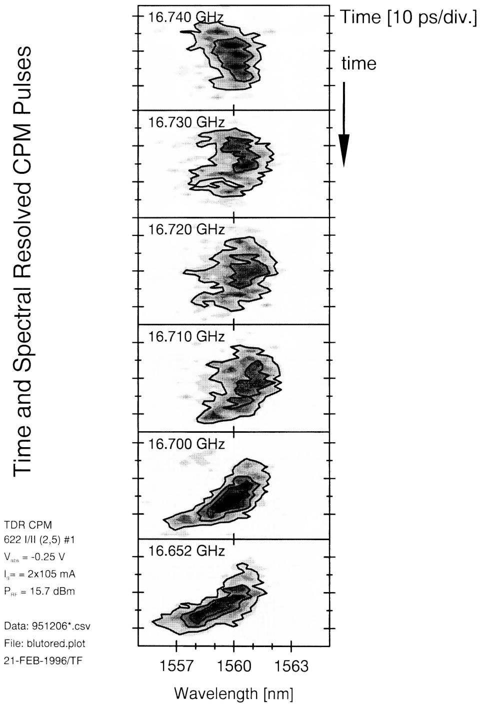

Figure 2.15: Measured contour plots of the time-resolved spectra of the CPM pulses for different modulation frequencies.

2.5.2 Hybrid mode-locked CPM pulses for varying DC current and varying DC reverse bias

We have so far shown that the wavelength chirp characteristics of our large signal model are in good agreement with experimental measurements. However, it is also interesting to investigate the influence of the external applied current and reverse bias on the mode-locking properties of the CPM laser. The calculated data presented in the following were obtained for the

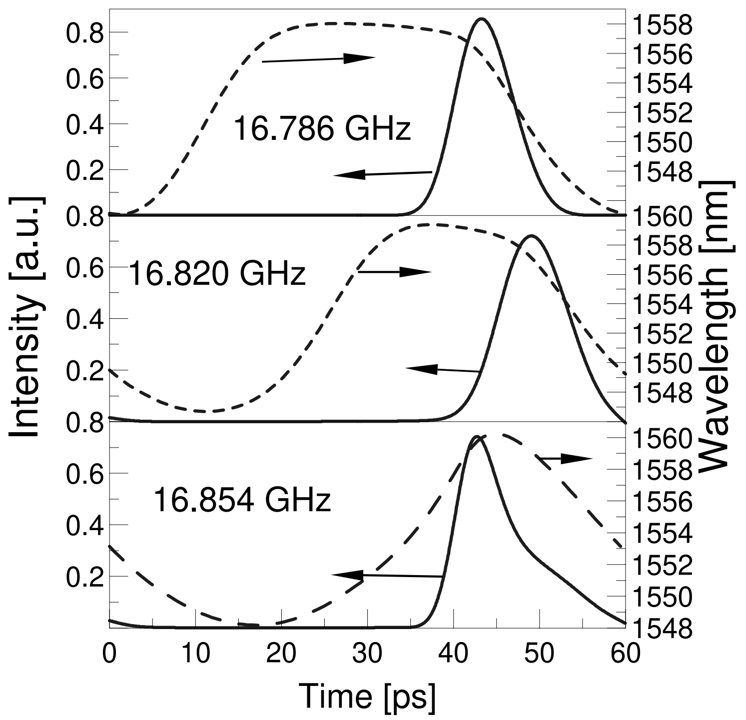

Figure 2.16: Calculated hybrid mode-locked CPM pulse and pulse chirp for different modulation frequencies. Parameters as in Fig. 2.14 except for $\alpha_{N_{qw}}$, which has been increased from 2.0 to 4.0.

case of hybrid mode-locking, since the corresponding measurements made at Tele Danmark R & D also were made on hybrid mode-locked CPM lasers. However, numerical simulations have shown that passive mode-locked CPM lasers reveal the same changes upon varying the gain current or saturable absorber bias.

Fig. 2.17 and 2.18 show the theoretical and experimental background free autocorrelations for different current values, respectively. The physical mechanisms resulting in the pulse broadening with increased injection current are the fast gain dynamics. The fast gain dynamics (SHB and carrier temperature effects) result in an almost instantaneous gain suppression. Accordingly an increased peak power leads to an enhanced gain suppression, which will result in pulse broadening. Thus, the CPM-pulses are broadened significantly, when the gain current and hence the pulse power is increased, since the peak power of the pulses is clamped by the fast gain dynamics.

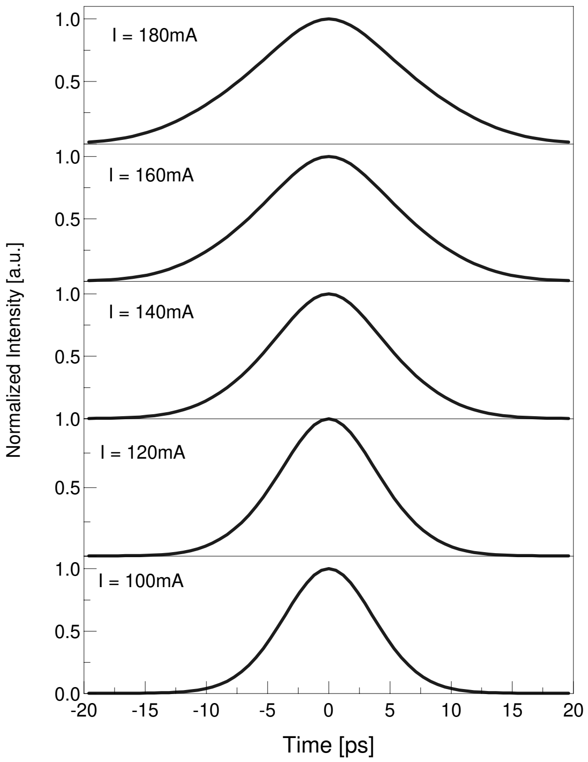

Figure 2.17: Calculated background free pulse autocorrelations for a 5 mm CPM laser with 80 μm saturable absorber for fixed bias voltage and varying current.

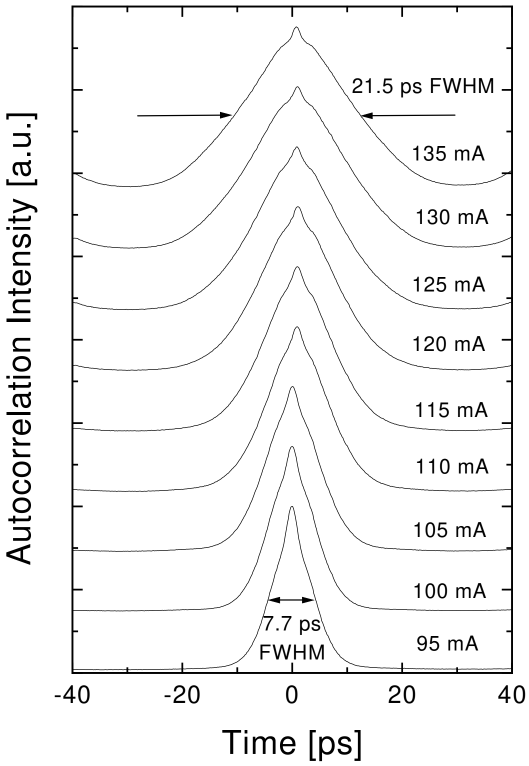

Figure 2.18: Measured autocorrelations of the pulses from a 5 mm CPM with a saturable absorber length of 80 μm for fixed reverse bias voltage and varying gain current.

This is actually shown in Fig. 2.19, where we in the stable mode-locking region see that the peak pulse power almost is clamped for current values higher than 120 mA, while the average pulse power continuous to increase linearly with injection current. The smallest pulse width is in accordance with our argumentation above expected to be obtained just above threshold. This is in good agreement with other experimental groups [6, 15], who obtained the smallest pulse-widths just above threshold for stable CPM operation.

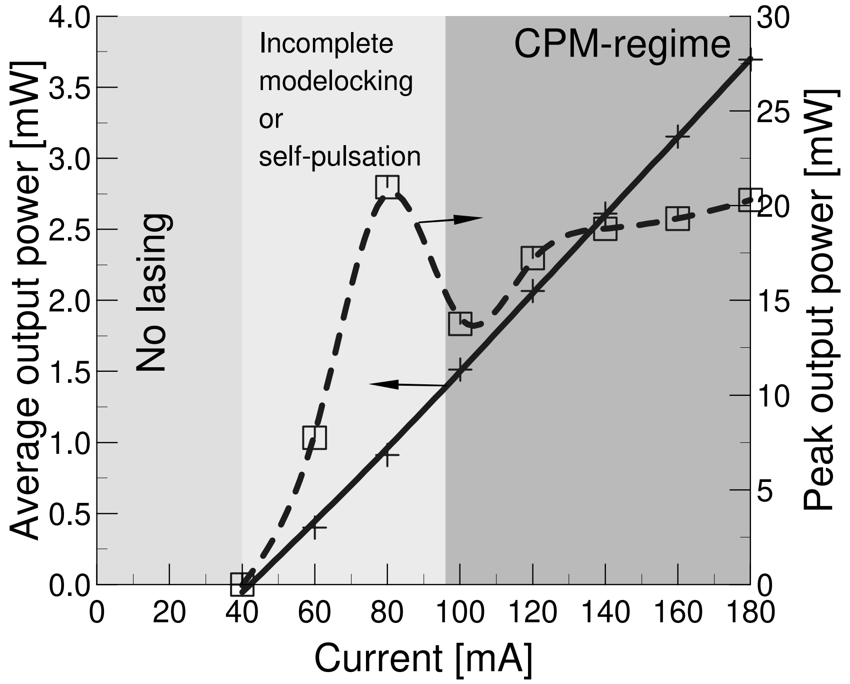

Figure 2.19: Light-current characteristic for a CPM laser diode. Different modes of operation are approximated by gray levels. Numerical data points are plotted by a mark, while the lines only are a guide for the eye.

The optical power spectra also depend strongly on the injection current. Fig. 2.20 shows the calculated optical power spectrum corresponding to the background free autocorrelations in Fig. 2.17. The calculated optical power spectrum is seen to broaden with increasing injection current, corresponding to an increasing instantaneous wavelength chirp over the CPM pulses. The enhanced wavelength chirp with pulse power is related to the carrier density induced refractive index change. For higher pulse power more stimulated recombinations will occur during the pulse passage at a particular point inside the laser cavity, which through the α-parameter results in an enhanced wavelength-chirp.
Furthermore, it is well known (see Figs. 2.12.b and 2.13.b), that the α-

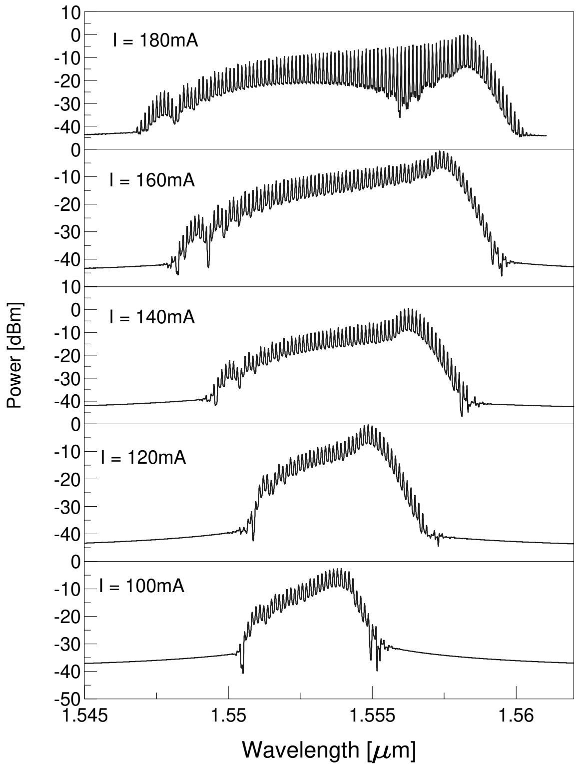

Figure 2.20: Calculated optical power spectrum for a 5 mm CPM laser with 80 μm saturable absorber for fixed reverse bias and varying current. The curves correspond to the curves in Fig. 2.17.

parameter in the gain sections results in a red-shift of the center wavelength of an optical pulse. The center wavelength of a passively mode-locked CPM-laser should accordingly experience a small red-shift, when the effect of the carrier density induced refractive index change is enhanced. This is in good agreement with our numerical results, where the center wavelength is shifted to slightly higher values for increasing injection current. The theoretical results are in very good agreement with experimental measurements. Figure 2.21 shows the measured optical power spectra corresponding to the data shown in Fig. 2.18. We see that the measured optical power spectrum broadens with injection current and we observe also a red-shift of the center wavelength in agreement with our theory.

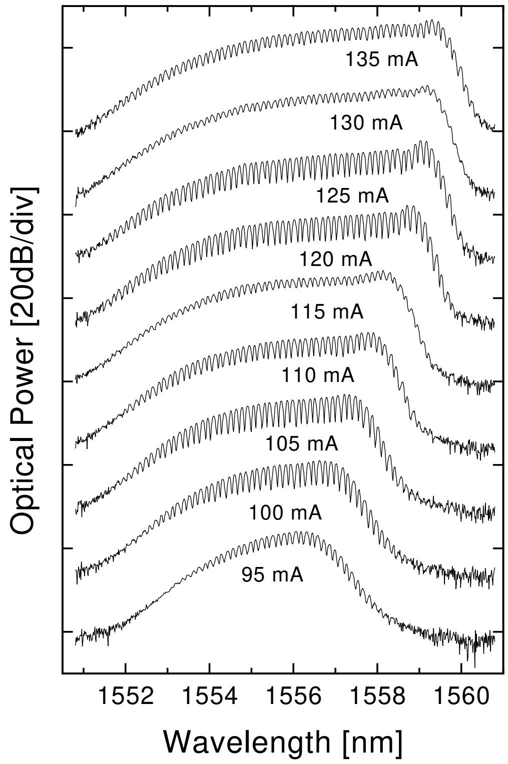

Figure 2.21: Measured optical power spectrum for a 5 mm CPM laser with 80 μm saturable absorber for fixed reverse bias and varying current. The curves correspond to the curves in Fig. 2.18.

Above we have discussed the effect of injection current variations in the region of stable CPM mode-locking. To illustrate the CPM laser operation beyond the stable mode-locking regions we have in Fig. 2.19 also included calculated data for low current values. At low current values the CPM laser tends to operate in a self-pulsation regime [53]. This was also observed in measurements on CPM lasers in Refs. [6, 15, 46]. The CPM laser still produces "mode-locked" pulses, which due to the self-pulsation are strongly amplitude modulated. The average emitted power is thus much lower than the peak power, see Fig. 2.19.

The variation of the CPM pulses upon varied current values suggests that one also may expect strong changes for varying DC-reverse bias values applied to the saturable absorber for a fixed current value. We have calculated the CPM laser characteristics in the case of a forward gain current of 120 mA. Stable CPM operation is obtained when the DC-reverse bias is varied between -0.4 V and -1.0 V, while the laser starts to self-pulsate for a reverse bias of -1.2 V. The pulse peak power is found to increase with increasing reverse bias, while the average pulse power decreases. This implies that the pulses become narrower for increasing reverse bias, which is shown in Fig. 2.22, where we have plotted the background free autocorrelations for DC reverse bias values of -0.4 V (τ_d=16ps), -0.6 V (τ_d=12ps), -0.8 V (τ_d=8ps), and -1.0 V (τ_d=6ps). The used value for the diffusion time τ_d is added in parenthesis for each bias value, since τ_d depends on the reverse bias [17, 18].

The theoretical calculations (Fig. 2.22) reveal that the pulse width decreases slightly upon increasing the reverse bias due to the faster recovery time of the saturable absorber (τ_d), while the optical power spectrum remains almost unchanged. These theoretical results are in good agreement with experimental measurements [16], which showed that the pulse width and optical power spectrum only changed slightly upon increasing reverse bias. It should be noted that the calculated changes in pulse-width upon increasing reverse bias are relatively small compared to the changes in pulse-width observed for different cavity lengths and for changed values of the confinement factor.

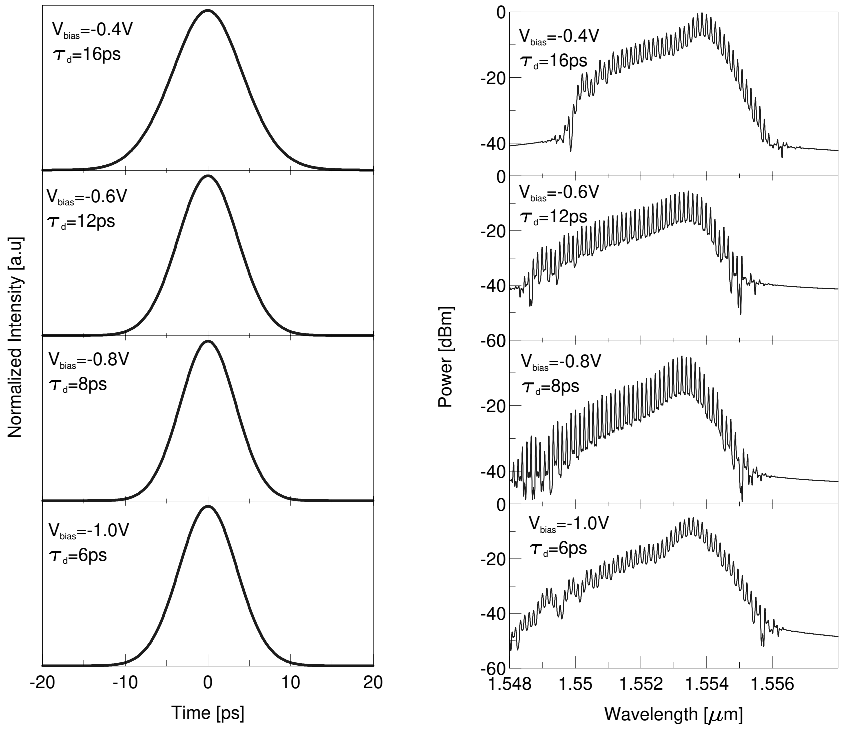

Figure 2.22: Calculated background free autocorrelations and optical power spectra for a 5 mm CPM laser with 80 μm saturable absorber for fixed current (I = 120 mA) and varying reverse bias.

2.5.3 Summary

In this section we have shown that the wavelength chirp of the CPM pulses can be partially controlled by the external modulation frequency. The observed changes in wavelength chirp upon varying the external modulation frequency are in good agreement with our explanation of the chirp in section 2.4.

Furthermore, the effects of spectral hole burning and carrier heating are found to result in significant pulse broadening upon increased injection current. Varying DC values of the saturable absorber bias are in contrast found to result in minor changes of the pulse width and of the optical power spectrum.

2.6 Discussion

In this chapter we have discussed the pulse-shaping mechanisms of monolithic CPM laser diodes. We find that the steady state pulse width is characterized by a balance between pulse broadening in the gain sections and pulse compression in the saturable absorber section. The shortest pulse-widths are obtained when the laser is operated just above threshold [6, 15]. The CPM pulses are found to broaden with increasing injection current since the pulse peak power is clamped due to gain suppression resulting from spectral hole burning and carrier heating.

The main emphasis in this chapter has been devoted to the CPM laser fabricated at Tele Danmark R & D, which is a 5 mm CPM laser diode with an 80 μm saturable absorber. The pulse-width of this device is typically 6-20 ps depending on the operation conditions. Our large signal model is developed to give an accurate description of the carrier dynamics for optical pulses down-to a FWHM of a few hundred femtoseconds. However, the description of pulses with a FWHM of a few picoseconds does not require such a detailed modelling. In this case it can be an advantage to adiabatically eliminate the rate equation for the "local" carrier density and carrier temperature, which results in an effective gain compression factor; see Eq. (2.2a), where the gain compression factor resulting from the adiabatic elimination of the "local" carrier density in the valence band is shown. It should be noted that the maximum differential gain a_N depends on the total carrier density N_{qw} through τ_2. The change of the differential gain with the total carrier density N_{qw} in the saturable absorber has a significant influence on the mode-locking properties of the laser and should also be incorporated in a simplified model, where the rate equations for the "local" gain determing carrier density and carrier temperature are adiabatically eliminated.

Pulse widths of 1-2 picoseconds are predicted by our model, when we investigate short cavities or use a high confinement factor Γ. In App. B we have included some "old" results obtained for CPM lasers for varied cavity and saturable absorber length. The data presented in App. B have been obtained by a large signal model, which differs from the model presented in section 2.2. The main difference is that we have chosen fixed values for τ_2 in the gain ($\tau_2 = \tau_{1,c} = 50$ fs) and in the absorber section ($\tau_2 = \tau_{1,c} = 100$ fs). Furthermore, we did not include the effect of index and gain dispersion in the wave-propagation equation. The carrier induced refractive index changes in the saturable absorber were modelled by an α-parameter. The CPM laser studied had 5 quantum wells and we used a confinement factor Γ of 0.2. However, for the 5 mm cavity we also used a confinement factor of 0.05. As shown in this chapter a low confinement factor results in broader pulses. The use of $\Gamma = 0.2$ resulted in pulses with a FWHM of 3.2 ps, which should be compared to 5.1 ps for Γ=0.05 for the 5 mm cavity.
The theoretical calculations presented in App. B show that long CPM laser diodes seem to have an optimum absorber length, while the pulse width only varies slightly for short laser diodes. The almost constant pulse width for the short laser diodes is attributed to the fast gain dynamics in the saturable absorber, which are very efficient in the case studied in App. B. However, for the longer laser diodes the influence of the fast gain dynamics on the CPM operation are similar to the case studied in this chapter. Thus to minimize the pulse width the CPM laser should be designed to exhibit strong spectral hole burning in the saturable absorber, while the effect of the fast gain dynamics in the gain sections should be minimized. The trend of an optimum saturable absorber length for a given cavity length (App. B) is, due to the similarities for the mode-locking mechanisms for the long laser cavities, also expected to be observed, when the model in section 2.2 is used.

The inclusion of gain dispersion and Group Velocity Dispersion (GVD) in our CPM laser model showed that their effect on the steady state pulse width is small. Here, it should be noted that the inclusion of the gain dispersion term $dg/d\omega$ is more important to incorporate than the GVD and $d^2g/d\omega^2$, since $dg/d\omega$ is not equal zero in either the gain sections or the saturable absorber section. Furthermore, the gain dispersion term $dg/d\omega$ has a significant influence on the obtained time-shift of chirped CPM pulses upon a single pass through the cavity. So in contrast to other theories we do not find that the pulse width [11, 13, 10] and wavelength chirp [36] are determined by GVD and gain dispersion.

In section 2.5 the effect of different DC-reverse bias values on the saturable absorber for a fixed current value are found to result in minor changes in the pulse width and the optical power spectrum. For high DC-reverse biases the cavity losses became so high that the laser started to self-pulsate, this can be compensated by increasing the gain current slightly. However, the pulse width and spectrum are still almost unchanged.
The wavelength chirp of the CPM-pulses is explained by the interplay of an effective time-shift backward in time of the CPM-pulses and the self-phase modulation in the gain section. The saturable absorber results in a "time-shift" of the CPM-pulse amplitude backward in time compared to the pulse phase (instantaneous wavelength), since the saturable absorber shaves off the pulse front. However, the phase of the pulse is not affected by the attenuation, but changes only due to the carrier induced refractive index changes. The induced wavelength chirp upon a single pass through the cavity has thus to balance the change in the pulse wavelength chirp induced by the "time-shift" of the pulse.
This explanation agrees well with calculations and measurements on a hybridly mode-locked CPM laser diode, where the wavelength chirp could be partially controlled by tuning the modulation frequency. In the case of a high α-parameter value resulting in a strongly chirped pulse we find that the gain dispersion terms, which basically are the coupling terms between the propagation-equation for the electrical field amplitude and phase, result in significant changes in the wavelength chirp (amplitude) of the CPM pulses. Here, especially the gain dispersion term $dg/d\omega$ in the saturable absorber leads to significant changes in the absorption for a highly chirped pulse. The "time-shift" of the pulse amplitude depends thus on both the value of $dg/d\omega$ and the instantaneous wavelength chirp, which leads to changes in both the pulse amplitude and phase steady state conditions.

The CPM laser may not only be used as a pulse source (transmitter side), but may also be used on the receiver side, where the CPM laser may be injection mode-locked.
Our large signal model reveals that injection mode-locking of the CPM laser

is possible. However, we have only made a few numerical simulations of injection mode-locked CPM lasers. The CPM laser was synchronized to an external pulse train, with a repetition frequency which approximately corresponded to the passive CPM mode-locking frequency or half the passive mode-locking frequency. The external pulse train was made up of hyperbolic secant shaped pulses with a FWHM of 5-8 ps corresponding to the pulse width of the passive mode-locked CPM laser.
The frequency band of effective mode-locking was as expected found to depend on the power of the injected pulses. Furthermore, the injection mode-locked pulse shape could be very asymmetric depending on the detuning. Our investigation has not been systematic, but does display the possibility of injection mode-locking the CPM laser.

In conclusion, we have shown that a detailed modelling of the material dynamics is important to understand the operating principles of monolithic colliding-pulse mode-locked laser diodes. Especially the inclusion of SHB and carrier heating in the gain sections and the inclusion of the QCSE in the saturable absorber are found to be necessary for explaining the CPM laser characteristics.

Bibliography

[1] M. C. Wu, Y. K. Chen, T. Tanbaum-Ek, R. A. Logan, M. A. Chin, G. Raybon, "Transform-Limited 1.4 ps Optical Pulses from a Monolithic Colliding-Pulse Mode-Locked Quantum Well Laser", Appl. Phys. Lett., **57**, pp. 759-761, 1990.

[2] Y. K. Chen, M. C. Wu, T. Tanbbun-Ek, R. A. Logan, M. A. Chin, "Subpicosecond Monolithic Colliding-Pulse Mode-Locked Multiple Quantum Well Lasers", Appl. Phys. Lett. **58** (12) pp. 1253, 1991.

[3] D. J. Derickson, R. J. Helkey, A. Mar, J. R. Karin, J. G. Wasserbauer, J. E. Bowers, "Short Pulse Generation Using Multisegment Mode-Locked semiconductor Lasers", IEEE Jour. Quantum Elec. **28** (10) pp. 2186, 1992.

[4] J. F. Martins-Filho, E. A. Avrutin, C. N. Ironside, J. S. Roberts, "Monolithic Multiple Colliding Pulse Mode-Locked Quantum-Well Lasers: Experiment and Theory", IEEE Journal of Selected Topics in Quantum Electronics, **1**, (2), pp. 539, 1995.

[5] Z. Wang, J. M. Nielsen, S. D. Brorson, B. Christensen, T. Franck, N. G. Jensen, A. M. Larsen, J. Nørregaard, E. Bødtker, "15.8 Gbit/s System Transmission Experiment using a 5.2 mm Long Monolithic Colliding-Pulse Modelocked Quantum Well Laser Diode", Electron. Lett. **31** pp.272, 1995.

[6] I. N. Duling, III, "Compact Sources of Ultrashort Pulses", Cambridge University Press, Cambridge, 1995.

[7] L. M. Zhang, J. E. Carrol, "Dynamic Response of Colliding-Pulse Mode-Locked Quantum-Well Lasers", IEEE Journal of Quantum Electronics, **31** (2), pp. 240-243, 1995.

[8] D. J. Jones, L. M. Zhang, J. E. Carrol, D. D. Marcenac, "Dynamics of Monolithic Passively Pulse Mode-Locked Semiconductor Lasers", IEEE Journal of Quantum Electronics, **31**, pp. 1051-1058, 1995.

[9] S. Bischoff, M. P. Sørensen, J. Mørk, S. D. Brorson, T. Franck, J. M. Nielsen, A. Møller-Larsen, "Pulse-Shaping mechanism in Colliding-Pulse Mode-Locked Laser Diodes", Appl. Phys. Lett. **67** (26) pp. 3877, 1995.

[10] R. G. M. P. Koumans, R. van Roijen, "Theory for Passive Mode-Locking in Semiconductor Laser Structures Including the Effects of Self-Phase Modulation, Dispersion and Pulse Collisions", IEEE Journal of Quantum Electronics, **32** (3), pp. 478, 1996.

[11] H. Haus, "Theory of Mode Locking with Slow Saturable Absorber", IEEE Jour. Quantum Electron., **11** (9), pp. 736, 1975

[12] E. P. Ippen, "Principles of Passive Mode Locking", Appl. Phys. B, **58**, pp. 159-170, Springer-Verlag, 1994.

[13] J. A. Leegwater, "Theory of Mode-Locked Semiconductor Lasers", IEEE Jour. of Quantum Electronics, **32** (10), pp. 1782-1790, 1996.

[14] S. Bischoff, S. D. Brorson, T. Franck, M. Hofmann, L. Prip, M. P. Sørensen, J. Mørk, "Modelling and Characterization of Colliding Pulse Mode-Locked (CPM) Quantum Well Lasers", SPIE'96, Physics and Simulation of Optoelectronic Devices IV, **2693**, pp. 477-488, San Jose, January 1996.

[15] Y.-K. Chen, M. C. Wu, "Monolithic Colliding-Pulse Mode-Locked Quantum Well Lasers", IEEE Jour. Quantum Electron., **28** (10), pp. 2176-2185, 1992

[16] S. D. Brorson, T. Franck, S. Bischoff, L. Prip, M. Hofmann, J. M. Nielsen, J. Mørk, "Pulsewidth Dependence upon Gain Current and Absorber Voltage in Monolithic CPM Lasers", Submitted to IEEE Photon. Technol. Lett.

[17] J. R. Karin, R. J. Helkey, D. J. Derickson, R. Nagarajan, D. S. Allin, J. E. Bowers and R. L. Thornton, "Ultrafast Dynamics in Field-Enhanced Saturable Absorbers", Appl. Phys. Lett. **64**, pp. 676-678, 1994

[18] J. Karin, "Ultrafast Dynamics in Semiconductor Laser Structures", ECE Technical Report #94-18, Department of Electrical and Computing Engineering, University of California at Santa Barbara, 1994.

[19] H. Haug, "Optical Nonlinearities and Instabilities in Semiconductors", Academic Press, San Diego, 1991.

[20] C. Weisbuch, B. Vinter, "Quantum Semiconductor Structures", Aca-

demic Press, Inc., San Diego, 1991.

[21] K. Fröjdh, "Carrier transport effects in semiconductor heterostructures for optical applications", Doctoral Thesis, Royal Inst. of Technol., Stockholm, Sweden, 1996.

[22] G. P. Agrawal, N. K. Dutta, "Semiconductor Lasers", Van Nostrand Reinhold, New York, 1993.

[23] H. E. Lassen, "Modelling and Experimental Characterization of Dynamical Properties of Semiconductor Optical Amplifiers", Doctoral Thesis, Electromagnetic Institute, The Technical University of Denmark, LD 79, April 1990.

[24] J. Mørk, M. Willatzen, J. Mark, M. Svendsen, C. P. Seltzer, "Characterization and Modelling of Ultrafast Carrier Dynamics in Quantum Well Optical Amplifiers", SPIE'95, Physics and Simulation of Optoelectronic Devices II, **2146**, Los Angeles, January 1994.

[25] A. Yariv, "Quantum Electronics", John Wiley & Sons, New York, 1989.

[26] M. Willatzen, "Theory of Gain in Bulk and Quantum-Well Semiconductor Lasers", Doctoral Thesis, Niels Bohr Institute, Ørsted Laboratory, University of Copenhagen, Denmark, 1993.

[27] A. Uskov, J. Mørk, J. Mark, "Wave Mixing in Semiconductor Laser Amplifiers Due to Carrier Heating and Spectral-Hole Burning", IEEE Jour. Quantum Electron., **30** (8), pp. 1769-1781, 1994.

[28] N. Tessler, R. Nagar, G. Eisenstein, "Structure Dependent Modulation Response in Quantum-Well Lasers", IEEE Jour. Quantum Electron., **28** (10), pp. 2242-2250, 1992.

[29] N. Tessler, G. Eisenstein, "On Carrier Injection and Gain Dynamics in Quantum Well Lasers", IEEE Jour. Quantum Electron., **29** (6), pp. 1586-1595, 1993

[30] J. Mark and J. Mørk, "Subpicosecond gain Dynamics in InGaAsP Optical Amplifiers: Experiment and Theory", Appl. Phys. Lett. **61**, (19) pp. 2281-2283, 1992.

[31] A. Uskov, J. Mørk, J. Mark, "Theory of Short-pulse Gain Saturation in Semiconductor Laser Amplifiers", IEEE Photon. Technol. Lett., **4** (5), 1992.

[32] M. Willatzen, J. Mark, J. Mørk, and C. P. Seltzer, "Carrier Temperature and Spectral Holeburning dynamics in InGaAsP Quantum Well Laser Amplifiers", Appl. Phys. Lett. **64**, (2) pp. 143-145, 1994.

[33] S. D. Brorson, S. Bischoff, J. Mørk, A. Møller-Larsen, J. M. Nielsen, "Femtosecond Carrier Dynamics and Modelocking in Monolithic CPM

Lasers", IEEE Photon. Technol. Lett., **8** (10), 1996.

[34] For a textbook discussion see: W. W. Chow, S. W. Koch, M. Sargent III, "Semiconductor-Laser Physics", Springer-Verlag, New York, 1994.

[35] K. L. Hall, G. Lenz, E. P. Ippen, "Femtosecond Time Domain Measurements of Group Velocity Dispersion in Diode Lasers at 1.5 μm", Jour. of Lightwave Technology, **10** (5), 1992.

[36] M. Schell, J. Yu, M. Tsuchiya, T. Kammiya, "Chirp of Passively and Actively Mode-Locked Semiconductor Lasers", Appl. Phys. Lett., **67** (13), pp. 1797-1799, 1995.

[37] M. Schell, M. Tsuchiya, T. Kamiya, Chirp and Stability of Mode-Locked Semiconductro Lasers, IEEE Jour. of Quantum Elec. **32** (7) 1180, 1996.

[38] J. Mørk, A. Mecozzi, "Response Function for Gain and Refractive Index Dynamics in Active Semiconductor Waveguides, Appl. Phys. Lett., **65** (14), pp. 1736-1738, 1994.

[39] M. Preisel, "Carrier Capture and Carrier Kinetics in Biased Qantum Well Devices", Doctoral Thesis, Niels Bohr Institute, Ørsted Laboratory, University of Copenhagen, Denmark, 1994.

[40] S. Haußer, "Rekombinationsmechanismen und Wellenleitung in Quantum Well Halbleiterlasern und -verstärkern", Physikalisches Institut der Universität Stuttgart, 1990.

[41] J. Mørk, J. Mark, C. P. Seltzer, "Carrier Heating in InGaAsP Laser Amplifiers Due to Two-Photon Absorption", Appl. Phys. Lett. **64**, (25) pp. 2206-2208, 1994.

[42] P. S. Zory, Jr., "Quantum Well Lasers", Academic Press, INC., New York, 1993.

[43] A. E. Siegman, "Lasers", University Science Books, Stanford University, 1986.

[44] M. S. Stix, E. P. Ippen, "Pulse Shaping in Passively Mode-Locked Ring Dye Lasers", IEEE Jour. Quantum Electron., **19** (4), pp. 520-525, 1983

[45] R. J. Helkey, "Subpicosecond Pulse Generation Using Modelocked Semiconductor Laser Diodes", Department of Electrical and Computing Engineering, University of California at Santa Barbara, 1993.

[46] T. Franck, S. D. Brorson, A. Møller-Larsen, J. M. Nielsen, and J. Mørk, "Synchronization Phase Diagrams of Monolithic Colliding Pulse Modelocked Lasers", IEEE Photon. Tech. Lett., **8**, pp. 40-42, 1996.

[47] J. Mørk, J. Mark, "Femtsekund Måleteknik og Optisk Switching", DOPS-NYT **3**, 1992.

[48] N. Peyghambarian, S. W. Koch, A. Mysyrowicz, "Introduction to Semiconductor Optics", Prentic Hall, New Jersey, 1993.

[49] Bjørn Jonsson, private communication, 1995.

[50] M. P. Sørensen, K. A. Shore, T. Geisler, P. L. Christiansen, J. Mørk, J. Mark, "Dynamics of Additive-Pulse Mode-Locked Fibre Lasers", Optics Communications **90**, pp. 65-69, 1992.

[51] M. Hofmann, S. Bischoff, T. Franck, L. Prip, K. Fröjdh, S. D. Brorson, J. Mørk, "Chirp of Hybridly Modelocked Monolithic CPM Diode Lasers", Submitted to Appl. Phys. Lett.

[52] G. P. Agrawal, N. A. Olsson, "Self-Phase Modulatiom and Spectral Broadening of Optical Pulses in Semiconductor Laser Amplifiers", IEEE Jour. of Quantum Elec. **25** (11) 2297, 1989.

[53] P. P. Vasil'ev, "High-Power High-Frequency Picosecond Pulse Generation by Passively Q-Switched 1.55 μm Diode Lasers", IEEE Jour. Quantum Electron., **29** (6), pp. 1687-1692, 1993

Chapter 3

Excitonic Semiconductor Response for Varying Material Thickness: Transition from Quantum-Well to Bulk

In the previous chapter we have discussed the Colliding-Pulse Mode-locked (CPM) quantum-well laser. Here, we will theoretically investigate the excitonic semiconductor response for varying material thickness. The goal of the work presented in this chapter is to understand and elucidate the transition from a two dimensional (2-D) transmission spectrum to a three-dimensional (3-D) transmission spectrum. The optical experiment corresponding to this is shown schematically in Fig. 3.1. The figure shows a semiconductor slab, which is excited by an incoming electrical field, E_{in}. A fraction of the incoming field will be reflected, E_{ref} and another fraction transmitted, E_{tra}.

Furthermore, there will be two counter propagating fields in the semiconductor slab after excitation. The semiconductor material could typically

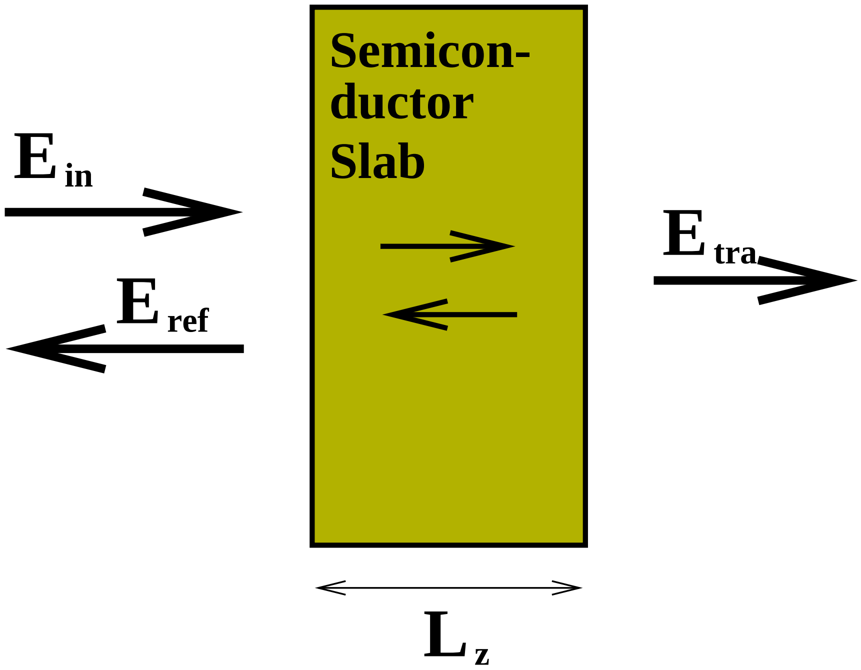

Figure 3.1: Schematic plot of a semiconductor slab with thickness, L_z, which is excited by an incoming light pulse, E_{in}. E_{ref} is the reflected field and E_{tra} is the transmitted field. The two counter propagating fields in the semiconductor slab after excitation are indicated by two arrows.

be GaAs or InGaAs. The basic equations for the semiconductor slab are presented in section 3.2. The derivation of the basic equations are, for the interested reader, included in the appendices C, D, E and F. In section 3.3 and 3.4 we will present numerical results for the linear optical response of GaAs.

3.1 Introduction

The optical properties of semiconductor materials have been investigated in great detail over the last years [1]. Within these studies, it has been shown that the linear optical response function (susceptibility) is dominated by bound electron-hole states (excitons) and the Coulomb enhanced scattering states. Not only Coulomb but also light propagation effects play an important role for the description of optical experiments, since incident and transmitted fields are related by the wave equation. So far, Coulomb and propagation effects have been treated self-consistently only for half-space samples (three dimensional samples, 3-D) [2] and for idealized multiple quantum wells (two dimensional samples, 2-D) [3]. The famous half-space problem has been solved by Stahl and co-workers [2] using the coherent wave approach. This approach clarified the origin of the exciton free surface layer (dead layer) and the role of the electronic boundary conditions. The theoretical work in the 2-D case has mainly been done for the case, where the lowest subband is sufficient to describe the electronic properties. This limits the validity of the 2-D theory to structures where the quantum well width is well below the 3-D exciton Bohr diameter.
The exciton binding energy and oscillator strength as a function of material thickness has been calculated by variational and perturbation methods. A detailed study of the exciton binding energy and oscillator strength for GaAs quantum wells with a width of up to 20 nm has been made in [4]. Concerning the transition from 2-D to 3-D structures, theories with fractional dimensional space [5, 6, 7], where the fractional dimension of the exciton is a fitting parameter, have been developed. A review of the recent literature is given in the paper by Zimmermann [7]. However, in these studies no relations were made to the influence of light propagation in a thin slab. To our knowledge optical transmission, reflection and absorption spectra have been calculated for the ideal 2-D and 3-D case only. The transition from 2-D to 3-D regime, especially non-stationary effects such as short pulse excitation have not been fully investigated previously. Furthermore, most of the work in this field is focussed on excitons and less on continuum states. However, due to the redistribution of oscillator strength in linear optics, the interplay between exciton and continuum states should be important in the 2-D to 3-D transition, because the 3-D continuum develops from higher 2-D subbands.

3.2 Basic equations

In this section the theoretical method used in calculating observable quantities is presented. The derivation of the governing equations is, for the interested reader, added in the appendices C, D, E and F.

The measurable quantities of interest in an optical experiment are the spectral transmission, α, or the reflection coefficient, R:

$$\alpha(\omega) = -\ln\left(\frac{I_t(\omega)}{I_0(\omega)}\right) \quad , \tag{3.1a}$$

$$R(\omega) = \left(\frac{I_r(\omega)}{I_0(\omega)}\right) \quad , \tag{3.1b}$$

where I_t, I_r, I_0 are the transmitted, reflected and incident intensity of the transversal field, E_T. From such measurements, the absorbed irradiance $w(\omega)$, i.e. the amount of light per unit length that stays in the sample, can be calculated from:

$$w(\omega) = \left[1 - \left(\frac{I_t(\omega)}{I_0(\omega)}\right) - \left(\frac{I_r(\omega)}{I_0(\omega)}\right)\right] \quad . \tag{3.2}$$

The observable quantities have to be computed by solving the wave equation to determine the transverse electrical field, E_T:

$$\left(\nabla^2 - \frac{1}{c^2}\frac{\partial^2}{\partial t^2}\right) E_T = \frac{4\pi}{c_0^2}\frac{\partial j}{\partial t} \quad , \tag{3.3}$$

where we implicitly assume that the total current, j, is purely transverse. This is always fulfilled for the plane wave excitation, which is considered throughout this chapter. The constants c and c_0 are the speed of light in the semiconductor slab and in vacuum, respectively. The current, j, or the polarization, P, is the source term for the electric field [1]. Thus, to obtain the measurable quantities, the equation of motion for the polarization is needed. The polarization is obtained from:

$$j = \frac{\partial P}{\partial t} = \left\langle \psi^\dagger \frac{\hbar e}{i2m_0}\nabla_{\mathbf{r}}\psi \right\rangle + h.a. \quad , \tag{3.4}$$

where $\Psi^\dagger$ and Ψ are the Heisenberg creation and annihilation operators, respectively. m_0 is the bare electron mass, $\hbar$ is Planck's constant, e is the electronic charge and $h.a.$ stands for the hermitian adjoint. The equations of motion for the Heisenberg creation and annihilation operators are determined by the total Hamiltonian which, besides the free parts, $H_{0,el}$, contains the Coulomb interaction, H_I, of the carriers and the carrier interaction with the light field, $H_{el,l}$:

$$\begin{aligned}
H_{el} &= H_{o,el} + H_{el,l} + H_I \quad , && (3.5a)\\
H_{0,el} &= \int d^3x \psi^\dagger(\vec{r}) \left(-\frac{\hbar^2}{2m_0}\Delta + V_L(\vec{r}) + V_c(\vec{r}) \right) \psi(r) \quad , && (3.5b)\\
H_{el,l} &= \int d^3r \psi^\dagger(\vec{r}) \left(-\frac{\hbar e}{i m_0 c}\vec{A}(\vec{r},t)\cdot\vec{\nabla} \right) \psi(\vec{r}) \quad , && (3.5c)\\
H_I &= \frac{1}{2}\int d^3r d^3r' \psi^\dagger(\vec{r})\psi^\dagger(\vec{r}')V(\vec{r}-\vec{r}')\psi(\vec{r}')\psi(\vec{r}) \quad . && (3.5d)
\end{aligned}$$

Here $H_{o,el}$ is free carrier Hamiltonian, which contains the kinetic energy, the lattice potential and the confinement potential including the boundary conditions at the interfaces between the sample and the outside world. $H_{el,l}$ is the carrier-light interaction Hamiltonian and H_I is the Hamiltonian of the carrier-carrier Coulomb interaction. $\vec{A}(\vec{r},t)$ is the transversal vector potential and $\vec{r}$ is the 3-dimensional space coordinate, $\vec{r} = (x,y,z) = (\vec{\rho},z)$. The Coulomb potential, $V(\vec{r})$ is in CGS units

$$V(\vec{r}) = \frac{e^2}{\varepsilon_0|\vec{r}|} \quad , \tag{3.6}$$

where ε_0 is the screening of the Coulomb potential due to off-resonant transitions. To study the basic effects of the 2-D to 3-D transition we first consider the ideal condition, where the potential V_c which confines the electrons in one direction (z - direction) of the sample is infinite,

$$V_c(z) = \begin{cases} 0 & \text{when } |z| < \frac{L_z}{2} \\ \infty & \text{when } |z| \geq \frac{L_z}{2} \end{cases} \quad , \tag{3.7}$$

where L_z is the total width of the sample. Effects of a finite confinement potential on the optical susceptibility are discussed e.g. in Ref.[4]. The transverse electrical field E_T is determined by the vector potential, $\vec{A}(\vec{r})$,

$$\vec{E}_T = -\frac{1}{c_0}\frac{\partial \vec{A}(r,\vec{t})}{\partial t} \approx \frac{i\omega_L}{c}\vec{A}(\vec{r},t) \quad . \tag{3.8}$$

In the following the slowly varying envelope and rotating wave approximation is applied, see appendix D. To obtain the polarization, which is the source term in the wave equation, the Heisenberg creation and annihilation operators are expanded in terms of the eigenfunctions of the free particle Hamiltonian. This is more convenient in our approach where we solve the equations of motion in momentum space:

$$\psi^\dagger(\vec{r}) = \sum_{\vec{k}_\parallel, n, \lambda} a^\dagger_{\vec{k}_\parallel, n, \lambda} \frac{e^{-i\vec{k}_\parallel \cdot \vec{\rho}}}{L} \overline{f}_{n,\lambda}(z) \overline{u}_\lambda(\vec{k}, \vec{r}) \quad , \tag{3.9a}$$

$$\psi(\vec{r}) = \sum_{\vec{k}_\parallel, n, \lambda} a_{\vec{k}_\parallel, n, \lambda} \frac{e^{i\vec{k}_\parallel \cdot \vec{\rho}}}{L} f_{n,\lambda}(z) u_\lambda(\vec{k}, \vec{r}) \quad . \tag{3.9b}$$

Here, $\lambda = c, v$ denotes either the conduction or valence band, respectively. $\vec{k}_\parallel$ is the in-plane momentum, u_λ is the Bloch function, and $L^2 L_z$ represents the volume of the crystal with L^2 being the area of the well. $\vec{k}$ is the total momentum. $\overline{u}_\lambda$ is the complex conjugate of the Bloch function u_λ. The quantum number of the subband is labeled by the index n. $a_{\vec{k}_\parallel, n, \lambda}$ is the electron annihilation operator and $a^\dagger_{\vec{k}_\parallel, n, \lambda}$ is the electron creation operator of a Bloch electron with the quantum numbers $\vec{k}_\parallel, n, \lambda$. The z dependence of the wave function $f_{n,\lambda}(z)$ is for the quantum numbers $n = 1, 3, 5, 7, \ldots$,

$$f_{n,\lambda}(z) = \begin{cases} \sqrt{\frac{2}{L_z}} \cos\left(n \frac{\pi}{L_z} z\right) & \text{when } |z| \leq \frac{L_z}{2} \\ 0 & \text{when } |z| \geq \frac{L_z}{2} \end{cases} \quad , \tag{3.10}$$

and for $n = 2, 4, 6, 8, \ldots$,

$$f_{n,\lambda}(z) = \begin{cases} \sqrt{\frac{2}{L_z}} \sin\left(n \frac{\pi}{L_z} z\right) & \text{when } |z| \leq \frac{L_z}{2} \\ 0 & \text{when } |z| \geq \frac{L_z}{2} \end{cases} \quad . \tag{3.11}$$

The Heisenberg equation of motion for the electron operators, which is derived in appendix F, yields within linear optical response theory,

$$\frac{\partial p_{\vec{k}_\parallel, n_1^v, n_2^c}}{\partial t} = -(i\omega_{\vec{k}_\parallel}^{n_1^v, n_2^c} + \gamma) p_{\vec{k}_\parallel}^{n_1^v, n_2^c} \tag{3.12}$$

$$+\frac{i}{\hbar}d_{c,v}^{\vec{k}_{\|},n_2^c,n_1^v}E_{\vec{k}_{\|}}^{n_2^c,n_1^v}$$
$$+\frac{i}{\hbar}\sum_{\vec{k}'_{\|}\neq\vec{k}_{\|},q_1^v,q_3^c}p_{\vec{k}'_{\|},q_1^v,q_3^c}V_{|\vec{k}'_{\|}-\vec{k}_{\|}|}^{q_1^v,n_2^c,q_3^c,n_1^v} \quad ,$$

Here, d_{cv}^{k,n_1^v,n_2^c} is the dipole-moment, which is a function of both the subband indices and the in-plane momentum $\vec{k}$ [1].

$$d_{cv}^{\vec{k},n_1^v,n_2^c} = d_{cv}^0 \frac{E_{gap}}{E_{gap}+\frac{\hbar^2|\vec{k}|^2}{2m_r}+((n_1^v)^2-1)\frac{\hbar^2\pi^2}{2m_vL_z^2}+((n_2^c)^2-1)\frac{\hbar^2\pi^2}{2m_cL_z^2}} \quad . \tag{3.13}$$

$w_k^{n_1^v,n_2^c} = w_k^{n_2^c}-w_k^{n_1^v}-E_{gap}$ is the transition frequency of the quantized states minus the bandgap energy. The constant γ is a phenomenologically introduced decay rate of the polarization function $\left(p_{\vec{k}}^{n_1^v,n_2^c}=\left\langle a^\dagger_{\vec{k},n_1,v}a_{\vec{k},n_2,c}\right\rangle\right)$. n_x^λ and q_x^λ are quantum numbers of the quantized states. $\vec{k}$ and $\vec{k}'$ are in-plane momentum vectors. Since we are interested only in the optical spectra we have neglected terms, which are attributed to intra-band transitions, (see appendix D). $V_{|\vec{q}|}^{n_1^{\lambda_1},n_2^{\lambda_2},n_3^{\lambda_3},n_4^{\lambda_4}}$ is the unscreened Coulomb potential, which for $n_x^{\lambda_x}=1,3,5,7,\ldots$ is given as

$$\begin{aligned}
V_{|\vec{q}|}^{n_1^{\lambda_1},n_2^{\lambda_2},n_3^{\lambda_3},n_4^{\lambda_4}} &= \frac{2\pi e^2}{L^2\epsilon_0|\vec{q}|}\frac{2}{\pi^2}\left(|\vec{q}|\frac{L_z}{\pi}\right)^2\left(e^{-|\vec{q}|L_z}-1\right) \qquad (3.14)\\
&\times\left[\frac{\cos\left((n_2^{\lambda_2}-n_3^{\lambda_3})\frac{\pi}{2}\right)}{\left(|\vec{q}|\frac{L_z}{\pi}\right)^2+(n_2^{\lambda_2}-n_3^{\lambda_3})^2}+\frac{\cos\left((n_2^{\lambda_2}+n_3^{\lambda_3})\frac{\pi}{2}\right)}{\left(|\vec{q}|\frac{L_z}{\pi}\right)^2+(n_2^{\lambda_2}+n_3^{\lambda_3})^2}\right]\\
&\times\left[\frac{\cos\left((n_1^{\lambda_1}-n_4^{\lambda_4})\frac{\pi}{2}\right)}{\left(|\vec{q}|\frac{L_z}{\pi}\right)^2+(n_1^{\lambda_1}-n_4^{\lambda_4})^2}+\frac{\cos\left((n_1^{\lambda_1}+n_4^{\lambda_4})\frac{\pi}{2}\right)}{\left(|\vec{q}|\frac{L_z}{\pi}\right)^2+(n_1^{\lambda_1}+n_4^{\lambda_4})^2}\right]\\
&+\frac{2\pi e^2}{L^2\epsilon_0|\vec{q}|}\frac{1}{\pi}|\vec{q}|\frac{L_z}{\pi}\frac{1}{\left(|\vec{q}|\frac{L_z}{\pi}\right)^2+(n_2^{\lambda_2}-n_3^{\lambda_3})^2}\\
&\times\left(\delta_{n_1^{\lambda_1}-n_4^{\lambda_4},n_2^{\lambda_2}-n_3^{\lambda_3}}(1+\delta_{n_1^{\lambda_1}-n_4^{\lambda_4},0})+\delta_{n_1^{\lambda_1}+n_4^{\lambda_4},n_2^{\lambda_2}-n_3^{\lambda_3}}\right)\\
&+\frac{2\pi e^2}{L^2\epsilon_0|\vec{q}|}\frac{1}{\pi}|\vec{q}|\frac{L_z}{\pi}\frac{1}{\left(|\vec{q}|\frac{L_z}{\pi}\right)^2+(n_2^{\lambda_2}+n_3^{\lambda_3})^2}
\end{aligned}$$

$$\times\left(\delta_{n_1^{\lambda_1}-n_4^{\lambda_4},n_2^{\lambda_2}+n_3^{\lambda_3}}+\delta_{n_1^{\lambda_1}+n_4^{\lambda_4},n_2^{\lambda_2}+n_3^{\lambda_3}}\right) \quad .$$

The expression for the Coulomb potential for other combinations of quantum numbers is similar to the one given in Eq. (3.14). The derivation and a full listing of the Coulomb potential is given in appendix C.
The coupling to the light field is treated semi-classically and enters through $E_{\vec{k}}^{n_1^v,n_2^c}$ (see appendix D),

$$E_{\vec{k}}^{n_1^c,n_2^v}=\int_{-\frac{L_z}{2}}^{\frac{L_z}{2}} dz\overline{f}_{n_1^v}(z)E_T(z)f_{n_2^c}(z) \quad , \tag{3.15}$$

where the transverse field $E_T(z)$ is determined by solving the wave equation, (see appendix E). Often, in the description of optical experiments with semiconductors it is assumed that optical absorption occurs between quantized states with equal quantum number $n_1 = n_2$. This approximation assumes that the electric field is space independent or only is weakly space dependent. However, as we see from the expression for $E_{\vec{k}}^{n_1^c,n_2^v}$, transitions between states with unequal quantum number are allowed for spatially varying fields. In general, one can only neglect the transitions between quantized states with unequal quantum number as long as the material width (L_z) is much shorter than the wavelength of the exciting pulse. This case yields $E_{\vec{k}}^{n_1^c,n_2^v} \sim \delta_{n_1^c,n_2^v}$.
Assuming the incoming light field to consist of plane waves, we can solve Maxwell's equation in the frequency domain analytically, (see appendix E). Again we only give the solution for the quantum numbers $n_x^{\lambda^x} = 1, 3, 5, 7, \ldots$. The derivation of the wave equation and a full listing of the solution for different quantum numbers is added in appendix E:

$$\begin{aligned} E_T^{n_1^v,n_2^c}(z,\omega) &= \frac{4\pi}{L_z}\frac{c^2}{c_0^2}\tilde{P}_{n_1^v,n_2^c}(\omega) \\ &\cdot\left(\frac{cos\left((n_1^v-n_2^c)\frac{\pi}{L_z}z\right)}{(n_1^v-n_2^c)^2\frac{\pi^2c^2}{L_z^2\omega^2}-1}+\frac{cos\left((n_1^v+n_2^c)\frac{\pi}{L_z}z\right)}{(n_1^v+n_2^c)^2\frac{\pi^2c^2}{L_z^2\omega^2}-1}\right) \\ &+t_{n_1^v,n_2^c}(\omega)e^{i\frac{\omega}{c}z}+r_{n_1^v,n_2^c}(\omega)e^{-i\frac{\omega}{c}z} \quad . \end{aligned} \tag{3.16}$$

Here, $t_{n_1^v,n_2^c}$ and $r_{n_1^v,n_2^c}$ are functions, which have to be determined by applying the boundary conditions for the electrical field at the interfaces (continuity of field and first derivative). The "polarization" $\tilde{P}_{n_1^v,n_2^c}$ is defined as,

$$\tilde{P}_{n_1^v,n_2^c} = \frac{1}{L^2}\sum_{\vec{k}} d_{cv}^{\vec{k},n_1^v,n_2^c} p_{\vec{k}}^{n_1^v,n_2^c} \quad . \tag{3.17}$$

Using the boundary conditions for an index matched structure, the electric field can be determined to be (see also appendix E):

$$\begin{aligned}
E_T(z,\omega) = \; & E_{in}e^{ik_z z} \\
& -2\pi\frac{\omega}{c}\frac{c^2}{c_0^2}\frac{e^{ik_z\frac{L_z}{2}}}{k_z\frac{L_z}{2}}\frac{e^{ik_z z}+e^{-ik_z z}}{2}\sum_{n_1^v,n_2^c}\tilde{P}_{n_1^v,n_2^c}(\omega) \\
& \times\left(\frac{\cos\left((n_1^v-n_2^c)\frac{\pi}{2}\right)}{(n_1^v-n_2^c)^2\frac{\pi^2c^2}{L_z^2\omega^2}-1}+\frac{\cos\left((n_1^v+n_2^c)\frac{\pi}{2}\right)}{(n_1^v+n_2^c)^2\frac{\pi^2c^2}{L_z^2\omega^2}-1}\right) \\
& +2\pi\frac{\omega}{c}\frac{c^2}{c_0^2}\frac{1}{k_z\frac{L_z}{2}}\sum_{n_1^v,n_2^c}\tilde{P}_{n_1^v,n_2^c}(\omega) \\
& \times\left(\frac{\cos\left((n_1^v-n_2^c)\frac{\pi}{L_z}z\right)}{(n_1^v-n_2^c)^2\frac{\pi^2c^2}{L_z^2\omega^2}-1}+\frac{\cos\left((n_1^v+n_2^c)\frac{\pi}{L_Z}z\right)}{(n_1^v+n_2^c)^2\frac{\pi^2c^2}{L_z^2\omega^2}-1}\right) \\
& -2\pi\frac{\omega}{c}\frac{c^2}{c_0^2}\frac{e^{ik_z\frac{L_z}{2}}}{k_z\frac{L_z}{2}}\frac{e^{ik_z z}+e^{-ik_z z}}{2}\sum_{m_1^v,m_2^c}\tilde{P}_{m_1^v,m_2^c}(\omega) \\
& \times\left(\frac{\cos\left((m_1^v-m_2^c)\frac{\pi}{2}\right)}{(m_1^v-m_2^c)^2\frac{\pi^2c^2}{L_z^2\omega^2}-1}-\frac{\cos\left((m_1^v+m_2^c)\frac{\pi}{2}\right)}{(m_1^v+m_2^c)^2\frac{\pi^2c^2}{L_z^2\omega^2}-1}\right) \\
& +2\pi\frac{\omega}{c}\frac{c^2}{c_0^2}\frac{1}{k_z\frac{L_z}{2}}\sum_{m_1^v,m_2^c}\tilde{P}_{m_1^v,m_2^c}(\omega) \\
& \times\left(\frac{\cos\left((m_1^v-m_2^c)\frac{\pi}{L_z}z\right)}{(m_1^v-m_2^c)^2\frac{\pi^2c^2}{L_z^2\omega^2}-1}-\frac{\cos\left((m_1^v+m_2^c)\frac{\pi}{L_Z}z\right)}{(m_1^v+m_2^c)^2\frac{\pi^2c^2}{L_z^2\omega^2}-1}\right) \\
& +2\pi\frac{\omega}{c}\frac{c^2}{c_0^2}\frac{e^{ik_z\frac{L_z}{2}}}{k_z\frac{L_z}{2}}\frac{e^{ik_z z}+e^{-ik_z z}}{2}\sum_{m_1^v,n_2^c}\tilde{P}_{m_1^v,n_2^c}(\omega)
\end{aligned} \tag{3.18}$$

$$
\begin{aligned}
&\times \left(\frac{\sin\left((m_1^v - n_2^c)\frac{\pi}{2}\right)}{(m_1^v - n_2^c)^2 \frac{\pi^2 c^2}{L_z^2 \omega^2} - 1} + \frac{\sin\left((m_1^v + n_2^c)\frac{\pi}{2}\right)}{(m_1^v + n_2^c)^2 \frac{\pi^2 c^2}{L_z^2 \omega^2} - 1} \right) \\
&+2\pi \frac{\omega}{c} \frac{c^2}{c_0^2} \frac{1}{k_z \frac{L_z}{2}} \sum_{m_1^v, n_2^c} \tilde{P}_{m_1^c, n_2^v}(\omega) \\
&\times \left(\frac{\sin\left((m_1^v - n_2^c)\frac{\pi}{L_z} z\right)}{(m_1^v - n_2^c)^2 \frac{\pi^2 c^2}{L_z^2 \omega^2} - 1} + \frac{\sin\left((m_1^v + n_2^c)\frac{\pi}{L_Z} z\right)}{(m_1^v + n_2^c)^2 \frac{\pi^2 c^2}{L_z^2 \omega^2} - 1} \right) \\
&+2\pi \frac{\omega}{c} \frac{c^2}{c_0^2} \frac{e^{ik_z \frac{L_z}{2}}}{k_z \frac{L_z}{2}} \frac{e^{ik_z z} + e^{-ik_z z}}{2} \sum_{n_1^v, m_2^c} \tilde{P}_{n_1^v, m_2^c}(\omega) \\
&\times \left(\frac{\sin\left((m_2^c - n_1^v)\frac{\pi}{2}\right)}{(m_2^c - n_1^v)^2 \frac{\pi^2 c^2}{L_z^2 \omega^2} - 1} + \frac{\sin\left((n_1^v + m_2^c)\frac{\pi}{2}\right)}{(n_1^v + m_2^c)^2 \frac{\pi^2 c^2}{L_z^2 \omega^2} - 1} \right) \\
&+2\pi \frac{\omega}{c} \frac{c^2}{c_0^2} \frac{1}{k_z \frac{L_z}{2}} \sum_{n_1^v, m_2^c} \tilde{P}_{n_1^v, m_2^c}(\omega) \\
&\times \left(\frac{\sin\left((m_2^c - n_1^v)\frac{\pi}{L_z} z\right)}{(m_2^c - n_1^v)^2 \frac{\pi^2 c^2}{L_z^2 \omega^2} - 1} + \frac{\sin\left((n_1^v + m_2^c)\frac{\pi}{L_Z} z\right)}{(n_1^v + m_2^c)^2 \frac{\pi^2 c^2}{L_z^2 \omega^2} - 1} \right) \quad .
\end{aligned}
$$

Here, n_x^λ labels the quantized states 1, 3, 5, ... and m_x^λ labels the quantized states 2, 4, 6, ... ω is the optical carrier frequency, and $k_z = \omega/c$. E_{in} is the electrical field of the incoming light field. The term $E_{\vec{k}}^{n_1^c, n_2^v}$ is now calculated by inserting Eq. (3.18) into Eq. (3.15). Eq. (3.12) can be solved to yield the polarizations of the different transitions which in turn determine the transversal E-field and thus the transmission. In this way, linear spectra can be calculated in the frequency domain. Our approach uses a time domain integration. The transformation of the E-field to the time domain is done by assuming the spectral frequency to be equal to the optical carrier frequency, ω_l, which is an approximation similar to the slowly varying envelope approximation. This approximation allows us to calculate short pulse excitation and non-stationary effects very efficiently. Note however that this approximation breaks down at $(n_1^v \pm n_2^c) \frac{\pi^2 c^2}{L_z^2 \omega_L^2} - 1 = 0$. In this case, the sample thickness is a multiple of $\lambda/2$, where λ is the wavelength. So, in the following we will restrict our investigation to the case where

$L_z < \lambda/2$. However, we expect to obtain the basic features of the 2-D to 3-D transition to take place before $L_z \approx \lambda/2$.

3.3 Stationary transmission spectra

In the following, stationary transmission spectra for the case of GaAs are presented. The relative electron mass (m_c/m_0), the relative hole mass (m_v/m_0), the refractive index n_g and the phenomenological dephasing rate γ used in our calculations are given in table 3.1, where m_0 is the free electron mass.

symbol	unit	value
m_v	m_0	0.3770
m_c	m_0	0.0655
n_g	-	3.6786
a_0	Å	128
γ_k	s^{-1}	$2 \cdot 10^{12}$
d^0_{cv}	$[e] \cdot$ Å	$e \cdot 7.2$

Table 3.1: Parameter values for GaAs.

Fig. 3.2 shows a comparison of transmission spectra when including and neglecting non-diagonal subband transitions in the interaction matrix, Eq.(3.12). The figure confirms that for a sample width smaller than the wavelength of light, the influence of the non-diagonal terms is indeed negligible. In the following, we restrict our analysis to samples smaller than half the wavelength of light where the neglection of transitions between states with different subband quantum numbers is an excellent approximation. In Fig. 3.3 we show the exciton binding energy obtained from the transmission spectrum as a function of the material thickness L_z. For comparison we have included the curve for the exciton binding energy if only one quantized state is considered. We see that one quantized state is only sufficient to describe the exciton binding energy as long as the quantum well width is less than 15 nm, which is about 1.25 times the 3-D Bohr radius. Furthermore, we

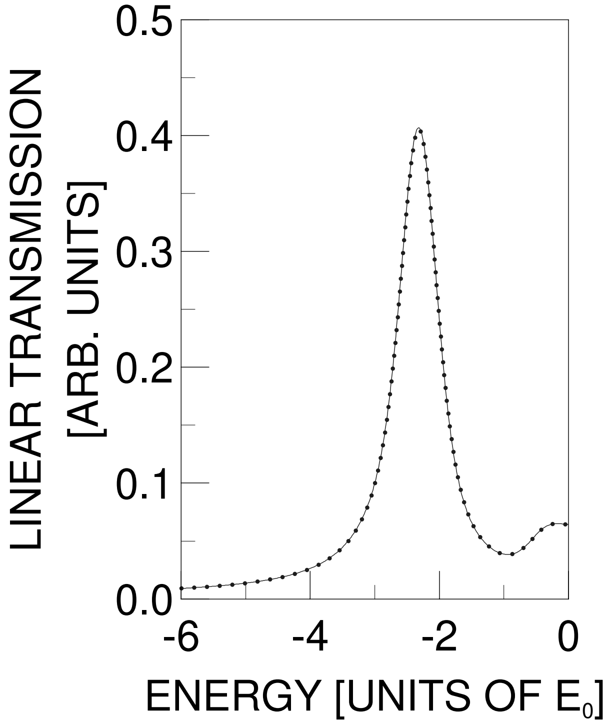

Figure 3.2: The linear transmission spectrum for $L_z = 10$ nm, where the off-diagonal transitions are included (—) and when the off-diagonal transitions are neglected ($\cdot\cdot\cdot$). Two subbands must be included in the calculations. E_0 is the ideal 3-D exciton binding energy.

see that the ideal 2-D exciton binding energy is only obtained for a material width of less than 1 nm, while the ideal 3-D exciton binding energy is almost reached for $L_z = 80$ nm. Fig. 3.4 shows the peak height of the lowest subband 1s exciton in the transmission spectrum for three different cases. The dotted line represents the 1s exciton peak height when all subband transitions are taken into account. The dashed line represents the case when the transmission spectrum is calculated by considering only the lowest subband. Finally, the solid line depicts the 1s exciton peak height in

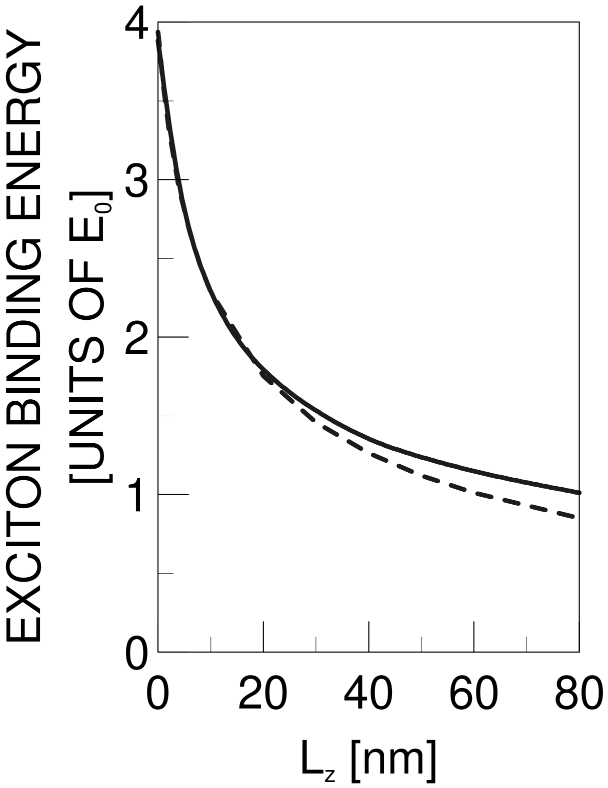

Figure 3.3: The binding energy of the 1s exciton for GaAs as a function of the material thickness L_z, (—). (- - -) 1s exciton binding energy, when only one quantized state is considered. E_0 is the ideal 3-D exciton binding energy.

the case where the wave-propagation equation and the Semiconductor Bloch equations (SBE) are solved by including all subband contributions; however, only the contributions of the lowest subband to the linear transmission are plotted. The dashed line in Fig. 3.4 once more shows the importance of including more than one subband for a material width larger than 15 nm. The difference between the solid and the dotted lines indicates how the higher subband contributions increase the peak height of the first subband exciton. The change of the transmission spectrum due to the Coulomb potential is elucidated by the solid line. The difference between the solid and dotted line depends to some degree on the chosen phenomenological decay rate γ, which determines the width of the 1s excitons. The tail of the second and higher subband transition lines increase the lowest 1s exciton peak height depending on the decay rate and material width. To illustrate this behavior further, the transmission spectra for some material widths corresponding to the dotted line are shown in Figs. 3.5 and 3.7, while a few transmission spectra corresponding to the solid line are plotted in Fig. 3.6. The linear transmission spectra shown in Fig. 3.5 are for the material widths $L_z =$ 1 nm, 10 nm, 20 nm and 60nm. We see with increasing material width a significant decrease of both exciton binding energy and peak height. The decrease in the exciton binding energy and the decrease of the exciton peak height is a result of the dependence of the Coulomb potential on the sample thickness. However, the inclusion of more than one subband leads to an increase in the exciton binding energy and peak height compared to the calculations where only one subband is considered. A numerical analysis shows that this increment of the binding energy and the peak height is caused by the Coulomb matrix elements which are off diagonal with respect to the subband indices. Thus it can be concluded that with increasing sample width the off-diagonal Coulomb matrix elements cause a gradual transfer of oscillator strength from the energetically higher exciton peaks to the lowest 1s exciton peak, see Fig. 3.7. This is elucidated by Fig. 3.6, which shows the "pure" lowest subband 1s exciton plus continuum for different sample thickness. The second and higher 1s exciton plus their continuum are subtracted (omitted) in this figure. There is a significant reduction in the continuum of the transmission spectrum at the positions of the higher subband excitons, which is a result of the transfer of oscillator strength by the Coulomb potential.

In Fig. 3.5 we have, for $L_z = 1$nm, included a plot of the imaginary part of the susceptibility at the center of the sample (short-long dashed line). The difference between the susceptibility and the linear transmission spectrum verifies that the inclusion of the propagation effects are important. We observe that the inclusion of the propagation effects result in a reduction in the 1s exciton peak height and significant broadening of the 1s exciton. This

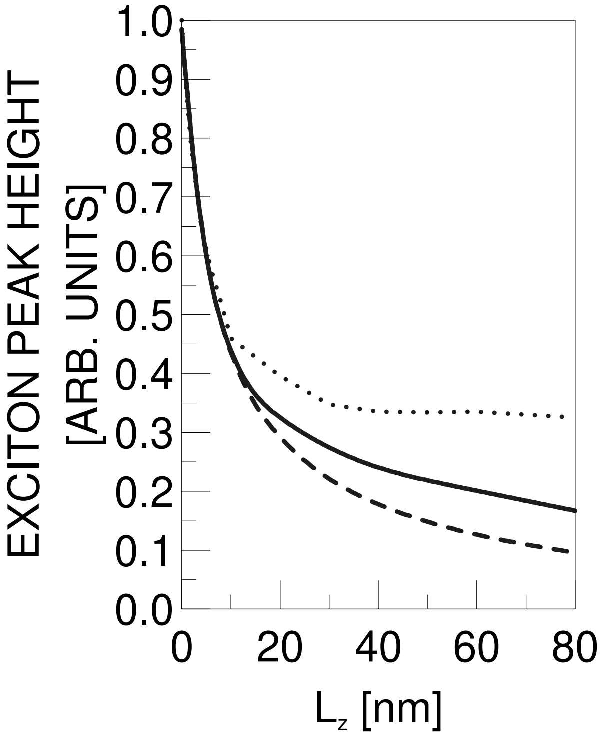

Figure 3.4: The 1s exciton peak height in the linear transmission spectrum as a function of the material thickness (· · ·). The long dashed curve shows the 1s exciton peak height, if only one quantized state is taken into account. The solid line shows the lowest subband contribution to the peak height, when all quantized states are included.

corresponds to the radiative damping mechanism for exciton polaritons in low dimensional systems [3]. Furthermore, since the polarization is space dependent, the definition of an effective space independent susceptibility is somewhat arbitrary, especially when more than one subband is needed to describe the optical properties of the sample.

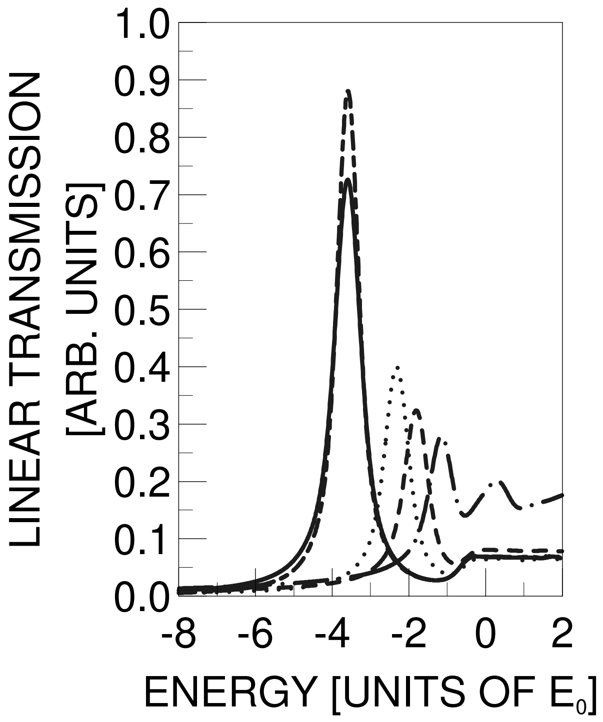

Figure 3.5: The linear transmission spectrum for the material thickness of 1nm (—), 10 nm (· · ·), 20 nm (- - -) and 60 nm (- · · -). The imaginary part of $\chi(\omega, z = 0)$ is plotted for L_z = 1nm (– – –). E_0 is the ideal 3-D exciton binding energy.

In Fig. 3.7, the 2-D to 3-D transition is indicated by showing the vanishing oscillator strength of the second and higher subband 1s excitons with increasing material thickness. The change in exciton binding energy for the first subband 1s exciton is small, when the material width is increased from L_z = 40 nm to L_z = 80 nm. There is also little effect on the peak height. However, it should be noted that this is due to a compensation effect, since the change in peak height also depends on the linewidth of the higher subbands, which can compensate for the peak decrease with increasing thickness. Nevertheless, the second subband exciton and higher subband excitons lose a significant amount of oscillator strength with increasing material thickness. Thus, the 3-D absorption spectrum is expected to be obtained for the thickness where the second and higher subband 1s excitons will have an oscillator strength comparable to their continuum.

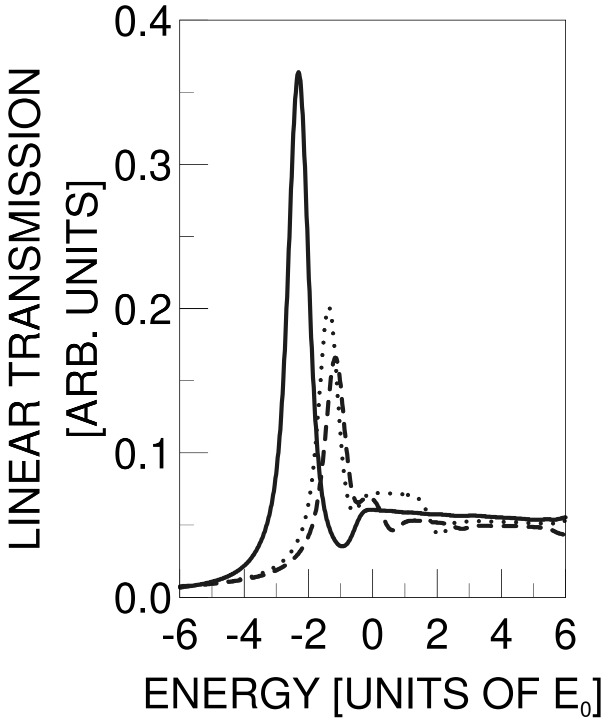

Figure 3.6: The linear transmission spectrum for the material thickness of 10 nm (—), 40 nm (· · ·) and 60 nm (- · -). The propagation equation and SBE are solved by inclusion of higher subbands. The linear transmission is calculated by only considering the lowest subband. E_0 is the 3-D exciton binding energy.

The complexity of the Coulomb potential in our approach makes it compu-

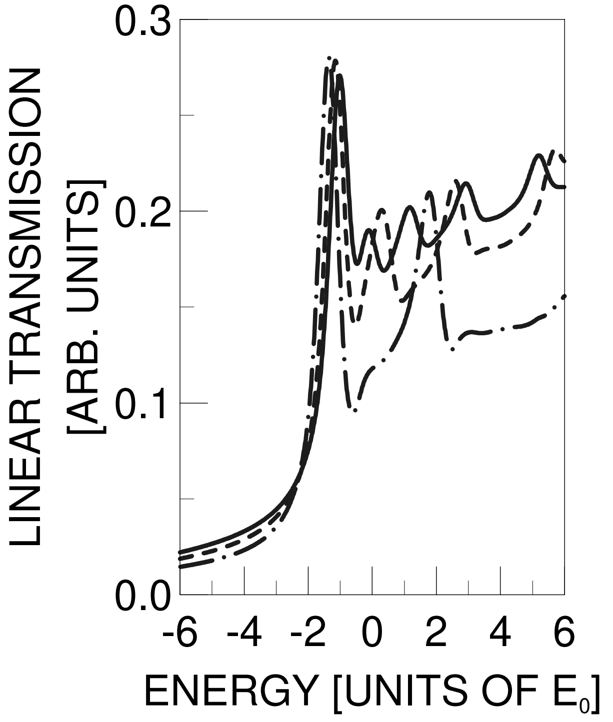

Figure 3.7: The linear transmission spectrum for the material thickness of 40 nm (– · –), 60 nm (- - -) and 80 nm (—). E_0 is the ideal 3-D exciton binding energy.

tationally very demanding to study the full transition to the 3-D absorption spectrum. One should keep in mind that we have shown that the transitions between unequal quantum numbers are negligible when the material width is much smaller than the wavelength. However, the full transition to the 3-D spectrum is expected to occur at a material width comparable with the optical wavelength. In this case, the transitions between unequal quantum numbers have to be taken into account and the Fourier transform of the solution of the wave-propagation equation has to be calculated without any approximations. This will increase the computational demands considerably. On the other hand, the studies given above for a thickness smaller than half the wavelength already yield the basic transition mechanisms.

3.4 Non-stationary effects

In the previous section we studied how the transition from the 2-D to the 3-D transmission spectrum takes place for different sample thicknesses. The spectra contain the information to which extent certain electronic states of the material system are excited after the light is switched off. However, the same information is also contained in the temporal interference of the polarization of different electronic states. In Fig. 3.8, we present a logarithmic plot of the incident and transmitted electrical fields for the case of a 60 nm sample where the input pulse is a hyperbolic-secant shaped pulse with a Full Width at Half Maximum (FWHM) of 80 fs. In the figure we have also included a logarithmic plot of the absolute value of the polarization at the center of the sample. The transmitted electrical field and the polarization exhibit a dominant oscillation with a period of 260 fs. This oscillation is due to the beating of the lowest subband 1s exciton with the third subband 1s exciton (260 fs). The beating between the second and first subband is not seen in the figure since the corresponding period is about 688 fs. However, the beating between the first subband and energetically higher excitons than the second is visible in the figure as a superposition of oscillations with different periods and different oscillator strengths weightend by the pulse spectra.

Figure 3.9 shows the dynamic evolution of the polarizations of different subbands. It can be recognized that after the pulse is switched on all states develop according to their respective oscillator strength and decay after the pulse maximum, corresponding to their detuning with respect to the pulse. Thus, at different times different subbands contribute to the development of the total electron density, because the subband polarizations determine the weight of the z-dependent confinement functions. The expectation value of

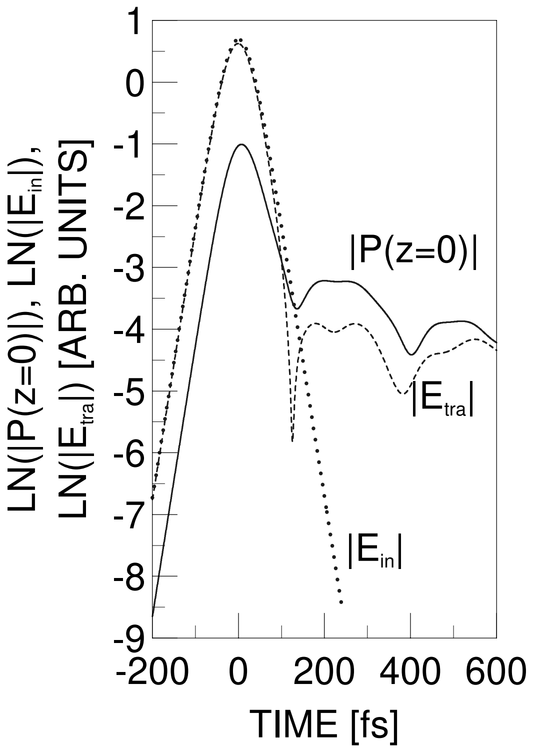

Figure 3.8: Plot of the incident, E_{in}, transmitted, E_{tra}, electrical field and the absolute value of the polarization at the center of the sample. The material thickness is $L_z = 60$ nm.

the electron density is given by

$$< N >= \frac{1}{L^2} \sum_{k,n_1} |P_k^{n_1,n_1}|^2 \quad . \tag{3.19}$$

It should be noted, that Eq. (3.19) is only valid when the transitions between states with unequal quantum number can be neglected.

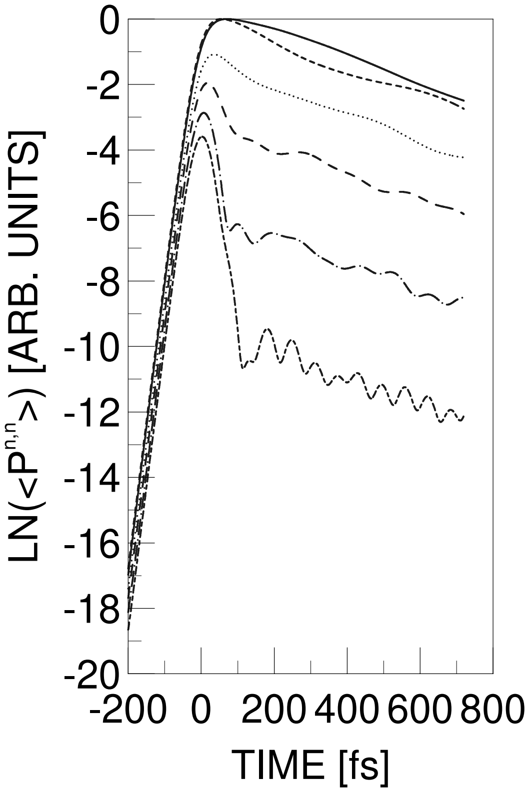

Figure 3.9: The polarization ($< P^{n,n} >= \frac{1}{L^2} \sum_k |p_k^{n,n}|^2$) as function of time after excitation by a pulse with FWHM of 80 fs. The material thickness is L_z = 60 nm. The different curves are for the subband polarizations $< P^{1,1} >$ (—), $< P^{2,2} >$ (- - -), $< P^{3,3} >$ (· · ·), $< P^{4,4} >$ (– –), $< P^{5,5} >$ (– · –) and $< P^{6,6} >$ (– - –).

Figure 3.10 shows the resulting electron density as a function of the space coordinate z at the time T = -200fs, -80fs, 0fs, 80fs, 160fs and 240fs. The time is measured with respect to the pulse peak. The excitation pulse is again chosen to be a hyperbolic secant pulse with a FWHM of 80 fs and the material thickness is 60 nm. Note that the space axis has been nor-

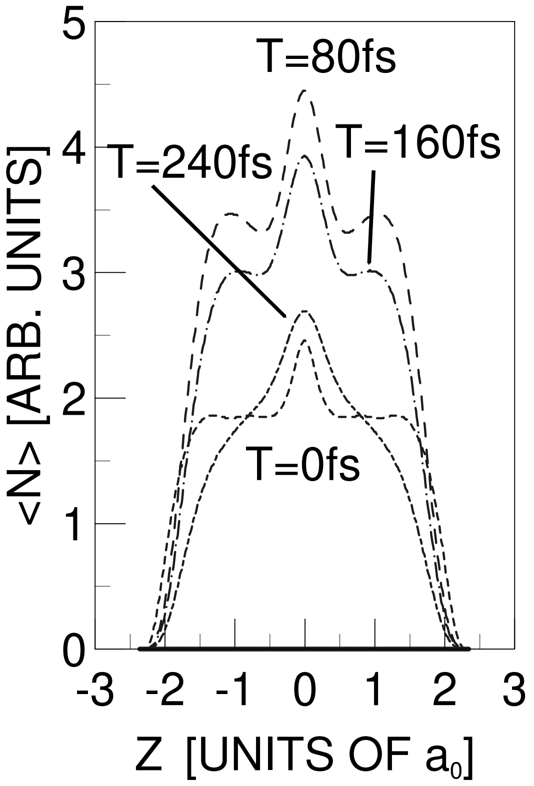

Figure 3.10: The electron density ($< N >= \frac{1}{L^2} \sum\limits_{k,n} |p_k^{n,n}|^2$) as function of the space coordinate z after excitation by a pulse with FWHM of 80 fs. The material thickness is $L_z = 60$ nm. The electron density is shown for the times -200fs (—), -80fs (· · ·), 0fs (- - -), 80fs (– –), 160fs (– · –) and 240fs (– - –). a_0 is the ideal 3-D Bohr radius.

malized with respect to the 3-D exciton Bohr radius. The figure shows the development of an electronic mode structure which is determined by the width of the material and is similar to the optical mode structure in a laser cavity. We see an almost homogeneous electron density in the structure

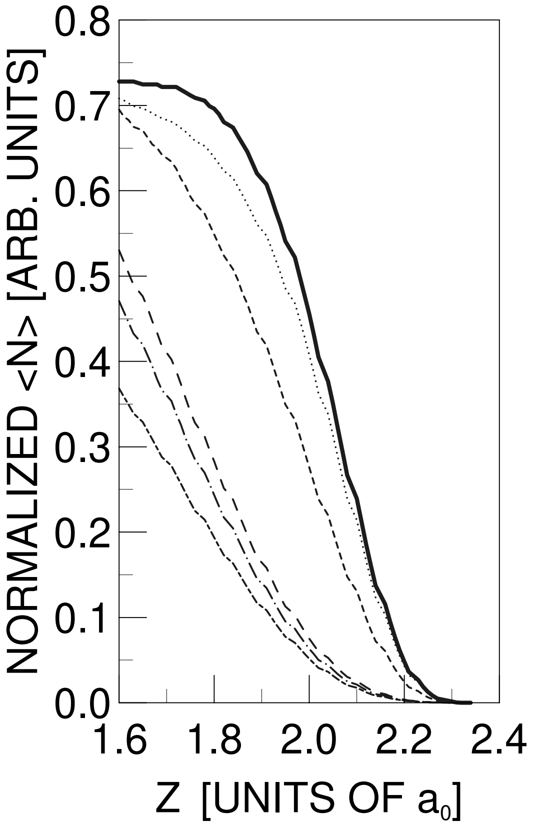

Figure 3.11: The normalized electron density ($< N >= \frac{1}{L^2} \sum_{k,n} |p_k^{n,n}|^2$) as function of the space coordinate z after excitation by a pulse with FWHM of 80 fs. All curves have been normalized to a height of one. The material thickness is $L_z = 60$ nm. The electron density is shown for the times -200fs (—), -80fs ($\cdot\cdot\cdot$), 0fs (- - -), 80fs (– –), 160fs (– $\cdot$ $\cdot$ –) and 240fs (– - –). a_0 is the ideal 3-D Bohr radius.

with a characteristic peak at the sample center before the pulse peak has passed through the sample. The peak at the center of the sample is a result

of the early development of an electron mode structure. Not all transitions are equally excited, as seen in Fig. 3.9. The peak at the center in Fig. 3.10 corresponds to the highest odd-numbered (n_x^λ = 1, 3, 5, ..) quantized state which contributes significantly to the electron-hole density expectation value. The observation of an almost homogeneous electron density agrees well with the common approximation that the absorption spectrum is space independent in a semiconductor structure. However, on the trailing edge of the optical pulse the picture changes. The almost spatially homogeneous electron density at early times and the development of the electronic mode structure can be understood when we look at the expectation value of the polarization for the different subband transitions, Fig. 3.9. The resulting polarization starts to adiabatically follows the optical pulse. This explains the almost homogeneous polarization at early times. The material "does not know" the spectral width of the exciting pulse, and so all states (frequencies) are excited by the pulse front. However, with time, the spectral properties of the exciting pulse become noticeable and the electronic mode structure develops.
The solution of the half-space problem [2] shows that the stationary electronic mode-structure exhibits a characteristic exciton free layer of the order of one Bohr radius at the interface, the so called "dead layer".

Figure 3.11 shows the space dependent electron density near the material interface at different time-points corresponding to the graphs in Fig. 3.10. However, the curves in Fig. 3.11 have been normalized to a peak height of one. The development of an exciton free layer (dead layer) with time can be observed near the material interface. The width of the dead layer is for L_z = 60 nm only one third of the 3-D Bohr radius, while the exciton free layer (dead layer) in the half-space problem has a width of approximately one Bohr radius [2]. This shows that our results have still not reached the ideal 3-D case.

3.5 Summary

In summary, we have derived the equations for the optical properties of an arbitrary thick semiconductor sample including Coulomb and light propagation effects. For sample thicknesses of less than half the wavelength we have described the basic effects of how the transition from the 2-D to the 3-D regime of semiconductor material takes place. The change of the 2-D transmission spectrum towards the 3-D transmission spectrum is explained by showing the importance of the off-diagonal Coulomb potential elements which increase the exciton binding energy and transfer oscillator strength from higher 1s excitons to the lowest quantized state 1s exciton. Furthermore, we see the development of a dead layer with increasing material thickness which is an important factor in the theories applied for solving the half-space problem.

Bibliography

[1] For a textbook discussion see: H. Haug, S. W. Koch, "Quantum Theory of the Optical and Electronic Properties of Semiconductors", World Scientific, Singapore 1993.

[2] For a textbook discussion see: A. Stahl, I. Balslev, "Electrodynamics of the Semiconductor Band Edge", Springer Tracts in Modern Physics Vol. 110, Springer-Verlag, Berlin Heidelberg 1987.

[3] T. Stroucken, A. Knorr, P. Thomas, S. W. Koch "Coherent Dynamics of Radiatively Coupled Quantum-well Excitons", Phys. Rev. B **53**, 2026, 1996.

[4] L. C. Andreani, A. Pasquarello, "Accurate theory of Excitons in GaAs-$Ga_{1-x}Al_xAs$ Quantum Wells", Phys. Rev. B **42**, 8928, 1990.

[5] R. Zimmermann, "Excitonic Spectra in Semiconductor Nanostructures", Adv. Solid State Phys. **30**, 295, 1990.

[6] X.-F. He, "Excitons in Anisotropic Solids: The Model of Fractional-Dimensional Space", Phys. Rev. B **43**, 2063, 1991.

[7] R. Zimmermann, "Excitonic Spectra in Semiconductor Nanostructures", Proc. Int. Conf. Optical Properties of Nanostructures, Jpn. J. Appl. Phys. **34** suppl. 34-1, 228, 1995.

[8] R. C. Miller, D. A. Kleinman, W. T. Tsang, A. C. Gossard, Observation of the Excited Level of Excitons in GaAs Quantum Wells", Phys. Rev. B **24**, 1134, 1981.

[9] E. S. Kotoles, J. Y. Chi, "Experimental Exciton Binding Energies in GaAs/$Al_xGa_{1-x}As$ Quantum Wells as a Function of Well Width", Phys. Rev. B **37**, 6632, 1988.

[10] A. Knorr, S. Hughes, T. Stroucken, S. W. Koch, "Theory of Ultra-

fast Spatio-Temporal Dynamics in Semiconductor Heterostructures", Chemical Physics, 100, 1996.

[11] For a textbook discussion see: W. W. Chow, S. W. Koch, M. Sargent III, "Semiconductor Laser Physics", Springer-Verlag, Berlin, 1994.

[12] H. Haken, "Quantum Field Theory of Solids, An Introduction", North-Holland, New-York, 1988.

[13] A. Yariv, "Quantum Electronics", third edition, John Wiley & Sons, New-York, 1989.

[14] N. Peyghambarian, S. W. Koch, A. Mysyrowics, "Introduction to Semiconductor Optics", Predentice Hall, New Jersey, 1993.

Chapter 4

Modulational Instability of Electromagnetic Waves in Media with Periodic or Random Perturbations

In this chapter the propagation of electromagnetic waves (light) is investigated in media with periodic or random fluctuations. The propagation of electromagnetic waves in optical fibers is theoretically described by the Non-Linear Schrödinger Equation (NLSE) [1, 2], where perturbation terms for the processes of loss, gain, self-steepening etc. can be added [3]. Here, we investigate the case of the propagation of the perturbed Continuous Wave (CW) steady state solution in the case of a periodic or random modulation of the non-linear term in the NLSE. Such modulations appear during electromagnetic wave propagation in fibers with periodic (random) fluctuations of the fiber core. The propagation of optical solitons in media with random fluctuation of the fiber core is investigated in Ref. [4].

The phenomenon that a non-linear system exhibits an instability which leads to a modulation of the perturbed steady state solution is often referred to as Modulational Instability (MI). The instability is, in the case of the NLSE, a result of the joint action of the non-linearity and the dispersion of the medium. A simple analysis of the linearized problem for the NLSE shows that the small initial modulation of a steady state plane wave with wavelength larger than a critical value is unstable and leads to exponential growth of the wave amplitude [1, p.107]. The next stage of the wave evolution is more complicated to analyse and requires the use of methods based on finite-zone potentials [5, 6], or the finite mode number representation [7]. These investigations showed that the long-term evolution results in periodic returns to the initial modulated steady-state solution, repeatedly passing through a stage where the wave is transformed into a chain of nonlinear pulses (solitons). It has been suggested that this technique may be used to generate a chain of ultra short optical pulses at high repetition rates [8].
The results mentioned above have focussed on the case of a homogeneous medium. However, the inhomogeneity of a medium changes the parameters of the MI process [9]. New regions of MI have been predicted in Refs. [10, 11]. In section 4.1, the wave behavior of these new MI regions is analysed in the parametric instability region under the joint action of periodic modulation and the self-steepening effect. In section 4.2, MI is investigated in the case of random fluctuations. Here, we predict stochastic parametric resonance in the case of random modulation of the medium. It should be mentioned that the influence of inhomogeneities and noise on the instabilities of nonlinear waves has attracted an increasing amount of attention in recent years [12, 13].

4.1 MI in media with periodically varying nonlinearity.

In this section we shall study MI of electromagnetic waves in a periodically modulated medium. Furthermore, the influence of the self-steepening effect on the MI conditions will be investigated.

The wave equation for the slowly varying envelope of the electromagnetic field in a Kerr-like medium with variable nonlinearity is [1]

$$iu_x + \nu u_{\tau\tau} + 2\varepsilon(x) \mid u \mid^2 u = -i\alpha \left(|u|^2 u\right)_\tau \quad . \tag{4.1}$$

Here, $\nu = +1$ and $\nu = -1$ represents negative and positive group velocity dispersion, respectively. u_x is the derivative of u with respect to the space coordinate x, while the index τ accounts for the derivative of u with respect to time. The term on the right hand side accounts for the self-steepening effect. The steady state solution of Eq. (4.1) is

$$u = A\exp\{i\phi\} \quad , \qquad \phi = 2A^2 \int_0^x \varepsilon(x')dx' \quad . \tag{4.2}$$

Here, we can assume A to be real without any loss of generality. Let us now consider the stability of the wave solution Eq. (4.2) with respect to a small perturbation of the form

$$u = (A + \psi(x,\tau))\exp\{i\phi\} \quad , \qquad \mid \psi \mid \ll A \quad . \tag{4.3}$$

Inserting Eq. (4.3) into Eq. (4.1) and linearizing with respect to the perturbation term ψ, we obtain an equation for $\psi(x,\tau)$,

$$i\psi_x + \nu\psi_{\tau\tau} + 2A^2\varepsilon(x)(\psi + \overline{\psi}) = -i\alpha A^2(2\psi_\tau + \overline{\psi}_\tau) \quad , \tag{4.4}$$

where $\overline{\psi}$ is the complex conjugate of ψ. In the following, we assume the perturbation ψ to have the form

$$\psi(x,\tau) = C(x)e^{i\Omega\tau} + \overline{B}(x)e^{-i\Omega\tau} \quad . \tag{4.5}$$

Inserting Eq. (4.5) into Eq. (4.4), we obtain the following system of equations

$$ib_x - 3\alpha A^2\Omega b - \nu\Omega^2 c = 0 \quad , \tag{4.6a}$$
$$ic_x - \nu\Omega^2 b + 4\varepsilon(x)A^2 b - \alpha A^2\Omega c = 0 \quad . \tag{4.6b}$$

Here, $c(x) = C(x) - B(x)$ and $b(x) = C(x) + B(x)$. Introducing $\tilde{b}$ defined as $\tilde{b}(x) = be^{2i\alpha A^2\Omega x}$ we find a closed equation for $\tilde{b}$:

$$\tilde{b}_{xx} + \Omega^2 \left(\Omega^2 - 4\nu A^2 + \alpha^2 A^4 + 4\nu\tilde{\varepsilon}(x)A^2\right)\tilde{b} = 0 \quad , \tag{4.7}$$

where $\varepsilon(x) = 1 - \tilde{\varepsilon}(x)$. Choosing the particular form of the variation $\varepsilon(x) = 1 - \varepsilon_0 \cos(ax)$, (in which we put $0 < \varepsilon_0 \ll 1$), we obtain, instead of Eq. (4.7) the Mathieu equation [14],

$$
\begin{aligned}
0 &= \tilde{b}_{xx} + \omega_0^2 (1 + h\cos(ax))\tilde{b} \quad , & (4.8a) \\
h &= \frac{4A^2\varepsilon_0\nu}{\Omega^2 - 4A^2\nu + \alpha^2 A^4} \quad , & (4.8b) \\
\omega_0^2 &= \Omega^2 \left(\Omega^2 - 4A^2\nu + \alpha^2 A^4\right) \quad . & (4.8c)
\end{aligned}
$$

We find, by applying the standard method for the case $0 < h \ll 1$ [14], that the wave is unstable in the region of parametric resonances which occur when $\omega_0 = ma/2$. Here, m has a positive integer value, $m = 1, 2, 3, \ldots$. In the region of the first parametric resonance ($m = 1$) we have $a = 2\omega_0 + \delta$ (δ is the width of the MI region), i.e. the wave is unstable for modulations with frequency

$$\Omega^2 = 2A^2(\nu - \frac{\alpha^2}{4}A^4) + \left(4A^4(\nu - \frac{\alpha^2 A^2}{2})^2 + \frac{a^2}{4}\right)^{\frac{1}{2}} \quad . \tag{4.9}$$

The width of the MI region is

$$\mid \delta \mid < \frac{\mid h\omega_0 \mid}{2} = \frac{2\varepsilon_0 A^2 \Omega}{\sqrt{\Omega^2 - 4A^2\nu + \alpha^2 A^4}} \quad . \tag{4.10}$$

The dependence of Ω on a for different values of α is presented in Fig. 4.1 for the case $A = 1.0$. We see that the critical value of Ω decreases for increasing α values. We can use the following estimate (Eq. (4.11)) for Ω, when $a >> \Delta = (4A^2 + \alpha^2 A^4)$,

$$\Omega \approx \left(\frac{a}{2} - 2A^2 - \frac{\alpha^2 A^4}{2}\right)^{\frac{1}{2}} \quad . \tag{4.11}$$

This expression coincides with the result obtained in [11]. For small a ($a << \Delta$) Ω can be approximated by

$$\Omega \approx \frac{a}{2(4A^2 + \alpha A^4)^{\frac{1}{2}}} \tag{4.12}$$

The appearance of the new MI instability region at higher modulation frequencies indicates that it is possible to generate a chain of ultrashort pulses

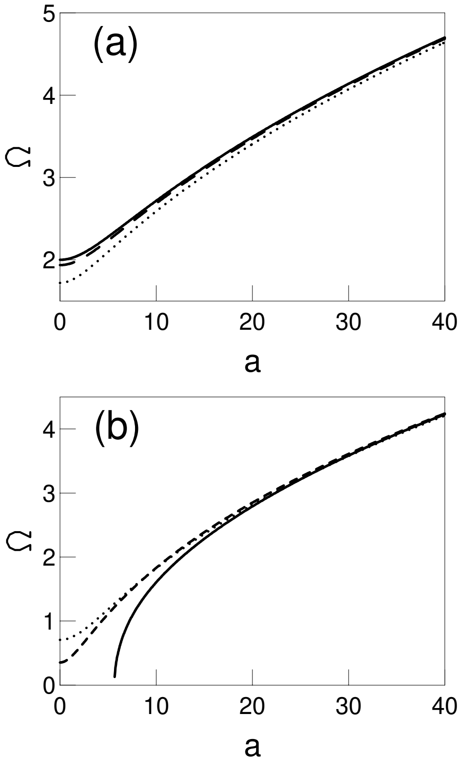

Figure 4.1: The MI frequency Ω as a function of a for $A = 1.0$ and $\alpha = 0$ (solid curve), $\alpha = 0.5$ (dashed) and $\alpha = 1.0$ (dotted). Figure (a) and (b) are for negative and positive group velocity dispersion, respectively.

with high repetition rates. This is confirmed by numerical solutions of the NLSE, Eq. (4.1). The initial condition is the perturbed steady state solution, where the initial condition for ψ is

$$\psi(0, \tau) = q \cos(\Omega\tau) + iv \sin(\Omega\tau) \quad . \tag{4.13}$$

Examples of the space-time evolution for different parameter values are displayed in Fig. 4.2-4.4 for the case of parametric MI. The NLSE is solved numerically by means of the Fourier split step method [1], which is based

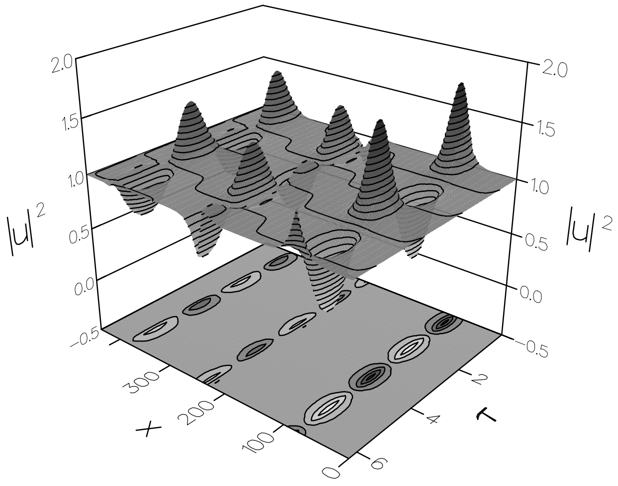

Figure 4.2: Space-time evolution of $|u|^2$ for $\nu = +1$, $q = v = 1 \cdot 10^{-4}$, A=1.0, $\varepsilon_0 = 0.1$, $\Omega = 4.1888$, $\alpha = 0$ and $a = 30.83355$.

on the analytical solutions for the linear and and nonlinear parts of the NLSE. The solution is advanced in space (x) by alternating small steps of the non-linear and linear equation, respectively. The analytical results found previously are applicable at the initial stage of the evolution of the numerical solution. However, the linear stability analysis remains valid. Therefore, we have numerically verified the predicted regions of MI and performed investigations for the case of long propagation distances, too.

First we considered the first (standard) region of MI, corresponding to the case when $\Omega^2 < 4A^2$ and with $\alpha = 0$. The MI region is extended when Δ has a small value. We estimated the value of Δ to be $\Delta \approx \frac{16A^4\varepsilon_0^2}{a^2}$ for the case $\Omega = 2A + \Delta$ and for small values of a, by applying the standard method [15]. For $a = 4$, $A = 2$, $\varepsilon_0 = 0.1$ we have $\Delta = 0.64$, which is found to be in good agreement with results of the full numerical simulations.

We have studied MI in the case of negative group velocity dispersion ($\nu = 1$) for both large and small values of a, when the critical parametric frequency of modulations is either far from or close to the first MI region. The space-time evolution of $| u |^2$ is plotted in Fig. 4.2 for $A = 1$, $\Omega = 4.1887$, $\varepsilon_0 = 0.1$

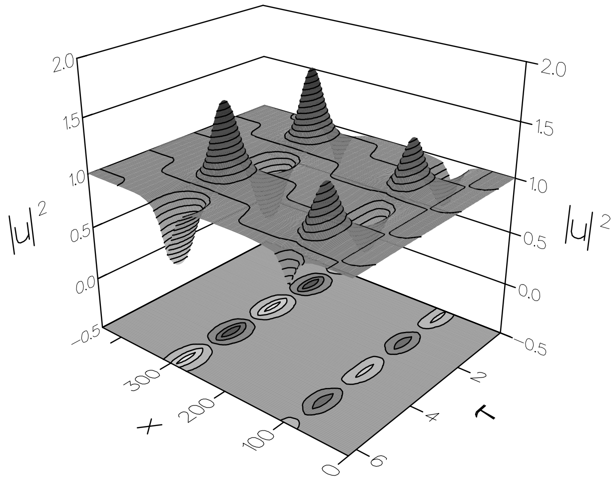

Figure 4.3: Space-time evolution of $|u|^2$ for $\nu = -1$, $q = v = 1 \cdot 10^{-4}$, A=1.0, $\varepsilon_0 = 0.1$, $\Omega = 4.1888$, $\alpha = 0$ and $a = 38.88$.

and $a = 30.83$. The figure shows the first parametric resonance for parameters satisfying Eq. (4.8). The space-time evolution of the perturbed steady state solution is periodic with the period $T_e = 149.48$. The approximate formulae for this recurrence phenomenon with period T_e can be obtained by using arguments as in Refs. [5] and [16] with $\psi = q \exp(\gamma x) \approx \psi_{sat}$, where ψ_{sat} is the saturated value of ψ.

$$T_t \simeq \frac{2 \log |\, \varepsilon \,|}{\gamma} \quad , \epsilon = \frac{\psi_{sat}}{q} \quad . \tag{4.14}$$

$T_t = 143.34$ for the parameter values used in Fig. 4.2, which is in good agreement with the numerical obtained value of $T_e = 149.48$. In the case where a is taken equal to 15.222 we have $\Omega \simeq 2.4$, i.e. the value is near the MI point $\Omega = 2A = 2$. Here the values of T_e and T_t are $T_e = 131.26$ and $T_t = 128.9$, respectively. In Fig. 4.3 the space-time evolution is displayed for the case of positive group velocity dispersion, showing that MI also exists in the case of positive group velocity dispersion. Here, the numerical and theoretical values of the recurrence period are $T_e = 186.44$ and $T_t = 178.736$. The effect of including the self-steepening effect is shown in

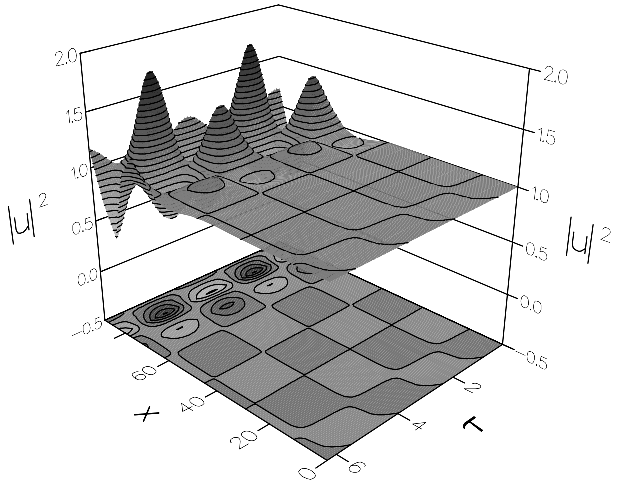

Figure 4.4: Space-time evolution of $|u|^2$ for $\nu = +1$, $q = v = 1 \cdot 10^{-4}$, A=1.0, $\varepsilon_0 = 0.1$, $\Omega = 4.1888$, $\alpha = 0.5$ and $a = 31.1168$.

Fig. 4.4. The self-steepening parameter is set to $\alpha = 0.5$, while the other parameter values are $q = v = 1 \cdot 10^{-4}$, $A = 1.0$, $\epsilon_0 = 0.1$, $\Omega = 4.1888$ and $a = 31.1168$. We see that the the self-steepening effect leads to a reduction of the gain (amplification) and to a shift of the position of the parametric resonance frequencies towards lower frequencies.
From the results of the numerical simulations, we can conclude that there probably still exists some modification of the periodic finite-zone solutions with parameters varying in space. The first expansion term of the solution must give the result from linear stability analysis. In this case a perturbation theory for finite-zone potentials can be developed (some results in this direction are obtained in [17]). So far, we have only considered the solutions of the numerical model for some specific normalized values. Therefore, we shortly want to estimate the various effects for the case of an optical fiber by an examples where the nonlinear term in the NLSE is modulated.

In the case of a periodic modulation of the fiber core the typical parameter values are: $\beta_2 = -20ps^2/km$, $\gamma = 2W^{-1}km^{-1}$ and $\varepsilon_0 \approx 10^{-3}$. We chose the initial pump power to be $P_0 = 7W$. The position of parametric resonance is approximately 4.9 THz for $l = 2\pi/a = 50m$ and the maximum gain frequency of ordinary MI is 2.4 THz. The increment is $g_m = 0.01km^{-1}$, with $\delta = 0.008$ THz. The above analysis shows that by using varying parameters of the medium we are able to generate ultra short optical pulses in optical media.

4.2 MI in media with randomly varying non-linearity.

In this section we will study modulational instability of the nonlinear waves (4.14) when $\varepsilon(x)$ is a random function. The problem under consideration is described by equation (4.8) with $\tilde{\varepsilon}(x)$ chosen as white Gaussian-distributed noise:

$$\begin{aligned} 0 &= \tilde{b}_{xx} + \omega_0^2(1 + h\tilde{\varepsilon}(x))\tilde{b} \quad , & (4.15a)\\ h &= \frac{4A\ 2\nu}{\Omega^2 - 4A^2\nu + \alpha^2 A^4} \quad , & (4.15b)\\ < \tilde{\varepsilon} > &= 0 \quad , & (4.15c)\\ < \tilde{\varepsilon}(x)\tilde{\varepsilon}(x') > &= 2\sigma^2\delta(x - x') \quad . & (4.15d) \end{aligned}$$

The analytical analysis is performed by rewriting Eq. (4.15a) as a set of two coupled first order differential equations,

$$\begin{aligned} \tilde{b}_x &= y, & (4.16a)\\ y_x &= -\omega_o^2\tilde{b} - \omega_o^2 h\tilde{\varepsilon}(x)\tilde{b} \quad . & (4.16b) \end{aligned}$$

In the following, the decoupling and averaging of Eq. (4.16) is done by the standard method [18, p.62].

$$\Delta\tilde{b} = \int_x^{x+\Delta x} \tilde{b}_x dx = y\Delta x \quad , \qquad (4.17a)$$

$$
\begin{aligned}
\Delta y &= \int_{x}^{x+\Delta x} y_x dx && (4.17b)\\
&= -\omega_o^2 \tilde{b} \Delta x - \omega_o^2 h \tilde{b} \int_{x}^{x+\Delta x} \tilde{\varepsilon}(x) dx \quad .
\end{aligned}
$$

The average expectation value of Eqs. (4.17) is

$$
\begin{aligned}
< \Delta \tilde{b} > &= y \Delta x \quad , && (4.18a)\\
< \Delta y > &= -\omega_o^2 \tilde{b} \Delta x \quad . && (4.18b)
\end{aligned}
$$

In the following we will make use of the relation,

$$
\int_{x}^{x+\Delta x} \int_{x}^{x+\Delta x} 2\sigma^2 \delta(x' - x'') dx'' dx' = 2\sigma^2 \Delta x \quad . \qquad (4.19)
$$

The expectation value of a certain parameter value i.e. $\tilde{b}^2$ is defined by

$$
< \tilde{b}^2 > = \int_{-\infty}^{\infty} \int_{-\infty}^{\infty} P(\tilde{b}, y, x) \tilde{b}^2 \; dy \; d\tilde{b} \quad , \qquad (4.20)
$$

where $P(\tilde{b}, y, x)$ is the probability function [18], which is related to the Fokker-Planck equation, $\frac{\partial P}{\partial x} = LP$, where, L is an operator. Here and in the following we are using the same notation as in Ref. [18]. The differential equation (equation of motion) for the expectation value of $\tilde{b}^2$ is in this notation,

$$
\begin{aligned}
\frac{d < \tilde{b}^2 >}{dx} &= \int_{-\infty}^{\infty} \int_{-\infty}^{\infty} (LP(\tilde{b}, y, x)) \tilde{b}^2 \; dy \; d\tilde{b} && (4.21a)\\
&= \int_{-\infty}^{\infty} \int_{-\infty}^{\infty} P(\tilde{b}, y, x) L^\dagger \tilde{b}^2 \; dy d\tilde{b} \quad , && (4.21b)
\end{aligned}
$$

where $L^\dagger$ is the adjoint operator of L. The Fokker-Planck equation is in our case,

$$
\frac{\partial P}{\partial x} = \left(-\frac{\partial}{\partial \tilde{b}} \alpha_{\tilde{b}} - \frac{\partial}{\partial y} \alpha_y + \frac{1}{2} \frac{\partial^2}{\partial y^2} \alpha_{yy} \right) P(\tilde{b}, y, x) \qquad (4.22a)
$$

$$
\begin{aligned}
&= \left(-y\frac{\partial}{\partial\tilde{b}} + \omega_0^2\tilde{b}\frac{\partial}{\partial y}\omega_0^2\tilde{b} + \omega_0^4 h^2\tilde{b}^2\sigma^2\frac{\partial^2}{\partial y^2}\right)P(\tilde{b},y,x) && (4.22b)\\
&= -yP_{\tilde{b}} + \omega_0^2\tilde{b}P_y + \omega_0^4 h^2\tilde{b}^2\sigma^2 P_{yy} \quad , && (4.22c)\\
\alpha_{\tilde{b}} &= \lim_{\Delta x\to 0}\frac{<\tilde{b}>}{\Delta x} = y \quad , && (4.22d)\\
\alpha_y &= \lim_{\Delta x\to 0}\frac{<y>}{\Delta x} = -\,\omega_o^2\tilde{b} \quad , && (4.22e)\\
\alpha_{\tilde{b}y} &= \lim_{\Delta x\to 0}\frac{<\tilde{b}y>}{\Delta x} = 0 \quad , && (4.22f)\\
\alpha_{\tilde{b}\tilde{b}} &= \lim_{\Delta x\to 0}\frac{<\tilde{b}\tilde{b}>}{\Delta x} = 0 \quad , && (4.22g)\\
\alpha_{yy} &= \lim_{\Delta x\to 0}\frac{<yy>}{\Delta x} = \omega_0^4 h^2\tilde{b}^2 2\sigma^2 \quad . && (4.22h)
\end{aligned}
$$

Thus, the operator L and its adjoint operator $L^\dagger$ are

$$
\begin{aligned}
L &= -y\frac{\partial}{\partial\tilde{b}} + \omega_0^2\tilde{b}\frac{\partial}{\partial y} + \omega_0^4 h^2\tilde{b}^2\sigma^2\frac{\partial^2}{\partial y^2} \quad , && (4.23a)\\
L^\dagger &= y\frac{\partial}{\partial\tilde{b}} - \omega_0^2\tilde{b}\frac{\partial}{\partial y} + \omega_0^4 h^2\tilde{b}^2\sigma^2\frac{\partial^2}{\partial y^2} \quad . && (4.23b)
\end{aligned}
$$

The averaged expectation values for $\tilde{b}^2$, $\tilde{b}y$ and y^2 can now be determined by the following equations:

$$
\begin{aligned}
\frac{d<\tilde{b}^2>}{dx} &= \int_{-\infty}^{\infty}\int_{-\infty}^{\infty} P(\tilde{b},y,x)L^\dagger\tilde{b}^2\; d\tilde{b}dy && (4.24a)\\
&= 2<\tilde{b}y> \quad ,\\
\frac{d<\tilde{b}y>}{dx} &= \int_{-\infty}^{\infty}\int_{-\infty}^{\infty} P(\tilde{b},y,x)L^\dagger\tilde{b}y\; d\tilde{b}dy && (4.24b)\\
&= <y^2> -\omega_0^2<\tilde{b}^2> \quad ,\\
\frac{d<y^2>}{dx} &= \int_{-\infty}^{\infty}\int_{-\infty}^{\infty} P(\tilde{b},y,x)L^\dagger y^2\; d\tilde{b}dy && (4.24c)\\
&= -2\omega_0^2<\tilde{b}y> +2\omega_0^4 h^2\sigma^2<\tilde{b}^2> \quad .
\end{aligned}
$$

The initial conditions for this set of coupled ordinary differential equations for $x = 0$ are:

$$\begin{aligned} \tilde{b}(x=0) &= b_0 = C_0 + B_0 \quad , && (4.25a) \\ \tilde{b}_x(x=0) &= y_0 = -i(\alpha A^2 \Omega b_0 + \nu \Omega^2 c_0) \quad , && (4.25b) \\ c(x=0) &= c_0 = C_0 - B_0 \quad . && (4.25c) \end{aligned}$$

The Eqs. (4.24.a-c) for the expectation values of $\tilde{b}^2$ and $\tilde{b}y$ can be reduced to

$$\begin{aligned} <\tilde{b}^2>_{xxx} + 4\omega_0^2 <\tilde{b}^2>_x - 4\omega_0^4 \sigma^2 h^2 <\tilde{b}^2> &= 0 \quad , && (4.26a) \\ <\tilde{b}y>_{xxx} + 4\omega_0^2 <\tilde{b}y>_x - 4\omega_0^4 \sigma^2 h^2 <\tilde{b}y> &= 0 \quad . && (4.26b) \end{aligned}$$

The solution of these equations yields,

$$\begin{aligned} <\tilde{b}^2> \approx\ & e^{\omega_0^2\sigma^2h^2x}\left(b_1 + \frac{\sigma^2 b_2}{4} + \frac{b_3}{4\omega_0^2}\right) && (4.27a) \\ & + e^{-\frac{1}{2}\omega_0^2h^2\sigma^2x}\Big[\Big(\frac{b_2}{2\omega_0} - \frac{\omega_0 h^2\sigma^2}{2}b_1 - \frac{3\sigma^2h^2b_3}{16\omega_0}\Big)\sin(2\omega_0 x) \\ & - \Big(\frac{b_3}{4\omega_0^2} + \frac{\sigma^2 b_2}{4}\Big)\cos(2\omega_0 x)\Big] \quad , \\ <\tilde{b}y> \approx\ & \omega_0^2 e^{\omega_0^2h^2\sigma^2x}\left(b_1 + \frac{b_3}{4\omega_0^2} + \frac{\sigma^2h^2b_2}{4}\right) && (4.27b) \\ & + e^{-\frac{1}{2}\omega_0^2h^2\sigma^2x}\Big[-\frac{1}{4}(\omega_0^2\sigma^2 b_2 + b_3)\cos(2\omega_0 x) \\ & + \frac{1}{2}(\omega_0^3h^2\sigma^2b_1 - \omega_0 b_2 - \frac{1}{8}h^2\sigma^2\omega_0 b_3)\sin(2\omega_0 x)\Big] \quad . \end{aligned}$$

Here, the parameters b_1, b_2 and b_3 are

$$b_1 = b_0^2 \ , \qquad b_2 = 2b_0 y_0 \ , \qquad b_3 = 2y_0^2 - 2\omega_0^2 b_0^2 \quad . \tag{4.28}$$

The analytical estimate for the expectation value of $<\tilde{b}^2>$ predicts that its growth is exponential, while the oscillations with frequency $2\omega_0$ will decay exponentially during propagation. This exponential growth corresponds to the existence of stochastic parametric resonance (MI). The random modulated media were parametrically excited when the harmonics were equal to $\frac{2\omega_0}{n}$. However, in the stochastic case, all harmonics are present in the random process. Accordingly, there will be stochastic parametric resonance for any modulation of the non-linear plane wave. This is verified by the numerical simulations of the NLSE which are shown in Fig. 4.5-4.7. The

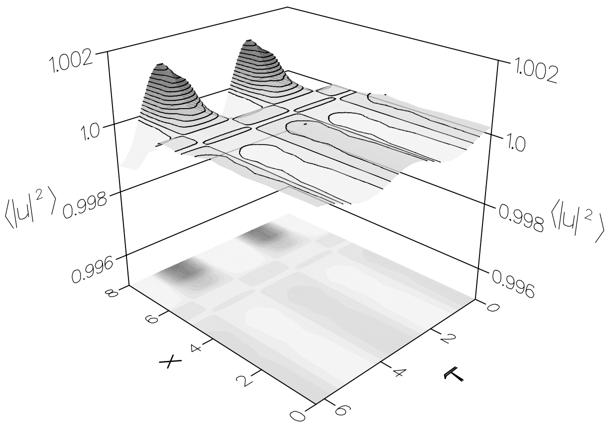

Figure 4.5: Space-time evolution of $|u|^2$ for $\nu = +1$, $q = 1 \cdot 10^{-4}$, $v = 0$,A=1.0, $\Omega = 4.1888$, $\sigma^2 = 0.04992$, $\alpha = 0$ and using 140 realizations.

numerical solution of the NLSE is again obtained by the Fourier split step method, where the random term enters in the nonlinear part [19, 20]. This corresponds to the Stratonovich's interpretation, which, as stated in Ref. [18], is more natural from a physical point of view. In Fig. 4.5 and 4.6 the space-time evolution of the mean square $< \mid u \mid^2 >$ is plotted in the case of negative group velocity dispersion. The space-time evolution for positive group velocity dispersion is shown in Fig. 4.7. In all cases we obtain MI as predicted by Eq. (4.27). The validity of our analytical estimate, Eq.(4.27), is investigated numerically by performing an averaging over 140 realizations of the maximum amplitude of u^2 for the cases corresponding to Fig. 4.5-4.7. The results are shown in Fig. 4.8-4.10. In Fig.4.8 $\log\{< max(\mid u \mid)^2 > -1\}$ is plotted versus the propagation distance as a solid line. The dashed line in Fig. 4.8 is the analytically estimated exponential growth rate $\gamma_{theor} = \omega_0^2 h^2 \sigma^2$. The agreement between the numerical and theoretical growth rate is seen to be good for short propagation

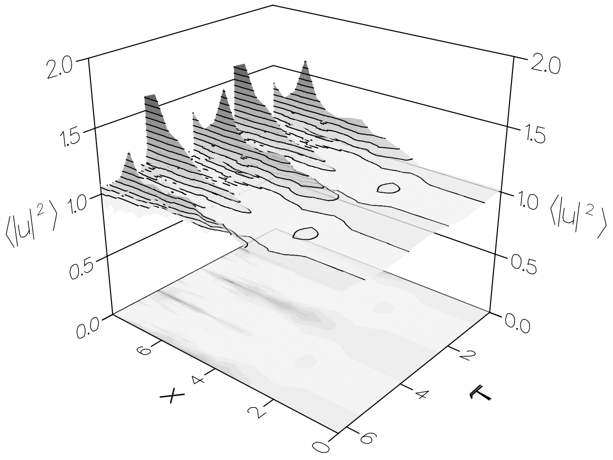

Figure 4.6: Space-time evolution of $|u|^2$ for $\nu = +1$, $q = 1 \cdot 10^{-2}$, $v = 0$,A=1.0, $\Omega = 4.1888$, $\sigma^2 = 0.1$, $\alpha = 0$ and using 140 realizations.

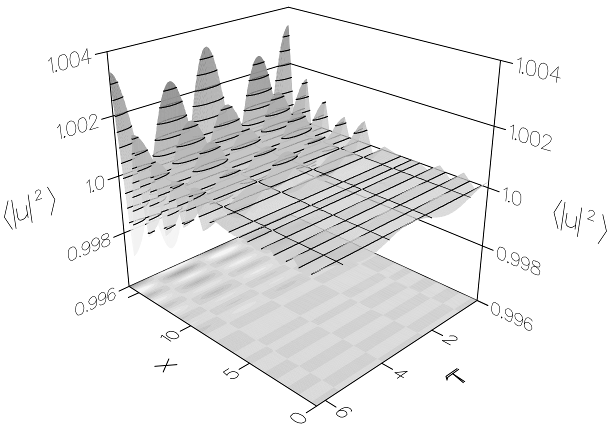

Figure 4.7: Space-time evolution of $|u|^2$ for $\nu = -1$, $q = 1 \cdot 10^{-4}$, $v = 0$,A=1.0, $\Omega = 4.1888$, $\sigma^2 = 0.04992$, $\alpha = 0$ and using 140 realizations.

distances. Furthermore, we also observe the predicted initial decaying oscillations with frequency $\approx 2\omega_0$. The growth rate corresponding to Figs. 4.6

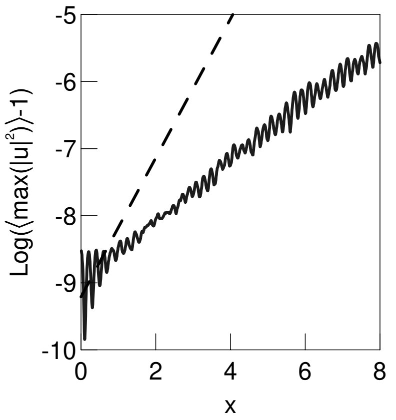

Figure 4.8: $Log(< max(|u|^2|) > -1)$ versus x for $\nu = +1$, $q = 1 \cdot 10^{-4}$, $v = 0$,A=1.0, $\Omega = 4.1888$, $\sigma^2 = 0.04992$, $\alpha = 0$ and using 140 realizations. The dashed line is the theoretical predicted initial growth rate.

and 4.7 are shown in 4.9 and 4.10, respectively. It is evident that the analytical estimate (dashed line) is valid for very short propagation distances only. However, the decaying oscillations with frequency $\approx 2\omega_0$ are observed in all cases.

The increment rate is found to decrease with propagation distance, which is also evident in all simulations. Thus, our linearization approach only applies for very short propagation distances.

4.3 Summary

In this chapter we have investigated analytically and numerically the influence of periodic modulations of fiber parameters on the modulational instability of nonlinear plane waves. We show the existence of MI in the

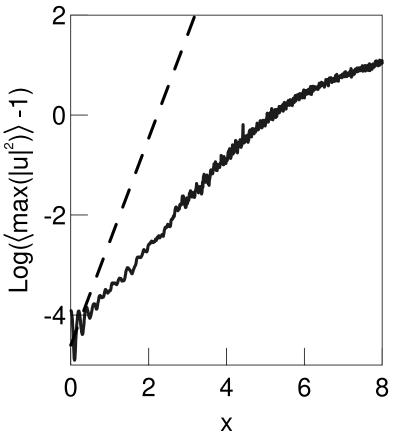

Figure 4.9: $Log(< max(|u|^2|) > -1)$ versus x for $\nu = +1$, $q = 1 \cdot 10^{-2}$, $v = 0$,A=1.0, $\Omega = 4.1888$, $\sigma^2 = 0.1$, $\alpha = 0$ and using 140 realizations. The plotted line is the theoretical predicted initial growth rate.

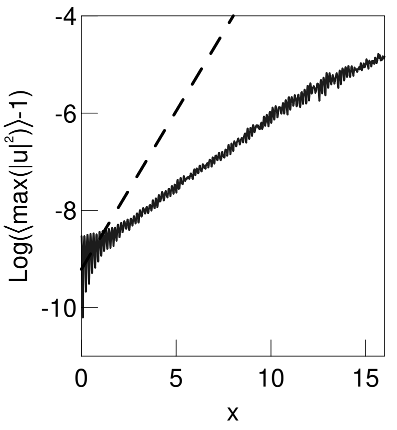

Figure 4.10: $Log(< max(|u|^2|) > -1)$ versus x for $\nu = -1$, $q = 1 \cdot 10^{-4}$, $v = 0$,A=1.0, $\Omega = 4.1888$, $\sigma^2 = 0.04992$, $\alpha = 0$ and using 140 realizations. The plotted line is the theoretical predicted initial growth rate.

positive group velocity region in the case of periodic or random modulation of the non-linearity in the NLSE. We also briefly considered that the self-steepening effect shifts the region of parametric resonance to lower frequencies, which is confirmed by numerical simulations. The periodicity of the solution in space analogous to Fermi-Pasta-Ulam recurrence is observed for the case of a periodic modulation of the media.

In the case of a random varying non-linearity, we have observed stochastic parametric resonance both numerically and analytically. Using the linearization procedure for the modified NLSE, the values of the wave increments have been calculated. The numerical simulations are in good agreement with the theoretical predictions for short propagation distances.

Bibliography

[1] G. P. Agrawal, "Nonlinear Fiber Optics", Academic Press,N.Y.,1990.,

[2] F. Kh. Abdullaev, S. A. Darmanyan, P. Khabibullaev, "Optical Solitons", Springer-Verlag, Berlin-Heidelberg, 1993.

[3] J. G. Caputo, M. P. Sørensen, N. Lazaridis, "The Fiber ring Laser Studied by Collective Coordinates", Jour. Optic Soc. America B, **12** (1), 1995.

[4] F. Kh. Abdullaev, J. H. Hensen, S. Bischoff, M. P. Sørensen, "Propagation of Optical Solitons in Random Media", In preparation.

[5] E. R. Tracy and H. H. Chen, Phys. Rev. A37. 815 (1988).

[6] N. A. Akhmediev, N. N. Kulagin and V. M. Eleonsky, Sov.Phys.-JETP, **62**, 894,(1985).

[7] S. Trillo and S. Wabnitz, In "Nonlinearity with Disorder", Eds. F.Kh.Abdullaev, A.R.Bishop and S.Pnevmatikos, (Springer-Verlag, Heidelberg,1992).

[8] A. Hasegawa, Opt.Lett.,**9**, 288 (1984).

[9] Yu. Kivshar and M. Peyrard, Phys. Rev. A46, 3198 (1992).

[10] F. Matera, A. Mecozzi, M. Romagnoli, M. Settembre Opt. Lett. **18(18)**, 1499 (1993).

[11] F. Kh. Abdullaev. Pisma JTP **20**, 25 (1994). (In Russian).

[12] Yu. S. Kivshar, S. Turytsin, Phys. Rev. **49**, R2536 (1994).

[13] K. Rasmussen, P. L. Christiansen, Yu. Gaididei. Phys. Lett. A, in press (1995).

[14] L. D. Landau and E. M. Lifshitz, Mechanics, (Pergamon Press,London,1973).

[15] A. H. Nayfeh. Introduction to perturbation techniques. Wiley, Chich-

ester, 1981.

[16] F. Kh. Abdullaev, S. A. Darmanyan, S. Bischoff, P. L. Christiansen, M. P. Sørensen, Opt. Commun. , **108**, 60 (1994).

[17] D. W. McLaughlin, Physica D3, 335 (1983).

[18] see for a text book discussion: R. Kubo, M. Toda, N. Hashitsume, Statistical Physics II, Nonequilibrium Statistical Mechanics, Springer-Verlag 1985.

[19] O. Bang, Coherent energy transport, thermal effects and radiative decay in ordered molecular monolayers by nonlinear dynamical models, Ph.D.-Thesis, The Danish center for applied mathematics and Mechanics, The Technical University of Denmark, 1993.

[20] F. If, Spectral algorithms and numerical solution of some nonlinear partial differential equations, Ph.D.-Thesis, The Danish center for applied mathematics and Mechanics, The Technical University of Denmark, 1986.

Chapter 5

Conclusion

In this work we have presented results from three different topics in the field of semiconductor and fiber optics.

In chapter 2 a large signal model for colliding-pulse mode-locked semiconductor lasers has been developed. Results of the model are shown to be in good agreement with experimental results as regards both the resulting pulse-width and the pulse chirp. We find that the pulse width is determined by the opposite effects of pulse broadening in the gain sections and pulse shortening in the saturable absorber. The chirp of the pulses are understood to arise mainly from self-phase modulation in the gain sections in combination with a net time shift due to saturation of the absorber. These results demonstrate the importance of a detailed modelling of the material dynamics to understand the operation principles of monolithic colliding-pulse mode-locked laser diodes. Especially the inclusion of spectral hole burning and carrier heating are necessary to understand the pulse broadening for increased gain currents. The detailed model for the saturable absorber showed that the quantum confined Stark effect is responsible for the synchronization of the CPM pulse train with an external modulation of the bias on the saturable absorber.

In chapter 3 we have derived the equations for the optical properties of an arbitrary thick semiconductor sample, including Coulomb and light propagation effects. For sample thicknesses less than half the wavelength we have described the basic effects of how the transition from the two-dimensional transmission spectrum towards the three-dimensional transmission spectrum is explained by showing the importance of the off-diagonal Coulomb potential elements, which increase the exciton binding energy and transfer oscillator strength from higher 1s excitons to the lowest 1s exciton. Furthermore, we observe the development of an exciton free layer with increasing material thickness, which is an important factor in the theories applied for solving the halfspace problem.

In chapter 4 have analytically and numerical investigated the influence of periodic or random perturbations of the non-linearity in the non-linear Schrödinger equation. It has been demonstrated that modulational instability occurs for both negative and positive dispersion, when the non-linearity is varied. The self-steepening effect is found to reduce the regions of modulational instability in the case of periodic modulations of the non-linearity. Furthermore it has been shown that modulational instability exist for any perturbation of the steady state solution, when the coefficient in front of the non-linearity in the non-linear Schrödinger equation is fluctuating randomly.

Appendix A

Material Dynamics of Semiconductor QWs.

The material dynamics/response of a semiconductor laser can be described by the Semiconductor Bloch Equations (SBE) [1, 2]. The SBE give a very general description of the material dynamics/response. The wave-propagation inside the semiconductor is described by Maxwell's equations. Maxwell's equation (wave-propagation equation) and the SBE have thus to be solved self-consistently. The self-consistent solution of Maxwell's equations and the SBE is computational very demanding. Therefore, the material dynamics/response is often described by a simpler model than the SBE. However, when the light is propagating perpendicular to the QW, we can solve Maxwell's equations analytically. This is done for the case of linear optics in chapter 3.

In this appendix we will present the derivation of a rate equation model from semi-classical density matrix equations for an edge emitting quantum well laser diode. The derived rate equation model has been shown to give a good description of the gain properties in semiconductor amplifiers [3, 4, 5, 6].

In section A.1 we will present the derivation of the rate equation model from the density-matrix formalism for semiconductor lasers [4, 7, 8, 9]. The derived rate equation model is extended by taking into account the injection and removal of carriers from the quantum well by a phenomenological introduced rate equation. This is done in section A.2. In section A.3 we discuss the case of a reverse biased quantum well laser diode. The gain spectra calculated by many-body theory [10] for the case of a reverse biased QW semiconductor are fitted by our model by introducing a reverse bias dependent bandgap shrinkage parameter, resulting from the Quantum Confined Stark Effect (QCSE) and by letting the maximum differential gain vary with the applied reverse bias. Furthermore, the rate equation model has a slightly different form in the case of a low carrier density, since we here approximate the Fermi-Dirac carrier distribution function with a Maxwell-Boltzmann carrier distribution function.

A.1 Semiclassical density-matrix formalism

The polarization induced by an electromagnetic filed in a semiconductor medium can be calculated by the semiclassical density matrix formalism. The equations of motion for the diagonal and off-diagonal elements in the density matrix formalism are [4, 7, 8, 9],

$$\begin{aligned}
\frac{\partial \rho_{c,k}(t)}{\partial t} &= -\frac{\rho_{c,k}(t)-f_{c,k}(t)}{\tau_{1,c}} - \frac{\rho_{c,k}(t)-f^{L}_{c,k}(t)}{\tau_{h,c}} - \frac{\rho_{c,k}(t)-f^{eq}_{c,k}(t)}{\tau_s} \\
&\quad -\frac{i}{\hbar}\cdot\left[d^*_k\rho_{cv,k}(t)-d_k\rho_{vc,k}(t)\right]E(z,t)+\Lambda_{c,k} \quad , \qquad \text{(A.1a)} \\
\frac{\partial \rho_{v,k}(t)}{\partial t} &= -\frac{\rho_{v,k}(t)-f_{v,k}(t)}{\tau_{1,v}} - \frac{\rho_{v,k}(t)-f^{L}_{v,k}(t)}{\tau_{h,v}} - \frac{\rho_{v,k}(t)-f^{eq}_{v,k}(t)}{\tau_s} \\
&\quad -\frac{i}{\hbar}\cdot\left[d^*_k\rho_{cv,k}(t)-d_k\rho_{vc,k}(t)\right]E(z,t)+\Lambda_{v,k} \quad , \qquad \text{(A.1b)} \\
\frac{\partial \rho_{cv,k}(t)}{\partial t} &= \left(-i\omega_k-\frac{1}{\tau_2}\right)\rho_{cv,k}(t) \qquad \text{(A.1c)} \\
&\quad -\frac{i}{\hbar}d_k\left(\rho_{c,k}(t)+\rho_{v,k}(t)-1\right)E(z,t) \quad ,
\end{aligned}$$

$$\rho_{vc,k} = \rho^*_{cv,k} \quad . \tag{A.1d}$$

The first term on the Right Hand Side (RHS) in equation A.1a and A.1b describes the relaxation of the carrier distribution $\rho_{x,k}(t)$ towards a quasi Fermi-Dirac distribution with a time constant $\tau_{1,c}$ $(\tau_{1,v})$ determined by carrier-carrier scattering [2]. The second term on the RHS in Eq. (A.1a) and Eq. (A.1b) accounts for the relaxation of the quasi Fermi-Dirac distribution at the carrier temperature T_x (x=c,v) towards the quasi Fermi-Dirac distribution at the carrier temperature T_L with a time constant $\tau_{h,x}$ determined by carrier-phonon scattering. Here, T_L is the lattice temperature. The quasi Fermi-Dirac distribution yields,

$$f_{x,k} = \frac{1}{1 + exp\left[\frac{E_{x,k} - E_{f,x}}{k_B T_x}\right]} \quad , \tag{A.2}$$

where $\hbar$ is Plancks constant, k_B is the Boltzmann constant and $E_{f,x}$ is the Fermi energy. Furthermore, we assume the band structure to be parabolic, where the energy $E_{x,k} = \frac{\hbar^2 k^2}{2m_x}$ is measured positive from the band edge into the band. m_x is the effective electron/hole mass. The third term on the RHS in Eqs. (A.1a) and (A.1b) accounts for the relaxation of the carrier distribution towards its equilibrium Fermi-Dirac distribution with a time constant τ_s. It should be noted that $\tau_s > \tau_{h,x} > \tau_{1,x}$.

The fourth term in Eq. (A.1a) and (A.1b) accounts for stimulated emission and absorption. Here, $E(z,t)$ is the electromagnetic field in the semiconductor and d_k is the dipole-moment, while d_k^* is the complex conjugate of d_k. $\Lambda_{x,k}$ denotes pumping due to current injection.

ω_k is the optical carrier frequency and τ_2 is the dephasing time of the polarization. In the following we assume $d_k = d_k^*$, which implies that d_k is real. The macroscopic polarization is defined by the off-diagonal matrix elements $\rho_{cv,k}$ and $\rho_{vc,k}$ [7],

$$P(t) = \frac{1}{V}\sum_k d_k(\rho_{cv,k}(t) - \rho_{vc,k}(t)) \quad , \tag{A.3}$$

where V is the volume of the active region.

We will assume that the semiconductor is undoped. In this case the total carrier density in the valence band and conduction band will be equal due to charge neutrality. The total carrier density in the conduction (valence) band of the quantum well is determined by summing the carrier distribution function over all k-states,

$$N_{qw}(t) = \frac{1}{V}\sum_k \rho_{x,k}(t) \quad . \tag{A.4}$$

The physical processes of carrier-carrier scattering and carrier-phonon scattering are intraband processes, that do not affect the total carrier density. Accordingly, the total carrier density in the conduction (valence) band is

$$N_{qw}(t) = \frac{1}{V}\sum_k f_{x,k}(t) = \frac{1}{V}\sum_k f^L_{x,k}(t) \quad . \tag{A.5}$$

An equation of motion for the total carrier density N_{qw} is determined by summing equation (A.1a) or (A.1b), over all k-states,

$$\begin{aligned}
\frac{dN_{qw}}{dt} &= -\frac{0}{\tau_{1,x}} - \frac{0}{\tau_{h,x}} - \frac{N_{qw} - N^{eq}_{qw}}{\tau_s} && \text{(A.6a)}\\
&\quad -\frac{i}{\hbar V}\sum_k \left[d^*_k \rho_{cv,k} - d_k \rho_{vc,k}\right] E(z,t) + \sum_k \frac{\Lambda_{x,k}}{V} \quad , &&\\
&\approx \frac{I}{eV} - \frac{N_{qw}}{\tau_s} - \frac{i}{\hbar V}\sum_k \left[d^*_k \rho_{cv,k} - d_k \rho_{vc,k}\right] E(z,t) \quad , && \text{(A.6b)}\\
I &= e\sum_k \Lambda_{x,k} \; . && \text{(A.6c)}
\end{aligned}$$

Here, we have made the assumption that

$$N^{eq}_{qw} = \frac{1}{V}\sum_k f^{eq}_{x,k} \approx 0 \; . \tag{A.7}$$

This is for typical semiconductor lasers a very good approximation. The external current I is defined by Eq. (A.6c), where e is the electronic charge. Before proceeding with the determination of the summation term in Eq. (A.6b), we will introduce the carrier energy density $U_x(t)$, $x = v, c$. The definition of the carrier energy density is,

$$U_x(t) = \frac{1}{V}\sum_k E_{x,k}\rho_{x,k}(t) \quad . \tag{A.8}$$

The carrier energy may also be obtained by summing the quasi Fermi-Dirac distribution characterized by the carrier temperature T_x, if we assume elastic carrier-carrier collisions, since elastic carrier-carrier collisions do not result in energy dissipation. Thus the carrier energy density is

$$
\begin{aligned}
U_x(t) &= \frac{1}{V}\sum_k E_{x,k}\rho_{x,k}(t) \quad , && \text{(A.9a)}\\
&= \frac{1}{V}\sum_k E_{x,k} f_{x,k}(t) \quad , && \text{(A.9b)}\\
&= U_x(N_{qw}, T_x) \quad , && \text{(A.9c)}\\
U_x(N_{qw}, T_L) &= \frac{1}{V}\sum_k E_{x,k} f^L_{x,k}(t) \quad , && \text{(A.9d)}
\end{aligned}
$$

Rate equations for the carrier energy in the conduction and valence band are obtained by multiplying the respective equations of motion (Eq. (A.1a) and Eq. (A.1b)) with the corresponding carrier energy ($E_{c,k}$ and $E_{v,k}$) and performing the summation over all k-states. The rate equation of the carrier energy for the electrons ($x = c$) or holes ($x = v$) is accordingly,

$$
\begin{aligned}
\frac{dU_x}{dt} &= -\frac{0}{\tau_{1,c}} - \frac{U_x(T_x) - U_x(T_L)}{\tau_{h,x}} - \frac{U_x(T_x)}{\tau_s} && \text{(A.10a)}\\
&\quad -\frac{i}{\hbar V}\sum_k \left[d_k^*\rho_{cv,k}E_{x,k} - d_k\rho_{vc,k}E_{x,k}\right]E(z,t)\\
&\quad +\sum_k \frac{\Lambda_{c,k}E_{x,k}}{V} \ ,\\
\frac{dU_x}{dt} &= < E_x^p > \frac{I}{eV} - \frac{U_x}{\tau_s} - \frac{U_x - U_x^L}{\tau_{h,x}} + K_x < |E(z,t)|^2 > && \text{(A.10b)}\\
&\quad -\frac{i}{\hbar V}\sum_k \left[d_k^*\rho_{cv,k}E_{x,k} - d_k\rho_{vc,k}E_{x,k}\right]E(z,t) \quad .
\end{aligned}
$$

Here, we have phenomenological taken into account the effect of Free Carrier Absorption (FCA) [4, 11], which is represented by the term $K_x\left\langle|E(z,t)|^2\right\rangle$ in Eq. (A.10b). The FCA accounts for the process, when a carrier through interaction with a phonon absorbs a photon, whereby it is transferred to a higher energy within the band. The constant K_x is expressed by the free carrier absorption cross section σ_x,

$$K_x = \epsilon_0 n n_g v_g \sigma_x N_{qw} \quad , \tag{A.11}$$

where ϵ_0 is the vacuum permitivity, n is the refractive index, n_g is the group refractive index and v_g is the group velocity.

So far we have derived a rate equations for the total carrier density N_{qw} and the carrier energy density in the conduction U_c and valence band U_v, respectively. However, the coupling to the light field (electromagnetic field) is still governed by a k summation over the off-diagonal matrix elements. In the following we will adiabatically eliminate the polarization/off-diagonal elements in the slowly varying envelope approximation. The adiabatic elimination of the polarization is a good approximation of the equations of motion for the off diagonal density matrix elements in Eq. (A.1) as long as the dephasing time of the polarization τ_2 is very short, $\tau_2 \ll \tau_{1,c} \ll \tau_{h,x}$. Furthermore, the adiabatic elimination of the polarization is only valid, if τ_2 is much smaller than the optical pulse width. The dephasing time of the hole distribution function due to carrier carrier scattering $\tau_{1,v}$ is typically shorter than the dephasing time of the polarization τ_2 [2]. Therefore we will also adiabatically eliminate $\tau_{1,v}$.

The adiabatic elimination of the dephasing time of the polarization corresponds to assume the process to be instantaneous. The equations of motion for the off-diagonal matrix element is,

$$\begin{aligned} \frac{\partial \rho_{cv,k}(t)}{\partial t} &= \left(-i\omega_k - \frac{1}{\tau_2}\right) \rho_{cv,k}(t) && \text{(A.12a)} \\ &\quad - \frac{i}{\hbar} d_k \left(\rho_{c,k}(t) + \rho_{v,k}(t) - 1\right) E(z,t) \quad , \\ \rho_{vc,k} &= \rho^*_{cv,k} \quad , && \text{(A.12b)} \end{aligned}$$

Let us now make the Slowly Varying Envelope Approximation (SVEA) for both the electrical field and the polarization,

$$\begin{aligned} \rho_{cv,k} &= \varrho_{cv,k}(t) e^{-i\omega_0 t} \quad , && \text{(A.13a)} \\ E(z,t) &= \frac{1}{2}\left(A(z,t) e^{i\omega_0 t} + c.c.\right) \quad , && \text{(A.13b)} \end{aligned}$$

where c.c. stands for the complex conjugate, and ω_0 is the optical carrier frequency.
Substituting the expression for the polarization, Eq. (A.13a), and the electrical field, Eq. (A.13b), into Eq. (A.12a), and assuming the derivative of $\varrho_{cv,k}$ with time to be zero, $\varrho_{cv,k}$ is a function of the diagonal matrix elements,

$$\begin{aligned}\varrho_{c,k}(t) &\approx \frac{id_k\left(\rho_{c,k}(t)+\rho_{v,k}(t)-1\right)}{2\hbar}\cdot\frac{1}{i(\omega_0-\omega_k)-\gamma_2} \qquad \text{(A.14a)}\\ &\quad\cdot\left[A^*(z,t)+A(z,t)e^{2i\omega_0 t}\right] \quad ,\\ &\approx \frac{id_k\left(\rho_{c,k}(t)+\rho_{v,k}(t)-1\right)}{2\hbar}\cdot\frac{1}{i(\omega_0-\omega_k)-\gamma_2} \qquad \text{(A.14b)}\\ &\quad\cdot A^*(z,t) \quad ,\end{aligned}$$

where we made the Rotating Wave Approximation (RWA), in Eq. (A.14b). The constant γ_2 is equal to $\frac{1}{\tau_2}$.

The SVEA is also made in the equation of motion for the diagonal matrix elements $\rho_{c,k}$ and $\rho_{v,k}$ (Eq. (A.1a) and Eq. (A.1b)), where the off-diagonal matrix elements are expressed by the found relations in Eq. (A.13a) and Eq. (A.14b):

$$\begin{aligned}\frac{\partial\rho_{c,k}}{\partial t} &= -\frac{\rho_{c,k}-f_{c,k}}{\tau_{1,c}}-\frac{\rho_{c,k}-f^L_{c,k}}{\tau_{h,c}} \qquad \text{(A.15a)}\\ &\quad -\frac{i}{\hbar}\left[d^*_k\varrho_{cv,k}(t)A(z,t)-d_k\varrho^*_{vc,k}(t)A^*(z,t)\right.\\ &\quad \left.+d^*_k\varrho^*_{cv,k}(t)A^*(z,t)e^{-2i\omega_0 t}-d_k\varrho_{vc,k}(t)A(z,t)e^{2i\omega_0 t}\right]E(z,t) \quad ,\\ &\approx -\frac{\rho_{c,k}(t)-f_{c,k}(t)}{\tau_{1,c}}-\frac{\rho_{c,k}-f^L_{c,k}}{\tau_{h,c}} \qquad \text{(A.15b)}\\ &\quad -\frac{|d_k|^2\left(\rho_{c,k}(t)+\rho_{v,k}(t)-1\right)}{2\hbar^2}\frac{\gamma_2}{(\omega_0-\omega_k)^2+\gamma_2^2}|A(z,t)|^2 \quad ,\end{aligned}$$

where we in Eq. (A.15b) made the RWA approximation. The equation of motion for $\rho_{v,k}$ will be equal to Eq. (A.15b) except that index c has to be replaced by the index v. Carrier-carrier scattering drives the carrier distribution much faster to its quasi Fermi-Dirac distribution, than carrier-phonon scattering, $\tau_{1,c} \ll \tau_{h,c}$ and $\tau_{1,v} \ll \tau_{h,v}$. We will in the following neglect the effect of carrier-phonon scattering in the equation of motion for $\rho_{c,k}$ and $\rho_{v,k}$, since the carrier temperature T_c and T_v can be determined by the equation of motion (rate equation) for the carrier density N_{qw} and energy density U_c and U_v, respectively. The effect of the relaxation of the carrier distribution towards its quasi Fermi-Dirac distribution characterized by the lattice temperature T_L is thus already captured by the rate equation for the carrier density and carrier energy density. Thus, the equation of motion for $\rho_{c,k}$ and $\rho_{v,k}$ are

$$\begin{aligned}
\frac{\partial \rho_{c,k}(t)}{\partial t} &= -\frac{\rho_{c,k}(t) - f_{c,k}(t)}{\tau_{1,c}} \qquad \text{(A.16a)} \\
&\quad - \frac{|d_k|^2 \left(\rho_{c,k}(t) + \rho_{v,k}(t) - 1\right)}{2\hbar^2} \frac{\gamma_2^{-1}}{\left(\frac{\omega_0 - \omega_k}{\gamma_2}\right)^2 + 1} |A(z,t)|^2 \quad , \\
\frac{\partial \rho_{v,k}(t)}{\partial t} &= -\frac{\rho_{v,k}(t) - f_{v,k}(t)}{\tau_{1,v}} \qquad \text{(A.16b)} \\
&\quad - \frac{|d_k|^2 \left(\rho_{c,k}(t) + \rho_{v,k}(t) - 1\right)}{2\hbar^2} \frac{\gamma_2^{-1}}{\left(\frac{\omega_0 - \omega_k}{\gamma_2}\right)^2 + 1} |A(z,t)|^2 \quad .
\end{aligned}$$

The rate equations for N_{qw}, U_c and U_v were obtained by summing over all k-states. However, stimulated emissions occur only for a narrow frequency band around the optical carrier frequency, ω_0. So in the following we make the assumption, that the summation over a narrow frequency band ($\omega \in [\omega_0 - \Delta\omega, \omega_0 + \Delta\omega]$,(a few k-states)) should be sufficient to determine the optical gain. This approximation is valid, when the width of the spectrum of the optical field is much smaller than γ_2. This is normally always the case in semiconductor laser diodes, since pulses with a width of a few pico-seconds typically have a spectral width of a few THz [4, 11].

The amount of stimulated emission/absorption of the semiconductor is hence determined by a small fraction of the total carrier density. Therefore, we define this fraction of the total carrier density N_{qw} as the "local" gain determining carrier density. The definition of the "local" carrier densities in the conduction n_c and valence band n_v is,

$$n_c = \frac{1}{V}\sum_{k\in I_{opt}} \rho_{c,k} \quad , \tag{A.17a}$$

$$n_v = \frac{1}{V}\sum_{k\in I_{opt}} \rho_{v,k} \quad . \tag{A.17b}$$

Rate equations for the "local" gain determining carrier density n_c and n_v are obtained by summing the equations (A.16a) and (A.16b) over $k \in I_{opt}$. The summation over $k \in I_{opt}$ cannot be done analytically, since we have a Lorentzian line-shape function $L(\omega_k)$,

$$L(\omega_k) = \frac{\gamma_2^{-1}}{\left(\frac{\omega_0-\omega_k}{\gamma_2}\right)^2 + 1} \quad . \tag{A.18}$$

The Lorentzian line-shape function has a Full Width at Half Maximum (FWHM) of $2 \cdot \gamma_2$, and a area of π, $\int_{-\infty}^{\infty} L(\omega)d\omega = \pi$. The summation over $k \in I_{opt}$ can be performed analytically, if we replace the Lorentzian line-shape function with a "Hat" line-shape function $B(\omega_k)$,

$$B(\omega_k) = \begin{cases} 0 & \text{when } \omega_k \leq \omega_0 - \frac{\pi}{2}\gamma_2 \\ \gamma_2^{-1} & \text{when } \omega_0 - \frac{\pi}{2}\gamma_2 \leq \omega_k \leq \omega_0 + \frac{\pi}{2}\gamma_2 \\ 0 & \text{when } \omega_k \geq \omega_0 - \frac{\pi}{2}\gamma_2 \end{cases} \quad . \tag{A.19}$$

A schematic plot of the Lorentzian and "hat" line-shape functions is shown in Fig. A.1. The area of the "hat" line-shape functions is equal to the area of the Lorentzian line-shape function.

The "hat" line-shape function is used to approximate the Lorentzian line-shape function in Eqs. (A.16), so that we can perform the summation over $k \in I_{opt}$ of these equations analytically. The equations for $\rho_{c,k}$ and $\rho_{v,k}$, where the Lorentzian line-shape function is replaced with the "hat" line-shape function, are

$$\frac{\partial n_c}{\partial t} = -\frac{n_c - \overline{n}_c}{\tau_{1,c}} \tag{A.20a}$$

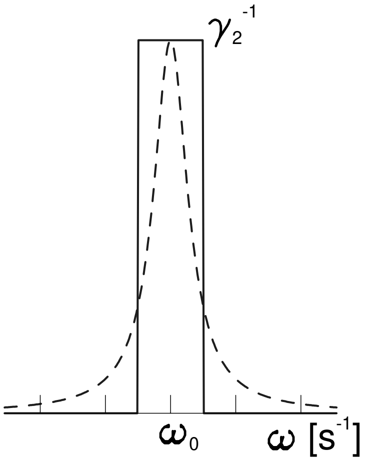

Figure A.1: Plot of the Lorentzian line-shape function (- - -) and the "hat" line-shape function.

$$-\frac{|d_k|^2\,(n_c+n_v-1)}{2\hbar^2}\gamma_2^{-1}|A(z,t)|^2 \quad ,$$

$$\frac{\partial n_v}{\partial t} = -\frac{n_v-\overline{n}_v}{\tau_{1,v}} -\frac{|d_k|^2\,(n_c+n_v-1)}{2\hbar^2}\gamma_2^{-1}|A(z,t)|^2 \quad , \tag{A.20b}$$

where $\overline{n}_c$ and $\overline{n}_v$ are the "local" carrier densities determined by the summation over the quasi Fermi-Dirac distribution with carrier temperature T_c and T_v, respectively. The "local" carrier densities n_c and n_v are found by replacing the summation over the possible k-states ($k \in I_{opt}$) by an integral over the Density Of States (DOS) function. The DOS function for a QW is [2]

$$D(E) = \frac{m_r}{\pi L_{qw}\hbar^2} \quad , \tag{A.21}$$

where L_{qw} is the width of the QW. m_r is the effective electron mass,

$$m_r = \left(\frac{1}{m_c}+\frac{1}{m_v}\right)^{-1} \quad . \tag{A.22}$$

The electron density in the conduction and valence band are calculated by using the effective electron mass in the conduction and valence band, respectively. However, here we are interested in the electron density, which may recombine by stimulated emission, and therefore we have to use the relative electron mass, m_r. The maximum number of states that can recombine by stimulated emission are

$$N_0 = \int_{\hbar\omega_0 - \frac{\pi}{2}\gamma_2\hbar}^{\hbar\omega_0 + \frac{\pi}{2}\gamma_2\hbar} \frac{m_r}{\pi\hbar^2 L_{qw}} H(E - E_0) dE \quad , \tag{A.23}$$

where $H(E - E_0)$ is a heavy side function,

$$H(E - E_0) = \begin{cases} 0 & \text{when } E < E_0 \\ 1 & \text{when } E \geq E_0 \end{cases} \quad , \tag{A.24}$$

since only states with an energy above E_0 are allowed states. N_0 is the maximum carrier density, which may recombine by stimulated emission. The occupation probability of a state in the conduction or valence band is determined by the respective Fermi-Dirac distribution. The width of the "hat" line-shape function is very small, and to a good approximation the Fermi-Dirac distribution may be approximated by having a constant value across the "hat" line-shape function. With these approximations the "local" carrier density in the conduction and valence band are

$$\text{(A.25a)}$$

$$\overline{n}_c \approx \frac{N_0}{1 + exp\left[\frac{E_{c,0} - E_{f,c}}{k_B T_c}\right]} \quad , \tag{A.25b}$$

$$\overline{n}_v \approx \frac{N_0}{1 + exp\left[\frac{E_{v,0} - E_{f,v}}{k_B T_v}\right]} \quad , \tag{A.25c}$$

where $E_{c,0}$ and $E_{v,0}$ are the "photon" energy measured from the conduction and valence band edge into the band,

$$E_{c,0} = \frac{m_v}{m_v + m_c}(\hbar\omega_k - E_g - E_c - E_v) \quad , \tag{A.26a}$$

$$E_{v,0} = \frac{m_c}{m_v + m_c}(\hbar\omega_k - E_g - E_c - E_v) \quad . \tag{A.26b}$$

Here, $\hbar\omega_k$ is the photon energy, E_g is the bandgap energy and E_c and E_v is the energy of the lowest quantized state in the conduction and valence band, respectively [12]. The energies E_c and E_v are measured from the bottom of the quantum well and are for the parameter values given in table 2.1, E_c = 36.2835 meV and E_v = 3.2340 meV. The definition of $E_{c,0}$ and $E_{v,0}$ in Eq. (A.26) imply that E_0 is zero in Eq. (A.23) and Eq. (A.24).

The introduction of the "local" carrier densities and the adiabatically elimination of the polarization enables us to write down a set of rate equations for the total carrier density N_{qw} and the "local" carrier density n_c and n_v, which are

$$\frac{\partial N_{qw}}{\partial t} = \frac{I}{eV} - \frac{|d_k|^2\gamma_2^{-1}}{2\hbar^2}(n_c + n_v - N_0)|A(z,t)|^2 - \frac{N_{qw}}{\tau_s} \quad \text{(A.27a)}$$

$$\frac{\partial n_c}{\partial t} = -\frac{n_c - \overline{n}_c}{\tau_{1,c}} - \frac{|d_k|^2\gamma_2^{-1}}{2\hbar^2}(n_c + n_v - N_0)|A(z,t)|^2 \quad ,\text{(A.27b)}$$

$$\frac{\partial n_v}{\partial t} = -\frac{n_v - \overline{n}_v}{\tau_{1,v}} - \frac{|d_k|^2\gamma_2^{-1}}{2\hbar^2}(n_c + n_v - N_0)|A(z,t)|^2 \quad .\text{(A.27c)}$$

Here, n_c and n_v are the "local" carrier densities, which relax towards the "local" carrier densities $\overline{n}_c$ and $\overline{n}_v$ determined by their quasi Fermi-Dirac distributions.

The rate equation for the carrier energy density is still somewhat more complicated, since we here multiply the off-diagonal matrix elements by the carrier energy. However, before discussing the rate equation for the carrier energy we will introduce the photon density $S(z,t)$ in the rate equations for the total and "local" carrier densities, Eq. (A.27). The definition of the photon density is [4]

$$S(z,t) = \frac{\epsilon_0 n n_g}{2\hbar\omega_0}|A(z,t|^2 \quad . \quad \text{(A.28)}$$

where ϵ_0 is the electrical permitivity, n is the refractive index and n_g is the group refractive index. The rate equations for the total and "local" carrier density are, when the photon density is introduced,

$$\frac{\partial N_{qw}}{\partial t} = \frac{I}{eV} - \frac{|d_k|^2\gamma_2^{-1}\omega_0}{\hbar\epsilon_0 n n_g}(n_c + n_v - N_0)S - \frac{N_{qw}}{\tau_s} \quad , \text{(A.29a)}$$

$$\frac{\partial n_c}{\partial t} = -\frac{n_c - \overline{n}_c}{\tau_{1,c}} - \frac{|d_k|^2\gamma_2^{-1}\omega_0}{\hbar\epsilon_0 n n_g}(n_c + n_v - N_0)S \quad , \tag{A.29b}$$

$$\frac{\partial n_v}{\partial t} = -\frac{n_v - \overline{n}_v}{\tau_{1,v}} - \frac{|d_k|^2\gamma_2^{-1}\omega_0}{\hbar\epsilon_0 n n_g}(n_c + n_v - N_0)S \quad . \tag{A.29c}$$

This concludes the derivation of the rate equations for the total (N_{qw}) and the "local" carrier densities (n_c and n_v). However, to determine the "local" carrier density $\overline{n}_c$ and $\overline{n}_v$ we have to calculate the carrier temperature in the conduction and valence band, respectively. The carrier temperature can be determined, when we know the carrier density (N_{qw}) and the carrier energy density (U_c, U_v).

A.1.1 Rate equation for the carrier temperature

In this subsection we will derive a rate equation for the carrier temperature in the conduction and valence band from the carrier energy rate equation, see Eq. (A.10b). The equation for the carrier energy density is

$$\begin{aligned}\frac{dU_x}{dt} &= < E_x^p > \frac{I}{eV} - \frac{U_x}{\tau_s} - \frac{U_x - U_x^L}{\tau_{h,x}} + K_x < |E(z,t)|^2 > \\ &\quad -\frac{i}{\hbar V}\sum_k \left[d_k^* \rho_{cv,k} E_{x,k} - d_k \rho_{vc,k} E_{x,k}\right] E(z,t) \quad ,\end{aligned} \tag{A.30}$$

where $x = c, v$ for the conduction and valence band, respectively. The summation over all k-states accounts for the effect of stimulated emission. However, the process of stimulated emission occurs mainly in a very narrow energy band as discussed in the previous section. Therefore, the summation over all k-states in Eq. (A.30) can be replaced by a summation over a few k-states, $(\sum_k \approx \sum_{k\in I_{opt}})$. Furthermore, the energy $E_{x,k}$ may be assumed almost constant as long as $k \in I_{opt}$. With these approximations the rate equation for the carrier energy density becomes

$$\begin{aligned}\frac{dU_x}{dt} &= < E_x^p > \frac{I}{eV} - \frac{U_x}{\tau_s} - \frac{U_x - U_x^L}{\tau_{h,x}} + K_x < |E(z,t)|^2 > \\ &\quad -E_{x,0}\frac{|d_k|^2\gamma_2^{-1}\omega_0}{\hbar\epsilon_0 n n_g}(n_c - n_v - N_0)S(z,t) \quad .\end{aligned} \tag{A.31}$$

The carrier energy changes due to carrier injection, the first term on the RHS of Eq. (A.31), is in the following treatment neglected, since a detailed treatment of carrier capture processes in quantum well's is beyond the scope of this thesis. Thus, the injection current is assumed not to change the carrier energy distribution. We also assume the events of spontaneous emissions not to change the carrier energy distribution. With these assumptions the rate equation for the carrier energy density yields,

$$\begin{aligned}\frac{dU_x}{dt} &= -\frac{U_x - U_x^L}{\tau_{h,x}} \\ &+ \left(\sigma_x N_{qw} \hbar\omega_0 v_g - E_{x,0}\frac{|d_k|^2\gamma_2^{-1}\omega_0}{\hbar\epsilon_0 n n_g}(n_c - n_v - N_0)\right) S(z,t) \quad .\end{aligned} \tag{A.32}$$

The rate equation for the energy density U_x and total carrier density N_{qw} enables us to calculate the carrier temperature. The carrier temperature enters in the determination of the "local" carrier densities $\overline{n}_c$ and $\overline{n}_v$, see Eq. (A.25). The carrier energy density is thus only used to determine the carrier temperature. So instead of solving a rate equation for the carrier energy density, we may derive a rate equation for the carrier temperature.

Rate equation for the carrier temperature in the case of a Maxwell-Boltzmann distribution. We will first derive a rate equation for the carrier temperature, when the carrier density is so low that the Maxwell-Boltzmann distribution is a good approximation of the Fermi-Dirac distribution. We assume this to be the case in the saturable absorber of the Colliding-Pulse Mode-Locked (CPM) QW laser. The definition of the Maxwell-Boltzmann distribution is,

$$f_{B,x}(E) = \exp\left(\frac{E_{f,x} - E}{K_B T_x}\right) \quad . \tag{A.33}$$

The total carrier density N_{qw} in the conduction ($x = c$) or the valence band ($x = v$) is

$$N_{qw,x} = \int_0^\infty f_{B,x}(E) D(E) dE \quad , \tag{A.34a}$$

$$= \frac{m_x k_B T_x}{\pi L_{qw} \hbar^2} exp\left(\frac{E_{f,x}}{k_B T_x}\right) \quad . \tag{A.34b}$$

The energy density is in the case of a Maxwell-Boltzmann distribution,

$$\begin{aligned}
U_{qw,x} &= \int_0^\infty E f_{B,x}(E) D(E) dE \quad , && \text{(A.35a)}\\
&= \frac{m_x}{\pi L_{qw} \hbar^2} \int_0^\infty E \exp\left(\frac{E_{f,x} - E}{k_B T_x}\right) dE \quad , && \text{(A.35b)}\\
&= \frac{m_x k_B T_x}{\pi L_{qw} \hbar^2} k_B T_x \exp\left(\frac{E_{f,x}}{k_B T_x}\right) \quad , && \text{(A.35c)}\\
&= k_B T_x N_{qw,x} \quad . && \text{(A.35d)}
\end{aligned}$$

The Eqs. (A.34b) and (A.35d) are used to express the Fermi energy and carrier temperature by the carrier density and carrier energy density,

$$\begin{aligned}
T_x &= \frac{U_x}{k_B N_{qw}} \quad , && \text{(A.36a)}\\
E_{f,x} &= ln\left[\frac{N_{qw} \pi L_{qw} \hbar^2}{m_x k_B T_x}\right] k_B T_x \quad . && \text{(A.36b)}
\end{aligned}$$

The expression for the carrier temperature can now be inserted into the rate equation for the carrier energy density. Hereby one obtains a rate equation for the carrier temperature,

$$\begin{aligned}
k_B N_{qw} \frac{dT_x}{dt} &= -k_B T_x \frac{dN_{qw}}{t} - \frac{k_B N_{qw} (T_x - T^L)}{\tau_{h,x}} + \Big(\sigma_x N_{qw} \hbar\omega_0 v_g && \text{(A.37a)}\\
&\quad - E_{x,0} \frac{|d_k|^2 \gamma_2^{-1} \omega_0}{\hbar \epsilon_0 n n_g} (n_c - n_v - N_0)\Big) S(z,t) \quad , \\
\frac{dT_x}{dt} &= -\frac{(T_x - T^L)}{\tau_{h,x}} + \Big(\frac{\sigma_x}{k_B} \hbar\omega_0 v_g && \text{(A.37b)}\\
&\quad + \left(T_x - \frac{E_{\hbar\omega_0,x}}{k_B}\right) \frac{1}{N_{qw}} \frac{|d_k|^2 \gamma_2^{-1} \omega_0}{\hbar \epsilon_0 n n_g} (n_c - n_v - N_0)\Big) S(z,t) \quad .
\end{aligned}$$

This equation is the rate equation for the carrier temperature, which in chapter 2 has been used to describe the material dynamics in the saturable absorber. In the gain sections the Fermi-Dirac distribution function cannot be approximated by the Maxwell-Boltzmann distribution function.

Rate equation for the carrier temperature in the case of a Fermi-Dirac distribution, where the changes in carrier density are relative small. In this case we chose to linearize the carrier energy changes with respect to the changes in carrier density and carrier temperature [13].

$$\Delta U_c = \left.\frac{\partial U_x}{\partial N_{qw}}\right|_{T_L} \Delta N_{qw} + \left.\frac{\partial U_c}{\partial T_c}\right|_{N_{qw}} \Delta T_c \quad . \tag{A.38}$$

The change in carrier density ΔN_{qw} are approximated by the changes resulting from stimulated emissions. The change in carrier density due to the injection current and the life-time are neglected, since these processes were also neglected in the derivation of the rate equation for the carrier energy density. The rate equation for the carrier energy density is

$$\begin{aligned} \frac{dU_x}{dt} &= -\frac{U_x - U_x^L}{\tau_{h,x}} \qquad \text{(A.39)} \\ &+ \left(\sigma_x N_{qw} \hbar\omega_0 v_g - E_{x,0} \frac{|d_k|^2 \gamma_2^{-1} \omega_0}{\hbar \epsilon_0 n n_g} (n_c - n_v - N_0)\right) S(z,t) \quad . \end{aligned}$$

A rate equation for the carrier temperature can be found by combining Eqs. (A.38) and (A.39) [13],

$$\begin{aligned} \frac{dT_c}{dt} &= \left(\frac{dU_c}{dT_c}\right)^{-1} \left(\sigma_c N_{qw} \hbar\omega_0 v_g + \left(\frac{dU_c}{dN_{qw}} - E_{c,0}\right)\right. \qquad \text{(A.40)} \\ &\left.\frac{|d_k|^2 \gamma_2^{-1} \omega_0}{\hbar \epsilon_0 n n_g} (n_c - n_v - N_0)\right) S(z,t) - \frac{T_c - T_L}{\tau_{h,c}} \quad . \end{aligned}$$

Here, the coefficients $\frac{dU_c}{dT_c}$ and $\frac{dU_c}{dN_{qw}}$ are unknown. However, their value can be determined form the definitions of the total carrier density and carrier energy density.

In Ref. [14] we find the following definitions and recurrence formulas for the Fermi-Dirac distribution function:

$$F_j(\eta) = \frac{1}{\Gamma(j+1)} \int_0^\infty \frac{\epsilon^j \, d\epsilon}{1 + exp[\epsilon - \eta]} \quad , \tag{A.41}$$

where $\Gamma(n+1) = n!$, $\epsilon = \frac{E}{k_B T_c}$ and $\eta = \frac{E_{f,c}}{k_B T_c}$. The different F_j functions can be determined by the relation,

$$\frac{d}{d\eta} F_j(\eta) = F_{j-1}(\eta) \tag{A.42}$$

This relation is in the following used to determine dU_c/dN_{qw}.

At quasi Fermi-Dirac equilibrium the carrier density in a QW is

$$N_{qw} = \int_0^\infty \rho(E) f_c(E) dE \quad , \tag{A.43a}$$

$$= \frac{m_c k_B T}{\pi L_{qw} \hbar^2} F_0(\eta) \quad , \tag{A.43b}$$

$$= \frac{m_x k_B T}{\pi L_{qw} \hbar^2} ln \left(1 + exp \left(\frac{E_{f,x}}{k_B T_x} \right) \right) \quad . \tag{A.43c}$$

The corresponding carrier energy density is

$$U_c = \int_0^\infty E \rho(E) f_c(E) dE \quad , \tag{A.44a}$$

$$= \frac{m_c (k_B T)^2}{\pi L_{qw} \hbar^2} F_1(\eta) \quad . \tag{A.44b}$$

The term we would like to calculate is $\frac{dU_c}{dN_{qw}}$, which can be approximated by

$$\frac{dU_c}{dN_{qw}} = \frac{dU_c}{dE_{f,c}} \frac{dE_{f,c}}{dN_{qw}} \quad , \tag{A.45}$$

where the RHS can be evaluated analytically:

$$\frac{\partial U_c}{\partial E_{f,c}} = \frac{m_c k_B T}{\pi L_{qw} \hbar^2} F_0(\eta) \quad , \tag{A.46a}$$

$$= \frac{m_c k_B T_c}{\pi L_{qw} \hbar^2} ln\left(1 + exp\left(\frac{E_{f,c}}{k_B T_c}\right)\right) \quad , \tag{A.46b}$$

$$= N_{qw} \tag{A.46c}$$

$$\frac{\partial E_{f,c}}{\partial N_{qw}} = \frac{\pi L_{qw} \hbar^2}{m_c} \frac{exp\left(\frac{N_{qw} \pi L_{qw} \hbar^2}{m_c k_B T_c}\right)}{exp\left(\frac{N_{qw} \pi L_{qw} \hbar^2}{m_x k_B T_c}\right) - 1} \quad , \tag{A.46d}$$

$$= \frac{\pi L_{qw} \hbar^2}{m_c} \left(1 + exp\left(-\frac{E_{f,c}}{k_B T_x}\right)\right) \quad . \tag{A.46e}$$

The other term we have to evaluate is $\frac{dU_c}{dT_c}$, which expressed by the function $F_j(\eta)$ is

$$\frac{\partial U_x}{\partial T_x} = \frac{2 m_x k_B T}{\pi L_{qw,x} \hbar^2} F_1(\eta) - \frac{m_x E_{f,x} k_B}{\pi L_{qw,x} \hbar^2} F_0(\eta) \tag{A.47}$$

This term cannot be evaluated analytically. Therefore, one has to find the value for $\frac{dU_c}{dT_c}$ numerically. We have done this and found that the approximate value of $\frac{dU_c}{dT_c}$ is 24 J/K in the case of carrier densities $N_{qw} \geq 1.0 \cdot 10^{24} m^{-3}$.

This completes the derivation of a rate equation model for the material dynamics from the semiconductor density matrix formalism.

A.1.2 Rate equations found from density matrix formalism.

In this subsection we summarize the rate equation model derived from the semi-classical density matrix equations. The rate equations for the material dynamics are,

$$\frac{dN_{qw}}{dt} = \frac{I}{eV} - v_g g S(z,t) - \frac{N_{qw}}{\tau_s} \quad , \tag{A.48a}$$

$$\frac{dn_c}{dt} = -\frac{n_c - \overline{n}_c}{\tau_{1,c}} - v_g g S(z,t) \quad , \tag{A.48b}$$

$$\frac{dn_v}{dt} = -\frac{n_v - \overline{n}_v}{\tau_{1,v}} - v_g g S(z,t) \quad , \tag{A.48c}$$

$$\begin{aligned} \frac{dT_c}{dt} &= -\frac{T_c - T_L}{\tau_{h,c}} \\ &+ \left(\frac{dU_c}{dT_c}\right)^{-1} \left[\sigma_c N_{qw} \hbar\omega_0 + \left(\frac{dU_c}{dN_{qw}} - E_{c,0}\right) g\right] v_g S(z,t) \quad , \end{aligned} \tag{A.48d}$$

$$\begin{aligned} \frac{dT_v}{dt} &= -\frac{T_v - T_L}{\tau_{h,v}} \\ &+ \left(\frac{dU_v}{dT_v}\right)^{-1} \left[\sigma_v N_{qw} \hbar\omega_0 + \left(\frac{dU_v}{dN_{qw}} - E_{v,0}\right) g\right] v_g S(z,t) \quad . \end{aligned} \tag{A.48e}$$

Here, v_g is the group velocity (c/n_g), and g is gain,

$$g = a_N(n_c + n_v - N_0) \quad , \tag{A.49a}$$

$$a_N = \frac{|d_k|^2 \gamma_2^{-1} \omega_0}{\hbar\epsilon_0 n c} \quad . \tag{A.49b}$$

The value of the dipole moment can be determined by

$$|d_k|^2 = \frac{e^2}{4m_0\omega_k^2} \left(\frac{m_0}{m_c} - 1\right) \frac{E_g(E_g + \Delta_0)}{E_g + \frac{2\Delta_0}{3}} \quad , \tag{A.50}$$

where the parameter values typically used for the CPM laser are given in table A.1. We have fitted the gain spectra in the saturable absorber according to many-body gain calculations A.3. To obtain a good agreement between the calculated spectra and the fitting function we had to multiply the value of $|d_k|^2$ by a factor 1.15. Due to the uncertainties in the determination of the dipole moment, and since we have not included the effect of Coulomb enhancement which could explain the factor of 1.15 in our model, we have throughout this Thesis used the value of $|d_k|^2$ given by equation A.50 multiplied by 1.15 for both the gain and absorber gain spectra calculations.

The rate equations in the case of a low density saturable absorber, where the carrier density is assumed small has a slightly different temperature equation, since we the Fermi-Dirac distribution function can be approximated by a Maxwell-Boltzmann distribution. The rate equations for the carrier

Symbol	Name	Value
E_g	Bandgap energy	0.75 eV
λ_0	Wavelength	1.55 μm
Δ_0	Spin-orbit splitting	0.33 eV
m_0	Electron mass	$9.1095 \cdot 10^{-31} kg$
m_c	Effective electron mass	0.041 m_0
m_v	Effective hole mass	0.460 m_0
e	Electron charge	$1.602 \cdot 10^{-19}$ C
n	Refractive index	3.40

Table A.1: Typical parameter values.

temperature in the saturable absorber is

$$\begin{aligned}
\frac{dT_c}{dt} &= -\frac{T_c - T_L}{\tau_{h,c}} + \frac{\sigma_c}{k_B}\hbar\omega_0 v_g S(z,t) && \text{(A.51a)} \\
&+ \left[(T_c - E_{c,0}k_B)\frac{g}{N_{qw}}\right] v_g S(z,t) \quad , \\
\frac{dT_v}{dt} &= -\frac{T_v - T_L}{\tau_{h,v}} + \frac{\sigma_v}{k_B}\hbar\omega_0 v_g S(z,t) && \text{(A.51b)} \\
&+ \left[(T_v - E_{v,0}k_B)\frac{g}{N_{qw}}\right] v_g S(z,t) \quad .
\end{aligned}$$

So far we have considered a two level gain model, where the carrier injection is directly into the QW's. The drift/diffusion from the contact layers to the QW's is not taken into account by the rate equations in Eq. (A.48). In the next section we show how the effect of drift/diffusion through the separate confinement region can be taken into account by an additional rate equation.

A.2 Carrier transport rate equation

Quantum well semiconductor lasers modulation properties depend strongly on the carrier transport from the contact layers to the quantum well. The process of carrier transport through the separate confinement structure [10] and the carrier capture process have to be taken into account to understand the modulation properties of QW semiconductor lasers [10, 15, 16, 17]. The derived rate equation model in section A.1 is a detailed model for a two-level system. In this appendix we will present a phenomenological rate equation describing the carrier transport through the separate confinement region, which previously has been used in [16, 17] to describe the modulation properties of multiple QW semiconductor lasers.

A.2.1 Rate equation for separate confinement region

The transport through the separate confinement region is described by a phenomenological rate equation model, which is taken from [16, 17]. The effect of carrier capture, which is included in Refs. [16, 17] is not taken into account here. We do not include the effect of carrier capture, since carrier capture is a complicated process, which needs a detailed modelling to be taken appropriate into account. Furthermore, we do not want to have a to complicated model for the material dynamics.

Our rate equation model for the conduction band is with the phenomenological rate equation for the separate confinement region:

$$\frac{dN_d}{dt} = \frac{I}{eA_{vol}L_d} - \frac{M_{qw}L_{qw}}{L_d}\frac{\eta_d N_d - N_{qw}}{\tau_d} - \frac{N_d}{\tau_{s_d}} \quad , \tag{A.52a}$$

$$\frac{dN_{qw}}{dt} = \frac{\eta_d N_d - N_{qw}}{\tau_d} - v_g g S(z,t) - \frac{N_{qw}}{\tau_{s_{qw}}} \quad , \tag{A.52b}$$

$$\frac{dn_c}{dt} = -\frac{n_c - \overline{n}_c}{\tau_{1,c}} - v_g g S(z,t) \quad , \tag{A.52c}$$

$$
\begin{aligned}
\frac{dT_c}{dt} &= -\frac{T_c - T_L}{\tau_{h,c}} \\
&\quad + \left(\frac{dU_c}{dT_c}\right)^{-1} \left[\sigma_c N_{qw} \hbar\omega_0 + \left(\frac{dU_c}{dN_{qw}} - E_{c,0}\right) g\right] v_g S(z,t) \quad .
\end{aligned} \tag{A.52d}
$$

The rate equation for the valence band is similar. The parameters introduced in the rate equation for the separate confinement region are: L_d, width of the separate confinement region; $A_{vol} L_d$, volume of the separate confinement region; τ_d, drift/diffusion time through the separate confinement region; M_{qw}, number of quantum well's; τ_{s_d}, lifetime of the carriers in the separate confinement region; η_d, ratio between the carrier density in the reservoir (N_d) and in the quantum wells (N_{qw}) at thermal equilibrium:

$$
\eta_d = \frac{N_{qw}^{eq}}{N_d^{eq}} = \frac{L_d}{M_{qw} L_{qw}} \frac{\hat{N}_{qw}^{eq}}{\hat{N}_d^{eq}} \quad , \tag{A.53}
$$

where $\hat{N}_{qw}$a and $\hat{N}_d$ are carrier numbers.

A.3 Reverse biased semiconductor QW

The gain spectra and the changes in the refractive index have been calculated by Krister Fröjdh for different reverse biases and for variable (low) carrier densities [10]. The calculations incorporate the different layers of the semiconductor e.g. quantum wells, barriers etc. The many-body calculations are made for semiconductor waveguides identical to those employed in the CPM lasers fabricated at at Tele Danmark R & D [18, 19, 20], (see also section 2.3). The method used by K. Fröjdh is explained in greater detail in Ref. [10].

In order to treat the case of a reverse bias within our model we allow the bandgap energy and the differential gain to depend on the reverse bias, and fit these variations to get a good agreement with the spectra calculated by the method presented in Ref. [10].

The change in refractive index is approximated by a function, which fits the many-body theory calculations very well.

A.3.1 The fitted refractive index and gain spectra of the saturable absorber for varying reverse bias

In this section we will present the modification of the gain and refractive index spectra resulting from applying an external reverse bias on a QW semiconductor waveguide. We will first present the modification of the bandgap energy due to the Quantum Confined Stark Effect (QCSE) and change in carrier density:

$$\begin{aligned}\Delta E_g &= +24.7meV \cdot \frac{N_{qw}}{1 \cdot 10^{24} m^{-3}} + (E_{g,ref} - 4.3meV) \\ &\quad -2.4meV \cdot \left(tanh \left(6.6 \frac{N_{qw} - 0.7 \cdot 10^{24} m^{-3}}{1 \cdot 10^{24} m^{-3}} \right) - 1 \right) \cdot \frac{V_{abs}}{1V} \\ &\quad -17.5meV \cdot \left(\frac{N_{qw}}{1 \cdot 10^{24} m^{-3}} \right)^2 \quad ,\end{aligned} \tag{A.54}$$

where the third term on the right hand-side accounts for the change in bandgap energy due to the external field. The other terms account for the bandgap dependence upon changing carrier density. $E_{g,ref}$ is a reference bandgap energy, such that the effect of bandgap shrinkage in the gain sections [21] can be taken into account in Eq. (A.54).

The many-body theory calculations made by K. Fröjdh show that the maximum differential gain in our derived rate equation model should depend weakly on the applied reverse bias and carrier density to obtain a good fit of the calculated main-body gain spectra.

$$a_N = a_{N,ref} \cdot \left(1.0 - 0.05 \cdot tanh \left(5 \frac{N_{qw} - 0.4 \cdot 10^{24} m^{-3}}{1 \cdot 10^{24} m^{-3}} \right) \cdot \frac{V_{abs}}{1V} \right) \quad , \tag{A.55}$$

where $a_{N,ref}$ is the maximum differential gain defined by Eq. (A.48). The maximum differential gain decreases thus slightly for increasing reverse bias.

The change in refractive index as a function of reverse bias and different carrier densities in the quantum well have been fitted by an appropriate function, which yields

$$\begin{aligned}
\Delta n &= c_e tanh(c_{d,th}(\hbar\omega_o - c_{b,th})) && \text{(A.56a)}\\
&\quad \times sech^2(c_{d,sh}(\hbar\omega_0 - c_{b,sh})) \quad , &&\\
c_e &= (0.0236V_{abs}^2 - 0.0253V_{abs} - 0.0372)N_{qw}^2 && \text{(A.56b)}\\
&\quad +(-0.0336V_{abs}^2 + 0.0298V_{abs} + 0.1130)N_{qw} &&\\
&\quad +(0.0099V_{abs}^2 - 0.0027V_{abs} + 0.0473) \quad , &&\\
c_{d,th} &= (-73.6915V_{abs}^2 - 81.5364V_{abs} + 118.2515)N_{qw}^2 && \text{(A.56c)}\\
&\quad +(114.8810V_{abs}^2 + 103.1500V_{abs} - 321.3437)N_{qw} &&\\
&\quad +(-42.4236V_{abs}^2 - 22.5849V_{abs} + 292.9468) \quad , &&\\
c_{d,sh} &= (19.8439V_{abs}^2 - 60.3754V_{abs} + 91.4131)N_{qw}^2 && \text{(A.56d)}\\
&\quad +(-28.2869V_{abs}^2 + 83.5414V_{abs} - 119.5204)N_{qw} &&\\
&\quad +(8.5475V_{abs}^2 - 24.2069V_{abs} + 77.0356) \quad , &&\\
c_{b,th} &= (0.0011V_{abs}^2 - 0.0025V_{abs} + 0.0024)N_{qw}^2 && \text{(A.56e)}\\
&\quad +(-0.0022V_{abs}^2 + 0.0037V_{abs} + 0.0029)N_{qw} &&\\
&\quad +(0.0011V_{abs}^2 - 0.0012V_{abs} + E_{g,ref} + 0.0459) \quad , &&\\
c_{b,sh} &= (0.0017V_{abs}^2 + 0.0045V_{abs} + 0.0075)N_{qw}^2 && \text{(A.56f)}\\
&\quad +(-0.0025V_{abs}^2 - 0.0080V_{abs} - 0.0086)N_{qw} &&\\
&\quad +(0.0008V_{abs}^2 + 0.0038V_{abs} + E_{g,ref} + 0.0437) \quad . &&
\end{aligned}$$

Here, V_{abs} and N_{qw} are measured in units of volts and m^{-3}, respectively. Eq. (A.56) is only a good approximation of the change in the refractive index Δn as long as the carrier density N_{qw} is less than $1.0 \cdot 10^{24} m^{-3}$ and the reverse bias is kept within the range of -2.0 V and 0.4 V. Furthermore, the refractive index spectra are only valid for energies close to the bandedge, e.g. for $E_{g,ref} = 0.75eV$ the photon energy has to be kept between 0.76 eV - 0.82eV. Gain and refractive index spectra for a reference bandgap energy $E_{g,ref} = 0.75$ eV are shown in Figs. A.4 and A.5 for reverse biases of 0.0 V and -2.0 V, respectively.

A.4 Gain and material dispersion

In this section we discuss how the gain and and index dispersion are included in the wave-propagation equation. Furthermore, we calculate the gain dispersion coefficients for the case, where the carrier distribution is described by a quasi Fermi-Dirac distribution.

A.4.1 The dispersion terms in the wave-propagation equation.

The wave-propagation equation for the slowly varying electrical field envelope function in a semiconductor waveguide can be derived from Maxwells equations [2, 21, 22].

$$\begin{aligned}\pm\frac{\partial\mathcal{A}^{\pm}(z,t)}{\partial z} &= -\left(\frac{1}{v_g}+i\frac{\Gamma}{2}\left.\frac{\partial g}{\partial\omega}\right|_{\omega_0}\right)\frac{\partial\mathcal{A}^{\pm}(z,t)}{\partial t} \\ &+\left(\frac{i}{2}\beta_2-\frac{\Gamma}{4}\left.\frac{\partial^2 g}{\partial\omega^2}\right|_{\omega_0}\right)\frac{\partial^2\mathcal{A}^{\pm}(z,t)}{\partial t^2} \\ &+\frac{1}{2}\left(g_{\omega_0}-\alpha_{int}-i\Delta k\right)\mathcal{A}^{\pm}(z,t), \quad ,\end{aligned} \tag{A.57}$$

where $\mathcal{A}$ is the complex slowly varying complex electrical field amplitude. The constant v_g is the group velocity, Γ is the optical field confinement factor and α_{int} is the internal losses. β_2 derives from the Group Velocity Dispersion (GVD) and $\left.\frac{\partial g}{\partial\omega}\right|_{\omega_0}$ and $\left.\frac{\partial^2 g}{\partial\omega^2}\right|_{\omega_0}$ describe gain dispersion at the optical carrier frequency ω_0. The second derivatives of the electrical field are estimated by the previous time step in our numerical scheme. But before we discuss how the dispersion terms are taken into account we will express the complex field amplitude by a real field amplitude A and a phase factor Φ:

$$\mathcal{A}^{\pm}(z,t) = A^{\pm}(z,t)e^{i\Phi^{\pm}(z,t)} \quad . \tag{A.58}$$

Thus, the space and time derivatives of the complex field amplitude are,

$$\frac{\partial \mathcal{A}^\pm}{\partial t} = \left[\frac{\partial A^\pm}{\partial t} + i\frac{\partial \Phi^\pm}{\partial t}A^\pm\right] exp[i\Phi^\pm] \quad , \tag{A.59a}$$

$$\frac{\partial \mathcal{A}^\pm}{\partial z} = \left[\frac{\partial A^\pm}{\partial z} + i\frac{\partial \Phi^\pm}{\partial z}A^\pm\right] exp[i\Phi^\pm] \quad , \tag{A.59b}$$

$$\begin{aligned}\frac{\partial^2 \mathcal{A}^\pm}{\partial t^2} = &\left[\frac{\partial^2 A^\pm}{\partial t^2} + i\frac{\partial^2 \Phi^\pm}{\partial t^2}A^\pm\right.\\ &\left.+2i\frac{\partial \Phi^\pm}{\partial t}\frac{\partial A^\pm}{\partial t} - \left(\frac{\partial \Phi^\pm}{\partial t}\right)^2 A^\pm\right] exp[i\Phi^\pm] \quad .\end{aligned} \tag{A.59c}$$

Eqs. (A.58) and (A.59) are now inserted into the wave-propagation equation, which becomes

$$\begin{aligned}+\frac{1}{v_g}\frac{\partial A^\pm}{\partial t} = &\mp\frac{\partial A^\pm}{\partial z} + \frac{\Gamma}{2}\left.\frac{\partial g}{\partial \omega}\right|_{\omega_0} A^\pm \frac{\partial \Phi^\pm}{\partial t}\\ &+\frac{1}{2}(\Gamma g_{\omega_0} - \alpha_{int})A^\pm + \frac{\Gamma}{4}\left.\frac{\partial^2 g}{\partial \omega^2}\right|_{\omega_0}\left(\left(\frac{\partial \phi^\pm}{\partial t}\right)^2 A^\pm - \frac{\partial^2 A^\pm}{\partial t^2}\right)\\ &-\frac{\beta_2}{2}\left(\frac{\partial^2 \phi^\pm}{\partial t^2}A^\pm + 2\frac{\partial \phi^\pm}{\partial t}\frac{\partial A^\pm}{\partial t}\right) \quad ,\end{aligned} \tag{A.60a}$$

$$\begin{aligned}+\frac{1}{v_g}\frac{\partial \Phi^\pm}{\partial t} = &\mp\frac{\partial \Phi^\pm}{\partial z} - \Gamma\Delta k - \frac{\Gamma}{2}\left.\frac{\partial g}{\partial \omega}\right|_{\omega_0}\frac{1}{A^\pm}\frac{\partial A^\pm}{\partial t}\\ &-\frac{\Gamma}{4}\left.\frac{\partial^2 g}{\partial \omega^2}\right|_{\omega_0}\left(\frac{\partial^2 \phi}{\partial t^2} + \frac{2}{A^\pm}\frac{\partial \phi^\pm}{\partial t}\frac{\partial A^\pm}{\partial t}\right)\\ &-\frac{\beta_2}{2}\left(\left(\frac{\partial \phi}{\partial t}\right)^2 - \frac{1}{A^\pm}\frac{\partial^2 A^\pm}{\partial t^2}\right) \quad .\end{aligned} \tag{A.60b}$$

The effect of the dispersion coefficients for the pulse-widthes considered are very small and we have therefore first estimated the first order time derivatives without the inclusion of the dispersion terms. Thereafter, we have used the first order time derivatives to calculate a correction term resulting from the dispersion:

$$\frac{\partial \Phi^{\pm,0}}{\partial t} = \mp v_g\frac{\partial \Phi^\pm}{\partial z} \approx (\omega - \omega_0) \quad , \tag{A.61a}$$

$$\frac{\partial A^{\pm,0}}{\partial t} = \mp v_g \frac{\partial A^{\pm}}{\partial z} + \frac{v_g}{2}\left(\Gamma g(\omega) - \alpha_{int}\right) A^{\pm} \quad , \tag{A.61b}$$

where we have assumed that the instantaneous wavelength is approximately constant for a very small propagation distance. Furthermore, we have replaced the Taylor expansion of the gain g with respect to the optical carrier frequency with the frequency dependent gain,

$$g_{\omega_0} + \left.\frac{\partial g}{\partial \omega}\right|_{\omega_0} (\omega - \omega_0) + \frac{1}{2}\left.\frac{\partial^2 g}{\partial \omega^2}\right|_{\omega_0} (\omega - \omega_0)^2 \approx g(\omega) \quad . \tag{A.62}$$

The first order approximation of the time derivatives is than used as a correction term to include the effect of gain and index dispersion,

$$\begin{aligned}
\frac{\partial A^{\pm}}{\partial t} &= \frac{\partial A^{\pm,0}}{\partial t} - v_g \frac{\Gamma}{4}\frac{\partial^2 g}{\partial \omega^2}\left(\frac{\frac{\partial A^{\pm,0}(t)}{\partial t} - \frac{\partial A^{\pm}(t-\Delta t)}{\partial t}}{\Delta t}\right) && \text{(A.63a)} \\
&\quad - v_g \frac{\beta_2}{2}\left(\frac{\frac{\partial \Phi^{\pm,0}(t)}{\partial t} - \frac{\partial \Phi^{\pm}(t-\Delta t)}{\partial t}}{\Delta t} + 2\frac{\partial A^{\pm,0}}{\partial t}\frac{\partial \Phi^{\pm,0}}{\partial t}\right) \quad , \\
\frac{\partial \Phi^{\pm}}{\partial t} &= \frac{\partial \Phi^{\pm,0}}{\partial t} - v_g \Gamma \Delta k - v_g \frac{\Gamma}{2}\frac{\partial g}{\partial \omega}\frac{1}{A^{\pm}}\frac{\partial A^{\pm,0}}{\partial t} && \text{(A.63b)} \\
&\quad + v_g \frac{\Gamma}{4}\frac{\partial^2 g}{\partial \omega^2}\left(\frac{\frac{\partial \Phi^{\pm,0}(t)}{\partial t} - \frac{\partial \Phi^{\pm}(t-\Delta t)}{\partial t}}{\Delta t} + \frac{2}{A^{\pm}}\frac{\partial \phi^{\pm,0}}{\partial t}\frac{\partial A^{\pm,0}}{\partial t}\right) \\
&\quad - v_g \frac{\beta_2}{2}\left(\left(\frac{\partial \Phi^{\pm,0}}{\partial t}\right)^2 - \frac{1}{A^{\pm}}\frac{\frac{\partial A^{\pm,0}(t)}{\partial t} - \frac{\partial A^{\pm}(t-\Delta t)}{\partial t}}{\Delta t}\right) \quad .
\end{aligned}$$

The above approximated method for including both the gain and index dispersion has been implemented and the numerical solution for a Gaussian pulse has been compared with analytical calculations. It is found that the numerical solution differs from the analytical results by less than 1.8 % for the time-steps (Δt) usually used in the CPM laser simulations. This is a satisfactory result compared to the other approximations made in our model.

A.4.2 Gain spectra and gain dispersion coefficients

The rate equation model describing the material dynamics are derived with the assumption of a "hat" line-shape function. Here, we will justify that the "hat" line-shape function (Eq. (A.19)) may be replaced by a Lorentzian (Eq. (A.18)) or even better a hyperbolic secant line-shape function $L_{sech}(\omega_k)$,

$$L_{sech}(\omega_k) = \gamma_2^{-1} sech\left(\frac{\omega_0 - \omega_k}{\gamma_2}\right) \quad . \tag{A.64}$$

The "hat", Lorentzian and hyperbolic secant line-shape function are for comparison plotted in Fig. A.2. The area below each line-shape function

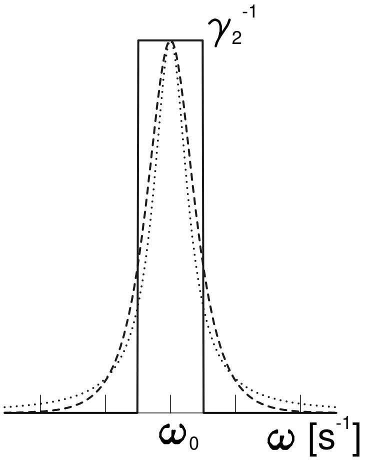

Figure A.2: Plot of the "hat' (—), Lorentzian (···) and hyperbolic secant line-shape function (- - -).

is π. The corresponding gain spectra for a carrier density of $N_{qw} = 1.4 \cdot 10^{24} m^{-3}$ and of $N_{qw} = 0.4 \cdot 10^{24} m^{-3}$ are plotted in Figs. A.3.a and A.3.b, respectively. The solid line in Fig. A.3 is the gain curve, calculated with a "hat" line-shape function. The gain curve for the "hat" line-shape function has two "cracks", which will result in a discontinuity in the first derivative of the gain with respect to the optical carrier frequency. Therefore, we want to

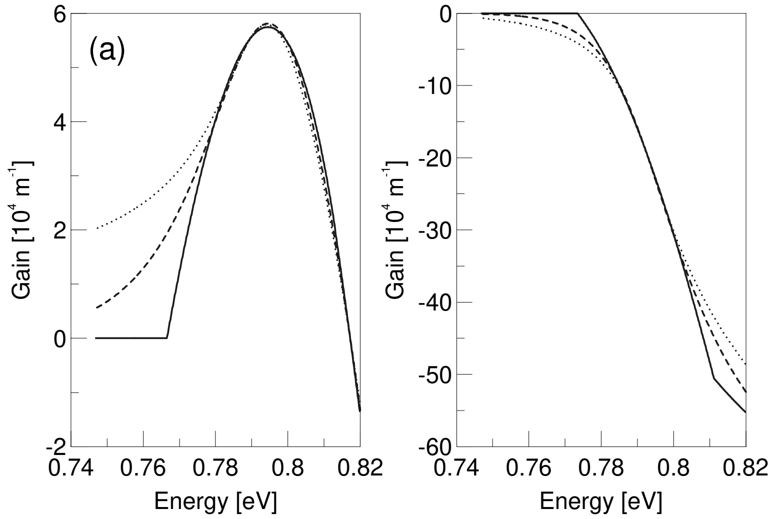

Figure A.3: Gain spectra for a "hat" (—), Lorentzian (···) and a hyperbolic secant (- - -) line-shape function. The total carrier density is in figure (a) $N_{qw} = 1.4 \cdot 10^{24} m^{-3}$ and in figure (b) $N_{qw} = 0.4 \cdot 10^{24} m^{-3}, V_{bias} = 0.0V$.

replace the "hat" line-shape function with a Lorentzian line-shape function, since than both the first and second derivative of the gain with respect to the optical carrier frequency will be continuous functions. However, for a Lorentzian line-shape function one overestimates the effect of homogeneous broadening and as seen in Fig. A.3 this leads to some absorption below the bandgap [2]. More realistic gain spectra are obtained by using a hyperbolic secant line-shape, which does not result in the long absorption tails below the bandgap [2].
So, in our large signal model of the CPM laser we have used a hyperbolic secant line-shape function to calculate the carrier density N_0. Furthermore, the use of a hyperbolic line-shape function enables us to calculate the gain dispersion coefficients as shown in the following.

The carrier density N_0, when we assume a hyperbolic line-shape function, yields

$$N_0 = \int_0^\infty \frac{m_r}{\pi\hbar^2 L_{qw}} sech\left(\frac{E - E_{c,0} + E_{v,0}}{\hbar\gamma_2}\right) dE \quad , \tag{A.65a}$$

$$= \frac{2m_r\gamma_2}{\pi L_{qw}\hbar}\left[\frac{\pi}{2} - ArcTan\left(\exp\left(-\frac{E_{c,0} + E_{v,0}}{\hbar\gamma_2}\right)\right)\right] . \tag{A.65b}$$

The energies $E_{c,0}$ and $E_{v,0}$ are the photon energy measured with respect to the band edge (see also Eq. (A.26)),

$$E_{c,0} = \frac{m_v}{m_v + m_c}(\hbar\omega_k - E_g - E_c - E_v) \quad , \tag{A.66a}$$

$$E_{v,0} = \frac{m_c}{m_v + m_c}(\hbar\omega_k - E_g - E_c - E_v) \quad , \tag{A.66b}$$

$$F_c = \frac{1}{1 + \exp\left(\frac{E_{c,0} - E_{f,c}}{k_B T_L}\right)} \quad , \tag{A.66c}$$

$$F_v = \frac{1}{1 + \exp\left(\frac{E_{v,0} - E_{f,v}}{k_B T_L}\right)} \quad . \tag{A.66d}$$

Thus, the first derivative of the gain g with respect to the optical carrier frequency ω_k yields

$$\frac{\partial g}{\partial\omega_k} = a_N\left(\frac{\partial N_0}{\partial\omega_k}(F_c + F_v - 1) + N_0\left(\frac{\partial F_c}{\partial\omega_k} + \frac{\partial F_v}{\partial\omega_k}\right)\right) , \tag{A.67a}$$

$$\frac{\partial N_0}{\partial\omega_k} = \frac{m_r}{\pi L_{qw}\hbar} sech\left(\frac{E_{v,0} + E_{c,0}}{\hbar\gamma_2}\right) \quad , \tag{A.67b}$$

$$\frac{\partial F_c}{\partial\omega_k} = -\frac{m_v}{m_c + m_v}\frac{\frac{\hbar}{k_B T_L} exp\left(\frac{E_{c,0} - E_{f,c}}{k_B T_L}\right)}{\left(1 + exp\left(\frac{E_{c,0} - E_{f,c}}{k_B T_L}\right)\right)^2} \quad , \tag{A.67c}$$

$$\frac{\partial F_v}{\partial\omega_k} = -\frac{m_c}{m_c + m_v}\frac{\frac{\hbar}{k_B T_L} exp\left(\frac{E_{v,0} - E_{f,v}}{k_B T_L}\right)}{\left(1 + exp\left(\frac{E_{v,0} - E_{f,v}}{k_B T_L}\right)\right)^2} \quad . \tag{A.67d}$$

The second derivative of the gain g with respect to the optical carrier frequency ω_k yields,

$$\frac{\partial g^2}{\partial\omega_k^2} = a_N\left[\frac{\partial^2 N_0}{\partial\omega_k^2}(F_c + F_v - 1) + 2\frac{\partial N_0}{\partial\omega_k}\left(\frac{\partial F_c}{\partial\omega_k} + \frac{\partial F_v}{\partial\omega_k}\right)\right. \tag{A.68a}$$

$$
\begin{aligned}
& +N_0\left(\frac{\partial^2 F_c}{\partial \omega_k^2}+\frac{\partial^2 F_v}{\partial \omega_k^2}\right)\Bigg] \quad , \\
\frac{\partial^2 N_0}{\partial \omega_k^2} &= -\frac{m_r}{\pi L_{qw}\hbar\gamma_2} tanh\left(\frac{E_{v,0}+E_{c,0}}{\hbar\gamma_2}\right) sech\left(\frac{E_{v,0}+E_{c,0}}{\hbar\gamma_2}\right) \qquad \text{(A.68b)} \\
\frac{\partial F_c^2}{\partial \omega_k^2} &= -\left(\frac{m_v}{m_c+m_v}\frac{\hbar}{k_B T_L}\right)^2 \qquad \text{(A.68c)} \\
& \times\frac{exp\left(\frac{E_{c,0}-E_{f,c}}{k_B T_L}\right)\left(1-exp\left(\frac{E_{c,0}-E_{f,c}}{k_B T_L}\right)\right)}{\left(1+exp\left(\frac{E_{c,0}-E_{f,c}}{k_B T_L}\right)\right)^3} \quad , \\
\frac{\partial F_v^2}{\partial \omega_k^2} &= -\left(\frac{m_c}{m_c+m_v}\frac{\hbar}{k_B T_L}\right)^2 \qquad \text{(A.68d)} \\
& \times\frac{exp\left(\frac{E_{v,0}-E_{f,v}}{k_B T_L}\right)\left(1-exp\left(\frac{E_{v,0}-E_{f,v}}{k_B T_L}\right)\right)}{\left(1+exp\left(\frac{E_{v,0}-E_{f,v}}{k_B T_L}\right)\right)^3} \quad .
\end{aligned}
$$

The resulting gain spectra and the values of the corresponding gain dispersion terms are shown in Figs. A.4 and A.5. The gain and its derivatives with respect to the optical carrier frequency are for low carrier densities calculated for a reverse bias of 0.0 V and -2.0 V in Figs. A.4 and A.5, respectively.

Figs. A.4.a and A.5.a display the calculated gain spectra, the derivative $dg/d\omega_k$ is shown in Figs. A.4.c and A.5.c and the derivative $d^2g/d\omega_k^2$ is shown in Figs. A.4.d and A.5.d. In Figs. A.4.b and A.5.b the change in the refractive index is shown for the case of an external reverse bias of 0.0 V and -2.0 V, respectively. The change in refractive index is calculated by the use of Eq. (A.56).

The above derivatives of the gain with respect of the optical carrier frequency are justified for not too large deviations from a Fermi-Dirac distribution, which is a good approximation in the case of the studied CPM laser.

The analytical expressions for both gain and its derivatives enable us to adjust the optical carrier frequency ω_0 dynamically in our large signal model.

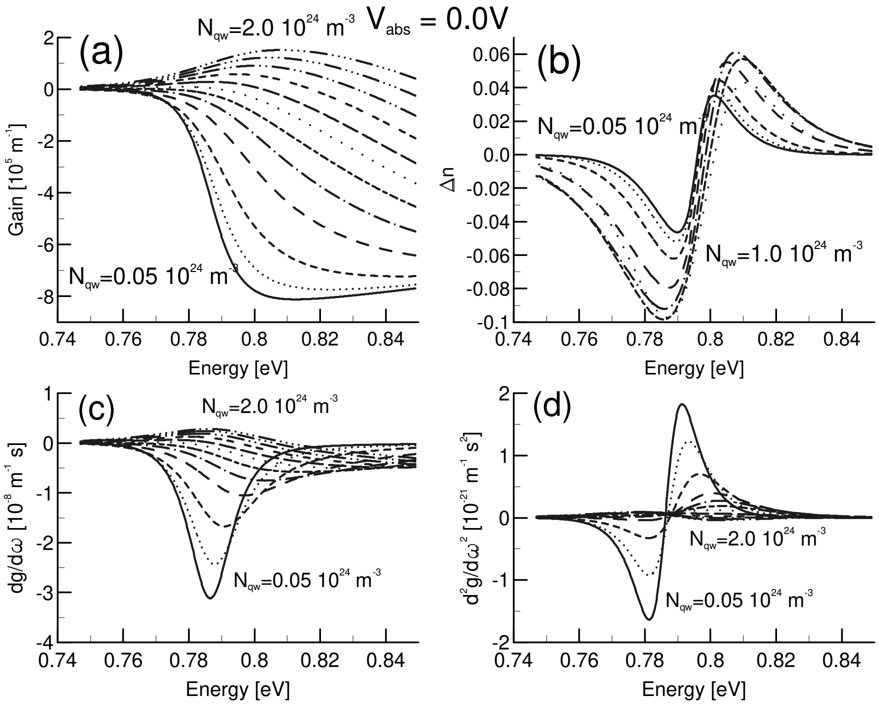

Figure A.4: Gain spectra as a function of wavelength. $N_{qw} = 0.05 \cdot 10^{24} m^{-3}$ (solid), $0.1 \cdot 10^{24} m^{-3}$ (....), $0.2 \cdot 10^{24} m^{-3}$ (- - - -), $0.4 \cdot 10^{24} m^{-3}$ (– –), and the last curve is $2.0 \cdot 10^{24} m^{-3}$ (-....-). The curves are calculated with a hyperbolic secant line-shape function.

The optical carrier frequency is thus updated after each round-trip. The CPM pulse amplitude is used to weighten the instantaneous frequency of the pulse such that the optical carrier frequency ω_0 corresponds to the center frequency of the CPM pulses.

We find in our numerical simulations of the CPM laser that the CPM pulse center wavelength always is shifted by a small value to the low energy side (lower optical carrier frequency) compared to the gain peak. The normally made assumption that $dg/d\omega$ is zero is thus not true. Actually we found that

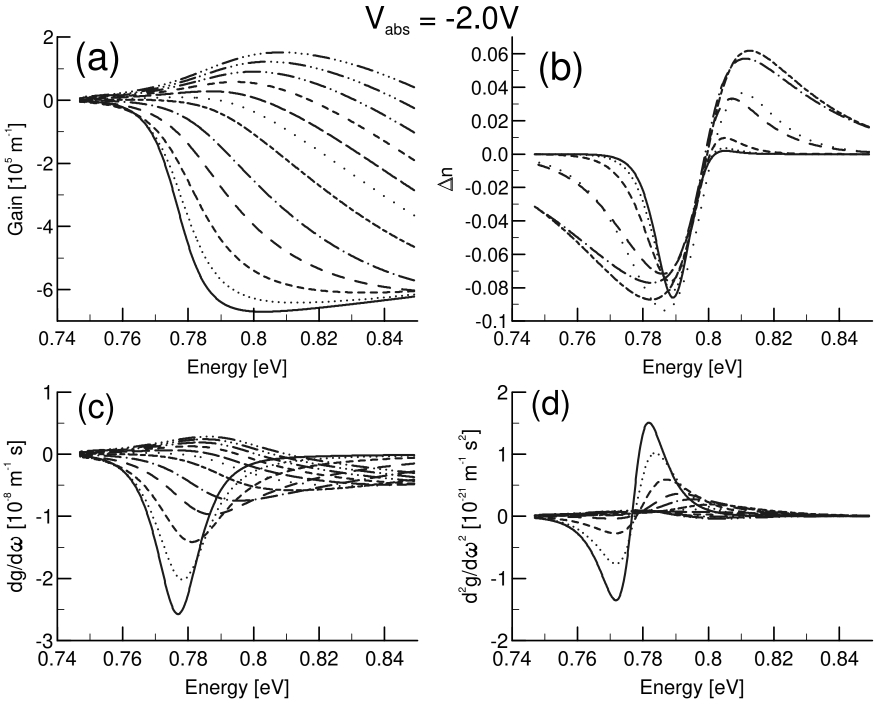

Figure A.5: Gain spectra as a function of wavelength. $N_{qw} = 0.05 \cdot 10^{24} m^{-3}$ (solid), $0.1 \cdot 10^{24} m^{-3}$ (....), $0.2 \cdot 10^{24} m^{-3}$ (- - - -), $0.4 \cdot 10^{24} m^{-3}$ (– –), and the last curve is $2.0 \cdot 10^{24} m^{-3}$ (-....-). The curves are calculated with a hyperbolic secant line-shape function.

the influence of the gain dispersion term $dg/d\omega$ on the CPM pulses is much more significant than the influence of the gain dispersion term $d^2g/d\omega^2$ [23]. However, it should be noted that the gain dispersion terms only result in minor changes in the pulse width and shape [23].

Bibliography

[1] H. Haug, S. W. Koch, "Quantum Theory of the Optical and Electronic Properties of Semiconductors" World Scientific, Singapore, 1993.
[2] W. W. Chow, S. W. Koch, M. Sargent III, "Semiconductor-Laser Physics", Springer-Verlag, New York, 1994.
[3] J. Mark and J. Mørk, "Subpicosecond gain Dynamics in InGaAsP Optical Amplifiers: Experiment and Theory", Appl. Phys. Lett. **61**, (19) pp. 2281-2283, 1992.
[4] J. Mørk, M. Willatzten, J. Mark, M. Svendsen, C. P. Seltzer, "Characterization and Modelling of Ultrafast Carrier Dynamics in Quantum Well Optical Amplifiers", SPIE'94, Physics and Simulation of Optoelectronic Devices II, **2146**, Los Angeles, January 1994.
[5] M. Willatzen, J. Mark, J. Mørk, and J. P. Seltzer, "Carrier Temperature and Spectral Holeburning dynamics in InGaAsP Quantum Well Laser Amplifiers", Appl. Phys. Lett. **64**, (2) pp. 143-145, 1994.
[6] S. D. Brorson, S. Bischoff, J. Mørk, A. Møller-Larsen, J. M. Nielsen, "Femtosecond Carrier Dynamics and Modelocking in Monolithic CPM Lasers", IEEE Photon. Technol. Lett., **8** (10), 1996.
[7] A. Yariv, "Quantum Electronics", John Wiley & Sons, New York, 1989.
[8] M. Willatzen, "Theory of Gain in Bulk and Quantum-Well Semiconductor Lasers", Doctoral Thesis, Niels Bohr Institute, Ørsted Laboratory, Univeristy of Copenhagen, Denmark, 1993.
[9] A. Uskov, J. Mørk, J. Mark, "Wave Mixing in Semiconductor Laser Amplifiers Due to Carrier Heating and Spectral-Hole Burning", IEEE Jour. Quantum Elec. **30** (8) pp. 1769-1781, 1994.
[10] K. Fröjdh, "Carrier transport effects in semiconductor heterostruc-

tures for optical applications", Doctoral Thesis, Royal Inst. of Technol., Stockholm, Sweden, 1996.

[11] J. Mørk, J. Mark, C. P. Seltzer, "Carrier Heating in InGaAsP Laser Amplifiers Due to Two-Photon Absorption", Appl. Phys. Lett., **64** (17), 1994.

[12] N. Peyghambarian, S. W. Koch, A. Mysyrowicz, "Introduction to Semiconductor Optics", Prentic Hall, New Jersey, 1993.

[13] A. Uskov, J. Mørk, J. Mark, "Theory of Short-Pulse Gain Saturation in Semiconductor Laser Amplifiers", IEEE Photon. Technol. Lett., **4** (5), 1992.

[14] J. S. Blakemore, "Solid State Physcis", W. B. Saunders Company, 1962.

[15] P. S. Zory, Jr., "Quantum Well Lasers", Academic Press, INC., New York, 1993.

[16] N. Tessler, R. Nagar, G. Eisenstein, "Structure Dependent Modulation Response in Quantum-Well Lasers", IEEE Jour. Quantum Electron., **28** (10), pp. 2242-2250, 1992.

[17] N. Tessler, G. Eisenstein, "On Carrier Injection and Gain Dynamics in Quantum Well Lasers", IEEE Jour. Quantum Electron., **29** (6), pp. 1586-1595, 1993.

[18] Z. Wang, J. M. Nielsen, S. D. Brorson, B. Christensen, T. Franck, N. G. Jensen, A. M. Larsen, J. Nørregaard, E. Bødtker, "15.8 Gbit/s System Transmission Experiment using a 5.2 mm Long Monolithic Colliding-Pulse Modelocked Quantum Well Laser Diode", Electron. Lett. **31** pp.272, 1995.

[19] S. D. Brorson, T. Franck, S. Bischoff, L. Prip, M. Hofmann, J. M. Nielsen, J. Mørk, "Pulsewidth Dependence upon Gain Current and Absorber Voltage in Monolithic CPM Lasers", Submitted to IEEE Photon. Technol. Lett.

[20] T. Franck, S. D. Brorson, A. Møller-Larsen, J. M. Nielsen, and J. Mørk, "Synchronization phase diagrams of monolithic colliding pulse modelocked lasers", IEEE Photon. Tech. Lett., **8**, pp. 40-42, 1996.

[21] G. P. Agrawal, N. K. Dutta, "Semiconductor Lasers", Van Nostrand Reinhold, New York, 1993.

[22] H. E. Lassen, "Modelling and Experimental Characterization of Dynamical Properties of Semiconductor Optical Amplifiers", Doctoral Thesis, Electromagnetic Institute, The Technical University of Denmark, LD 79, April 1990.

[23] S. Bischoff, S. D. Brorson, T. Franck, M. Hofmann, L. Prip, M. P.

Sørensen, J. Mørk, "Modelling and Characterization of Colliding Pulse Mode-Locked (CPM) Quantum Well Lasers", SPIE'96, Physics and Simulation of Optoelectronics Devices IV, **2693**, pp. 477-488, San Jose, January 1996.

Appendix B

CPM Pulses for Varying Cavity and Absorber Length

In this appendix the influence of varying the CPM cavity and saturable absorber length are discussed. The presented data are obtained by a somewhat simpler model as presented in section 2.2. The presented results may thus not be compared quantitatively with the results presented in chapter 2. However, the qualitative features discussed here are also expected to be observed for the more detailed model used in chapter 2.

The main difference between the model used here and the one presented in chapter 2 is that we have chosen fixed values for τ_2 and $\tau_{1,c}$ in the gain ($\tau_{1,c} = \tau_2 = 50$ fs) and absorber section ($\tau_{1,c} = \tau_2 = 100$ fs), respectively. The effects of carrier heating and spectral hole burning in the valence band are not taken into account. Furthermore, we do not take into account index and gain dispersion in the wave-propagation equation.

In Fig. B.1 we have shown a plot of the Full Width at Half Maximum (FWHM) of the CPM pulses for different cavity and saturable absorber lengths. The parameter values used are basically equal to the values given in table 2.1, except that we here have investigated the case of a semiconductor structure with 5 quantum wells, where the value of the the field confinement factor Γ was 0.2. However, for the case of a 5 mm cavity we also made calculations for a confinement factor value of 0.05, which are the data points shown in Fig. B.1. The shortest pulse width for the 5 mm cavity with a confinement factor of 0.2 was found to be 3.2 ps.

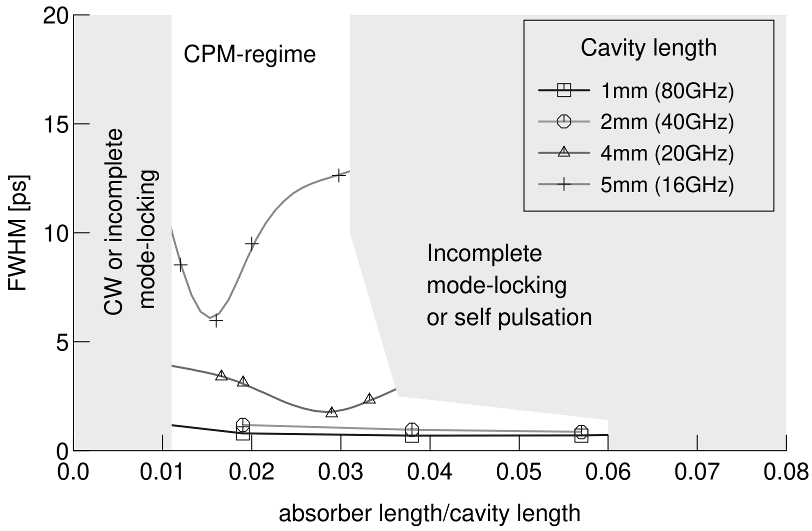

Figure B.1: Schematic plot of a monolithic CPM laser (lower figure). The top figure shows the pulse propagation in the laser cavity for a single round-trip, when steady state is reached.

In Fig. B.1 the injection current was kept constant for variations of the saturable absorber length, while the injection current was adjusted for varying cavity length. The figure shows that we for long laser diodes (4 mm and 5 mm) have an optimum length for the saturable absorber, while the short laser diodes (1 mm and 2 mm) generate the shortest pulses, when the saturable absorber length is close to its "maximum" length. Here, we by "maximum" length mean the saturable absorber length, where the CPM laser has not yet started to self-pulsate.

The optimum saturable absorber length obtained for the long laser diodes is also expected to be obtained by our more detailed laser model in chapter 2, since the pulse-shaping mechanism are similar.
The pulse-shaping mechanisms for the short laser cavities are somewhat different. Initially the start-up of the short laser diodes is similar to the start-up of the long laser diodes. Thus, the CPM pulses evolve from a broad pulse (modulation) over many round-trips. However, in the case of the short cavities at a certain point in this pulse-shaping transient the fast gain dynamics of the saturable absorber start to dominate, which results in an enhanced and very efficient pulse compression [1] based on the fast gain dynamics in the saturable absorber. These fast gain dynamics have been overestimated here, since we used fixed values for τ_2 and $\tau_{1,c}$. Furthermore, the effect of the fast gain dynamics in the saturable absorber increase for high confinement factors Γ as discussed in chapter 2.

The pulse dependence on the cavity length has already been discussed in chapter 2, and is as evident form Fig B.1 also observed for this simpler model.

Bibliography

[1] E. P. Ippen, "Principles of Passive Mode Locking", Appl. Phys. B **58** pp. 159-170, Lasers and Optics, Springer-Verlag, 1994.

Appendix C

The Interaction Hamiltonian

In this appendix we derive the unscreened Coulomb potential used in chapter 3. The equations describing the light propagation through a semiconductor slab with material width L_z were presented in chapter 3. The Hamiltonian describing the system is

$$H_{el} = H_{o,el} + H_{el,light} + H_I \quad , \tag{C.1}$$

where the terms on the right hand-side are

$$\begin{aligned} H_{0,el} &= \int d^3x \psi^\dagger(\vec{r}) \left(-\frac{\hbar}{2m}\Delta + V_L(\vec{r}) + V_c(\vec{r}) \right) \psi(\vec{r}) \quad , & \text{(C.2a)} \\ H_{el,l} &= \int d^3r \psi^\dagger(\vec{r}) \left(-\frac{\hbar e}{imc_0} \vec{A}(\vec{r}) \nabla \right) \psi(\vec{r}) \quad , & \text{(C.2b)} \\ H_I &= \frac{1}{2} \int d^3r d^3r' \psi^\dagger(\vec{r}) \psi^\dagger(\vec{r}') V(\vec{r}-\vec{r}'), \psi(\vec{r}') \psi(\vec{r}) \quad , & \text{(C.2c)} \end{aligned}$$

where $\vec{A}(\vec{r})$ is the transversal vector potential and the Coulomb potential is

$$V(\vec{r}-\vec{r}', z-z') = \frac{e^2}{\epsilon_0 |\vec{r}-\vec{r}'|} \quad . \tag{C.3}$$

Here, the Coulomb potential is given in CGS-units.

* Equation (C.2a) is the Hamiltonian for an electron in a potential field.
* Equation (C.2b) is the Hamiltonian for the interaction between electrons and light (linear term).
* Equation (C.2c) is the Hamiltonian for the Coulomb interaction between the electrons themselves.

The Coulomb potential is determined by the carrier-carrier interaction Hamiltonian H_I, which we want to calculate in this appendix. The treatment of the electron-light Hamiltonian, $H_{el,l}$, is presented in appendix D. The Heisenberg creation and annihilation operators are expanded in terms of the eigenfunctions of the free particle Hamiltonian, (see chapter 3),

$$\psi^\dagger(x) = \sum_{\vec{k}_\parallel, n} a^\dagger_{\vec{k}_\parallel,n,v} \overline{\phi}_{\vec{k}_\parallel,n,v}(x) + \sum_{\vec{k}_\parallel, n} a^\dagger_{\vec{k}_\parallel,n,c} \overline{\phi}_{\vec{k}_\parallel,n,c}(x) \quad , \tag{C.4a}$$

$$\psi(x) = \sum_{\vec{k}_\parallel, n} a_{\vec{k}_\parallel,n,v} \phi_{\vec{k}_\parallel,n,v}(x) + \sum_{\vec{k}_\parallel, n} a_{\vec{k}_\parallel,n,c} \phi_{\vec{k}_\parallel,n,c}(x) \quad . \tag{C.4b}$$

Here, index c and v stands for conduction or valence band, respectively. The function $\phi(x)$ is determined by an effective Hamiltonian,

$$\left(-\frac{\hbar^2}{2m}\Delta + V_{eff}(x)\right)\phi(x) = E\phi(x) \quad . \tag{C.5}$$

The unscreened Coulomb potential is now calculated by inserting equations (C.4) into the carrier-carrier interaction Hamiltonian. The calculations of the Coulomb potential by this approach is performed in the following section.

C.1 The Hamiltonian, H_I

The interaction Hamiltonian is [1]

$$H_I = \frac{1}{2}\int\int d^3r d^3r' \psi^\dagger(\vec{r})\psi^\dagger(\vec{r}')V(\vec{r}-\vec{r}')\psi(\vec{r}')\psi(\vec{r}) \quad . \tag{C.6}$$

The Heisenberg annihilation ψ and creation operator $\psi^\dagger$ are expressed in terms of Bloch functions,

$$\psi^\dagger(\vec{r}) = \sum_{\vec{k},\lambda} a^\dagger_{\vec{k},\lambda}\frac{e^{-i\vec{k}_{||}\cdot\vec{\rho}}}{L}\overline{f}_{n,\lambda}(z)\overline{u}_\lambda(\vec{k},\vec{r}) \quad , \tag{C.7a}$$

$$\psi(\vec{r}) = \sum_{\vec{k},\lambda} a_{\vec{k},\lambda}\frac{e^{i\vec{k}_{||}\vec{\rho}}}{L}f_{n,\lambda}(z)u_\lambda(\vec{k},\vec{r}) \quad . \tag{C.7b}$$

Here $\lambda = c, v$ denotes either the conduction or the valence band, respectively. $k_{x_{\|}}$ is an in-plane momentum. The three dimensional radius vector $\vec{r}$ is split into the z component and a two dimensional vector $\vec{\rho}$ for the in-plane coordinate. The z dependence of the eigenfunction f_{n_x,λ_x} depends on the confinement potential V_c.
Inserting Eqs. (C.7) into the interaction Hamiltonian yields,

$$\begin{aligned} H_I = \frac{1}{2} & \sum_{\substack{\vec{k}_{1_{\|}} \to \vec{k}_{4_{\|}} \\ n_1 \to n_4 \\ \lambda_1 \to \lambda_4}} a^\dagger_{\vec{k}_{1_{\|}},n_1,\lambda_1} a^\dagger_{\vec{k}_{2_{\|}},n_2,\lambda_2} a_{\vec{k}_{3_{\|}},n_3,\lambda_3} a_{\vec{k}_{4_{\|}},n_4,\lambda_4} \\ & \cdot \int\int d^3r d^3r' \frac{e^{-i\vec{k}_{1_{||}}\cdot\vec{\rho}}}{L}\overline{u}_{\lambda_1}(\vec{k}_1,\vec{r})\frac{e^{-i\vec{k}_{2_{||}}\cdot\vec{\rho}'}}{L}\overline{u}_{\lambda_2}(\vec{k}_2,\vec{r}')V(\vec{r}-\vec{r}')\frac{e^{i\vec{k}_{3_{||}}\cdot\vec{\rho}'}}{L} \\ & \cdot u_{\lambda_3}(\vec{k}_3,\vec{r}')\frac{e^{i\vec{k}_{4_{||}}\cdot\vec{\rho}}}{L}u_{\lambda_4}(\vec{k}_4,\vec{r})\overline{f}_{n_1,\lambda_1}(z)\overline{f}_{n_2,\lambda_2}(z')f_{n_3,\lambda_3}(z')f_{n_4,\lambda_4}(z) \quad . \end{aligned} \tag{C.8}$$

All functions entering equation (C.8) can be assumed to be slowly varying compared to the Bloch function $u_\lambda(\vec{k},\vec{r})$. Since we are only interested in states close to the bottom of the band we assume that $\vec{k} \approx \vec{0}$. Splitting the integral into a sum of small volume integrals the integral of the Bloch function $u_\lambda(\vec{k},\vec{r})$ becomes,

$$\frac{1}{L^3}\int d^3r \;\rightarrow\; \sum_n^N \frac{1}{N}\frac{1}{l^3}\int d^3r_n \quad , \tag{C.9a}$$

$$\frac{1}{l^3}\int d^3r_n \overline{u}_\lambda(\vec{k}\approx\vec{0},\vec{r}_n)u_{\lambda'}(\vec{k}'\approx\vec{0},\vec{r}_n) = \delta_{\lambda,\lambda'} \quad . \tag{C.9b}$$

Equation (C.9b) and the fact that all functions entering equation (C.8) are slowly varying compared to the Bloch functions can be used to remove the Bloch functions from the carrier-carrier interaction Hamiltonian.

$$\begin{aligned} H_I &= \frac{1}{2}\sum_{\substack{\vec{k}_{1_{||}}\rightarrow\vec{k}_{4_{||}}\\ n_1\rightarrow n_4\\ \lambda_1\rightarrow\lambda_4}} a^\dagger_{\vec{k}_{1_{||}},n_1,\lambda_1} a^\dagger_{\vec{k}_{2_{||}},n_2,\lambda_2} a_{\vec{k}_{3_{||}},n_3,\lambda_3} a_{\vec{k}_{4_{||}},n_4,\lambda_4} && \text{(C.10a)}\\ &\times\sum_m^M \frac{L}{M}\sum_{m'}^{M'}\frac{L}{M'} e^{-i\vec{k}_{1_{||}}\cdot\vec{\rho}} e^{-i\vec{k}_{2_{||}}\cdot\vec{\rho}'} V(\vec{r}-\vec{r}') e^{i\vec{k}_{3_{||}}\cdot\vec{\rho}'} e^{i\vec{k}_{4_{||}}\cdot\vec{\rho}} \\ &\times\overline{f}_{n_1,\lambda_1}(z)\overline{f}_{n_2,\lambda_2}(z')f_{n_3,\lambda_3}(z')f_{n_4,\lambda_4}(z)\delta_{\lambda_1,\lambda_4}\delta_{\lambda_2,\lambda_3} \quad , \\ &= \frac{1}{2}\sum_{\substack{\vec{k}_{1_{||}}\rightarrow\vec{k}_{4_{||}}\\ n_1\rightarrow n_4\\ \lambda_1\rightarrow\lambda_4}} a^\dagger_{\vec{k}_{1_{||}},n_1,\lambda_1} a^\dagger_{\vec{k}_{2_{||}},n_2,\lambda_2} a_{\vec{k}_{3_{||}},n_3,\lambda_3} a_{\vec{k}_{4_{||}},n_4,\lambda_4} && \text{(C.10b)}\\ &\times\int\!\!\int d^3r d^3r' \frac{1}{L^4} e^{-i\vec{k}_{1_{||}}\cdot\vec{\rho}} e^{-i\vec{k}_{2_{||}}\cdot\vec{\rho}'} V(\vec{r}-\vec{r}') e^{i\vec{k}_{3_{||}}\cdot\vec{\rho}'} e^{i\vec{k}_{4_{||}}\cdot\vec{\rho}} \\ &\times\overline{f}_{n_1,\lambda_1}(z)\overline{f}_{n_2,\lambda_2}(z')f_{n_3,\lambda_3}(z')f_{n_4,\lambda_4}(z)\delta_{\lambda_1,\lambda_4}\delta_{\lambda_2,\lambda_3} \quad . \end{aligned}$$

The in-plane coordinate $r\vec{h}o$ is now transformed to the coordinates for the center of mass $\vec{\rho}_c$ and the relative motion $\vec{\rho}_r$,

$$\begin{pmatrix}\rho\\ \rho'\end{pmatrix} = \begin{pmatrix}\vec{\rho}_c+\frac{1}{2}\vec{\rho}_r\\ \vec{\rho}_c-\frac{1}{2}\vec{\rho}_r\end{pmatrix} \quad , \tag{C.11a}$$

$$\begin{pmatrix}\vec{\rho}_c\\ \vec{\rho}_r\end{pmatrix} = \begin{pmatrix}\frac{\vec{\rho}+\vec{\rho}'}{2}\\ \vec{\rho}-\vec{\rho}'\end{pmatrix} \quad . \tag{C.11b}$$

The absolute value of the determinant of our transformation is

$$|det(\Phi)|^2 = \begin{vmatrix} 1 & 1/2 \\ 1 & -1/2 \end{vmatrix}^2 = 1 \quad . \tag{C.12}$$

The carrier-carrier interaction Hamiltonian after transformation yields,

$$\begin{aligned}
H_I &= \frac{1}{2} \sum_{\substack{\vec{k}_{1_{||}} \to \vec{k}_{4_{||}} \\ n_1 \to n_4 \\ \lambda_1, \lambda_2}} a^{\dagger}_{\vec{k}_{1_{||}}, n_1, \lambda_1} a^{\dagger}_{\vec{k}_{2_{||}}, n_2, \lambda_2} a_{\vec{k}_{3_{||}}, n_3, \lambda_2} a_{\vec{k}_{4_{||}}, n_4, \lambda_1} \qquad \text{(C.13a)} \\
&\times \int\int dz dz' \frac{1}{L^4} \overline{f}_{n_1,\lambda_1}(z) \overline{f}_{n_2,\lambda_2}(z') f_{n_3,\lambda_2}(z') f_{n_4,\lambda_1}(z) \\
&\times \int d^2\rho_r e^{-i\frac{\vec{k}_{1_{||}} - \vec{k}_{4_{||}}}{2} \cdot \vec{\rho}_r} V(\vec{\rho}_r, z - z') e^{i\frac{\vec{k}_{2_{||}} - \vec{k}_{3_{||}}}{2} \cdot \vec{\rho}_r} \\
&\times \int d^2\rho_c e^{-i(\vec{k}_{1_{||}} - \vec{k}_{4_{||}}) \cdot \vec{\rho}_c} e^{-i(\vec{k}_{2_{||}} - \vec{k}_{3_{||}}) \cdot \vec{\rho}_c} \quad , \\
&= \frac{1}{2} \sum_{\substack{\vec{k}_{1_{||}} \to \vec{k}_{4_{||}} \\ n_1 \to n_4 \\ \lambda_1, \lambda_2}} a^{\dagger}_{\vec{k}_{1_{||}}, n_1, \lambda_1} a^{\dagger}_{\vec{k}_{2_{||}}, n_2, \lambda_2} a_{\vec{k}_{3_{||}}, n_3, \lambda_2} a_{\vec{k}_{4_{||}}, n_4, \lambda_1} \qquad \text{(C.13b)} \\
&\times \int\int dz dz' \frac{1}{L^4} \overline{f}_{n_1,\lambda_1}(z) \overline{f}_{n_2,\lambda_2}(z') f_{n_3,\lambda_2}(z') f_{n_4,\lambda_1}(z) \\
&\times \int d^2\rho_r e^{-i\frac{\vec{k}_{1_{||}} - \vec{k}_{4_{||}}}{2} \cdot \vec{\rho}_r} V(\vec{\rho}_r, z - z') e^{i\frac{\vec{k}_{2_{||}} - \vec{k}_{3_{||}}}{2} \cdot \vec{\rho}_r} L^2 \\
&\times \delta_{\vec{k}_{1_{||}} - \vec{k}_{4_{||}}, \vec{k}_{3_{||}} - \vec{k}_{2_{||}}} \quad .
\end{aligned}$$

The in-plane momentum $\vec{k}_{4_{||}}$ is now replaced by $\vec{k}_{||}$, $\vec{k}_{3_{||}}$ by $\vec{k}'_{||}$ and $\vec{k}_{1_{||}}$ by $\vec{k}_{||} + \vec{q}_{||}$. In this case the Dirac delta function is non-zero only when $\vec{k}_{2_{||}} = \vec{k}'_{||} - \vec{q}_{||}$. Making the above substitutions the interaction Hamiltonian yields,

$$H_I = \frac{1}{2} \sum_{\substack{\vec{k}_{\|}, \vec{k}'_{\|}, \vec{q}_{\|} \\ n_1 \to n_4 \\ \lambda_1, \lambda_2}} a^\dagger_{\vec{k}_{||}+\vec{q}_{||}, n_1, \lambda_1} a^\dagger_{\vec{k}'_{||}-\vec{q}_{||}, n_2 \lambda_2} a_{\vec{k}'_{||}, n_3, \lambda_2} a_{\vec{k}_{||}, n_4, \lambda_1} \times \int\int dz dz' \frac{1}{L^2} \overline{f}_{n_1,\lambda_1}(z) \overline{f}_{n_2,\lambda_2}(z') f_{n_3,\lambda_2}(z') f_{n_4,\lambda_1}(z) \times \int d^2\rho_r e^{i\vec{q}_{||}\cdot\vec{\rho}_r} V(\vec{\rho}_r, z-z') \quad . \tag{C.14}$$

The integral over the area $\int d^2\rho_r$ is done by using cylindrical coordinates, and assuming $\vec{q}_{||}$ to point in a specific direction, i.e. the x-direction.

$$I_{\rho_r}(z-z') = \int d^2\rho_r e^{i\vec{q}_{\|}\cdot\vec{\rho}_r} V(\vec{\rho}_r, z-z') \quad , \tag{C.15a}$$

$$= \int_0^\infty \int_0^{2\pi} d\rho'_r d\phi' \frac{\rho'_r e^{-i|\vec{q}_{||}|\rho'_r \cos(\phi')} e^2}{\epsilon_0 \sqrt{(\rho'_r)^2 + (z-z')^2}} \quad , \tag{C.15b}$$

$$= \int_0^\infty d\rho'_r \frac{2\pi e^2 \rho'_r}{\epsilon_0 |\vec{q}_{||}| \sqrt{(\rho'_r)^2 + (z-z')^2}} \times J_0\left(|\vec{q}_{||}||z-z'|\right) \quad , \tag{C.15c}$$

$$= \frac{2\pi e^2}{\epsilon_0 |\vec{q}_{||}|} e^{-|\vec{q}_{||}||z-z'|} \quad , \tag{C.15d}$$

where $J_0\left(|\vec{q}_{||}||z-z'|\right)$ is the zero order Bessel function. Inserting equation (C.15d) into equation (C.14) results in the Hamiltonian,

$$H_I = \frac{1}{2} \sum_{\substack{\vec{k}_{\|}, \vec{k}'_{\|}, \vec{q}_{\|} \\ n_1 \to n_4 \\ \lambda_1, \lambda_2}} a^\dagger_{\vec{k}_{\|}+\vec{q}_{\|}, n_1, \lambda_1} a^\dagger_{\vec{k}'_{\|}-\vec{q}_{\|}, n_2, \lambda_2} a_{\vec{k}'_{\|}, n_3, \lambda_2} a_{\vec{k}_{\|}, n_4, \lambda_1} \times \frac{2\pi e^2}{L^2 \epsilon_0 |\vec{q}_{\|}|} \int\int dz dz' e^{-|\vec{q}_{||}||z-z'|} \times \overline{f}_{n_1,\lambda_1}(z) \overline{f}_{n_2,\lambda_2}(z') f_{n_3,\lambda_2}(z') f_{n_4,\lambda_1}(z) \quad . \tag{C.16}$$

The z integration requires the knowledge of the eigenfunctions $f_{n,\lambda}$, which are determined by the confinement potential. In the following subsection we will calculate the Coulomb potential in the case of an infinite confinement potential V_c.

C.1.1 Infinite confinement potential

The eigenfunctions for a semiconductor slab with an infinite confinement potential are given by even and odd states [2].

Even eigenfunctions:

$$f_{n,\lambda}(z) = \begin{cases} \sqrt{\frac{2}{L_z}} \cos\left(n\frac{\pi}{L_z}z\right) & \text{when } |z| \leq \frac{L_z}{2}\ , \quad n\text{=1,3,5,...} \\ 0 & \text{when } |z| \geq \frac{L_z}{2} \end{cases} \tag{C.17}$$

Odd eigenfunctions:

$$f_{m,\lambda}(z) = \begin{cases} \sqrt{\frac{2}{L_z}} \sin\left(m\frac{\pi}{L_z}z\right) & \text{when } |z| \leq \frac{L_z}{2}\ , \quad m\text{=2,4,6,...} \\ 0 & \text{when } |z| \geq \frac{L_z}{2} \end{cases} \tag{C.18}$$

Here and in the following, the even eigenfunctions are labeled by the quantum number n, while odd quantized eigenfunctions are labeled by quantum number m. The z integration in equation (C.16) has to be calculated for all possible combinations of even and odd eigenfunctions. These calculations are trivial and so we have included the calculations for the case of even states only. The integration steps are analogue in the other cases.

The case with even eigenfunctions The eigenfunctions are as seen in equation (C.17) and (C.18) non-zero for $|z| < L_z/2$. First we make the coordinate transformation $x = \frac{\pi}{L_z}z$ and $x' = \frac{\pi}{L_z}z'$, hereby the integral becomes,

$$I_1 = \int_{-\frac{L_z}{2}}^{\frac{L_z}{2}} \int_{-\frac{L_z}{2}}^{\frac{L_z}{2}} dz dz' e^{-|\vec{q}_{\parallel}||z-z'|} \tag{C.19a}$$

$$
\begin{aligned}
&\times\overline{f}_{n_1,\lambda_1}(z)\overline{f}_{n_2,\lambda_2}(z')f_{n_3,\lambda_2}(z')f_{n_4,\lambda_1}(z) \quad , \\
= & \int_{-\frac{\pi}{2}}^{\frac{\pi}{2}} dx \frac{4}{\pi^2} e^{|\vec{q}_{\parallel}|\frac{L_z}{\pi}x} cos(n_1 x) cos(n_4 x) \qquad\qquad \text{(C.19b)} \\
&\times \underbrace{\int_{x}^{\frac{\pi}{2}} dx' e^{-|\vec{q}_{\parallel}|\frac{L_z}{\pi}x'} \frac{1}{2}\left(cos((n_2-n_3)x') + cos((n_2+n_3)x')\right)}_{I_{1,cos^4}} \\
&+ \int_{-\frac{\pi}{2}}^{\frac{\pi}{2}} dx \frac{4}{\pi^2} e^{-|\vec{q}_{\parallel}|\frac{L_z}{\pi}x} cos(n_1 x) cos(n_4 x) \\
&\times \underbrace{\int_{-\frac{\pi}{2}}^{x} dx' e^{|\vec{q}_{\parallel}|\frac{L_z}{\pi}x'} \frac{1}{2}\left(cos((n_2-n_3)x') + cos((n_2+n_3)x')\right)}_{I_{2,cos^4}} \quad .
\end{aligned}
$$

The integral I_{1,cos^4} yields,

$$
\begin{aligned}
I_{1,cos^4} = & \underbrace{-\frac{e^{-|\vec{q}_{\parallel}|\frac{L_z}{2}} |\vec{q}_{\parallel}|\frac{L_z}{\pi} cos\left((n_2-n_3)\frac{\pi}{2}\right)}{2\left(\left(|\vec{q}_{\parallel}|\frac{L_z}{\pi}\right)^2 + (n_2-n_3)^2\right)}}_{I_{1,cos^4,(n_2-n_3)}} \qquad\qquad \text{(C.20)} \\
& \underbrace{-\frac{e^{-|\vec{q}_{\parallel}|\frac{L_z}{2}} |\vec{q}_{\parallel}|\frac{L_z}{\pi} cos\left((n_2+n_3)\frac{\pi}{2}\right)}{2\left(\left(|\vec{q}_{\parallel}|\frac{L_z}{\pi}\right)^2 + (n_2+n_3)^2\right)}}_{I_{1,cos^4,(n_2+n_3)}} \\
& + \frac{e^{-|\vec{q}_{\parallel}|\frac{L_z}{\pi}x}\left(|\vec{q}_{||}|\frac{L_z}{\pi} cos\left((n_2-n_3)x\right) - (n_2-n_3) sin\left((n_2-n_3)x\right)\right)}{2\left(\left(|\vec{q}_{\parallel}|\frac{L_z}{\pi}\right)^2 + (n_2-n_3)^2\right)} \\
& + \frac{e^{-|\vec{q}_{\parallel}\frac{L_z}{\pi}x}\left(|\vec{q}_{\parallel}|\frac{L_z}{\pi} cos\left((n_2+n_3)x\right) - (n_2+n_3) sin\left((n_2+n_3)x\right)\right)}{2\left(\left(|\vec{q}_{\parallel}|\frac{L_z}{\pi}\right)^2 + (n_2+n_3)^2\right)} \quad .
\end{aligned}
$$

and the integral I_{2,cos^4} yields,

$$
\begin{aligned}
I_{2,cos^4} \quad = \quad & \underbrace{-\frac{e^{-|\vec{q}_{\|}|\frac{L_z}{2}}|\vec{q}_{\|}|\frac{L_z}{\pi}cos\left((n_2-n_3)\frac{\pi}{2}\right)}{2\left(\left(|\vec{q}_{\|}|\frac{L_z}{\pi}\right)^2+(n_2-n_3)^2\right)}}_{I_{2,cos^4,(n_2-n_3)}} \\
& \underbrace{-\frac{e^{-|\vec{q}_{\|}|\frac{L_z}{2}}|\vec{q}_{\|}|\frac{L_z}{\pi}cos\left((n_2+n_3)\frac{\pi}{2}\right)}{2\left(\left(|\vec{q}_{\|}|\frac{L_z}{\pi}\right)^2+(n_2+n_3)^2\right)}}_{I_{2,cos^4,(n_2+n_3)}} \\
& +\frac{e^{|\vec{q}_{\|}|\frac{L_z}{\pi}x}\left(|\vec{q}_{\|}|\frac{L_z}{\pi}cos\left((n_2-n_3)x\right)+(n_2-n_3)sin\left((n_2-n_3)x\right)\right)}{2\left(\left(|\vec{q}_{\|}|\frac{L_z}{\pi}\right)^2+(n_2-n_3)^2\right)} \\
& +\frac{e^{|\vec{q}_{\|}|\frac{L_z}{\pi}x}\left(|\vec{q}_{\|}|\frac{L_z}{\pi}cos\left((n_2+n_3)x\right)+(n_2+n_3)sin\left((n_2+n_3)x\right)\right)}{2\left(\left(|\vec{q}_{\|}|\frac{L_z}{\pi}\right)^2+(n_2+n_3)^2\right)}
\end{aligned}
\tag{C.21}
$$

The integrals $I_{1,cos^4,(n_2-n_3)} = I_{2,cos^4,(n_2-n_3)}$ and $I_{1,cos^4,(n_2+n_3)} = I_{2,cos^4,(n_2+n_3)}$ do not depend on x. Accordingly, these integrals have to be multiplied by the remaining integral in equations (C.19b).

$$
\begin{aligned}
I_{3,cos^4} \quad & = \int_{-\frac{\pi}{2}}^{\frac{\pi}{2}} dx \frac{4}{\pi^2} e^{|\vec{q}_{\|}|\frac{L_z}{\pi}x} \cos(n_1 x)\cos(n_4 x) \\
& = \int_{-\frac{\pi}{2}}^{\frac{\pi}{2}} dx \frac{2}{\pi^2} e^{|\vec{q}_{\|}|\frac{L_z}{\pi}x} \left(\cos((n_1-n_4)x)+\cos((n_1+n_4)x)\right) \\
& = \underbrace{\frac{2}{\pi^2}\frac{\left(e^{|\vec{q}_{\|}|L_z/2}-e^{-|\vec{q}_{\|}|L_z/2}\right)}{\left(|\vec{q}_{\|}|\frac{L}{\pi}\right)^2+(n_1-n_4)^2}|\vec{q}_{\|}|\frac{L_z}{\pi}cos\left((n_1-n_4)\frac{\pi}{2}\right)}_{I_{3,cos^4,(n_1-n_4)}}
\end{aligned}
\tag{C.22}
$$

$$
+\underbrace{\frac{2}{\pi^2}\frac{\left(e^{|\vec{q}_{\parallel}|L_z/2}-e^{-|\vec{q}_{\parallel}|L_z/2}\right)}{\left(|\vec{q}_{\parallel}|\frac{L}{\pi}\right)^2+(n_1+n_4)^2}|\vec{q}_{\parallel}|\frac{L_z}{\pi}cos\left((n_1+n_4)\frac{\pi}{2}\right)}_{I_{3,cos^4,(n_1+n_4)}} \quad .
$$

$$
\begin{aligned}
I_{4,cos^4} &= \int_{-\frac{\pi}{2}}^{\frac{\pi}{2}} dx\frac{4}{\pi^2}e^{-|\vec{q}_{\parallel}|\frac{L_z}{\pi}x}\cos(n_1x)\cos(n_4x) \\
&= \int_{-\frac{\pi}{2}}^{\frac{\pi}{2}} dx\frac{2}{\pi^2}e^{-|\vec{q}_{\parallel}|\frac{L_z}{\pi}x}\left(\cos((n_1-n_4)x)+\cos((n_1+n_4)x)\right) \\
&= \underbrace{\frac{2}{\pi^2}\frac{\left(e^{|\vec{q}_{\parallel}|L_z/2}-e^{-|\vec{q}_{\parallel}|L_z/2}\right)}{\left(|\vec{q}_{\parallel}|\frac{L}{\pi}\right)^2+(n_1-n_4)^2}|\vec{q}_{\parallel}|\frac{L_z}{\pi}cos\left((n_1-n_4)\frac{\pi}{2}\right)}_{I_{4,cos^4,(n_1-n_4)}} \\
&\quad +\underbrace{\frac{2}{\pi^2}\frac{\left(e^{|\vec{q}_{\parallel}|L_z/2}-e^{-|\vec{q}_{\parallel}|L_z/2}\right)}{\left(|\vec{q}_{\parallel}|\frac{L}{\pi}\right)^2+(n_1+n_4)^2}|\vec{q}_{\parallel}|\frac{L_z}{\pi}cos\left((n_1+n_4)\frac{\pi}{2}\right)}_{I_{4,cos^4,(n_1+n_4)}} \quad .
\end{aligned} \tag{C.23}
$$

Here, the integral $I_{3,cos^4}(n_1-n_4) = I_{4,cos^4}(n_1-n_4)$ and $I_{3,cos^4}(n_1+n_4) = I_{4,cos^4}(n_1+n_4)$. The remaining integral to be calculated contains products of cosine functions only. Accordingly, the integral will give Dirac delta function contributions in accordance with the relations,

$$
\int_{-\frac{\pi}{2}}^{\frac{\pi}{2}} cos(n_1x)cos(n_2x) = \begin{cases} 0 & \text{when } n_1 \neq n_2 \\ \frac{\pi}{2} & \text{when } n_1 = n_2,\ n_1 \neq 0 \\ \frac{2}{n_1}sin\left(n_1\frac{\pi}{2}\right) & \text{when } n_1 \neq n_2,\ n_2 = 0 \\ \pi & \text{when } n_1 = n_2 = 0 \end{cases} \tag{C.24}
$$

The interaction Hamiltonian can now be written down by using the results of the integration given above. Here, we use the fact that the $\vec{q}_{\parallel} = \vec{0}$ contribution, which diverges, is cancelled by the $\vec{q}_{\parallel} = \vec{0}$ terms from the electron-ion and ion-ion Coulomb potentials [3].

$$
\begin{aligned}
H_I \;=\; & \frac{1}{2} \sum_{\substack{\vec{k}_{||}, \vec{k}'_{||}, \vec{q}_{||} \neq \vec{0} \\ n_1 \to n_4 \\ \lambda_1, \lambda_2}} a^{\dagger}_{\vec{k}_{||}+\vec{q}_{||}, n_1, \lambda_1} a^{\dagger}_{\vec{k}'_{||}-\vec{q}_{||}, n_2, \lambda_2} a_{\vec{k}'_{||}, n_3, \lambda_2} a_{\vec{k}_{||}, n_4, \lambda_1} \qquad \text{(C.25a)} \\
& \times \frac{2\pi e^2}{L^2 \epsilon_0 |\vec{q}_{||}|} \\
& \times \frac{2}{\pi^2} \left(|\vec{q}_{||}| \frac{L_z}{\pi} \right)^2 \left[\frac{\cos\left((n_2 - n_3)\frac{\pi}{2}\right)}{\left(|\vec{q}_{||}|\frac{L_z}{\pi}\right)^2 + (n_2 - n_3)^2} + \frac{\cos\left((n_2 + n_3)\frac{\pi}{2}\right)}{\left(|\vec{q}_{||}|\frac{L_z}{\pi}\right)^2 + (n_2 + n_3)^2} \right] \\
& \times \left(e^{-|\vec{q}_{||}| L_z} - 1 \right) \left[\frac{\cos\left((n_1 - n_4)\frac{\pi}{2}\right)}{\left(|\vec{q}_{||}|\frac{L_z}{\pi}\right)^2 + (n_1 - n_4)^2} + \frac{\cos\left((n_1 + n_4)\frac{\pi}{2}\right)}{\left(|\vec{q}_{||}|\frac{L_z}{\pi}\right)^2 + (n_1 + n_4)^2} \right] \\
+ \; & \frac{1}{2} \sum_{\substack{\vec{k}_{||}, \vec{k}'_{||}, \vec{q}_{||} \\ n_1 \to n_4 \\ \lambda_1, \lambda_2}} a^{\dagger}_{\vec{k}_{||}+\vec{q}_{||}, \lambda_1} a^{\dagger}_{\vec{k}'_{||}-\vec{q}_{||}, \lambda_2} a_{\vec{k}'_{||}, \lambda_2} a_{\vec{k}_{||}, \lambda_1} \frac{2\pi e^2}{L^2 \epsilon_0 |\vec{q}_{||}|} \\
& \times \frac{1}{\pi} \left[\frac{|\vec{q}_{||}| \frac{L_z}{\pi} \left(\delta_{n_1 - n_4, n_2 - n_3} + \delta_{n_1 + n_4, n_2 - n_3} + \delta_{n_1 - n_4, 0} \delta_{n_2 - n_3, 0} \right)}{\left(|\vec{q}_{||}|\frac{L_z}{\pi}\right)^2 + (n_2 - n_3)^2} \right. \\
& \left. + \frac{|\vec{q}_{||}| \frac{L_z}{\pi} \left(\delta_{n_1 - n_4, n_2 + n_3} + \delta_{n_1 + n_4, n_2 + n_3} \right)}{\left(|\vec{q}_{||}|\frac{L_z}{\pi}\right)^2 + (n_2 + n_3)^2} \right] , \\
= \; & \frac{1}{2} \sum_{\substack{\vec{k}_{||}, \vec{k}'_{||}, \vec{q}_{||} \neq \vec{0} \\ n_1 \to n_4 \\ \lambda_1, \lambda_2}} a^{\dagger}_{\vec{k}_{||}+\vec{q}_{||}, n_1, \lambda_1} a^{\dagger}_{\vec{k}'_{||}-\vec{q}_{||}, n_2, \lambda_2} a_{\vec{k}'_{||}, n_3, \lambda_2} a_{\vec{k}_{||}, n_4, \lambda_1} \qquad \text{(C.25b)} \\
& \times V_{\vec{q}_{||}}^{n_1^{\lambda_1}, n_2^{\lambda_2}, n_3^{\lambda_2}, n_4^{\lambda_1}} .
\end{aligned}
$$

The calculations for other combinations of eigenfunctions $f_{n,\lambda}$ are analogous to the shown example. In the next section we will present a full listing of the Coulomb potential.

C.2 The Coulomb potential

In this section we give a full listing of the Coulomb potential for different combinations of even and odd eigenfunctions $f_{n,\lambda}$ in the case of an infinite confinement potential V_c. Here, $n_x = 1, 3, 5, 7, \ldots$ and $m_x = 2, 4, 6, 8, \ldots$ are the quantum numbers for even and odd eigenfunctions, respectively.

$$
\begin{aligned}
V_{\vec{q}_\parallel}^{n_1^{\lambda_1}, n_2^{\lambda_2}, n_3^{\lambda_2}, n_4^{\lambda_1}} &= \\
&\frac{2\pi e^2}{L^2 \epsilon_0 |\vec{q}_\parallel|} \frac{2}{\pi^2} \left(|\vec{q}_\parallel| \frac{L_z}{\pi} \right)^2 \left(e^{-|\vec{q}_\parallel| L_z} - 1 \right) \\
&\times \left[\frac{\cos\left((n_2^{\lambda_2} - n_3^{\lambda_2}) \frac{\pi}{2} \right)}{\left(|\vec{q}_\parallel| \frac{L_z}{\pi} \right)^2 + (n_2^{\lambda_2} - n_3^{\lambda_2})^2} + \frac{\cos\left((n_2^{\lambda_2} + n_3^{\lambda_2}) \frac{\pi}{2} \right)}{\left(|\vec{q}_\parallel| \frac{L_z}{\pi} \right)^2 + (n_2^{\lambda_2} + n_3^{\lambda_2})^2} \right] \\
&\times \left[\frac{\cos\left((n_1^{\lambda_1} - n_4^{\lambda_1}) \frac{\pi}{2} \right)}{\left(|\vec{q}_\parallel| \frac{L_z}{\pi} \right)^2 + (n_1^{\lambda_1} - n_4^{\lambda_1})^2} + \frac{\cos\left((n_1^{\lambda_1} + n_4^{\lambda_1}) \frac{\pi}{2} \right)}{\left(|\vec{q}_\parallel| \frac{L_z}{\pi} \right)^2 + (n_1^{\lambda_1} + n_4^{\lambda_1})^2} \right] \\
&+ \frac{2\pi e^2}{L^2 \epsilon_0 |\vec{q}_\parallel|} \frac{1}{\pi} |\vec{q}_\parallel| \frac{L_z}{\pi} \frac{1}{\left(|\vec{q}_\parallel| \frac{L_z}{\pi} \right)^2 + (n_2^{\lambda_2} - n_3^{\lambda_2})^2} \\
&\times \Big(\delta_{n_1^{\lambda_1} - n_4^{\lambda_1}, n_2^{\lambda_2} - n_3^{\lambda_2}} (1 + \delta_{n_1^{\lambda_1} - n_4^{\lambda_1}, 0}) \\
&\qquad + \delta_{n_1^{\lambda_1} + n_4^{\lambda_1}, n_2^{\lambda_2} - n_3^{\lambda_2}} \Big) \\
&+ \frac{2\pi e^2}{L^2 \epsilon_0 |\vec{q}_\parallel|} \frac{1}{\pi} |\vec{q}_\parallel| \frac{L_z}{\pi} \frac{1}{\left(|\vec{q}_\parallel| \frac{L_z}{\pi} \right)^2 + (n_2^{\lambda_2} + n_3^{\lambda_2})^2} \\
&\times \left(\delta_{n_1^{\lambda_1} - n_4^{\lambda_1}, n_2^{\lambda_2} + n_3^{\lambda_2}} + \delta_{n_1^{\lambda_1} + n_4^{\lambda_1}, n_2^{\lambda_2} + n_3^{\lambda_2}} \right)
\end{aligned}
\tag{C.26}
$$

$$
\begin{aligned}
V_{\vec{q}_\parallel}^{m_1^{\lambda_1}, n_2^{\lambda_2}, n_3^{\lambda_2}, m_4^{\lambda_1}} &= V_{\vec{q}_\parallel}^{n_2^{\lambda_2}, m_1^{\lambda_1}, m_4^{\lambda_1}, n_3^{\lambda_2}} = \\
&\frac{2\pi e^2}{L^2 \epsilon_0 |\vec{q}_\parallel|} \frac{2}{\pi^2} \left(|\vec{q}_\parallel| \frac{L_z}{\pi} \right)^2 \left(e^{-|\vec{q}_\parallel| L_z} - 1 \right)
\end{aligned}
\tag{C.27}
$$

$$\times \left[\frac{\cos\left((n_2^{\lambda_2} - n_3^{\lambda_2})\frac{\pi}{2}\right)}{\left(|\vec{q}_\parallel|\frac{L_z}{\pi}\right)^2 + (n_2^{\lambda_2} - n_3^{\lambda_2})^2} + \frac{\cos\left((n_2^{\lambda_2} + n_3^{\lambda_2})\frac{\pi}{2}\right)}{\left(|\vec{q}_\parallel|\frac{L_z}{\pi}\right)^2 + (n_2^{\lambda_2} + n_3^{\lambda_2})^2} \right]$$

$$\times \left[\frac{\cos\left((m_1^{\lambda_1} - m_4^{\lambda_1})\frac{\pi}{2}\right)}{\left(|\vec{q}_\parallel|\frac{L_z}{\pi}\right)^2 + (m_1^{\lambda_1} - m_4^{\lambda_1})^2} - \frac{\cos\left((m_1^{\lambda_1} + m_4^{\lambda_1})\frac{\pi}{2}\right)}{\left(|\vec{q}_\parallel|\frac{L_z}{\pi}\right)^2 + (m_1^{\lambda_1} + m_4^{\lambda_1})^2} \right]$$

$$+ \frac{2\pi e^2}{L^2 \epsilon_0 |\vec{q}_\parallel|} \frac{1}{\pi} |\vec{q}_\parallel| \frac{L_z}{\pi} \frac{1}{\left(|\vec{q}_\parallel|\frac{L_z}{\pi}\right)^2 + (n_2^{\lambda_2} - n_3^{\lambda_2})^2}$$

$$\times \Big(\delta_{m_1^{\lambda_1} - m_4^{\lambda_1}, n_2^{\lambda_2} - n_3^{\lambda_2}} (1 + \delta_{m_1^{\lambda_1} - m_4^{\lambda_1}, 0})$$

$$- \delta_{m_1^{\lambda_1} + m_4^{\lambda_1}, n_2^{\lambda_2} - n_3^{\lambda_2}} \Big)$$

$$+ \frac{2\pi e^2}{L^2 \epsilon_0 |\vec{q}_\parallel|} \frac{1}{\pi} |\vec{q}_\parallel| \frac{L_z}{\pi} \frac{1}{\left(|\vec{q}_\parallel|\frac{L_z}{\pi}\right)^2 + (n_2^{\lambda_2} + n_3^{\lambda_2})^2}$$

$$\times \left(\delta_{m_1^{\lambda_1} - m_4^{\lambda_1}, n_2^{\lambda_2} + n_3^{\lambda_2}} - \delta_{m_1^{\lambda_1} + m_4^{\lambda_1}, n_2^{\lambda_2} + n_3^{\lambda_2}} \right)$$

$$V_{\vec{q}_\parallel}^{m_1^{\lambda_1}, m_2^{\lambda_2}, m_3^{\lambda_2}, m_4^{\lambda_1}} = \tag{C.28}$$

$$\frac{2\pi e^2}{L^2 \epsilon_0 |\vec{q}_\parallel|} \frac{2}{\pi^2} \left(|\vec{q}_\parallel| \frac{L_z}{\pi} \right)^2 \left(e^{-|\vec{q}_\parallel| L_z} - 1 \right)$$

$$\times \left[\frac{\cos\left((m_2^{\lambda_2} - m_3^{\lambda_2})\frac{\pi}{2}\right)}{\left(|\vec{q}_\parallel|\frac{L_z}{\pi}\right)^2 + (m_2^{\lambda_2} - m_3^{\lambda_2})^2} - \frac{\cos\left((m_2^{\lambda_2} + m_3^{\lambda_2})\frac{\pi}{2}\right)}{\left(|\vec{q}_\parallel|\frac{L_z}{\pi}\right)^2 + (m_2^{\lambda_2} + m_3^{\lambda_2})^2} \right]$$

$$\times \left[\frac{\cos\left((m_1^{\lambda_1} - m_4^{\lambda_1})\frac{\pi}{2}\right)}{\left(|\vec{q}_\parallel|\frac{L_z}{\pi}\right)^2 + (m_1^{\lambda_1} - m_4^{\lambda_1})^2} - \frac{\cos\left((m_1^{\lambda_1} + m_4^{\lambda_1})\frac{\pi}{2}\right)}{\left(|\vec{q}_\parallel|\frac{L_z}{\pi}\right)^2 + (m_1^{\lambda_1} + m_4^{\lambda_1})^2} \right]$$

$$+ \frac{2\pi e^2}{L^2 \epsilon_0 |\vec{q}_\parallel|} \frac{1}{\pi} |\vec{q}_\parallel| \frac{L_z}{\pi} \frac{1}{\left(|\vec{q}_\parallel|\frac{L_z}{\pi}\right)^2 + (m_2^{\lambda_2} - m_3^{\lambda_2})^2}$$

$$\times \Big(\delta_{m_1^{\lambda_1} - m_4^{\lambda_1}, m_2^{\lambda_2} - m_3^{\lambda_2}} (1 + \delta_{m_1^{\lambda_1} - m_4^{\lambda_1}, 0})$$

$$- \delta_{m_1^{\lambda_1} + m_4^{\lambda_1}, m_2^{\lambda_2} - m_3^{\lambda_2}} \Big)$$

$$+\frac{2\pi e^2}{L^2\epsilon_0|\vec{q}_\parallel|}\frac{1}{\pi}|\vec{q}_\parallel|\frac{L_z}{\pi}\frac{1}{\left(|\vec{q}_\parallel|\frac{L_z}{\pi}\right)^2+(m_2^{\lambda_2}+m_3^{\lambda_2})^2}$$
$$\times\left(-\delta_{m_1^{\lambda_1}-m_4^{\lambda_1},m_2^{\lambda_2}+m_3^{\lambda_2}}+\delta_{m_1^{\lambda_1}+m_4^{\lambda_1},m_2^{\lambda_2}+m_3^{\lambda_2}}\right)$$

$$V_{\vec{q}_\parallel}^{m_1^{\lambda_1},m_2^{\lambda_2},n_3^{\lambda_2},n_4^{\lambda_1}} = V_{\vec{q}_\parallel}^{n_4^{\lambda_1},n_3^{\lambda_2},m_2^{\lambda_2},m_1^{\lambda_1}} = \tag{C.29}$$
$$\frac{2\pi e^2}{L^2\epsilon_0|\vec{q}_\parallel|}\frac{2}{\pi^2}\left(|\vec{q}_\parallel|\frac{L_z}{\pi}\right)^2\left(e^{-|\vec{q}_\parallel|L_z}+1\right)$$
$$\times\left[\frac{\sin\left((m_2^{\lambda_2}-n_3^{\lambda_2})\frac{\pi}{2}\right)}{\left(|\vec{q}_\parallel|\frac{L_z}{\pi}\right)^2+(m_2^{\lambda_2}-n_3^{\lambda_2})^2}+\frac{\sin\left((m_2^{\lambda_2}+n_3^{\lambda_2})\frac{\pi}{2}\right)}{\left(|\vec{q}_\parallel|\frac{L_z}{\pi}\right)^2+(m_2^{\lambda_2}+n_3^{\lambda_2})^2}\right]$$
$$\times\left[-\frac{\sin\left((m_1^{\lambda_1}-n_4^{\lambda_1})\frac{\pi}{2}\right)}{\left(|\vec{q}_\parallel|\frac{L_z}{\pi}\right)^2+(m_1^{\lambda_1}-n_4^{\lambda_1})^2}-\frac{\cos\left((m_1^{\lambda_1}+n_4^{\lambda_1})\frac{\pi}{2}\right)}{\left(|\vec{q}_\parallel|\frac{L_z}{\pi}\right)^2+(m_1^{\lambda_1}+n_4^{\lambda_1})^2}\right]$$
$$+\frac{2\pi e^2}{L^2\epsilon_0|\vec{q}_\parallel|}\frac{1}{\pi}|\vec{q}_\parallel|\frac{L_z}{\pi}\frac{1}{\left(|\vec{q}_\parallel|\frac{L_z}{\pi}\right)^2+(m_2^{\lambda_2}-n_3^{\lambda_2})^2}$$
$$\times\left(\delta_{m_1^{\lambda_1}-n_4^{\lambda_1},m_2^{\lambda_2}-n_3^{\lambda_2}}+\delta_{m_1^{\lambda_1}+n_4^{\lambda_1},m_2^{\lambda_2}-n_3^{\lambda_2}}\right)$$
$$+\frac{2\pi e^2}{L^2\epsilon_0|\vec{q}_\parallel|}\frac{1}{\pi}|\vec{q}_\parallel|\frac{L_z}{\pi}\frac{1}{\left(|\vec{q}_\parallel|\frac{L_z}{\pi}\right)^2+(m_2^{\lambda_2}+n_3^{\lambda_2})^2}$$
$$\times\left(\delta_{m_1^{\lambda_1}-n_4^{\lambda_1},m_2^{\lambda_2}+n_3^{\lambda_2}}+\delta_{m_1^{\lambda_1}+n_4^{\lambda_1},m_2^{\lambda_2}+n_3^{\lambda_2}}\right)$$

$$V_{\vec{q}_\parallel}^{n_1^{\lambda_1},n_2^{\lambda_2},n_3^{\lambda_2},m_4^{\lambda_1}} = 0 \quad , \tag{C.30a}$$
$$V_{\vec{q}_\parallel}^{n_1^{\lambda_1},n_2^{\lambda_2},m_3^{\lambda_2},n_4^{\lambda_1}} = 0 \quad , \tag{C.30b}$$
$$V_{\vec{q}_\parallel}^{n_1^{\lambda_1},m_2^{\lambda_2},n_3^{\lambda_2},n_4^{\lambda_1}} = 0 \quad , \tag{C.30c}$$
$$V_{\vec{q}_\parallel}^{m_1^{\lambda_1},n_2^{\lambda_2},n_3^{\lambda_2},n_4^{\lambda_1}} = 0 \quad , \tag{C.30d}$$
$$V_{\vec{q}_\parallel}^{m_1^{\lambda_1},m_2^{\lambda_2},m_3^{\lambda_2},n_4^{\lambda_1}} = 0 \quad , \tag{C.30e}$$

$$V_{\vec{q}_{\|}}^{m_1^{\lambda_1},m_2^{\lambda_2},n_3^{\lambda_2},m_4^{\lambda_1}} = 0 \quad , \tag{C.30f}$$

$$V_{\vec{q}_{\|}}^{m_1^{\lambda_1},n_2^{\lambda_2},m_3^{\lambda_2},m_4^{\lambda_1}} = 0 \quad , \tag{C.30g}$$

$$V_{\vec{q}_{\|}}^{n_1^{\lambda_1},m_2^{\lambda_2},m_3^{\lambda_2},m_4^{\lambda_1}} = 0 \quad . \tag{C.30h}$$

This concludes the appendix on the interaction Hamiltonian. The main result of the appendix is the complete list of the Coulomb potential for different quantum number n_x and m_x.

Bibliography

[1] H. Haken, "Quantum Field Theory of Solids, An Introduction", North-Holland, New-York, 1988.
[2] N. Peyghambarian, S. W. Koch, A. Mysyrowics, "Introduction to Semiconductor Optics", Prentic Hall, New Jersey, 1993.
[3] For a textbook discussion see: W. W. Chow, S. W. Koch, M. sargent III, "Semiconductor Laser Physics", Springer-Verlag, Berlin, 1994.

Appendix D

The Light Hamiltonian

In chapter 3 we presented the excitonic semiconductor response for varying material thickness. As stated in the chapter we neglected terms attributed to intra-band transitions. However, we did not show the derivation of the terms, which account for the interaction between light and matter. The derivation is shown in this appendix. The Hamiltonian describing our system is

$$H_{el} = H_{0,el} + H_{el,l} + H_I \quad , \tag{D.1}$$

where the terms on the right hand-side have been explained in chapter 3. In the following we will investigate the electron-light Hamiltonian.

$$H_{el,l} = \int d^3r \psi^\dagger(\vec{r}) \left(-\frac{\hbar e}{imc_0} \vec{A}(\vec{r}) \nabla \right) \psi(\vec{r}) \quad . \tag{D.2}$$

The different symbols have been declared previously, (see chapter 3). It should be mentioned that we in our treatment have neglected the non-linear electron-light Hamiltonian,

$$H^{nl}_{el,l} = \int d^3r \psi^\dagger(\vec{r}) \left(-\frac{1}{2m} \frac{e^2}{c_0^2} \vec{A}^2 \right) \psi(\vec{r}) \quad . \tag{D.3}$$

The neglection of the non-linear light Hamiltonian is justified for small values of $\vec{A}$. Since $\vec{A}$ is an operator this means in effect that the matrix elements of $\vec{A}$ must be sufficiently small for the field considered. In our numerical treatment we only considered the case of linear optics, where a weak optical excitation is required of the semiconductor sample. Furthermore, we are only interested in the optical transitions close to the band-edge, $\vec{k} \approx 0$.

D.1 The linear light Hamiltonian

The Heisenberg annihilation and creation operators are expanded in terms of the eigenfunctions of the free particle Hamiltonian (see appendix C), which are inserted into the linear light Hamiltonian,

$$\begin{aligned} H_{el,l} \;=\; & \sum_{\substack{\vec{k}_{1_\parallel}\vec{k}_{2_\parallel} \\ n_1, n_2}} \int d^3r a^\dagger_{\vec{k}_{1_\parallel},n_1,v} \frac{e^{-i\vec{k}_{1_\parallel}\cdot\vec{\rho}}}{L} \overline{f}_{n_1,\lambda_1}(z)\overline{u}_{\lambda_1}(\vec{k}_1,\vec{r}) \\ & \times \left(-\frac{\hbar e}{mic_0}\vec{A}(\vec{r})\nabla\right) a_{\vec{k}_{2_\parallel},n_2,c} \frac{e^{i\vec{k}_{2_\parallel}\cdot\vec{\rho}}}{L} f_{n_2,\lambda_2}(z)u_{\lambda_2}(\vec{k}_2,\vec{r}) \\ & + h.a. \quad , \end{aligned} \tag{D.4}$$

where $h.a.$ stands for hermitian adjoint. All functions entering equation (D.4) can be assumed to be slowly varying compared to the Bloch function $u_\lambda(\vec{k},\vec{r})$. By splitting the integral into a summation over many small volume integrals, the equation for the light Hamiltonian yields,

$$H_{el,l} \;=\; \sum_{\substack{\vec{k}_{1_\parallel}\vec{k}_{2_\parallel} \\ n_1, n_2}} a^\dagger_{\vec{k}_{1_\parallel},n_1,v} a_{\vec{k}_{2_\parallel},n_2,c} \sum_m^M \frac{1}{M}\frac{L}{l^3} e^{-i(\vec{k}_{1_\parallel}-\vec{k}_{2_\parallel})\cdot\vec{\rho}} \overline{f}_{n_1,v} \tag{D.5}$$

$$
\times \left(-\frac{\hbar e}{mic_0}\vec{A}(\vec{r})\right) \left\{ f_{n_2,c} \underbrace{\int_{l^3} d^3 r_l \overline{u}_v(\vec{k}_1 \approx \vec{0}, \vec{r}) \nabla u_c(\vec{k}_2 \approx \vec{0}, \vec{r})}_{Interband \quad transition} \right.
$$

$$
+ \left(i\frac{\partial}{\partial \vec{\rho}} \left(\vec{k}_{2_\parallel} \cdot \vec{\rho}\right) f_{n_2,c} + \frac{\partial f_{n_2,c}}{\partial z} \right)
$$

$$
\left. \times \underbrace{\int_{l^3} d^3 r_l \overline{u}_v(\vec{k}_1 \approx \vec{0}, \vec{r}) u_c(\vec{k}_2 \approx \vec{0}, \vec{r})}_{Intraband \quad transition} \right\} + h.a. \quad .
$$

The volume integrals in equation D.5 yield,

$$
\frac{1}{l^3} \int_{l^3} dr_l^3 \overline{u}_{\lambda_1}(\vec{k}_1 \approx \vec{0}, \vec{r}) \nabla u_{\lambda_2}(\vec{k}_2 \approx \vec{0}, \vec{r}) = \chi_{\lambda_1,\lambda_2} \quad , \tag{D.6a}
$$

$$
\frac{1}{l^3} \int_{l^3} d^3 r_l \overline{u}_{\lambda_1}(\vec{k}_1 \approx \vec{0}, \vec{r}) u_{\lambda_2}(\vec{k}_2 \approx \vec{0}, \vec{r}) = \delta_{\lambda_1,\lambda_2} \quad , \tag{D.6b}
$$

where $\chi_{\lambda_1,\lambda_2}$ is related to the dipole moment, see equation (D.17). The diagonal values of χ are $\chi_{c,c} = \chi_{v,v} = 0$ [1]. The treatment of the intra-band transitions is omitted in the following since we want to calculate the optical transmission spectrum near the bandgap. The electron-light Hamiltonian, if only inter-band transitions are considered, yields

$$
H_{el,l} = \sum_{\substack{\vec{k}_{1_\parallel}, \vec{k}_{2_\parallel} \\ n_1, n_2}} a^\dagger_{\vec{k}_{1_\parallel},n_1,v} a_{\vec{k}_{2_\parallel},n_2,c} \int d^3 r \frac{1}{L^2} e^{-i(\vec{k}_{1_\parallel} - \vec{k}_{2_\parallel}) \cdot \vec{\rho}} \overline{f}_{n_1,v} \tag{D.7}
$$

$$
\times \left(-\frac{\hbar e}{mic_0}\vec{A}(\vec{r})\right) f_{n_2,c} \chi_{v,c} + h.a. \quad .
$$

The area integral ($\int d^2\rho$) can be calculated, since the electrical field is assumed to consist of plane waves.

$$\begin{aligned} H_{el,l} &= \sum_{\substack{\vec{k}_{\parallel} \\ n_1, n_2}} a^{\dagger}_{\vec{k}_{\parallel},n_1,v} a_{\vec{k}_{\parallel},n_2,c} \int dz \overline{f}_{n_1,v} \\ &\quad \times \left(-\frac{\hbar e}{mic_0} \vec{A}(\vec{r}) \right) f_{n_2,c} \chi_{v,c} \quad . \end{aligned} \tag{D.8}$$

Here, the vector potential $\vec{A}$ is treated classically in our approach. The electrical field is expressed by the vector potential [1],

$$\vec{E} = -\frac{1}{c_0}\frac{\partial \vec{A}}{\partial t} - \nabla V(\vec{r}) \quad . \tag{D.9}$$

The scalar potential $V(\vec{r})$ must in the Coulomb Gauge case satisfy

$$\nabla \cdot \nabla V(\vec{r}) = \nabla^2 V(\vec{r}) = -4\pi \vec{\varrho}(\vec{r}) \quad , \tag{D.10}$$

where $\vec{\varrho}(\vec{r})$ is the charge density, which in this case is zero. Let us, for the vector potential and the electrical field, make the slowly varying envelope approximation.

$$\vec{A}(\vec{r}) \approx A(r)e^{-i\omega_l t} + \overline{A}(r)e^{i\omega_l t} \quad , \tag{D.11a}$$

$$\vec{E}_T = -\frac{1}{c_0}\frac{\partial \vec{A}(\vec{r})}{\partial t} \approx E_T e^{-i\omega_l t} + \overline{E}_T e^{i\omega_l t} = i\frac{\omega_l}{c_0}\frac{\partial \vec{A}(\vec{r})}{\partial t} \tag{D.11b}$$

One has to keep in mind that the light Hamiltonian is Hermitian adjoint, which implies that the light Hamiltonian yields,

$$\begin{aligned} H_{el,l} &= \sum_{\substack{\vec{k}_{\parallel} \\ n_1, n_2}} a^{\dagger}_{\vec{k}_{\parallel},n_1,v} a_{\vec{k}_{\parallel},n_2,c} \int dz \overline{f}_{n_1,\lambda_1} \\ &\quad \times \left(-\frac{\hbar e}{mic_0} \left(A(\vec{r})e^{-i\omega_l t} + \overline{A}(\vec{r})e^{i\omega_l t} \right) \right) f_{n_2,\lambda_2} \chi_{\lambda_1,\lambda_2} \\ &\quad + \sum_{\substack{\vec{k}_{\parallel} \\ n_1, n_2}} a^{\dagger}_{\vec{k}_{\parallel},n_1,c} a_{\vec{k}_{\parallel},n_2,v} \int dz \overline{f}_{n_1,\lambda_1} \end{aligned} \tag{D.12}$$

$$\times \left(\frac{\hbar e}{mic_0} \left(A(\vec{r})e^{-i\omega_l t} + \overline{A}(\vec{r})e^{i\omega_l t} \right) \right) f_{n_2,\lambda_2} \chi_{\lambda_1,\lambda_2} \quad .$$

The vector potential expressed by the slowly varying envelope function of the electrical field is,

$$\vec{A}(\vec{r}) = -i\frac{c_0}{\omega_l} E_T e^{-i\omega_l t} + i\frac{c_0}{\omega_l}\overline{E}_T e^{i\omega_l t} \quad . \tag{D.13}$$

The annihilation and creation operators are in the interaction picture [2, p.124].

$$a_{\vec{k}_\|,n,\lambda} \rightarrow a_{\vec{k}_\|,n,\lambda} e^{-i\omega_{\vec{k}_\|,n,\lambda} t} \quad , \tag{D.14a}$$

$$a^\dagger_{\vec{k}_\|,n,\lambda} \rightarrow a^\dagger_{\vec{k}_\|,n,\lambda} e^{i\omega_{\vec{k}_\|,n,\lambda} t} \quad , \tag{D.14b}$$

where $\hbar\omega_{\vec{k}_\|,n,\lambda}$ is the energy of the electron. In the following we assume $\omega_{\vec{k}_\|,n,c} - \omega_{\vec{k}_\|,n,v} \approx \omega_l$. The light Hamiltonian becomes by using equation (D.13) and (D.14) and applying the Rotating Wave Approximation (RWA),

$$\begin{aligned} H_{el,l} = & - \sum_{\vec{k}_\| n_1,\, n_2} a^\dagger_{\vec{k}_\|,n_1,c} a_{\vec{k}_\|,n_2,v} d_{c,v}^{\vec{k}_\|,n_1,n_2} \\ & \times \int dz \overline{f}_{n_1,c}(z) f_{n_2,v}(z) E_T(z) \\ & - \sum_{\substack{\vec{k}_\|,\, \vec{k}_\| \\ n_1,\, n_2}} a^\dagger_{\vec{k}_\|,n_1,v} a_{\vec{k}_\|,n_2,c} d_{vc}^{\vec{k}_\|,n_1,n_2} \\ & \times \int dz \overline{f}_{n_1,v}(z) f_{n_2,c}(z) \overline{E}_T(z) \quad , \end{aligned} \tag{D.15a}$$

$$\begin{aligned} = & - \sum_{\vec{k}_\| n_1,\, n_2} a^\dagger_{\vec{k}_\|,n_1,c} a_{\vec{k}_\|,n_2,v} d_{c,v}^{\vec{k}_\|,n_1,n_2} E_{\vec{k}_\|}^{n_1^c,n_2^v} \\ & - \sum_{\vec{k}_\| n_1,\, n_2} a^\dagger_{\vec{k}_\|,n_1,v} a_{\vec{k}_\|,n_2,c} d_{v,c}^{\vec{k}_\|,n_1,n_2} \overline{E}_{\vec{k}_\|}^{n_1^v,n_2^c} \end{aligned} \tag{D.15b}$$

Here, the definition of the dipole moment is,

$$d_{\lambda_1,\lambda_2}^{\vec{k}_\parallel,n_1,n_2} = d_{\lambda_1,\lambda_2}^0 \frac{E_{gap}}{E_{gap} + \frac{\hbar^2|\vec{k}|^2}{2m_r} + ((n_1^v)^2 - 1)\frac{\hbar^2\pi^2}{2m_v L_z^2} + ((n_2^c)^2 - 1)\frac{\hbar^2\pi^2}{2m_c L_z^2}} \quad . \tag{D.16}$$

The reference dipole moment d_{cv}^0 at the bandgap energy is,

$$d_{\lambda_1,\lambda_2}^0 = \frac{\hbar e}{m\omega_{gab}} \chi_{\lambda_1,\lambda_2} \quad . \tag{D.17}$$

This concludes the treatment of the light Hamiltonian presented in this appendix. The approximations made in this appendix are the introduction of the slowly varying envelope approximation and the RWA.

Bibliography

[1] A. Yariv, "Quantum Electronics", third edition, John Wiley & Sons, New-York, 1989.
[2] H. Haken, "Quantum Field Theory of Solids, An Introduction", North-Holland, New-York, 1988.

Appendix E

The Wave-Propagation Equation, Maxwell's Equation.

In this appendix the analytical solution of Maxwell's equation (the wave propagation equation) is presented. The electrical field boundary conditions at the interfaces are presented in the second part of this appendix and are used to determine the electrical field for a semiconductor slab with a finite width.

E.1 The wave propagation equation

The electrical field vector potential $\vec{A}(\vec{r})$ is related to the expectation value of the current ($< j >$) by Maxwell's equations.

$$\left(\nabla_{\vec{r}}^2 - \frac{1}{c^2}\frac{\partial^2}{\partial t^2}\right)\vec{A} \quad = \quad -\frac{4\pi}{c_0} < \hat{j} > \quad , \tag{E.1a}$$

$$\left(\nabla_{\vec{r}}^2 - \frac{1}{c^2}\frac{\partial^2}{\partial t^2}\right)\vec{E}_T \quad = \quad \frac{4\pi}{c_0^2}\frac{\partial < \hat{j} >}{\partial t} \quad , \tag{E.1b}$$

where c and c_0 are the speed of light in the material and in vacuum, respectively. $\vec{E}_T$ is the transverse electrical field. Equation (E.1b) is determined by the relation between the electrical field and the vector potential

$$\vec{E}_T = -\frac{1}{c_0}\frac{\partial \vec{A}}{\partial t} \tag{E.2}$$

The expectation value of the current is determined by the linear light Hamiltonian, see also chapter 3 or appendix D,

$$H_{el,l} \quad = \quad -\frac{1}{c_0}\int d^3r\psi^\dagger \frac{\hbar e}{mi}\nabla\vec{A}\psi \tag{E.3a}$$

$$\quad = \quad -\frac{1}{c_0}\int d^3r\hat{j}\vec{A} \tag{E.3b}$$

The current and the expectation value of the current yield,

$$\hat{j} \quad = \quad \psi^\dagger\frac{\hbar e}{mi}\nabla\psi \quad , \tag{E.4a}$$

$$\left\langle \hat{j} \right\rangle \quad = \quad \left\langle \psi^\dagger\frac{\hbar e}{mi}\nabla\psi \right\rangle \tag{E.4b}$$

$$\quad = \quad -i\frac{\hbar e}{m}\left\langle \psi^\dagger\nabla\psi \right\rangle \quad , \tag{E.4c}$$

$$\approx \quad \underbrace{-i\frac{\hbar e}{mL^2}\left\langle \sum_{\substack{\vec{k}_\parallel \\ n_1, n_2 \\ \lambda_1, \lambda_2}} a^\dagger_{k_\parallel, n_1, \lambda_1} a_{k_\parallel, n_2, \lambda_2} \overline{f}_{n_1, \lambda_1} f_{n_2, \lambda_2} \chi_{\lambda_1, \lambda_2} \right\rangle}_{interband\ term} \tag{E.4d}$$

$$= -i\frac{\omega_{gab}}{L^2}\left\langle \sum_{\substack{k_\parallel \\ n_1, n_2 \\ \lambda_1, \lambda_2}} d_{\lambda_1,\lambda_2}^{\vec{k}_\parallel, n_1^{\lambda_1}, n_2^{\lambda_2}} \overline{f}_{n_1,\lambda_1} f_{n_2,\lambda_2} a^\dagger_{k_\parallel,\lambda_1} a_{k_\parallel,\lambda_2} \right\rangle \tag{E.4e}$$

$$= -i\frac{\omega_{gab}}{L^2} \sum_{\substack{k_\parallel \\ n_1, n_2 \\ \lambda_1, \lambda_2}} d_{\lambda_1,\lambda_2}^{\vec{k}_\parallel, n_1^{\lambda_1}, n_2^{\lambda_2}} \overline{f}_{n_1,\lambda_1} f_{n_2,\lambda_2} \left\langle a^\dagger_{k_\parallel,\lambda_1} a_{k_\parallel,\lambda_2} \right\rangle \tag{E.4f}$$

The dipole moment $d_{\lambda_1,\lambda_2}^{\vec{k}_\parallel, n_1^{\lambda_1}, n_2^{\lambda_2}}$ is non-zero for $\lambda_1 \neq \lambda_2$, only. The annihilation and creation operators are in the interaction picture [1, p. 124],

$$a_{\vec{k}_\parallel,n,\lambda} \rightarrow a_{\vec{k}_\parallel,n,\lambda} e^{-i\omega_{\vec{k}_\parallel,n,\lambda} t} \quad , \tag{E.5a}$$

$$a^\dagger_{\vec{k}_\parallel,n,\lambda} \rightarrow a^\dagger_{\vec{k}_\parallel,n,\lambda} e^{i\omega_{\vec{k}_\parallel,n,\lambda} t} \quad . \tag{E.5b}$$

The expectation value of the current in the interaction picture yields,

$$\begin{aligned}
\left\langle \hat{j} \right\rangle &= -i\frac{\omega_{gab}}{L^2} \sum_{\substack{\vec{k}_\parallel \\ n_1, n_2}} d_{c,v}^{\vec{k}_\parallel, n_1^c, n_2^v} \overline{f}_{n_1,c} f_{n_2,v} \\
&\quad \times \left\langle a^\dagger_{k_\parallel,c} a_{k_\parallel,v} \right\rangle e^{-i(\omega_{\vec{k}_\parallel,n_2^v} - \omega_{\vec{k}_\parallel,n_1^c})t} \\
&\quad -i\frac{\omega_{gab}}{L^2} \sum_{\substack{\vec{k}_\parallel \\ n_1, n_2}} d_{v,c}^{\vec{k}_\parallel, n_1^v, n_2^c} \overline{f}_{n_1,v} f_{n_2,c} \\
&\quad \times \left\langle a^\dagger_{k_\parallel,v} a_{k_\parallel,c} \right\rangle e^{-i(\omega_{\vec{k}_\parallel,n_2^c} - \omega_{\vec{k}_\parallel,n_1^v})t} \quad ,
\end{aligned} \tag{E.6a}$$

$$\approx -i\frac{\omega_{gab}}{L^2} \sum_{\substack{\vec{k}_\parallel \\ n_1, n_2}} d_{c,v}^{\vec{k}_\parallel, n_1^c, n_2^v} \overline{f}_{n_1,c} f_{n_2,v} \left\langle a^\dagger_{k_\parallel,c} a_{k_\parallel,v} \right\rangle e^{i\omega_l t} \tag{E.6b}$$

$$-i\frac{\omega_{gab}}{L^2}\sum_{\substack{\vec{k}_\parallel\\ n_1,n_2}} d_{v,c}^{\vec{k}_\parallel,n_1^v,n_2^c}\overline{f}_{n_1,v}f_{n_2,c}\left\langle a^\dagger_{k_\parallel,v}a_{k_\parallel,c}\right\rangle e^{-i\omega_l t} \quad ,$$

where we in equation (E.6b) have assumed $\omega_{\vec{k}_\parallel,n_2^c}-\omega_{\vec{k}_\parallel,n_1^v}\approx\omega_l$. ω_l is the optical carrier frequency.
The electrical field in the slowly varying envelope approximation yields,

$$\vec{E}_T = E_T e^{-i\omega_l t}+\overline{E}_T e^{i\omega_l t} \quad . \tag{E.7}$$

The solution of the wave propagation equation (Maxwell's equation) is found in the frequency domain. We apply the slowly varying envelope approximation and split the equations into one equation for $e^{-i\omega_l t}$ and one for $e^{i\omega_l t}$. Furthermore, we assume $\omega_l\approx\omega$ and $\omega_{gab}\approx\omega$. Equation (E.1) yields, after applying the slowly varying envelope approximation and assuming the incoming electrical fields to consist of plane waves,

$$\left(\frac{\partial^2}{\partial z^2}+\frac{\omega^2}{c^2}\right)E_T(z,\omega) = -4\pi\frac{\omega^2}{c_0^2}P^{2D}_{n_1^v,n_2^c}(\omega)\overline{f}_{n_1^v}(z)f_{n_2^c}(z) \tag{E.8a}$$

$$\left(\frac{\partial^2}{\partial z^2}+\frac{\omega^2}{c^2}\right)\overline{E}_T(z,\omega) = -4\pi\frac{\omega^2}{c_0^2}\overline{P}^{2D}_{n_1^c,n_2^v}(\omega)\overline{f}_{n_1^v}(z)f_{n_2^c}(z) \quad . \tag{E.8b}$$

Here, $P^{2D}_{n_1^v,n_2^c}(\omega)$ and $\overline{P}^{2D}_{n_1^c,n_2^v}(\omega)$ are,

$$P^{2D}_{n_1^v,n_2^c}(\omega) = \frac{1}{L^2}\sum_{\vec{k}_\parallel,n_1^c,n_2^v} d_{v,c}^{\vec{k}_\parallel,n_1^v,n_2^c}\left\langle a^\dagger_{k_\parallel,v}a_{k_\parallel,c}\right\rangle \tag{E.9a}$$

$$= \frac{1}{L^2}\sum_{\vec{k}_\parallel,n_1^c,n_2^v} d_{v,c}^{\vec{k}_\parallel,n_1^v,n_2^c}p_{\vec{k}_\parallel,n_1^v,n_2^c} \tag{E.9b}$$

$$\overline{P}^{2D}_{n_1^c,n_2^v}(\omega) = \frac{1}{L^2}\sum_{\vec{k}_\parallel,n_1^v,n_2^c} d_{c,v}^{\vec{k}_\parallel,n_1^c,n_2^v}\left\langle a^\dagger_{k_\parallel,c}a_{k_\parallel,v}\right\rangle \tag{E.9c}$$

$$= \frac{1}{L^2}\sum_{\vec{k}_\parallel,n_1^c,n_2^v} d_{c,v}^{\vec{k}_\parallel,n_1^c,n_2^v}p^*_{\vec{k}_\parallel,n_1^c,n_2^v} \quad . \tag{E.9d}$$

The solution of equation (E.8a) is found by assuming the slowly varying envelope function E_T to yield,

$$E_T(z,\omega) = \sum_{n_1^v, n_2^c} E_T^{n_1^v, n_2^c}(z,\omega) \quad . \tag{E.10}$$

Furthermore, we introduce the polarization $P_{n_1^v, n_2^c}$,

$$P_{n_1^v, n_2^c} = \frac{1}{L^2} \sum_{\vec{k}_\parallel} d_{v,c}^{\vec{k}_\parallel, n_1^v, n_2^c} p_{\vec{k}_\parallel, n_1^v, n_2^c} \quad . \tag{E.11}$$

A particular solution of equation (E.8) is determined for each set of quantum numbers n_1^v and n_2^c. Here, we again label even eigenfunctions with quantum number n_x^λ, while odd eigenfunctions are labeled by m_x^λ.
The particular solutions of equation (E.8) for a particular set of eigenfunctions are,

$$\begin{aligned}
E_T^{n_1,n_2}(z,\omega) &= \frac{4\pi}{L_z}\frac{\omega^2}{c_0^2} P_{n_1,n_2}^{2D}(\omega) && \text{(E.12a)}\\
&\quad \times \left(\frac{cos\left((n_1-n_2)\frac{\pi}{L_z}z\right)}{(n_1-n_2)^2\frac{\pi^2}{L_z^2} - \frac{\omega^2}{c^2}} + \frac{cos\left((n_1+n_2)\frac{\pi}{L_z}z\right)}{(n_1+n_2)^2\frac{\pi^2}{L_z^2} - \frac{\omega^2}{c^2}} \right) \quad , \\
E_T^{m_1,m_2}(z,\omega) &= \frac{4\pi}{L_z}\frac{\omega^2}{c_0^2} P_{m_1,m_2}^{2D}(\omega) && \text{(E.12b)}\\
&\quad \left(\frac{cos\left((m_1-m_2)\frac{2\pi}{L_z}z\right)}{(m_1-m_2)^2\frac{4\pi^2}{L_z^2} - \frac{\omega^2}{c^2}} - \frac{cos\left((m_1+m_2)\frac{\pi}{L_z}z\right)}{(m_1+m_2)^2\frac{4\pi^2}{L_z^2} - \frac{\omega^2}{c^2}} \right) \quad , \\
E_T^{n_1,m_2}(z,\omega) &= \frac{4\pi}{L_z}\frac{\omega^2}{c_0^2} P_{n_1,m_2}^{2D}(\omega) && \text{(E.12c)}\\
&\quad \cdot \left(\frac{sin\left((2m_2-n_1)\frac{\pi}{L_z}z\right)}{(2m_2-n_1)^2\frac{\pi^2}{L_z^2} - \frac{\omega^2}{c^2}} + \frac{sin\left((2m_2+n_1)\frac{\pi}{L_z}z\right)}{(2m_2+n_1)^2\frac{\pi^2}{L_z^2} - \frac{\omega^2}{c^2}} \right) \quad , \\
&= E_T^{m_2,n_1}(z,\omega) \quad . && \text{(E.12d)}
\end{aligned}$$

Here, we have omitted the index for the conduction c and valence band v, since they are interchangeable.

So, the solution of the wave propagation equation (Maxwell's equation) in the frequency domain yields,

$$\begin{aligned} E_T(z,\omega) &= \sum_{n_1^v,n_2^c} E_T^{n_1^v,n_2^c} + \sum_{m_1^v,m_2^c} E_T^{m_1^v,m_2^c} + \sum_{n_1^v,m_2^c} E_T^{n_1^v,m_2^c} \\ &+ \sum_{m_1^v,n_2^c} E_T^{m_1^v,n_2^c} + t_f(\omega)e^{-i\frac{\omega}{c}z} r_f(\omega)e^{i\frac{\omega}{c}z} \quad , \end{aligned} \tag{E.13}$$

where $t_f(\omega)$ and $r_f(\omega)$ are arbitrary functions, which have to be chosen in agreement with the boundary conditions at the interfaces of the semiconductor slab.
In the following section we will derive expressions of the functions $t_f(\omega)$ and $r_f(\omega)$.

E.2 The boundary conditions

In this section we derive the conditions which the electrical field has to satisfy at the boundaries of the semiconductor slab. The semiconductor slab is shown in Fig. E.1. As indicated on the figure, there are three regions, where the electrical field has to be considered. In the following we will consider the general case where we have the refractive index n_{g_1} in the region with E_{in} and E_{ref}. The semiconductor has the refractive index n_{g_2} and the region with the transmitted electrical field has the refractive index n_{g_3}. In this case, the slowly varying envelope function of the electrical field in these three regions yield,

$$E_I(z) = E_{in}e^{in_{g1}\frac{\omega}{c_0}z} + E_{ref}e^{-in_{g1}\frac{\omega}{c_0}z} \tag{E.14a}$$

$$E_{II}(z) = E_t e^{in_{g2}\frac{\omega}{c_0}z} + E_r e^{-in_{g2}\frac{\omega}{c_0}z} + E_T^{inho}(z) \tag{E.14b}$$

$$E_{III}(z) = E_{tra}e^{in_{g3}\frac{\omega}{c_0}z} \quad . \tag{E.14c}$$

In the following, we have introduced the wave vector $k_z = \frac{\omega}{c_0}$.
The electrical field and its first derivative have to be continuous at the semiconductor slab boundaries, $(z = \pm L_z/2)$. The incoming light field E_{in} is known and we can, by using the boundary conditions, derive expressions

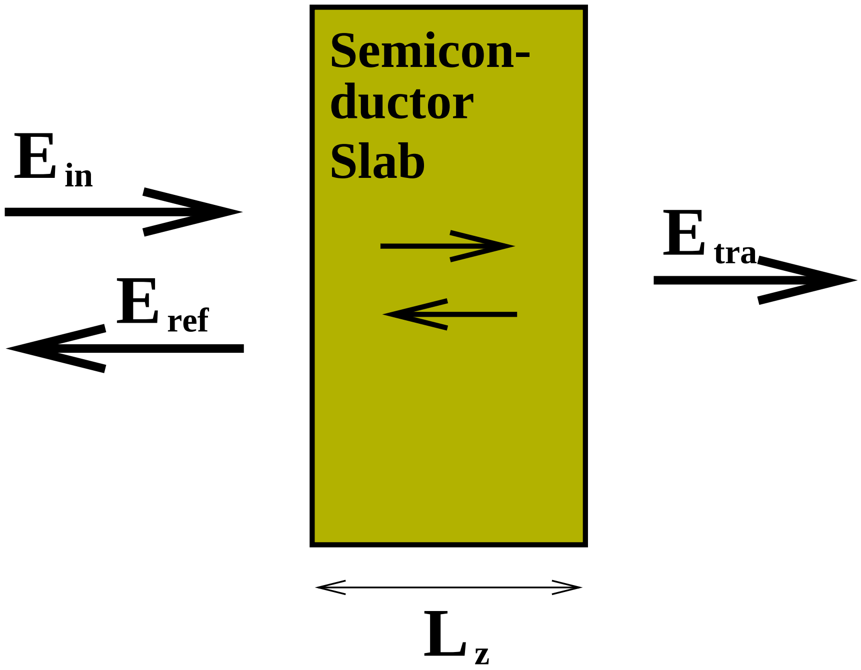

Figure E.1: Schematic plot of a semiconductor slab with thickness L_z, which is excited by an incoming light pulse E_{in}. E_{ref} is the reflected field and E_{tra} is the transmitted field. The two counter propagating fields in the semiconductor slab after excitation are indicated by two arrows.

for the reflected, transmitted and internal light fields.

$$
\begin{aligned}
E_t \quad &= \quad E_{in} \frac{2}{1+\frac{n_{g_2}}{n_{g_1}}} \frac{e^{i(n_{g_2}-n_{g_1})k_z \frac{L_z}{2}}}{1-\frac{\left(1-\frac{n_{g_2}}{n_{g_3}}\right)\left(1-\frac{n_{g_2}}{n_{g_1}}\right)}{\left(1+\frac{n_{g_2}}{n_{g_1}}\right)\left(1+\frac{n_{g_2}}{n_{g_3}}\right)} e^{i4n_{g_2}k_z \frac{L_z}{2}}} \\
&\quad - \frac{E_t^{inho}\left(-\frac{L_z}{2}\right)}{1+\frac{n_{g_2}}{n_{g_1}}} \frac{e^{in_{g_2}k_z \frac{L_z}{2}}}{1-\frac{\left(1-\frac{n_{g_2}}{n_{g_3}}\right)\left(1-\frac{n_{g_2}}{n_{g_1}}\right)}{\left(1+\frac{n_{g_2}}{n_{g_1}}\right)\left(1+\frac{n_{g_2}}{n_{g_3}}\right)} e^{i4n_{g_2}k_z \frac{L_z}{2}}}
\end{aligned}
\tag{E.15a}
$$

$$
\begin{aligned}
& +\frac{E_T^{inho}\left(\frac{L_z}{2}\right)}{1+\frac{n_{g_2}}{n_{g_1}}} \frac{\frac{1-\frac{n_{g_2}}{n_{g_1}}}{1+\frac{n_{g_2}}{n_{g_3}}} e^{i3n_{g_2}k_z\frac{L_z}{2}}}{1-\frac{\left(1-\frac{n_{g_2}}{n_{g_3}}\right)\left(1-\frac{n_{g_2}}{n_{g_1}}\right)}{\left(1+\frac{n_{g_2}}{n_{g_1}}\right)\left(1+\frac{n_{g_2}}{n_{g_3}}\right)} e^{i4n_{g_2}k_z\frac{L_z}{2}}} \quad , \\
E_r \quad = \quad & -\frac{E_T^{inho}\left(\frac{L_z}{2}\right)}{1+\frac{n_{g_2}}{n_{g_3}}} e^{in_{g_2}k_z\frac{L_z}{2}} \qquad\qquad \text{(E.15b)} \\
& -E_{in}\frac{2\left(1-\frac{n_{g_2}}{n_{g_3}}\right)}{\left(1+\frac{n_{g_2}}{n_{g_1}}\right)\left(1+\frac{n_{g_2}}{n_{g_3}}\right)} \frac{e^{i(3n_{g_2}-n_{g_1})k_z\frac{L_z}{2}}}{1-\frac{\left(1-\frac{n_{g_2}}{n_{g_3}}\right)\left(1-\frac{n_{g_2}}{n_{g_1}}\right)}{\left(1+\frac{n_{g_2}}{n_{g_1}}\right)\left(1+fracn_{g_2}n_{g_3}\right)} e^{i4n_{g_2}k_z\frac{L_z}{2}}} \\
& +\frac{\left(1-\frac{n_{g_2}}{n_{g_3}}\right)E_T^{inho}\left(-\frac{L_z}{2}\right)}{\left(1+\frac{n_{g_2}}{n_{g_1}}\right)\left(1+\frac{n_{g_2}}{n_{g_3}}\right)} \frac{e^{i3n_{g_2}k_z\frac{L_z}{2}}}{1-\frac{\left(1-\frac{n_{g_2}}{n_{g_3}}\right)\left(1-\frac{n_{g_2}}{n_{g_1}}\right)}{\left(1+\frac{n_{g_2}}{n_{g_1}}\right)\left(1+\frac{n_{g_2}}{n_{g_3}}\right)} e^{i4n_{g_2}k_z\frac{L_z}{2}}} \\
& -\frac{\left(1-\frac{n_{g_2}}{n_{g_3}}\right)E_T^{inho}\left(\frac{L_z}{2}\right)}{\left(1+\frac{n_{g_2}}{n_{g_1}}\right)\left(1+\frac{n_{g_2}}{n_{g_3}}\right)} \frac{\frac{1-\frac{n_{g_2}}{n_{g_1}}}{1+\frac{n_{g_2}}{n_{g_3}}} e^{i5n_{g_2}k_z\frac{L_z}{2}}}{1-\frac{\left(1-\frac{n_{g_2}}{n_{g_3}}\right)\left(1-\frac{n_{g_2}}{n_{g_1}}\right)}{\left(1+\frac{n_{g_2}}{n_{g_1}}\right)\left(1+\frac{n_{g_2}}{n_{g_3}}\right)} e^{i4n_{g_2}k_z\frac{L_z}{2}}} \quad .
\end{aligned}
$$

The reflected field E_{ref} yields,

$$
\begin{aligned}
E_{ref} \quad = \quad & E_{in}\frac{1-\frac{n_{g_2}}{n_{g_1}}}{1+\frac{n_{g_2}}{n_{g_1}}} \frac{e^{-i2n_{g_2}k_z\frac{L_z}{2}}}{1-\frac{\left(1-\frac{n_{g_2}}{n_{g_3}}\right)\left(1-\frac{n_{g_2}}{n_{g_1}}\right)}{\left(1+\frac{n_{g_2}}{n_{g_1}}\right)\left(1+\frac{n_{g_2}}{n_{g_3}}\right)} e^{i4n_{g_2}k_z\frac{L_z}{2}}} \qquad\qquad \text{(E.16)} \\
& -\frac{\left(1-\frac{n_{g_2}}{n_{g_1}}\right)E_T^{inho}\left(-\frac{L_z}{2}\right)}{2\left(1+\frac{n_{g_2}}{n_{g_1}}\right)} \frac{e^{-in_{g_1}k_z\frac{L_z}{2}}}{1-\frac{\left(1-\frac{n_{g_2}}{n_{g_3}}\right)\left(1-\frac{n_{g_2}}{n_{g_1}}\right)}{\left(1+\frac{n_{g_2}}{n_{g_1}}\right)\left(1+\frac{n_{g_2}}{n_{g_3}}\right)} e^{i4n_{g_2}k_z\frac{L_z}{2}}} \\
& +\frac{\left(1-\frac{n_{g_2}}{n_{g_1}}\right)^2 E_T^{inho}\left(\frac{L_z}{2}\right)}{2\left(1+\frac{n_{g_2}}{n_{g_1}}\right)\left(1+\frac{n_{g_2}}{n_{g_3}}\right)} \frac{e^{i(2n_{g_2}-n_{g_1})k_z\frac{L_z}{2}}}{1-\frac{\left(1-\frac{n_{g_2}}{n_{g_3}}\right)\left(1-\frac{n_{g_2}}{n_{g_1}}\right)}{\left(1+\frac{n_{g_2}}{n_{g_1}}\right)\left(1+\frac{n_{g_2}}{n_{g_3}}\right)} e^{i4n_{g_2}k_z\frac{L_z}{2}}} \\
& -\frac{E_T^{inho}\left(\frac{L_z}{2}\right)}{2}\frac{1+\frac{n_{g_2}}{n_{g_1}}}{1+\frac{n_{g_2}}{n_{g_3}}} e^{i(2n_{g_2}-n_{g_1}k_z\frac{L_z}{2}}
\end{aligned}
$$

$$
\begin{aligned}
&-E_{in}\frac{1-\frac{n_{g_2}}{n_{g_3}}}{1+\frac{n_{g_2}}{n_{g_3}}}\frac{e^{i(4n_{g_2}-2n_{g_1})k_z\frac{L_z}{2}}}{1-\frac{\left(1-\frac{n_{g_2}}{n_{g_3}}\right)\left(1-\frac{n_{g_2}}{n_{g_1}}\right)}{\left(1+\frac{n_{g_2}}{n_{g_1}}\right)\left(1+\frac{n_{g_2}}{n_{g_3}}\right)}e^{i4n_{g_2}k_z\frac{L_z}{2}}}\\
&+\frac{E_T^{inho}\left(-\frac{L_z}{2}\right)}{2\left(1+\frac{n_{g_2}}{n_{g_3}}\right)}\frac{e^{i(4n_{g_2}-n_{g_1})k_z\frac{L_z}{2}}}{1-\frac{\left(1-\frac{n_{g_2}}{n_{g_3}}\right)\left(1-\frac{n_{g_2}}{n_{g_1}}\right)}{\left(1+\frac{n_{g_2}}{n_{g_1}}\right)\left(1+\frac{n_{g_2}}{n_{g_3}}\right)^2}e^{i4n_{g_2}k_z\frac{L_z}{2}}}\\
&-\frac{\left(1-\frac{n_{g_2}}{n_{g_3}}\right)E_T^{inho}\left(\frac{L_z}{2}\right)}{2\left(1+\frac{n_{g_2}}{n_{g_3}}\right)^2}\frac{\left(1-\frac{n_{g_2}}{n_{g_1}}\right)e^{i(6n_{g_2}-n_{g_1})k_z\frac{L_z}{2}}}{1-\frac{\left(1-\frac{n_{g_2}}{n_{g_3}}\right)\left(1-\frac{n_{g_2}}{n_{g_1}}\right)}{\left(1+\frac{n_{g_2}}{n_{g_1}}\right)\left(1+\frac{n_{g_2}}{n_{g_3}}\right)}e^{i4n_{g_2}k_z\frac{L_z}{2}}}\\
&+\frac{E_T^{inho}\left(-\frac{L_z}{2}\right)}{2}e^{-in_{g_1}k_z\frac{L_z}{2}} \quad .
\end{aligned}
$$

The experimental observable transmission is, of course, related to the transmitted electrical field, (see chapter 3).

$$
\begin{aligned}
E_{tra} \;=\; &\frac{E_T^{inho}\left(\frac{L_z}{2}\right)}{2}e^{-in_{g_3}k_z\frac{L_z}{2}}\\
&+E_{in}\frac{1+\frac{n_{g_2}}{n_{g_3}}}{1+\frac{n_{g_2}}{n_{g_1}}}\frac{e^{i(2n_{g_2}-n_{g_1}-n_{g_3})k_z\frac{L_z}{2}}}{1-\frac{\left(1-\frac{n_{g_2}}{n_{g_3}}\right)\left(1-\frac{n_{g_2}}{n_{g_1}}\right)}{\left(1+\frac{n_{g_2}}{n_{g_1}}\right)\left(1+\frac{n_{g_2}}{n_{g_3}}\right)}e^{i4n_{g_2}k_z\frac{L_z}{2}}}\\
&-\frac{\left(1+\frac{n_{g_2}}{n_{g_3}}\right)E_T^{inho}\left(-\frac{L_z}{2}\right)}{2\left(1+\frac{n_{g_2}}{n_{g_1}}\right)}\frac{e^{i(2n_{g_2}-n_{g_3})k_z\frac{L_z}{2}}}{1-\frac{\left(1-\frac{n_{g_2}}{n_{g_3}}\right)\left(1-\frac{n_{g_2}}{n_{g_1}}\right)}{\left(1+\frac{n_{g_2}}{n_{g_1}}\right)\left(1+\frac{n_{g_2}}{n_{g_3}}\right)}e^{i4n_{g_2}k_z\frac{L_z}{2}}}\\
&+\frac{\left(1-\frac{n_{g_2}}{n_{g_1}}\right)E_T^{inho}\left(\frac{L_z}{2}\right)}{2\left(1+\frac{n_{g_2}}{n_{g_1}}\right)}\frac{e^{i(4n_{g_2}-n_{g_3})k_z\frac{L_z}{2}}}{1-\frac{\left(1-\frac{n_{g_2}}{n_{g_3}}\right)\left(1-\frac{n_{g_2}}{n_{g_1}}\right)}{\left(1+\frac{n_{g_2}}{n_{g_1}}\right)\left(1+\frac{n_{g_2}}{n_{g_3}}\right)}e^{i4n_{g_2}k_z\frac{L_z}{2}}}\\
&-\frac{E_T^{inho}\left(\frac{L_z}{2}\right)}{2}\frac{1-\frac{n_{g_2}}{n_{g_3}}}{1+\frac{n_{g_2}}{n_{g_3}}}e^{-in_{g_3}k_z\frac{L_z}{2}}
\end{aligned}
\tag{E.17}
$$

$$-E_{in}\frac{\left(1-\frac{n_{g2}}{n_{g3}}\right)^2}{\left(1+\frac{n_{g2}}{n_{g3}}\right)\left(1+\frac{n_{g2}}{n_{g1}}\right)}\frac{e^{i(2n_{g2}-n_{g1}-n_{g3})k_z\frac{L_z}{2}}}{1-\frac{\left(1-\frac{n_{g2}}{n_{g3}}\right)\left(1-\frac{n_{g2}}{n_{g1}}\right)}{\left(1+\frac{n_{g2}}{n_{g1}}\right)\left(1+\frac{n_{g2}}{n_{g3}}\right)}e^{i4n_{g2}k_z\frac{L_z}{2}}}$$

$$+\frac{\left(1-\frac{n_{g2}}{n_{g3}}\right)^2 E_T^{inho}\left(-\frac{L_z}{2}\right)}{2\left(1+\frac{n_{g2}}{n_{g1}}\right)\left(1+\frac{n_{g2}}{n_{g3}}\right)}\frac{e^{i(2n_{g1}-n_{g3})k_z\frac{L_z}{2}}}{1-\frac{\left(1-\frac{n_{g2}}{n_{g3}}\right)\left(1-\frac{n_{g2}}{n_{g1}}\right)}{\left(1+\frac{n_{g2}}{n_{g1}}\right)\left(1+\frac{n_{g2}}{n_{g3}}\right)}e^{i4n_{g2}k_z\frac{L_z}{2}}}$$

$$-\frac{\left(1-\frac{n_{g2}}{n_{g3}}\right)^2\left(1-\frac{n_{g2}}{n_{g1}}\right) E_T^{inho}\left(\frac{L_z}{2}\right)}{2\left(1+\frac{n_{g2}}{n_{g3}}\right)^2\left(1+\frac{n_{g2}}{n_{g1}}\right)}\frac{e^{i(4n_{g2}-n_{g3})k_z\frac{L_z}{2}}}{1-\frac{\left(1-\frac{n_{g2}}{n_{g3}}\right)\left(1-\frac{n_{g2}}{n_{g1}}\right)}{\left(1+\frac{n_{g2}}{n_{g1}}\right)\left(1+\frac{n_{g2}}{n_{g3}}\right)}e^{i4n_{g2}k_z\frac{L_z}{2}}}$$

The equations for the transmitted, reflected and internal electrical fields become simpler if one considers an index matched semiconductor structure, $n_{g_1} = n_{g_2} = n_{g_3}$. In the following subsection we present the functions for the electrical field for an index matched semiconductor structure.

E.2.1 Index matched semiconductor sample

The boundary conditions derived in the previous section are, in the case of an index matched semiconductor structure, $n_{g_1} = n_{g_2} = n_{g_3}$:

$$E_t = E_{in} - \frac{E_T^{inho}\left(-\frac{L_z}{2}\right)}{2}e^{ik_z\frac{L_z}{2}} \quad , \tag{E.18a}$$

$$E_r = -\frac{E_T^{inho}\left(\frac{L_z}{2}\right)}{2}e^{ik_z\frac{L_z}{2}} \quad , \tag{E.18b}$$

$$E_{tra} = E_{in} + \frac{E_T^{inho}\left(\frac{L_z}{2}\right)}{2}e^{-ik_z\frac{L_z}{2}} - \frac{E_T^{inho}\left(-\frac{L_z}{2}\right)}{2}e^{ik_z\frac{L_z}{2}} \tag{E.18c}$$

$$E_{ref} = \frac{E_T^{inho}\left(-\frac{L_z}{2}\right)}{2}e^{-ik_z\frac{L_z}{2}} - \frac{E_T^{inho}\left(\frac{L_z}{2}\right)}{2}e^{ik_z\frac{L_z}{2}} \quad . \tag{E.18d}$$

Here, $k_z = \frac{\omega}{c}$. Thus, the electrical field E_I, E_{II} and E_{III} can be expressed by the incoming light field E_{in} and the particular solution of the inhomogeneous wave propagation equation.

The electrical field in region I.

$$\begin{aligned} E_I(z,\omega) &= E_{in}e^{ik_zz} \\ &-i2\pi\frac{\omega}{c_0}\frac{c^2}{c_0^2}e^{-ik_zz}\sum_{n_1^v,n_2^c}P_{n_1^v,n_2^c}(\omega)\frac{\sin\left(k_z\frac{L_z}{2}\right)}{k_z\frac{L_z}{2}} \\ &\left(\frac{\cos\left((n_1^v-n_2^c)\frac{\pi}{2}\right)}{(n_1^v-n_2^c)^2\frac{\pi^2c^2}{L_z^2\omega^2}-1}+\frac{\cos\left((n_1^v+n_2^c)\frac{\pi}{2}\right)}{(n_1^v+n_2^c)^2\frac{\pi^2c^2}{L_z^2\omega^2}-1}\right) \\ &-i2\pi\frac{\omega}{c_0}\frac{c^2}{c_0^2}e^{-ik_zz}\sum_{m_1^v,m_2^c}P_{m_1^v,m_2^c}(\omega)\frac{\sin\left(k_z\frac{L_z}{2}\right)}{k_z\frac{L_z}{2}} \\ &\left(\frac{\cos\left((m_1^v-m_2^c)\frac{\pi}{2}\right)}{(m_1^v-m_2^c)^2\frac{\pi^2c^2}{L_z^2\omega^2}-1}-\frac{\cos\left((m_1^v+m_2^c)\frac{\pi}{2}\right)}{(m_1^v+m_2^c)^2\frac{\pi^2c^2}{L_z^2\omega^2}-1}\right) \\ &-2\pi\frac{\omega}{c}d_{cv}e^{-ik_zz}\sum_{m_1^v,n_2^c}P_{m_1^v,n_2^c}(\omega)\frac{\cos\left(k_z\frac{L_z}{2}\right)}{k_z\frac{L_z}{2}} \\ &\left(\frac{\sin\left((m_1^v-n_2^c)\frac{\pi}{2}\right)}{(m_1^v-n_2^c)^2\frac{\pi^2c^2}{L_z^2\omega^2}-1}+\frac{\sin\left((m_1^v+n_2^c)\frac{\pi}{2}\right)}{(m_1^v+n_2^c)^2\frac{\pi^2c^2}{L_z^2\omega^2}-1}\right) \\ &-2\pi\frac{\omega}{c}\frac{c^2}{c_0^2}d_{cv}e^{-ik_zz}\sum_{n_1^v,m_2^c}P_{n_1^v,m_2^c}(\omega)\frac{\cos\left(k_z\frac{L_z}{2}\right)}{k_z\frac{L_z}{2}} \\ &\left(\frac{\sin\left((m_2^c-n_1^v)\frac{\pi}{2}\right)}{(m_2^c-n_1^v)^2\frac{\pi^2c^2}{L_z^2\omega^2}-1}+\frac{\sin\left((n_1^v+m_2^c)\frac{\pi}{2}\right)}{(n_1^v+m_2^c)^2\frac{\pi^2c^2}{L_z^2\omega^2}-1}\right) \quad . \end{aligned} \tag{E.19}$$

Here, $n_x^\lambda = 1,3,5,7...$ and $m_x^{c,v} = 2,4,6,8...$, corresponding to even and odd eigenfunctions.

The electrical field in the semiconductor sample,

$$\begin{aligned} E_{II}(z,\omega) &= E_{in}e^{ik_zz} \\ &-2\pi\frac{\omega}{c}\frac{c^2}{c_0^2}\frac{e^{ik_z\frac{L_z}{2}}}{k_z\frac{L_z}{2}}\frac{e^{ik_zz}+e^{-ik_zz}}{2}\sum_{n_1^v,n_2^c}P_{n_1^v,n_2^c}(\omega) \\ &\left(\frac{\cos\left((n_1^v-n_2^c)\frac{\pi}{2}\right)}{(n_1^v-n_2^c)^2\frac{\pi^2c^2}{L_z^2\omega^2}-1}+\frac{\cos\left((n_1^v+n_2^c)\frac{\pi}{2}\right)}{(n_1^v+n_2^c)^2\frac{\pi^2c^2}{L_z^2\omega^2}-1}\right) \end{aligned} \tag{E.20}$$

$$+2\pi\frac{\omega}{c}\frac{c^2}{c_0^2}\frac{1}{k_z\frac{L_z}{2}}\sum_{n_1^v,n_2^c}P_{n_1^v,n_2^c}(\omega)$$

$$\left(\frac{\cos\left((n_1^v-n_2^c)\frac{\pi}{L_z}z\right)}{(n_1^v-n_2^c)^2\frac{\pi^2c^2}{L_z^2\omega^2}-1}+\frac{\cos\left((n_1^v+n_2^c)\frac{\pi}{L_Z}z\right)}{(n_1^v+n_2^c)^2\frac{\pi^2c^2}{L_z^2\omega^2}-1}\right)$$

$$-2\pi\frac{\omega}{c}\frac{c^2}{c_0^2}\frac{e^{ik_z\frac{L_z}{2}}}{k_z\frac{L_z}{2}}\frac{e^{ik_zz}+e^{-ik_zz}}{2}\sum_{m_1^v,m_2^c}P_{m_1^v,m_2^c}(\omega)$$

$$\left(\frac{\cos\left((m_1^v-m_2^c)\frac{\pi}{2}\right)}{(m_1^v-m_2^c)^2\frac{\pi^2c^2}{L_z^2\omega^2}-1}-\frac{\cos\left((m_1^v+m_2^c)\frac{\pi}{2}\right)}{(m_1^v+m_2^c)^2\frac{\pi^2c^2}{L_z^2\omega^2}-1}\right)$$

$$+2\pi\frac{\omega}{c}\frac{c^2}{c_0^2}\frac{1}{k_z\frac{L_z}{2}}\sum_{m_1^v,m_2^c}P_{m_1^v,m_2^c}(\omega)$$

$$\left(\frac{\cos\left((m_1^v-m_2^c)\frac{\pi}{L_z}z\right)}{(m_1^v-m_2^c)^2\frac{\pi^2c^2}{L_z^2\omega^2}-1}-\frac{\cos\left((m_1^v+m_2^c)\frac{\pi}{L_Z}z\right)}{(m_1^v+m_2^c)^2\frac{\pi^2c^2}{L_z^2\omega^2}-1}\right)$$

$$+2\pi\frac{\omega}{c}\frac{c^2}{c_0^2}\frac{e^{ik_z\frac{L_z}{2}}}{k_z\frac{L_z}{2}}\frac{e^{ik_zz}-e^{-ik_zz}}{2}\sum_{m_1^v,n_2^c}P_{m_1^v,n_2^c}(\omega)$$

$$\left(\frac{\sin\left((m_1^v-n_2^c)\frac{\pi}{2}\right)}{(m_1^v-n_2^c)^2\frac{\pi^2c^2}{L_z^2\omega^2}-1}+\frac{\sin\left((m_1^v+n_2^c)\frac{\pi}{2}\right)}{(m_1^v+n_2^c)^2\frac{\pi^2c^2}{L_z^2\omega^2}-1}\right)$$

$$+2\pi\frac{\omega}{c}\frac{c^2}{c_0^2}\frac{1}{k_z\frac{L_z}{2}}\sum_{m_1^v,n_2^c}P_{m_1^v,n_2^c}(\omega)$$

$$\left(\frac{\sin\left((m_1^v-n_2^c)\frac{\pi}{L_z}z\right)}{(m_1^v-n_2^c)^2\frac{\pi^2c^2}{L_z^2\omega^2}-1}+\frac{\sin\left((m_1^v+n_2^c)\frac{\pi}{L_Z}z\right)}{(m_1^v+n_2^c)^2\frac{\pi^2c^2}{L_z^2\omega^2}-1}\right)$$

$$+2\pi\frac{\omega}{c}\frac{c^2}{c_0^2}\frac{e^{ik_z\frac{L_z}{2}}}{k_z\frac{L_z}{2}}\frac{e^{ik_zz}-e^{-ik_zz}}{2}\sum_{n_1^v,m_2^c}P_{n_1^v,m_2^c}(\omega)$$

$$\left(\frac{\sin\left((m_2^c-n_1^v)\frac{\pi}{2}\right)}{(m_2^c-n_1^v)^2\frac{\pi^2c^2}{L_z^2\omega^2}-1}+\frac{\sin\left((n_1^v+m_2^c)\frac{\pi}{2}\right)}{(n_1^v+m_2^c)^2\frac{\pi^2c^2}{L_z^2\omega^2}-1}\right)$$

$$+2\pi\frac{\omega}{c}\frac{c^2}{c_0^2}\frac{1}{k_z\frac{L_z}{2}}\sum_{n_1^v,m_2^c}P_{n_1^v,m_2^c}(\omega)$$
$$\left(\frac{\sin\left((m_2^c-n_1^v)\frac{\pi}{L_z}z\right)}{(m_2^c-n_1^v)^2\frac{\pi^2c^2}{L_z^2\omega^2}-1}+\frac{\sin\left((n_1^v+m_2^c)\frac{\pi}{L_Z}z\right)}{(n_1^v+m_2^c)^2\frac{\pi^2c^2}{L_z^2\omega^2}-1}\right) \quad .$$

The electrical field in region III (The transmitted signal) is,

$$\begin{aligned}
E_{III}(z,\omega) \quad = \quad & E_{in}e^{ik_zz} \qquad \text{(E.21)}\\
& -i2\pi\frac{\omega}{c}\frac{c^2}{c_0^2}e^{ik_zz}\sum_{n_1^v,n_2^c}P_{n_1^v,n_2^c}(\omega)\frac{\sin\left(k_z\frac{L_z}{2}\right)}{k_z\frac{L_z}{2}}\\
& \left(\frac{\cos\left((n_1^v-n_2^c)\frac{\pi}{2}\right)}{(n_1^v-n_2^c)^2\frac{\pi^2c^2}{L_z^2\omega^2}-1}+\frac{\cos\left((n_1^v+n_2^c)\frac{\pi}{2}\right)}{(n_1^v+n_2^c)^2\frac{\pi^2c^2}{L_z^2\omega^2}-1}\right)\\
& -i2\pi\frac{\omega}{c}\frac{c^2}{c_0^2}e^{ik_zz}\sum_{m_1^v,m_2^c}P_{m_1^v,m_2^c}(\omega)\frac{\sin\left(k_z\frac{L_z}{2}\right)}{k_z\frac{L_z}{2}}\\
& \left(\frac{\cos\left((m_1^v-m_2^c)\frac{\pi}{2}\right)}{(m_1^v-m_2^c)^2\frac{\pi^2c^2}{L_z^2\omega^2}-1}-\frac{\cos\left((m_1^v+m_2^c)\frac{\pi}{2}\right)}{(m_1^v+m_2^c)^2\frac{\pi^2c^2}{L_z^2\omega^2}-1}\right)\\
& +2\pi\frac{\omega}{c}\frac{c^2}{c_0^2}e^{ik_zz}\sum_{m_1^v,n_2^c}d_{v,c}^{\vec{k}_\parallel,m_1^v,n_2^c}P_{m_1^v,n_2^c}(\omega)\frac{\cos\left(k_z\frac{L_z}{2}\right)}{k_z\frac{L_z}{2}}\\
& \left(\frac{\sin\left((m_1^v-n_2^c)\frac{\pi}{2}\right)}{(m_1^v-n_2^c)^2\frac{\pi^2c^2}{L_z^2\omega^2}-1}+\frac{\sin\left((m_1^v+n_2^c)\frac{\pi}{2}\right)}{(m_1^v+n_2^c)^2\frac{\pi^2c^2}{L_z^2\omega^2}-1}\right)\\
& +2\pi\frac{\omega}{c}\frac{c^2}{c_0^2}e^{ik_zz}\sum_{n_1^v,m_2^c}P_{n_1^v,m_2^c}(\omega)\frac{\cos\left(k_z\frac{L_z}{2}\right)}{k_z\frac{L_z}{2}}\\
& \left(\frac{\sin\left((m_2^c-n_1^v)\frac{\pi}{2}\right)}{(m_2^c-n_1^v)^2\frac{\pi^2c^2}{L_z^2\omega^2}-1}+\frac{\sin\left((n_1^v+m_2^c)\frac{\pi}{2}\right)}{(n_1^v+m_2^c)^2\frac{\pi^2c^2}{L_z^2\omega^2}-1}\right) \quad .
\end{aligned}$$

Equations (E.19-E.21) are the analytical solution of the wave propagation equation (Maxwell's equation) in the case where the slowly varying envelope approximation has been made. The equations represent the solution in the case of an index matched structure. An analytical solution in the case of different refractive indices can also be determined. However, if the semiconductor structure is not index matched we cannot treat the interaction Hamiltonian as in appendix C. The topic of different refractive indices is a research topic in itself and is not considered here since we are interested in the transition from the 2-D to 3-D transmission spectrum only.

E.2.2 Connection to the light Hamiltonian

In the final section of this appendix we present the analytical expressions for the terms $E^{n_1^c,n_2^v}_{\vec{k}_{\|}}$ and $\overline{E}^{n_1^c,n_2^v}_{\vec{k}_{\|}}$, which were derived in the appendix about the light Hamiltonian, (appendix D). In appendix D the terms $E^{n_1^c,n_2^v}_{\vec{k}_{\|}}$ and $\overline{E}^{n_1^c,n_2^v}_{\vec{k}_{\|}}$ are in equation (D.16) defined as,

$$E^{n_1^c,n_2^v}_{\vec{k}}(\omega) = \int \overline{f}_{n_1^c}(z)E_T(z,\omega)f_{n_2^v}(z)dz \quad , \tag{E.22a}$$

$$\overline{E}^{n_1^v,n_2^c}_{\vec{k}}(\omega) = \int \overline{f}_{n_1^v}(z)\overline{E}_T(z,\omega)f_{n_2^c}(z)dz \quad . \tag{E.22b}$$

The integration of equation (E.22) is performed by treating the three cases of combination of even and odd eigenfunctions separately.
$E^{n_1^c,n_2^v}_{\vec{k}_{\|}}$ in the case of even eigenfunctions f_{n_1} and f_{n_2} yields,

$$\begin{aligned} E^{n_1^c,n_2^v}_{\vec{k}_{\|}} = & \int_{-\frac{L_z}{2}}^{\frac{L_z}{2}} E_{in}\frac{2}{L_z}\cos\left(n_1^c\frac{\pi}{L_z}z\right)\cos\left(n_2^v\frac{\pi}{L_z}z\right)e^{ik_z z}dz \\ & +2\pi\frac{\omega}{c}\frac{c^2}{c_0^2}\frac{e^{ik_z\frac{L_z}{2}}}{k_z\frac{L_z}{2}}\frac{\sin\left(k_z\frac{L_z}{2}\right)}{k_z\frac{L_z}{2}}\sum_{q_1^v,q_2^c}P_{q_1^v,q_2^c}(\omega) \\ & \left(\frac{\cos\left((q_1^v-q_2^c)\frac{\pi}{2}\right)}{(q_1^v-q_2^c)^2\frac{\pi^2c^2}{L_z^2\omega^2}-1}+\frac{\cos\left((q_1^v+q_2^c)\frac{\pi}{2}\right)}{(q_1^v+q_2^c)^2\frac{\pi^2c^2}{L_z^2\omega^2}-1}\right) \\ & \left(\frac{\cos\left((n_1^c-n_2^v)\frac{\pi}{2}\right)}{(n_1^c-n_2^v)^2\frac{\pi^2c^2}{L_z^2\omega^2}-1}+\frac{\cos\left((n_1^c+n_2^v)\frac{\pi}{2}\right)}{(n_1^c+n_2^v)^2\frac{\pi^2c^2}{L_z^2\omega^2}-1}\right) \end{aligned} \tag{E.23}$$

$$
\begin{aligned}
&+\pi\frac{\omega}{c}\frac{c^2}{c_0^2}\frac{1}{k_z\frac{L_z}{2}}\sum_{q_1^v,q_2^c}P_{q_1^v,q_2^c}(\omega)\\
&\left(\frac{\delta_{q_1^v-q_2^c,n_1^c-n_2^v}(1+\delta_{q_1^v-q_2^c,0})+\delta_{q_1^v-q_2^c,n_1^c+n_2^v}}{(q_1^v-q_2^c)^2\frac{\pi^2c^2}{L_z^2\omega^2}-1}\right.\\
&\left.+\frac{\delta_{q_1^v+q_2^c,n_1^c-n_2^v}+\delta_{q_1^v+q_2^c,n_1^c+n_2^v}}{(q_1^v+q_2^c)^2\frac{\pi^2c^2}{L_z^2\omega^2}-1}\right)\\
&+2\pi\frac{\omega}{c}\frac{c^2}{c_0^2}\frac{e^{ik_z\frac{L_z}{2}}}{k_z\frac{L_z}{2}}\frac{\sin\left(k_z\frac{L_z}{2}\right)}{k_z\frac{L_z}{2}}\sum_{m_1^v,m_2^c}P_{m_1^v,m_2^c}(\omega)\\
&\left(\frac{\cos\left((m_1^v-m_2^c)\frac{\pi}{2}\right)}{(m_1^v-m_2^c)^2\frac{\pi^2c^2}{L_z^2\omega^2}-1}-\frac{\cos\left((m_1^v+m_2^c)\frac{\pi}{2}\right)}{(m_1^v+m_2^c)^2\frac{\pi^2c^2}{L_z^2\omega^2}-1}\right)\\
&\left(\frac{\cos\left((n_1^c-n_2^v)\frac{\pi}{2}\right)}{(n_1^c-n_2^v)^2\frac{\pi^2c^2}{L_z^2\omega^2}-1}+\frac{\cos\left((n_1^c+n_2^v)\frac{\pi}{2}\right)}{(n_1^c+n_2^v)^2\frac{\pi^2c^2}{L_z^2\omega^2}-1}\right)\\
&+\pi\frac{\omega}{c}\frac{c^2}{c_0^2}\frac{1}{k_z\frac{L_z}{2}}\sum_{m_1^v,m_2^c}P_{m_1^v,m_2^c}(\omega)\\
&\left(\frac{\delta_{m_1^v-m_2^c,n_1^c-n_2^v}(1+\delta_{m_1^v-m_2^c,0})+\delta_{m_1^v-m_2^c,n_1^c+n_2^v}}{(m_1^v-m_2^c)^2\frac{\pi^2c^2}{L_z^2\omega^2}-1}\right.\\
&\left.-\frac{\delta_{m_1^v+m_2^c,n_1^c-n_2^v}+\delta_{m_1^v+m_2^c,n_1^c+n_2^v}}{(m_1^v+m_2^c)^2\frac{\pi^2c^2}{L_z^2\omega^2}-1}\right)\qquad .
\end{aligned}
$$

Here and in the following quantum number q_x^λ is used for even eigenfunction states, while quantum number m_x^λ is used for odd eigenfunction states. $E_{\vec{k}_\parallel}^{n_1^c,n_2^v}$ in the case of odd eigenfunctions f_{n_1} and f_{n_2} yields,

$$
\begin{aligned}
\tilde{E}_{\vec{k}_\parallel}^{n_1^c,n_2^v} &= \int_{-\frac{L_z}{2}}^{\frac{L_z}{2}} E_{in}\frac{2}{L_z}\sin\left(n_1^c\frac{\pi}{L_z}z\right)\sin\left(n_2^v\frac{\pi}{L_z}z\right)e^{ik_zz}dz \qquad \text{(E.24)}\\
&+2\pi\frac{\omega}{c}\frac{c^2}{c_0^2}\frac{e^{ik_z\frac{L_z}{2}}}{k_z\frac{L_z}{2}}\frac{\sin\left(k_z\frac{L_z}{2}\right)}{k_z\frac{L_z}{2}}\sum_{q_1^v,q_2^c}P_{q_1^v,q_2^c}(\omega)
\end{aligned}
$$

$$\left(\frac{\cos\left((q_1^v-q_2^c)\frac{\pi}{2}\right)}{(q_1^v-q_2^c)^2\frac{\pi^2c^2}{L_z^2\omega^2}-1}+\frac{\cos\left((q_1^v+q_2^c)\frac{\pi}{2}\right)}{(q_1^v+q_2^c)^2\frac{\pi^2c^2}{L_z^2\omega^2}-1}\right)$$
$$\left(\frac{\cos\left((n_1^c-n_2^v)\frac{\pi}{2}\right)}{(n_1^c-n_2^v)^2\frac{\pi^2c^2}{L_z^2\omega^2}-1}-\frac{\cos\left((n_1^c+n_2^v)\frac{\pi}{2}\right)}{(n_1^c+n_2^v)^2\frac{\pi^2c^2}{L_z^2\omega^2}-1}\right)$$
$$+\pi\frac{\omega}{c}\frac{c^2}{c_0^2}\frac{1}{k_z\frac{L_z}{2}}\sum_{q_1^v,q_2^c}P_{q_1^v,q_2^c}(\omega)$$
$$\left(\frac{\delta_{q_1^v-q_2^c,n_1^c-n_2^v}(1+\delta_{q_1^v-q_2^c,0})-\delta_{q_1^v-q_2^c,n_1^c+n_2^v}}{(q_1^v-q_2^c)^2\frac{\pi^2c^2}{L_z^2\omega^2}-1}\right.$$
$$\left.+\frac{\delta_{q_1^v+q_2^c,n_1^c-n_2^v}-\delta_{q_1^v+q_2^c,n_1^c+n_2^v}}{(q_1^v+q_2^c)^2\frac{\pi^2c^2}{L_z^2\omega^2}-1}\right)$$
$$+2\pi\frac{\omega}{c}\frac{c^2}{c_0^2}\frac{e^{ik_z\frac{L_z}{2}}}{k_z\frac{L_z}{2}}\frac{\sin\left(k_z\frac{L_z}{2}\right)}{k_z\frac{L_z}{2}}\sum_{m_1^v,m_2^c}P_{m_1^v,m_2^c}(\omega)$$
$$\left(\frac{\cos\left((m_1^v-m_2^c)\frac{\pi}{2}\right)}{(m_1^v-m_2^c)^2\frac{\pi^2c^2}{L_z^2\omega^2}-1}-\frac{\cos\left((m_1^v+m_2^c)\frac{\pi}{2}\right)}{(m_1^v+m_2^c)^2\frac{\pi^2c^2}{L_z^2\omega^2}-1}\right)$$
$$\left(\frac{\cos\left((n_1^c-n_2^v)\frac{\pi}{2}\right)}{(n_1^c-n_2^v)^2\frac{\pi^2c^2}{L_z^2\omega^2}-1}-\frac{\cos\left((n_1^c+n_2^v)\frac{\pi}{2}\right)}{(n_1^c+n_2^v)^2\frac{\pi^2c^2}{L_z^2\omega^2}-1}\right)$$
$$+\pi\frac{\omega}{c}\frac{c^2}{c_0^2}\frac{1}{k_z\frac{L_z}{2}}\sum_{m_1^v,m_2^c}P_{m_1^v,m_2^c}(\omega)$$
$$\left(\frac{\delta_{m_1^v-m_2^c,n_1^c-n_2^v}(1+\delta_{m_1^v-m_2^c,0})-\delta_{m_1^v-m_2^c,n_1^c+n_2^v}}{(m_1^v-m_2^c)^2\frac{\pi^2c^2}{L_z^2\omega^2}-1}\right.$$
$$\left.-\frac{\delta_{m_1^v+m_2^c,n_1^c-n_2^v}-\delta_{m_1^v+m_2^c,n_1^c+n_2^v}}{(m_1^v+m_2^c)^2\frac{\pi^2c^2}{L_z^2\omega^2}-1}\right) \quad .$$

$E_{\vec{k}_{\parallel}}^{n_1^c,n_2^v}$ in the case of an odd eigenfunctions f_{n_1} and an even eigenfunction f_{n_2} yields,

$$\begin{aligned}
E_{\vec{k}_{\parallel}}^{n_1^c,n_2^v} &= \int\limits_{-\frac{L_z}{2}}^{\frac{L_z}{2}} E_{in}\frac{2}{L_z}\sin\left(n_1^c\frac{\pi}{L_z}z\right)\cos\left(n_2^v\frac{\pi}{L_z}z\right)e^{ik_z z}dz \qquad \text{(E.25)}\\
&+i2\pi\frac{\omega}{c}\frac{c^2}{c_0^2}\frac{e^{ik_z\frac{L_z}{2}}}{k_z\frac{L_z}{2}}\frac{\cos\left(k_z\frac{L_z}{2}\right)}{k_z\frac{L_z}{2}}\sum_{m_1^v,q_2^c}P_{m_1^v,q_2^c}(\omega)\\
&\left(\frac{\sin\left((m_1^v-q_2^c)\frac{\pi}{2}\right)}{(m_1^v-q_2^c)^2\frac{\pi^2c^2}{L_z^2\omega^2}-1}-\frac{\sin\left((m_1^v+q_2^c)\frac{\pi}{2}\right)}{(m_1^v+q_2^c)^2\frac{\pi^2c^2}{L_z^2\omega^2}-1}\right)\\
&\left(\frac{\cos\left((n_1^c-n_2^v)\frac{\pi}{2}\right)}{(n_1^c-n_2^v)^2\frac{\pi^2c^2}{L_z^2\omega^2}-1}-\frac{\cos\left((n_1^c+n_2^v)\frac{\pi}{2}\right)}{(n_1^c+n_2^v)^2\frac{\pi^2c^2}{L_z^2\omega^2}-1}\right)\\
&+i2\pi\frac{\omega}{c}\frac{c^2}{c_0^2}\frac{e^{ik_z\frac{L_z}{2}}}{k_z\frac{L_z}{2}}\frac{\cos\left(k_z\frac{L_z}{2}\right)}{k_z\frac{L_z}{2}}\sum_{q_1^v,m_2^c}P_{q_1^v,m_2^c}(\omega)\\
&\left(\frac{\sin\left((m_2^c-q_1^v)\frac{\pi}{2}\right)}{(m_2^c-q_1^v)^2\frac{\pi^2c^2}{L_z^2\omega^2}-1}-\frac{\sin\left((q_1^v+m_2^c)\frac{\pi}{2}\right)}{(q_1^v+m_2^c)^2\frac{\pi^2c^2}{L_z^2\omega^2}-1}\right)\\
&\left(\frac{\cos\left((n_1^c-n_2^v)\frac{\pi}{2}\right)}{(n_1^c-n_2^v)^2\frac{\pi^2c^2}{L_z^2\omega^2}-1}-\frac{\cos\left((n_1^c+n_2^v)\frac{\pi}{2}\right)}{(n_1^c+n_2^v)^2\frac{\pi^2c^2}{L_z^2\omega^2}-1}\right)\\
&+\pi\frac{\omega}{c}\frac{c^2}{c_0^2}\frac{1}{k_z\frac{L_z}{2}}\sum_{q_1^v,q_2^c}P_{q_1^v,q_2^c}(\omega)\\
&\left(\frac{\delta_{q_1^v-q_2^c,n_1^c-n_2^v}+\delta_{q_1^v-q_2^c,n_1^c+n_2^v}}{(q_1^v-q_2^c)^2\frac{\pi^2c^2}{L_z^2\omega^2}-1}\right.\\
&\left.+\frac{\delta_{q_1^v+q_2^c,n_1^c-n_2^v}+\delta_{q_1^v+q_2^c,n_1^c+n_2^v}}{(q_1^v+q_2^c)^2\frac{\pi^2c^2}{L_z^2\omega^2}-1}\right)\\
&+\pi\frac{\omega}{c}\frac{c^2}{c_0^2}\frac{1}{k_z\frac{L_z}{2}}\sum_{m_1^v,m_2^c}P_{m_1^v,m_2^c}(\omega)
\end{aligned}$$

$$\left(\frac{\delta_{m_1^v - m_2^c, n_1^c - n_2^v} + \delta_{m_1^v - m_2^c, n_1^c + n_2^v}}{(m_1^v - m_2^c)^2 \frac{\pi^2 c^2}{L_z^2 \omega^2} - 1} + \frac{\delta_{m_1^v + m_2^c, n_1^c - n_2^v} + \delta_{m_1^v + m_2^c, n_1^c + n_2^v}}{(m_1^v + m_2^c)^2 \frac{\pi^2 c^2}{L_z^2 \omega^2} - 1} \right) .$$

This concludes the appendix referring to the solution of the wave propagation equation (Maxwell's equation). The transformation of the E-field to the time domain is carried out by assuming the E-field to be equal to the optical carrier frequency ω_l, which is an approximation similar to the slowly varying envelope approximation. Note however, that this approximation breaks down at $(n_1^v \pm n_2^c)^2 \frac{\pi^2 c^2}{L_z^2 \omega_l^2} - 1 = 0$. In this case the sample thickness is a multiple of $\lambda/2$, where λ is the wavelength. So the numerical results shown in chapter 3 are for the case $L_z < \lambda/2$.

Bibliography

[1] H. Haken, "Quantum Field Theory of Solids, An Introduction", North-Holland, New-York, 1988.

Appendix F

The Heisenberg Equation of Motion

In this appendix the Heisenberg equation of motions are derived. The derivation of the equation of motion of the different operators requires the calculation of lengthy and time consuming commutator relations. We have omitted the actual calculations. However, the derivation of the first terms of the polarization are shown explicitly. The content of the appendix is as follows, first we present a listing of the resulting equations of motion, while in the second part we look at the simplified case of linear optics.

F.1 Equations of motion

The equation of motion in the Heisenberg picture is,

$$\frac{\partial \hat{\rho}}{\partial t} = \frac{i}{\hbar} [H, \hat{\rho}] \quad , \tag{F.1}$$

where $\hat{\rho}$ is the operator expectation value, which equation of motion we want to determine. H is the system Hamiltonian. The commutator is defined by,

$$[H,\hat{\rho}] = H\hat{\rho} - \hat{\rho}H \quad . \tag{F.2}$$

In the following, we will derive the equation of motion for the operator expectation values,

$$
\begin{aligned}
n^{n_1,n_2}_{e,\vec{k}_{\|}} &= \left\langle a^{\dagger}_{\vec{k}_{\|},n_1,c} a_{\vec{k}_{\|},n_2,c} \right\rangle \quad , && \text{(F.3a)}\\
n^{n_1,n_2}_{h,k} &= \left\langle b^{\dagger}_{\vec{k}_{\|},n_1} b_{\vec{k}_{\|},n_1} \right\rangle = \left\langle a_{\vec{k}_{\|},n_2,v} a^{\dagger}_{\vec{k}_{\|},n_1,v} \right\rangle \quad , && \text{(F.3b)}\\
p_{k,n_1,n_2} &= \left\langle b_{\vec{k}_{\|},n_1} a_{\vec{k}_{\|},n_2,c} \right\rangle = \left\langle a^{\dagger}_{\vec{k}_{\|},n_1,v} a_{\vec{k}_{\|},n_2,c} \right\rangle && \text{(F.3c)}\\
p^{*}_{k,n_1,n_2} &= \left\langle a^{\dagger}_{\vec{k}_{\|},n_1,c} b^{\dagger}_{\vec{k}_{\|},n_2} \right\rangle = \left\langle a^{\dagger}_{\vec{k}_{\|},n_1,c} a_{\vec{k}_{\|},n_2,v} \right\rangle \quad . && \text{(F.3d)}
\end{aligned}
$$

Here $b^{\dagger}_{\vec{k}_{\|},n}$ and $b_{\vec{k}_{\|},n}$ are the hole creation and annihilation operators, respectively. The free carrier Hamiltonian is in the electron-hole picture [1, p. 63],

$$
\begin{aligned}
H_{0,el} &= \sum_{\vec{k}_{\|},n} \epsilon_{\vec{k}_{\|},n,c} a^{\dagger}_{\vec{k}_{\|},n,c} a_{\vec{k}_{\|},n,c} + \epsilon_{\vec{k}_{\|},n,v} a^{\dagger}_{\vec{k}_{\|},n,v} a_{\vec{k}_{\|},n,v} \quad , && \text{(F.4a)}\\
&= \sum_{\vec{k}_{\|},n} \epsilon_{\vec{k}_{\|},n,c} a^{\dagger}_{\vec{k}_{\|},n,c} a_{\vec{k}_{\|},n,c} + \epsilon_{\vec{k}_{\|},n,v} \left(1 - b^{\dagger}_{\vec{k}_{\|},n} b_{\vec{k}_{\|},n}\right) && \text{(F.4b)}
\end{aligned}
$$

Since the origin of the energy is arbitrary, the constant term $\sum \epsilon_{\vec{k}_{\|},n,v}$ is usually omitted. In this case the free carrier Hamiltonian yields,

$$H_{0,el} = \sum_{\vec{k}_{\|},n} (E_{gab} + \epsilon_{e,\vec{k}_{\|},n}) a^{\dagger}_{\vec{k}_{\|},n,c} a_{\vec{k}_{\|},n,c} + \epsilon_{h,\vec{k}_{\|},n} b^{\dagger}_{\vec{k}_{\|},n} b_{\vec{k}_{\|},n} \quad . \tag{F.5}$$

In the following we will use the hole operator $b_{k_{\|},n}$ and the electron operator $a_{k_{\|},n}$. The energies $\epsilon_{e,\vec{k}_{\|},n}$ and $\epsilon_{h,\vec{k}_{\|},n}$ are

$$\epsilon_{e,\vec{k}_{\|},n^c} = \frac{\hbar^2 |\vec{k}_{\|}|^2}{2m_c} + ((n^c)^2 - 1)\frac{\hbar^2\pi^2}{2m_c L_z^2} \quad , \tag{F.6a}$$

$$\epsilon_{h,\vec{k}_{\|},n^v} = \frac{\hbar^2|\vec{k}_{\|}|^2}{2m_v} + ((n^v)^2-1)\frac{\hbar^2\pi^2}{2m_v L_z^2} \quad . \tag{F.6b}$$

m_c and m_v is the effective electron mass in the conduction and valence band respectively.
The equations of motion are now derived by calculating the commutator relations. However, one should remember that we are in the interaction picture, which in the case of the polarization $p_{\vec{k}_{\|},n_1,n_2}$ and $p^*_{\vec{k}_{\|},n_1,n_2}$ means,

$$\frac{\partial}{\partial t}\left(b_{\vec{k}_{\|},n_1}a_{\vec{k}_{\|},n_2}e^{-i\omega_l t}\right) = \frac{i}{\hbar}\left[H, b_{\vec{k}_{\|},n_1}a_{\vec{k}_{\|},n_2}e^{-i\omega_l t}\right] \quad , \tag{F.7a}$$

$$\frac{\partial}{\partial t}\left(a^\dagger_{\vec{k}_{\|},n_1}b^\dagger_{\vec{k}_{\|},n_2}e^{i\omega_l t}\right) = \frac{i}{\hbar}\left[H, a^\dagger_{\vec{k}_{\|},n_1}b^\dagger_{\vec{k}_{\|},n_2}e^{i\omega_l t}\right] \quad . \tag{F.7b}$$

Here, we assumed that $\omega_{\vec{k}_{\|},n_1^c} - \omega_{\vec{k}_{\|},n_2^v} \approx \omega_l$. In this case the equation of the polarization is,

$$\frac{\partial}{\partial t}\left(b_{\vec{k}_{\|},n_1}a_{\vec{k}_{\|},n_2}\right) = i\omega_l b_{\vec{k}_{\|},n_1}a_{\vec{k}_{\|},n_2} + \frac{i}{\hbar}\left[H, b_{\vec{k}_{\|},n_1}a_{\vec{k}_{\|},n_2}\right] \quad , \tag{F.8a}$$

$$\frac{\partial}{\partial t}\left(a^\dagger_{\vec{k}_{\|},n_1}b^\dagger_{\vec{k}_{\|},n_2}\right) = -i\omega_l a^\dagger_{\vec{k}_{\|},n_1}b^\dagger_{\vec{k}_{\|},n_2} + \frac{i}{\hbar}\left[H, a^\dagger_{\vec{k}_{\|},n_1}b^\dagger_{\vec{k}_{\|},n_2}\right] \tag{F.8b}$$

We will now present the equation of motions for the operator expectations values defined in Eq. (F.3). The equation of motion for the electron expectation value $n^{n_1^c,n_2^c}_{e,\vec{k}_{\|}}$ is,

$$\begin{aligned}
\frac{\partial n^{n_1^c,n_2^c}_{e,\vec{k}_{\|}}}{\partial t} = &+\frac{i}{\hbar}\left(\sum_{q_2^v} d_{v,c}^{\vec{k}_{\|},n_2^c,q_2^v} E^{n_2^c,q_2^v}_{\vec{k}_{\|}} p^*_{\vec{k}_{\|},n_1^c,q_2^v}\right. \\
&\left.-\sum_{q_1^v} d_{c,v}^{\vec{k}_{\|},q_1^v,n_1^c}\overline{E}^{q_1^v,n_1^c}_{\vec{k}_{\|}} p_{\vec{k},q_1^v,n_2^c}\right) \\
&-\frac{i}{\hbar}\sum_{\vec{q}_{\|}\neq\vec{0},q_1^c,q_2^c,q_3^c} n^{q_2^c,n_2^c}_{e,\vec{k}_{\|}} n^{q_1^c,q_3^c}_{e,\vec{k}_{\|}+\vec{q}_{\|}} V_{\vec{q}}^{q_1^c,q_2^c,q_3^c,n_1^c} \\
&+\frac{i}{\hbar}\sum_{\vec{q}_{\|}\neq\vec{0},q_1^c,q_3^c,q_4^c} n^{n_1^c,q_4^c}_{e,\vec{k}_{\|}} n^{q_1^c,q_3^c}_{e,\vec{k}_{\|}-\vec{q}_{\|}} V_{\vec{q}}^{q_1^c,n_2^c,q_3^c,q_4^c}
\end{aligned} \tag{F.9}$$

$$
\begin{aligned}
&-\frac{i}{\hbar}\sum_{\vec{q}_\parallel\neq\vec{0},q_1^c,q_2^v,q_3^v} p_{\vec{k}_\parallel,q_2^v,n_2^c}\,p^*_{\vec{k}_\parallel+\vec{q}_\parallel,q_1^c,q_3^v}\,V_{\vec{q}}^{q_1^c,q_2^v,q_3^v,n_1^c}\\
&+\frac{i}{\hbar}\sum_{\vec{q}_\parallel\neq\vec{0},q_2^v,q_3^v,q_4^c} p^*_{\vec{k}_\parallel,n_1^c,q_3^v}\,p_{\vec{k}_\parallel-\vec{q}_\parallel,q_2^v,q_4^c}\,V_{\vec{q}}^{n_2^c,q_2^v,q_3^v,q_4^c}\quad .
\end{aligned}
$$

The summation over the in-plane momentum $\vec{q}_\parallel$ is transformed to a summation over $\vec{k}'_\parallel$, since the Coulomb potential depends on the absolute value of the in-plane momentum $\vec{q}_\parallel$ only, (see appendix C). In this case, the equation of motion of the electron operator term $n_{e,\vec{k}_\parallel}^{n_1^c,n_2^c}$ yields,

$$
\begin{aligned}
\frac{\partial n_{e,\vec{k}_\parallel}^{n_1^c,n_2^c}}{\partial t} = &+\frac{i}{\hbar}\left(\sum_{q_2^v} d_{v,c}^{\vec{k}_\parallel,n_2^c,q_2^v}\,\overline{E}_{k}^{n_2^c,q_2^v}\,p^*_{\vec{k}_\parallel,n_1^c,q_2^v}\right.\\
&\left.-\sum_{q_1^v} d_{c,v}^{\vec{k}_\parallel,q_1^v,n_1^c}\,E_{\vec{k}}^{q_1^v,n_1^c}\,p_{\vec{k},q_1^v,n_2^c}\right)\\
&-\frac{i}{\hbar}\sum_{\vec{k}'_\parallel\neq\vec{k}_\parallel,q_1^c,q_2^c,q_4^c} n_{e,\vec{k}_\parallel}^{q_1^c,n_2^c}\,n_{e,\vec{k}'_\parallel}^{q_2^c,q_4^c}\,V_{|\vec{k}'_\parallel-\vec{k}_\parallel|}^{q_1^c,q_2^c,n_1^c,q_4^c}\\
&+\frac{i}{\hbar}\sum_{\vec{k}'_\parallel\neq\vec{k}_\parallel,q_1^c,q_3^c,q_4^c} n_{e,\vec{k}_\parallel}^{n_1^c,q_4^c}\,n_{e,\vec{k}'_\parallel}^{q_1^c,q_3^c}\,V_{|\vec{k}_\parallel-\vec{k}'_\parallel|}^{q_1^c,n_2^c,q_3^c,q_4^c}\\
&-\frac{i}{\hbar}\sum_{\vec{k}'_\parallel\neq\vec{k}_\parallel,q_1^c,q_2^v,q_3^v} p_{\vec{k}_\parallel,q_2^v,n_2^c}\,p^*_{\vec{k}'_\parallel,q_1^c,q_3^v}\,V_{|\vec{k}'_\parallel-\vec{k}_\parallel|}^{q_1^c,q_2^v,q_3^v,n_1^c}\\
&+\frac{i}{\hbar}\sum_{\vec{k}'_\parallel\neq\vec{k}_\parallel,q_2^v,q_3^v,q_4^c} p^*_{\vec{k}_\parallel,n_1^c,q_3^v}\,p_{\vec{k}_\parallel-\vec{q}_\parallel,q_2^v,q_4^c}\,V_{|\vec{k}_\parallel-\vec{k}'_\parallel|}^{q_1^c,q_2^v,q_3^v,n_1^c}\quad .
\end{aligned}
\tag{F.10}
$$

The equation of motion for the hole operator $n_{h,\vec{k}_\parallel}^{n_1^v,n_2^v}$ yields,

$$
\frac{\partial n_{h,\vec{k}_\parallel}^{n_1^v,n_2^v}}{\partial t} = \frac{i}{\hbar}\left(\sum_{q_1^c} d_{v,c}^{\vec{k}_\parallel,q_1^c,n_2^v}\,E_{\vec{k}_\parallel}^{q_1^c,n_2^v}\,p^*_{\vec{k}_\parallel,q_1^c,n_1^v}\right.
\tag{F.11}
$$

$$
\begin{aligned}
&-\sum_{q_1^v} d_{c,v}^{\vec{k}_\parallel,n_1^v,q_2^c}\overline{E}_{\vec{k}_\parallel}^{n_1^v,q_2^c} p_{\vec{k},n_2^v,q_2^c}\Bigg) \\
&-\frac{i}{\hbar}\sum_{\vec{q}_\parallel\neq\vec{0},q_1^v,q_3^v,q_4^v} n_{h,\vec{k}_\parallel}^{q_4^v,n_2^v} n_{h,\vec{k}_\parallel+\vec{q}_\parallel}^{q_3^v,q_1^v} V_{\vec{q}}^{q_1^v,n_1^v,q_3^v,q_4^v} \\
&+\frac{i}{\hbar}\sum_{\vec{q}_\parallel\neq\vec{0},q_1^v,q_2^v,q_3^v} n_{h,\vec{k}_\parallel}^{n_1^v,q_2^v} n_{h,\vec{k}_\parallel+\vec{q}_\parallel}^{q_3^v,q_1^v} V_{\vec{q}}^{q_1^v,q_2^v,q_3^v,n_2^v} \\
&-\frac{i}{\hbar}\sum_{\vec{q}_\parallel\neq\vec{0},q_1^c,q_3^v,q_4^c} p_{\vec{k}_\parallel,n_2^v,q_4^c} p^*_{\vec{k}_\parallel+\vec{q}_\parallel,q_1^c,q_3^v} V_{\vec{q}}^{q_1^c,n_2^v,q_3^v,q_4^c} \\
&+\frac{i}{\hbar}\sum_{\vec{q}_\parallel\neq\vec{0},q_1^c,q_2^v,q_4^c} p^*_{\vec{k}_\parallel,q_1^c,n_1^v} p_{\vec{k}_\parallel-\vec{q}_\parallel,q_2^v,q_4^c} V_{\vec{q}}^{q_1^c,q_2^v,q_3^v,q_4^c} \\
&+\frac{i}{\hbar}\sum_{\vec{q}_\parallel\neq\vec{0},q_1^v,q_4^v} n_{h,\vec{k}_\parallel}^{q_4^v,n_2^v} V_{\vec{q}}^{q_1^v,n_1^v,q_1^v,q_4^v} \\
&-\frac{i}{\hbar}\sum_{\vec{q}_\parallel\neq\vec{0},q_1^v,q_2^v} n_{h,\vec{k}_\parallel}^{n_1^v,q_2^v} V_{\vec{q}}^{q_1^v,q_2^v,q_1^v,n_2^v} \quad .
\end{aligned}
$$

The last two terms in Eq. (F.11) are equal and thus cancel each other. Furthermore, we again transform the in-plane momentum summation over $\vec{q}_\parallel$ to a summation over the in-plane momentum $\vec{k}'_\parallel$. In this case, the hole operator expectation value $n_{h,\vec{k}_\parallel}^{n_1^v,n_2^v}$ yields,

$$
\begin{aligned}
\frac{\partial n_{h,\vec{k}_\parallel}^{n_1^v,n_2^v}}{\partial t} &= \frac{i}{\hbar}\Bigg(\sum_{q_1^c} d_{v,c}^{\vec{k}_\parallel,q_1^c,n_2^v} E_{\vec{k}_\parallel}^{q_1^c,n_2^v} p^*_{\vec{k}_\parallel,q_1^c,n_1^v} \\
&\quad -\sum_{q_1^v} d_{c,v}^{\vec{k}_\parallel,n_1^v,q_2^c}\overline{E}_{\vec{k}_\parallel}^{n_1^v,q_2^c} p_{\vec{k},n_2^v,q_2^c}\Bigg) \\
&\quad -\frac{i}{\hbar}\sum_{\vec{k}'_\parallel\neq\vec{k}_\parallel,q_1^v,q_3^v,q_4^v} n_{h,\vec{k}_\parallel}^{q_4^v,n_2^v} n_{h,\vec{k}'_\parallel}^{q_3^v,q_1^v} V_{|\vec{k}'_\parallel-\vec{k}_\parallel|}^{q_1^v,n_1^v,q_3^v,q_4^v}
\end{aligned}
\tag{F.12}
$$

$$
\begin{aligned}
&+\frac{i}{\hbar}\sum_{\vec{k}'_{\|}\neq\vec{k}_{\|},q_1^v,q_2^v,q_3^v} n_{h,\vec{k}_{\|}}^{n_1^v,q_2^v} n_{h,\vec{k}'_{\|}}^{q_3^v,q_1^v} V_{|\vec{k}'_{\|}-\vec{k}_{\|}|}^{q_1^v,q_2^v,q_3^v,n_2^v} \\
&-\frac{i}{\hbar}\sum_{\vec{k}'_{\|}\neq\vec{k}_{\|},q_1^c,q_3^v,q_4^c} p_{\vec{k}_{\|},n_2^v,q_4^c} p^*_{\vec{k}'_{\|},q_1^c,q_3^v} V_{|\vec{k}'_{\|}-\vec{k}_{\|}|}^{q_1^c,n_2^v,q_3^v,q_4^c} \\
&+\frac{i}{\hbar}\sum_{\vec{k}'_{\|}\neq\vec{k}_{\|},q_1^c,q_2^v,q_4^c} p^*_{\vec{k}_{\|},q_1^c,n_1^v} p_{\vec{k}'_{\|},q_2^v,q_4^c} V_{|\vec{k}_{\|}-\vec{k}'_{\|}|}^{q_1^c,q_2^v,q_3^v,q_4^c} \qquad .
\end{aligned}
$$

The equation of motion for the polarization $p_{\vec{k}_{\|},n_1^v,n_2^c}$ yields,

$$
\begin{aligned}
\frac{\partial p_{\vec{k}_{\|},n_1^v,n_2^c}}{\partial t} = & -(i\omega_{\vec{k}_{\|}}^{n_1^v,n_2^c}+\gamma)p_{\vec{k}_{\|}}^{n_1^v,n_2^c} \\
& -\frac{i}{\hbar}\Bigg(-d_{c,v}^{\vec{k}_{\|},n_2^c,n_1^v} E_{\vec{k}_{\|}}^{n_2^c,n_1^v} \\
& +\sum_{q_1^c} n_{e,\vec{k}_{\|}}^{q_1^c,n_2^c} d_{c,v}^{\vec{k}_{\|},q_1^c,n_1^v} E_{\vec{k}_{\|}}^{q_1^c,n_1^v} + \sum_{q_2^v} n_{h,k}^{q_2^v,n_1^v} d_{c,v}^{\vec{k}_{\|},n_2^c,q_2^v} E_{\vec{k}_{\|}}^{n_2^c,q_2^v}\Bigg) \\
& +\frac{i}{\hbar}\sum_{\vec{q}_{\|}\neq\vec{0},q_1^c,q_3^c,q_4^c} n_{e,k+q}^{q_1^c,q_3^c} p_{\vec{k}_{\|},n_1^v,q_4^c} V_{\vec{q}_{\|}}^{q_1^c,n_2^c,q_3^c,q_4^c} \\
& -\frac{i}{\hbar}\sum_{\vec{q}_{\|}\neq\vec{0},q_1^v,q_2^v} p_{\vec{k}_{\|},q_1^v,n_2^v} V_{\vec{q}_{\|}}^{q_1^v,q_2^v,n_1^v,q_4^v} \\
& +\frac{i}{\hbar}\sum_{\vec{q}_{\|}\neq\vec{0},q_1^v,q_2^v,q_4^v} n_{h,\vec{k}_{\|}-\vec{q}_{\|}}^{q_4^v,q_2^v} p_{\vec{k}_{\|},q_1^v,n_2^c} V_{\vec{q}_{\|}}^{q_1^v,q_2^v,n_1^v,q_4^v} \\
& -\frac{i}{\hbar}\sum_{\vec{q}_{\|}\neq\vec{0},q_1^v,q_3^c,q_4^v} n_{h,\vec{k}_{\|}}^{q_4^v,n_1^v} p_{\vec{k}_{\|}+\vec{q}_{\|}}^{q_1^v,q_3^c} V_{\vec{q}_{\|}}^{q_1^v,n_2^c,q_3^c,q_4^v} \\
& +\frac{i}{\hbar}\sum_{\vec{q}_{\|}\neq\vec{0},q_1^v,q_3^c} p_{k+\vec{q}_{\|},q_1^v,q_3^c} V_{\vec{q}_{\|}}^{q_1^v,n_2^c,q_3^c,n_1^v} \\
& -\frac{i}{\hbar}\sum_{\vec{q}_{\|}\neq\vec{0},q_1^v,q_2^c,q_3^c} n_{e,\vec{k}_{\|}}^{q_2^c,n_2^c} p_{\vec{k}_{\|}+\vec{q}_{\|},q_1^v,q_3^c} V_{\vec{q}_{\|}}^{q_1^v,q_2^c,q_3^c,n_1^v} \qquad ,
\end{aligned}
\tag{F.13}
$$

while the equation of motion for the hermitian adjoint polarization operator $p_{\vec{k}_{\|},n_1^c,n_2^v}$ yields,

$$
\begin{aligned}
\frac{\partial p^*_{\vec{k}_{\|},n_1^c,n_2^v}}{\partial t} = \; & (i\omega_{\vec{k}_{\|}}^{n_1^c,n_2^v} - \gamma) p^*_{\vec{k}_{\|},n_1^c,n_2^v} \\
& + \frac{i}{\hbar} \left(-d_{v,c}^{\vec{k}_{\|},n_2^v,n_1^c} \overline{E}_{\vec{k}_{\|}}^{n_2^v,n_1^c} \right. \\
& \left. + \sum_{q_2^c} n_{e,\vec{k}_{\|}}^{n_1^c,q_2^c} d_{v,c}^{\vec{k}_{\|},n_2^v,q_2^c} E_{\vec{k}_{\|}}^{n_2^v,q_2^c} + \sum_{q_1^v} n_{h,k}^{n_2^v,q_1^v} d_{v,c}^{\vec{k}_{\|},q_1^v,n_1^c} E_{\vec{k}_{\|}}^{q_2^v,q_1^v} \right) \\
& - \frac{i}{\hbar} \sum_{\vec{q}_{\|}\neq\vec{0},q_1^c,q_2^c,q_3^c} n_{e,k+q}^{q_1^c,q_3^c} p^*_{\vec{k}_{\|},q_2^c,n_2^v} V_{\vec{q}_{\|}}^{q_1^c,q_2^c,q_3^c,n_1^c} \\
& + \frac{i}{\hbar} \sum_{\vec{q}_{\|}\neq\vec{0},q_1^v,q_4^v} p^*_{\vec{k}_{\|},n_1^c,q_4^v} V_{\vec{q}_{\|}}^{q_1^v,n_2^v,q_1^v,q_4^v} \\
& - \frac{i}{\hbar} \sum_{\vec{q}_{\|}\neq\vec{0},q_1^v,q_3^v,q_4^v} n_{h,\vec{k}_{\|}+\vec{q}_{\|}}^{q_3^v,q_1^v} p^*_{\vec{k}_{\|},n_1^v,q_4^v} V_{\vec{q}_{\|}}^{q_1^v,n_2^v,q_3^v,q_4^v} \\
& + \frac{i}{\hbar} \sum_{\vec{q}_{\|}\neq\vec{0},q_1^c,q_3^v,q_4^c} n_{e,\vec{k}_{\|}}^{n_1^c,q_4^c} p^*_{\vec{k}_{\|}+\vec{q}_{\|},q_1^c,q_3^v} V_{\vec{q}_{\|}}^{q_1^c,n_2^v,q_3^v,q_4^c} \\
& - \frac{i}{\hbar} \sum_{\vec{q}_{\|}\neq\vec{0},q_1^c,q_3^v} p^*_{k+\vec{q}_{\|},q_1^c,q_3^v} V_{\vec{q}_{\|}}^{q_1^c,n_2^v,q_3^v,n_1^c} \\
& + \frac{i}{\hbar} \sum_{\vec{q}_{\|}\neq\vec{0},q_1^c,q_2^v,q_3^v} n_{h,\vec{k}_{\|}}^{n_2^v,q_2^v} p^*_{\vec{k}_{\|}+\vec{q}_{\|},q_1^c,q_3^v} V_{\vec{q}_{\|}}^{q_1^c,q_2^v,q_3^v,n_1^c}
\end{aligned}
\tag{F.14}
$$

Here, the summation $\sum_{\vec{q}_{\|}\neq\vec{0}} p_{\vec{k}_{\|}} V_{\vec{q}_{\|}}$ in the equation of motion for the polarization and the summation $\sum_{\vec{q}_{\|}\neq\vec{0}} p^*_{\vec{k}_{\|}} V_{\vec{q}_{\|}}$ in the equation of motion for the hermitian adjoint polarizations has already been taken into account in the renormalization of the bandgap energy. These terms have to be neglected, since otherwise they would have been taken into account twice. Furthermore, we again transform the summation over $\vec{q}_{\|}$ to a summation over $\vec{k}_{\|}$.

The equation of motion for the polarization $p_{\vec{k}_{\|},n_1^v,n_2^c}$ yields,

$$
\begin{aligned}
\frac{\partial p_{\vec{k}_{\|},n_1^v,n_2^c}}{\partial t} \quad = \quad & -(i\omega_{\vec{k}_{\|}}^{n_1^v,n_2^c}+\gamma)p_{\vec{k}_{\|}}^{n_1^v,n_2^c} \\
& -\frac{i}{\hbar}\left(-d_{c,v}^{\vec{k}_{\|},n_2^c,n_1^v}E_{\vec{k}_{\|}}^{n_2^c,n_1^v}\right. \\
& \left.+\sum_{q_1^c} n_{e,\vec{k}_{\|}}^{q_1^c,n_2^c} d_{c,v}^{\vec{k}_{\|},q_1^c,n_1^v} E_{\vec{k}_{\|}}^{q_1^c,n_1^v} + \sum_{q_2^v} n_{h,k}^{q_2^v,n_1^v} d_{c,v}^{\vec{k}_{\|},n_2^c,q_2^v} E_{\vec{k}_{\|}}^{n_2^c,q_2^v}\right) \\
& +\frac{i}{\hbar}\sum_{\vec{k}'_{\|}\neq\vec{k}_{\|},q_1^c,q_3^c,q_4^c} n_{e,\vec{k}'_{\|}}^{q_1^c,q_3^c} p_{\vec{k}_{\|},n_1^v,q_4^c} V_{|\vec{k}'_{\|}-\vec{k}_{\|}|}^{q_1^c,n_2^c,q_3^c,q_4^c} \\
& +\frac{i}{\hbar}\sum_{\vec{k}'_{\|}\neq\vec{k}_{\|},q_1^v,q_2^v,q_4^v} n_{h,\vec{k}'_{\|}}^{q_4^v,q_2^v} p_{\vec{k}_{\|},q_1^v,n_2^c} V_{|\vec{k}_{\|}-\vec{k}'_{\|}|}^{q_1^v,q_2^v,n_1^v,q_4^v} \\
& -\frac{i}{\hbar}\sum_{\vec{k}'_{\|}\neq\vec{k}_{\|},q_1^v,q_3^c,q_4^v} n_{h,\vec{k}_{\|}}^{q_4^v,n_1^v} p_{\vec{k}'_{\|},q_1^v,q_3^c} V_{|\vec{k}'_{\|}-\vec{k}_{\|}|}^{q_1^v,n_2^c,q_3^c,q_4^v} \\
& +\frac{i}{\hbar}\sum_{\vec{k}'_{\|}\neq\vec{k}_{\|},q_1^v,q_3^c} p_{\vec{k}'_{\|},q_1^v,q_3^c} V_{|\vec{k}'_{\|}-\vec{k}_{\|}|}^{q_1^v,n_2^c,q_3^c,n_1^v} \\
& -\frac{i}{\hbar}\sum_{\vec{k}'_{\|}\neq\vec{k}_{\|},q_1^v,q_2^c,q_3^c} n_{e,\vec{k}_{\|}}^{q_2^c,n_2^c} p_{\vec{k}'_{\|},q_1^v,q_3^c} V_{|\vec{k}'_{\|}-\vec{k}_{\|}|}^{q_1^v,q_2^c,q_3^c,n_1^v} \quad ,
\end{aligned}
\tag{F.15}
$$

while the equation of motion for the hermitian adjoint polarization operator $p_{\vec{k}_{\|},n_1^c,n_2^v}$ yields,

$$
\begin{aligned}
\frac{\partial p^*_{\vec{k}_{\|},n_1^c,n_2^v}}{\partial t} \quad = \quad & (i\omega_{\vec{k}_{\|}}^{n_1^c,n_2^v}-\gamma)p^*_{\vec{k}_{\|},n_1^c,n_2^v} \\
& +\frac{i}{\hbar}\left(-d_{v,c}^{\vec{k}_{\|},n_2^v,n_1^c}\overline{E}_{\vec{k}_{\|}}^{n_2^v,n_1^c}\right. \\
& \left.+\sum_{q_2^c} n_{e,\vec{k}_{\|}}^{n_1^c,q_2^c} d_{v,c}^{\vec{k}_{\|},n_2^v,q_2^c} \overline{E}_{\vec{k}_{\|}}^{n_2^v,q_2^c} + \sum_{q_1^v} n_{h,k}^{n_2^v,q_1^v} d_{v,c}^{\vec{k}_{\|},q_1^v,n_1^c} \overline{E}_{\vec{k}_{\|}}^{q_2^v,q_1^v}\right)
\end{aligned}
\tag{F.16}
$$

$$
\begin{aligned}
& -\frac{i}{\hbar} \sum_{\vec{k}'_{\|} \neq \vec{k}_{\|}, q_1^c, q_2^c, q_3^c} n_{e,\vec{k}'_{\|}}^{q_1^c, q_3^c} p^*_{\vec{k}_{\|}, q_2^c, n_2^v} V_{|\vec{k}'_{\|} - \vec{k}_{\|}|}^{q_1^c, q_2^c, q_3^c, n_1^c} \\
& -\frac{i}{\hbar} \sum_{\vec{k}'_{\|} \neq \vec{k}_{\|}, q_1^v, q_3^v, q_4^v} n_{h,\vec{k}'_{\|}}^{q_3^v, q_1^v} p^*_{\vec{k}_{\|}, n_1^v, q_4^v} V_{|\vec{k}'_{\|} - \vec{k}_{\|}|}^{q_1^v, n_2^v, q_3^v, q_4^v} \\
& +\frac{i}{\hbar} \sum_{\vec{k}'_{\|} \neq \vec{k}_{\|}, q_1^c, q_3^v, q_4^c} n_{e,\vec{k}_{\|}}^{n_1^c, q_4^c} p^*_{\vec{k}'_{\|}, q_1^c, q_3^v} V_{|\vec{k}'_{\|} - \vec{k}_{\|}|}^{q_1^c, n_2^v, q_3^v, q_4^c} \\
& -\frac{i}{\hbar} \sum_{\vec{k}'_{\|} \neq \vec{k}_{\|}, q_1^c, q_3^v} p^*_{\vec{k}'_{\|}, q_1^c, q_3^v} V_{|\vec{k}'_{\|} - \vec{k}_{\|}|}^{q_1^c, n_2^v, q_3^v, n_1^c} \\
& +\frac{i}{\hbar} \sum_{\vec{k}'_{\|} \neq \vec{k}_{\|}, q_1^c, q_2^v, q_3^v} n_{h,\vec{k}_{\|}}^{n_2^v, q_2^v} p_{\vec{k}'_{\|}, q_1^c, q_3^v} V_{|\vec{k}'_{\|} - \vec{k}_{\|}|}^{q_1^c, q_2^v, q_3^v, n_1^c} \quad .
\end{aligned}
$$

This concludes the presentation of the equation of motions of the operator expectation values of interest. In the following section we present the governing equation of motion for the case of linear optics.

F.2 Linear optics

In this section we present the equations of motion for the case of linear optics. In chapter 3 we only consider the case of linear optics, so these are indeed the equations of interest. The equation of motion for the polarization operator $p_{\vec{k}_{\|}, n_1^v, n_2^c}$ is in the case of linear optics,

$$
\begin{aligned}
\frac{\partial p_{\vec{k}_{\|}, n_1^v, n_2^c}}{\partial t} = & -(i\omega_{\vec{k}_{\|}}^{n_1^v, n_2^c} + \gamma) p_{\vec{k}_{\|}}^{n_1^v, n_2^c} + \frac{i}{\hbar} d_{c,v}^{\vec{k}_{\|}, n_2^c, n_1^v} E_{\vec{k}_{\|}}^{n_2^c, n_1^v} \\
& + \frac{i}{\hbar} \sum_{\vec{k}'_{\|} \neq \vec{k}_{\|}, q_1^v, q_3^c} p_{\vec{k}'_{\|}, q_1^v, q_3^c} V_{|\vec{k}'_{\|} - \vec{k}_{\|}|}^{q_1^v, n_2^c, q_3^c, n_1^v} \quad ,
\end{aligned} \tag{F.17}
$$

while the equation of motion for the hermitian adjoint polarization operator $p_{\vec{k}_{\parallel},n_1^c,n_2^v}$ in the case of linear optics is,

$$
\begin{aligned}
\frac{\partial p^*_{\vec{k}_{\parallel},n_1^c,n_2^v}}{\partial t} &= (i\omega^{n_1^c,n_2^v}_{\vec{k}_{\parallel}} - \gamma)p^*_{\vec{k}_{\parallel},n_1^c,n_2^v} - \frac{i}{\hbar} d_{v,c}^{\vec{k}_{\parallel},n_2^v,n_1^c} \overline{E}^{n_2^v,n_1^c}_{\vec{k}_{\parallel}} \\
&- \frac{i}{\hbar} \sum_{\vec{k}'_{\parallel} \neq \vec{k}_{\parallel},q_1^c,q_3^v} p^*_{\vec{k}'_{\parallel},q_1^c,q_3^v} V^{q_1^c,n_2^v,q_3^v,n_1^c}_{|\vec{k}'_{\parallel}-\vec{k}_{\parallel}|} \quad .
\end{aligned}
\tag{F.18}
$$

This concludes the derivation of the equation of motion of the polarization operator used in chapter 3.

Bibliography

[1] For a textbook discussion see: W. W. Chow, S. W. Koch, M. Sargent III, "Semiconductor Laser Physics", Springer-Verlag, Berlin, 1994.

Ph. D. theses from IMM

1. **Larsen, Rasmus.** (1994). *Estimation of visual motion in image sequences. xiv* + 143 pp.
2. **Rygard, Jens Moberg.** (1994). *Design and optimization of flexible manufacturing systems. xiii* + 232 pp.
3. **Lassen, Niels Christian Krieger.** (1994). *Automated determination of crystal orientations from electron backscattering patterns. xv* + 136 pp.
4. **Melgaard, Henrik.** (1994). *Identification of physical models. xvii* + 246 pp.
5. **Wang, Chunyan.** (1994). *Stochastic differential equations and a biological system. xxii* + 153 pp.
6. **Nielsen, Allan Aasbjerg.** (1994). *Analysis of regularly and irregularly sampled spatial, multivariate, and multi-temporal data. xxiv* + 213 pp.
7. **Ersbøll, Annette Kjær.** (1994). *On the spatial and temporal correlations in experimentation with agricultural applications. xviii* + 345 pp.
8. **Møller, Dorte.** (1994). *Methods for analysis and design of heterogeneous telecommunication networks.* Volume 1-2, *xxxviii* + 282 pp., 283-569 pp.
9. **Jensen, Jens Christian.** (1995). *Teoretiske og eksperimentelle dynamiske undersøgelser af jernbanekøretøjer.* ATV Erhvervsforskerprojekt EF 435. *viii* + 174 pp.
10. **Kuhlmann, Lionel.** (1995). *On automatic visual inspection of reflective surfaces.* ATV Erhvervsforskerprojekt EF 385. Volume 1, *xviii* + 220 pp., (Volume 2, *vi* + 54 pp., fortrolig).
11. **Lazarides, Nikolaos.** (1995). *Nonlinearity in superconductivity and Josephson Junctions. iv* + 154 pp.
12. **Rostgaard, Morten.** (1995). *Modelling, estimation and control of fast sampled dynamical systems. xiv* + 348 pp.
13. **Schultz, Nette.** (1995). *Segmentation and classification of biological objects. xiv* + 194 pp.
14. **Jørgensen, Michael Finn.** (1995). *Nonlinear Hamiltonian systems. xiv* + 120 pp.

15. **Balle, Susanne M.** (1995). *Distributed-memory matrix computations.* *iii* + 101 pp.
16. **Kohl, Niklas.** (1995). *Exact methods for time constrained routing and related scheduling problems.* *xviii* + 234 pp.
17. **Rogon, Thomas.** (1995). *Porous media: Analysis, reconstruction and percolation.* *xiv* + 165 pp.
18. **Andersen, Allan Theodor.** (1995). *Modelling of packet traffic with matrix analytic methods.* *xvi* + 242 pp.
19. **Hesthaven, Jan.** (1995). *Numerical studies of unsteady coherent structures and transport in two-dimensional flows.* Risø-R-835(EN) 203 pp.
20. **Slivsgaard, Eva Charlotte.** (l995). *On the interaction between wheels and rails in railway dynamics.* *viii* + 196 pp.
21. **Hartelius, Karsten.** (1996). *Analysis of irregularly distributed points.* *xvi* + 260 pp.
22. **Hansen, Anca Daniela.** (1996). *Predictive control and identification - Applications to steering dynamics.* *xviii* + 307 pp.
23. **Sadegh, Payman.** (1996). *Experiment design and optimization in complex systems.* *xiv* + 162 pp.
24. **Skands, Ulrik.** (1996). *Quantitative methods for the analysis of electron microscope images.* *xvi* + 198 pp.
25. **Bro-Nielsen, Morten.** (1996). *Medical image registration and surgery simulation.* *xxvii* + 274 pp.
26. **Bendtsen, Claus.** (1996). *Parallel numerical algorithms for the solution of systems of ordinary differential equations.* *viii* + 79 pp.
27. **Lauritsen, Morten Bach.** (1997). *Delta-domain predictive control and identification for control.* *xxii* + 292 pp.
28. **Bischoff, Svend.** (1997). *Modelling colliding-pulse mode-locked semiconductor lasers.* *xxii* + 217 pp.